The Static and Dynamic Aspects of the Jahn-Teller and Pseudo-Jahn-Teller Interactions in Highly Symmetric Multimode Molecular Systems

A Thesis

Submitted for the Degree of

DOCTOR OF PHILOSOPHY

By

THIMMAKONDU SAMY VENKATESAN

SCHOOL OF CHEMISTRY

UNIVERSITY OF HYDERABAD

HYDERABAD 500 046

INDIA

March 2007

STATEMENT

I hereby declare that the matter embodied in this thesis is the result of investigations carried out by me in the School of Chemistry, University of Hyderabad, Hyderabad, under the supervision of **Prof. Susanta Mahapatra**.

In keeping with the general practice of reporting scientific observations, due acknowledgment has been made wherever the work described is based on the findings of other investigators.

Hyderabad-46 (**Thimmakondu Samy Venkatesan**)

March 2007

CERTIFICATE

Certified that the work contained in this thesis entitled "The static and dynamic aspects of the Jahn-Teller and pseudo-Jahn-Teller interactions in highly symmetric multimode molecular systems" has been carried out by Mr. **T. S. Venkatesan** under my supervision and the same has not been submitted elsewhere for a degree.

Hyderabad-46
March 2007

(**Prof. Susanta Mahapatra**)
Thesis Supervisor

Dean
School of Chemistry
University of Hyderabad
Hyderabad 500 046
INDIA

ACKNOWLEDGMENTS

With high regards and profound respect, I wish to express my deep sense of gratitude to **Prof. Susanta Mahapatra** for his constant encouragement throughout my research work and introducing me to this fascinating field of research. I have learnt a lot from his meticulous planning, dedication and hard work. The experience that I gained in the last five years through his suggestions, comments and even critiques will help me in all my future endeavors.

I extend my sincere thanks to the former and present Deans, School of Chemistry, for providing all necessary facilities to carry out my research work. I also thank all the faculty members for their inspiration. I would like to extend my thanks to Centre for Modelling Simulation and Design (CMSD) for providing all the computational facilities.

I am indebted to Profs. H. Köppel and L. S. Cederbaum, University of Heidelberg, Germany, for fruitful discussions on the joint collaborative project which is part of my PhD thesis. I would like to extend my thanks to Prof. H. D. Meyer for his very prompt and informative e-mail replies on the time-dependent calculations.

I thank Prof. N. Sathyamurthy, IIT Kanpur, for his interest in my research carrier and giving me a position in the initial days.

I express my heartful thanks to my lab mates Dr. R. Padmanaban, Subhas, Jayachander, Rajesh, Siva, Rakesh, Tanmoy and Susanta for many fruitful discussions and their warm company on various occasions. Special thanks to Gireesh for his wonderful company in the initial days of my research work. Their association will remain forever in my memory.

I am very thankful to all the research scholars in School of Chemistry for their suggestions and useful discussions in various regards of my research work.

I take this opportunity to thank my Tamil friends, Sundaram, Madhu, Senthil, Vairam, Prakash, Balaram, Selva, Arumugam, Francis, Dhamu, Jhoney, Gnanam,

Gaja, Kannapiran, Arun, Murali, Vijayan, Partha, Viji, and Drs. Mari, Philip, Nattamai, Perumal, and Anbu, who made my stay a very pleasant one and providing cheerful atmosphere in the campus.

Special thanks to my friend, advisor and badminton partner Prasanna Deep for his warm company on and off the field. Thanks to Mouli mama for teaching me the philosophy of life. I would like to extend my thanks to Dr. Grace for a careful reading of the entire thesis and suggestions.

Thanks to all the buddies who played badminton and cricket with me and made the break from research a very enjoyable one.

I would like to thank all my friends in the HCU campus for their warm company and affection on various occasions.

I take this opportunity in thanking all my teachers, especially Profs. Vaidhiyanathan, M. S. Ramachandran, S. Rajagopal, Dr. Liakath Ali Khan, Nousath Ali, JK, KSH, Mr(s). A. H. Venkatraman, Dhanabalan, M. Murugesan (late), and many more for whatever I am today.

As I have lot of friends, it is indeed a difficult task to mention them all here. I acknowledge each and every one of them for their contribution from the bottom of my heart.

Thanks to Swapna for her constant encouragement and support.

I thank all my relatives, in particular, Mrs. Ashamai, Maheswari, Gayathri and Mr. Rajagopal for their moral support, kind words and affection towards me.

I take immense pleasure in thanking my parents (**T. B. Samy** and **T. S. Mangaleshwari**) and brothers (Premnath and Jegannath) for their constant encouragement and support throughout my life. I also thank my sister-in-laws (Hemamalini and Meera) and their kids (Shanjay and Gokul) for their love and affection.

T. S. Venkatesan

List of Abbreviations

$\mathbf{1}_n$	n-dimensional unit matrix
BO	Born-Oppenheimer
cc-pVTZ	correlation consistent polarized valence triple - ζ
CIs	Conical intersection(s)
CP	Cyclopropane
CP^+	Cyclopropane radical cation
ET	Ethane
ET^+	Ethane radical cation
FC	Franck-Condon
FWHM	Full-width at half-maximum
JT	Jahn-Teller
LVC	Linear vibronic coupling
MCTDH	Multiconfiguration time-dependent Hartree
MP2	Second order Møller-Plesset perturbation theory
OVGF	outer valence Green's function
PES(s)	Potential energy surface(s)
PJT	pseudo-Jahn-Teller
QVC	Quadratic vibronic coupling
RT	Renner-Teller
SPFs	Single particle functions
VC	Vibronic coupling
WP	Wave packet

Contents

Chapter 1

Introduction

1.1 A brief overview of the vibronic coupling

The Jahn-Teller (JT) effect [1–8] - that a nonlinear molecule in an orbitally degenerate state spontaneously distorts to a configuration of reduced symmetry - is one of the most fascinating phenomena in chemistry. Since the classical work of Longuet-Higgins *et al.* [9–11] on the JT effect in a doubly degenerate (E) electronic state caused by the degenerate (e) vibrational modes (the so-called $E\times e$-JT effect), much effort has been devoted to elucidate its nature and importance in a wide variety of systems including, transition metal complexes [12], solid-state physics and chemistry [13–15], organic hydrocarbons, radicals and ions [2, 6, 16–20], and fullerenes [21]. The advent of high-resolution spectroscopic measurement techniques [22,23] have further motivated to invention of benchmark theoretical models [24–28] to better understand the static and dynamical aspects of multimode JT interactions in many other polyatomic molecular systems (see, for example, the review articles on the subject in Refs. [7] and [17] and the references therein).

The study of the splitting of degenerate electronic state of a nonlinear molecule was indeed the first treatment of conical intersections (CIs) [17, 29–38], published

in 1937 [1]. An overview of this interesting topic has been presented in the next section. This configurational instability of the molecules cause an intricate mixing of electronic and nuclear motions. Such a mixing, referred to as vibronic coupling (VC) [2–6, 39], leads to a breakdown of the well-known Born-Oppenheimer (BO) approximation [40, 41], and opens up new mechanistic pathways for the decay of excited molecular electronic states [17, 38, 39]. In this situation, the nuclear motion ceases to be confined to a single potential energy surface (PES), and electronic transitions take place during nuclear vibration [42, 43]. In order to deal with this nonadiabatic situation, it is useful to resort to a diabatic electronic basis [44] in order to avoid the singular nature of the associated nonadiabatic coupling elements in an adiabatic electronic basis.

In 1957, Öpik and Pryce first noted that effects similar to the JT effect may be inherent in systems with near (quasi-degenerate or pseudo-degenerate) electronic states [10]. This is known as pseudo-Jahn-Teller (PJT) effect in the literature [7, 17, 38, 45–47]. In the following year in 1958, Longuet-Higgins along with Öpik, Pryce and Sack worked on the dynamic aspects of the JT effect, that is to say, the interaction between the motions of the nuclei and the electrons [9]. In general, the dynamical coupling between the electronic and nuclear motions presents a complex problem to which the solution can only be obtained by lengthy numerical methods. However, there is one relatively simple case which can be studied algebraically, namely that of a doubly degenerate electronic state (E) whose degeneracy is removed in the first order by a doubly degenerate vibration (e). This situation occurs rather widely in physics and chemistry [2, 6, 9]. Other interesting cases in which non-degenerate vibrational modes involved in the JT activity are also found in the literature [2, 6, 13, 17, 24, 25, 48]. This can only be encountered in molecules possessing two- or four- fold axes of symmetry, for example, C_4, C_{4v}, C_{4h}, D_4, D_{2d}, D_{4h}, S_4, and D_{4d} point groups. This is known as $(E \times b)$-JT effect since the degeneracy is lifted by vibrational modes of b symmetries. Usually the vibrational modes of e symmetries participate in PJT activity

in this case. The other complicated cases are discussed elsewhere in the literature (see, for example, the Refs. [2] and [6] and the references therein).

Typically, the $(E \times e)$-JT CI exhibits a "Mexican hat" type of topography in the linear coupling limit - the lower potential surface comprising three equivalent minima and three equivalent saddle points linking pairs of minima and the upper one resembles a conical shape with its vertex touching the lower one at the point of 3-fold-symmetry [49]. Especially near CIs, the nonadiabatic coupling terms are of singular strength. In case of multimode CIs this often leads to a highly diffuse spectral envelope - the vibrational levels of the upper surface are completely mixed with the quasi-continuum of vibrational levels of the lower surface [17]. In a time-dependent picture this generally yields a femtosecond non-radiative decay of the upper electronic state [17, 25, 27, 28, 50].

Although linear molecules look like exceptions from the JT theorem, they too experience similar instabilities in their degenerate or pseudo-degenerate states when quadratic terms of VC are considered. This is known in the literature as the Renner-Teller (RT) coupling or glancing intersection, following the original paper of Renner in 1934 [51] that describes the vibronic interactions in degenerate Π electronic states of linear triatomic molecules. The JT effect as well as the PJT effect have been studied extensively over the past few decades (see, for example, the Refs. [2–8, 17, 19, 38] and the references therein). The JT effect has played a pivotal role in one of most important discoveries of modern physics - high temperature superconductivity (Nobel Prize in 1987) [52].

The concept of VC and the associated JT and PJT effects is of a much wider relevance, however, and applies to essentially all symmetric polyatomic molecular systems. The applications of VC theory cover the full range of molecular spectroscopy, including, in particular, optical and photoelectron spectroscopy. Typical spectroscopic phenomena associated with vibronic interactions are the appearance of nominally forbidden electronic bands, the excitation of nontotally symmetric modes, or unusual and complex vibronic fine structures of electronic

spectra [17, 38, 39]. In this thesis, our aim is to solve the complex vibronic spectra and study the nonradiative decay dynamics of multimode JT and related systems with the help of *ab initio* electronic structure calculations and quantum dynamical simulations.

The electronic states displaying the JT and PJT interactions are probed through photoelectron spectroscopic experiment. The photoelectron bands are calculated by solving the time-independent or time-dependent Schrödinger equation. The nonradiative decay dynamics of excited states is studied by recording the electronic population in time. Here, we again note that in order to deal with the PES crossings and to avoid the singular nature of the associated nonadiabatic coupling in an adiabatic electronic basis, we resort to a diabatic electronic basis. Model Hamiltonians are constructed on this basis and the relevant electronic coupling parameters of the Hamiltonians are calculated by *ab initio* methods. Multidimensional multiple CIs are established in the studied systems. The specific examples studied in this thesis are: the JT and PJT interactions in (i) the $\widetilde{X}^2A_1'$-$\widetilde{C}^2E'$ electronic manifold of tri-atomic boron cluster (B_3), (ii) the $\widetilde{X}^2E_g$-$\widetilde{A}^2A_{1g}$ electronic manifold of ethane radical cation (ET^+), and (iii) the $\widetilde{X}^2E'$-$\widetilde{A}^2E''$ electronic manifold of cyclopropane radical cation (CP^+). A full dimensional study including the most relevant vibrational degrees of freedom in case of (iii) is also carried out by the wave packet (WP) propagation approach within the multi-configuration time-dependent Hartree (MCTDH) scheme [53–55].

The three molecular systems noted above are susceptible to JT instabilities in their orbitally degenerate electronic states via suitable symmetry reducing nuclear displacements. They also undergo symmetry allowed PJT type of interactions with the neighboring electronic states via suitable vibrational modes. While electronic states of the CP^+ and ET^+ are probed by photoionizing the corresponding neutral species, anion photoelectron spectroscopy of B_3^- was used to probe the electronic states of B_3. The experimental photoelectron spectra of these systems reveal signatures of VC effects, and therefore, construction of

VC model using the elementary symmetry selection rules becomes a necessity in order to study the excited electronic states of these molecular systems. Here we note that we have used the concept of linear vibronic coupling (LVC) model of Köppel, Domcke, and Cederbaum [17] and extended it wherever necessary in terms of the dimensionless normal coordinates of the molecular system in order to deal with small-amplitude vibrations on the multi-sheeted coupled electronic states. Moreover, the motivation behind all these studies stems from the fact that dynamical calculations on these systems are not available in the literature. The time-independent quantum dynamical simulations are done by developing softwares in-house with the help of the Lanczos algorithm [56] (cf. Appendix A). On the other hand, the time-dependent quantum dynamical studies are done using the Heidelberg MCTDH package [53–55].

1.2 The importance of CIs and their ramifications in chemical dynamics

The well-known Wigner-von Neumann "non-crossing rule" guarantees for diatomic molecules that electronic states of the same symmetry cannot cross but must avoid each other [57]. This is due to the fact that the inter-atomic distance is the only available coordinate. But this rule fails when applied to polyatomic molecules, for which electronic states of the same symmetry are allowed to cross, due to the existence of three or more nuclear degrees of freedom. When electronic states do cross, they can form a CI, which is a (3N-6-2)-dimensional seam (or hyperline) of the electronic energy for an N-atom molecule. Historically, the crossing of electronic PESs was discovered in the early 1930s [1, 29, 51]. Approximately about two decades latter an intense theoretical research activity started in this area attempting to identify and characterize different kinds of curve crossings in molecules. Research papers by Teller [29] and by Herzberg and Longuet-

Higgins [30] are particularly notable in this context. They provide deep insights into the subject predicting a variety of physical phenomena that emerge from PES crossings. The field has undergone a monumental growth thereafter following the outstanding contributions of several research groups [2–4, 6, 13, 17, 31, 58–60].

A typical dynamical outcome that bears the signature of CIs of PESs is the femtosecond decay of excited molecular electronic states [17, 38, 39]. The corresponding electronic transition reveals seemingly diffuse and overlapping bands that exhibit highly complex and dense line structure under high resolution. On the lower electronic state (adiabatic) the phenomena of the geometric phase [61–63], bifurcation of the wave packet [64] and dissipative vibrational motions [65] are observed. We note that, at such intersections, the non-adiabatic coupling elements exhibit a singularity, causing a complete breakdown of the BO approximation [17].

It is now fairly accepted that CIs serve as the "bottleneck" in photophysical and photochemical transitions [33–35] and also referred to as *photochemical funnels* in the literature [66]. The book edited by Domcke, Yarkony and Köppel represents an excellent collection of articles in this emerging area of chemical dynamics [38]. Strictly speaking, with respect to the mainstream computational chemistry which considers electronic structure calculations of polyatomic molecules with fixed nuclei and the nuclear dynamics along the adiabatic PES, the CIs and the associated JT and PJT vibronic coupling effects are important extensions which take into account the coupling between the electronic and nuclear motions [7].

1.3 Current state of the research and organization of the thesis

As mentioned in section 1.1, dynamical calculations are not available on B_3, ET^+, and CP^+. Therefore, in the following paragraphs, we will give a brief account of the available experimental and electronic structure results of the representative examples cited above.

The photodetachment spectrum of B_3^- is recorded at three different photon energies: 355 (3.496 eV), 266 (4.661 eV), and 193 *nm* (6.424 eV) by Zhai *et al.* [67]. The overall spectrum indicated four bands; three of them are attributed to the ground $\widetilde{X}^2A_1'$ and the excited $\widetilde{A}^2A_2''$ and $\widetilde{C}^2E'$ electronic states of B_3 and one the appearing in the 4.0-5.0 eV electron binding energy range is due to a two-electron transition, highlighting strong electron correlation in the boron trimer [67]. Despite a poor energy resolution, the experimental band indicated an unidentified sharp splitting of $\sim 1100\ cm^{-1}$ in the $\widetilde{C}^2E'$ band which is found to be due to a progression along the JT active vibrational mode ν_2 [68].

Electronic structure calculations elucidating various stationary points of the PESs and the vertical ionization energies of boron clusters and their anions are carried out in the literature at various levels of theory [67]. However, a dynamical study to unravel the vibrational structure of the photoelectron band is missing till date. This motivated us to devise a theoretical model to treat the nuclear dynamics of B_3 cluster with the aid of an *ab initio* based quantum dynamical approach [68]. In this approach, we construct a model vibronic Hamiltonian of the final $\widetilde{X}^2A_1'$ -$\widetilde{C}^2E'$ coupled electronic manifold of B_3 in terms of the dimensionless normal coordinates of the electronic ground state of B_3^- in a diabatic electronic representation [44] and simulate the nuclear dynamics in this manifold to calculate the photodetachment spectrum.

The photoelectron spectrum of ethane (ET) in a wide range of electron binding energy has been recorded by different experimental groups using Ne I, He I, He

II and synchrotron radiations as ionization sources [69–71]. Among these, the He I (21.22 eV) recording of Turner *et al.* [69] seems to be better resolved. The photoelectron band observed in the 11.5-40.0 eV electron binding energy range revealed ionization from three outer valence and two inner valence orbitals of ET. The spectrum has been subdivided into three ionization regions: 11.5-14.5 eV, 14.5-16.5 eV, and 20.0-40.0 eV. The first ionization region has three band maxima occurring at $\sim$ 12.00 eV, $\sim$ 12.72 eV, and $\sim$ 13.50 eV [69]. The ionization bands expected in this region are due to ^2E_g and $^2A_{1g}$ electronic states of the ET^+. The vibrational progression with irregular spacings begins at $\sim$ 11.57 eV [69]. The bands at 12.00 and 12.75 eV are attributed to the components of the JT split ^2E_g electronic manifold and one at 13.50 eV is due to the $^2A_{1g}$ electronic state of ET^+ [69]. These bands are highly overlapping and bear signatures of PJT interactions between the $\widetilde{X}^2E_g$ and $\widetilde{A}^2A_{1g}$ electronic states of the radical cation. The second band is attributed to the ^2E_u electronic state of ET^+ and the features in the 20-26 eV energy region are associated with the ionizations from the inner $2a_{2u}$ and $2a_{1g}$ molecular orbitals of ET. Above 25 eV, the structures are featureless [71].

Theoretical studies were carried out in the past in order to elucidate various stationary points on the PESs of ET^+ [72, 73]. These earlier electronic structure calculations reported an ambiguity on the characterization of the ground electronic state of ET^+. Despite these electronic structure studies, a rigorous dynamical study to unravel the vibrational structures of the photoelectron band is still missing in the literature. In our present work, we aim to reconsider the electronic structure calculations with increased sophistication and examine the vibronic structure of the photoelectron band for the first time with the aid of a model vibronic coupling approach [17]. Here, we consider the first photoelectron band observed in the 11.5-14.5 eV ionization energy range pertinent to the vibronic structure of the $\widetilde{X}^2E_g$ -$\widetilde{A}^2A_{1g}$ electronic manifold of ET^+.

The photoelectron spectrum of cyclopropane (CP) has been recorded by vari-

ous experimental groups [69, 74–81]. Among these, the recent 21.22 eV recording of Holland *et al.* [75] using synchrotron and He I radiation as ionization sources seems to be better resolved. The photoelectron band recorded by these authors in the 9-20 eV electron binding energy range exhibits a twin band centered around $\sim$ 11 eV, a broad band at $\sim$ 13.2 eV, and two strongly overlapping bands at $\sim$ 15.7 and $\sim$ 16.5 eV (cf. Fig. 5.1). These bands emerge from the ionization of an electron from the $3e'$, $1e''$, $3a_1'$, and $1a_2''$ molecular orbitals of CP, respectively. Among them, the first two bands are of special interest and are considered here. They represent the vibronic structures of the JT split $\widetilde{X}^2E'$ and $\widetilde{A}^2E''$ electronic states of CP^+. The first photoelectron band exhibits a strong first-order splitting indicated by the large separation between the maxima of the twin band. The observed energy difference of $\sim$ 0.78 eV [75] between the maxima is explained as being due to JT distortion from the equilibrium geometry of CP. This is further confirmed by recording the optical Rydberg emission spectrum of CP which exhibits a similar splitting of $\sim$ 6400 cm^{-1} [77]. The second band exhibits a highly diffuse pattern and is structureless. This indicates that the underlying nuclear motion in the $\widetilde{A}^2E''$ electronic manifold is strongly perturbed by complex vibronic interactions. We have unraveled these issues and the details are presented in chapter 5.

In the past, theoretical studies were carried out to understand the structural changes of CP resulting from the photoionization process [82–86]. These results agree that the first vertical ionization of CP occurs from a degenerate pair of in-plane e' orbitals. Moreover, the photoelectron spectrum was compared with the vertical ionization energies calculated using Koopman's theorem [87] and also by considering electron reorganization and correlation effects using a many-body Green's function method [84, 88]. The theoretical value of the vertical ionization potential of $\sim$ 10.7 eV obtained by von Niessen, Cederbaum, and Kraemer [88] using the Green's function method is in very good agreement with the experimental value of $\sim$ 10.6 eV. Bouma *et al.* [86] reported a value of $\sim$ 10.3

eV for the same quantity. Energy minimization studies have revealed that the photoionization from the e' orbital of CP leads to species of C_{2v} symmetry; one is characterized by two long C-C bonds and one short C-C bond and the another one by two short and one long C-C bonds. The former corresponds to the $^2B_2$ and the latter to the $^2A_1$ component. With the use of a MINDO/2 method, the JT stabilization energies of these two structures relative to a hypothetical D_{3h} cationic species were reported to be ~ 9.5 and ~ 9.2 kcal mol^{-1}, respectively [82]. JT splittings of ~ 1.55 and ~ 1.63 eV have been calculated for these two structures applying Koopman's theorem, which are twice as large as the experimentally observed splitting of ~ 0.80 eV [77].

Although there were some activities on the theoretical side [82–86, 88] to elucidate various stationary points on the PESs of CP^+ and the vertical ionization energies as stated above, a rigorous dynamical study to unravel the vibrational structure of the photoelectron band is still missing. In our present work, we set out to study the static and dynamic aspects of the JT and PJT vibronic coupling effects in the two low-lying degenerate electronic states of CP^+.

The rest of the thesis is organized as follows. In chapter 2, we present the theoretical framework of multimode VC. In particular, we have provided an outline of the concept of adiabatic approximation and the necessity of a diabatic electronic basis to investigate the JT and PJT interactions in multimode molecular systems. In this regard, a simple and heuristic model, the so-called LVC scheme is discussed. The VC involving degenerate vibrational modes and degenerate electronic states has also been introduced in this chapter. We have also discussed the role of totally and nontotally symmetric vibrational modes in establishing a VC model and the calculation of vibronic eigenvalue spectrum by a numerically exact solution of the time-independent Schrödinger equation with the help of Lanczos algorithm [56]. Finally, the calculation of complex vibronic spectra of molecules with a large electronic and vibrational degrees of freedom by a time-dependent WP propagation approach within the MCTDH scheme [53–55] is illustrated.

Chapter 3 provides a theoretical study of the photodetachment spectroscopy of B_3^- anion with the aid of a quantum dynamical approach. The theoretical results [68] are compared with the available experimental photoelectron spectra of B_3^- [67]. Both B_3^- and B_3 possess D_{3h} symmetry at the equilibrium configuration of their electronic ground state. Distortion of B_3 along its degenerate vibrational mode ν_2 splits the degeneracy of its excited $\widetilde{C}^2E'$ electronic manifold and exhibits $(E\otimes e)$-JT activity. The components of the JT split PES form CIs, and they can also undergo PJT crossings with the $\widetilde{X}^2A_1'$ electronic ground state of B_3 via the degenerate ν_2 vibrational mode. The impact of the JT and PJT interactions on the nuclear dynamics of B_3 in its $\widetilde{X}^2A_1'$-$\widetilde{C}^2E'$ electronic states is examined here by establishing a diabatic model Hamiltonian. The parameters of the electronic part of this Hamiltonian are calculated by performing electronic structure calculations and the nuclear dynamics on it is simulated by solving quantum eigenvalue equation.

In chapter 4, we report a theoretical account on the static and dynamic aspects of the JT and PJT interactions in the ground ($\widetilde{X}^2E_g$) and first excited ($\widetilde{A}^2A_{1g}$) electronic states of ET^+ [89]. The findings are compared with the experimental photoionization spectrum of ET [69]. The present theoretical approach is based on a model diabatic Hamiltonian and with the parameters derived from *ab initio* calculations. The optimized geometry of ET in its electronic ground state ($\widetilde{X}^1A_{1g}$) revealed an equilibrium staggered conformation belonging to the D_{3d} point group. At the vertical configuration, ET^+ belongs to this point group. The ground and low-lying electronic states of this radical cation are of $\widetilde{X}^2E_g$, $\widetilde{A}^2A_{1g}$, $\widetilde{B}^2E_u$, and $\widetilde{C}^2A_{2u}$ symmetry. Elementary symmetry selection rule (cf. Eq. 4.2) suggests that the degenerate electronic states of the radical cation are prone to the JT distortion when perturbed along the degenerate vibrational modes of e_g symmetry. The $\widetilde{A}^2A_{1g}$ state is estimated to be ~ 0.345 eV above the $\widetilde{X}^2E_g$ state and ~ 2.405 eV below the $\widetilde{B}^2E_u$ state at the vertical configuration. The symmetry selection rule (cf. Eq. 4.3a) also suggests that PJT crossings of the $\widetilde{A}^2A_{1g}$ and

the $\widetilde{X}^2E_g$ electronic states of the radical cation along the vibrational modes of e_g symmetry and such crossings appear to be energetically favorable also. The irregular vibrational progressions, with numerous shoulders and small peaks, observed below 12.55 eV in the experimental recording are manifestations of the dynamic $(E \times e)$-JT effect. Our findings revealed that the PJT activity of the degenerate vibrational modes is particularly strong in the $\widetilde{X}^2E_g$-$\widetilde{A}^2A_{1g}$ electronic manifold which leads to a broad and diffuse structure of the observed photoelectron band [89].

In chapter 5, the static and dynamic aspects of the JT and PJT interactions in the ground ($\widetilde{X}^2E'$) and first excited ($\widetilde{A}^2E''$) electronic of the CP^+ are investigated with the aid of an *ab initio* based quantum dynamical approach. Nuclear dynamical simulations on the resulting four coupled electronic states including fourteen relevant vibrational modes are carried out by a WP propagation approach employing the MCTDH algorithm [53–55]. The theoretical results are compared with the most recent experimental recording of Holland *et al.* using He I and synchrotron radiation as excitation sources [75]. A model diabatic Hamiltonian up to a quadratic vibronic coupling (QVC) scheme including intermode coupling terms and *ab initio* calculated coupling parameters are employed in the quantum dynamical simulations. For the $\widetilde{X}^2E'$ electronic manifold, the observed splitting of the maxima of ~ 0.78 eV in the bimodal profile compares well with the time-independent and time-dependent results of ~ 0.80 eV and ~ 0.81 eV, respectively, within the LVC approach [90, 91]. Two Condon active (a_1') and three JT active (e') vibrational modes are found to contribute mostly to the nuclear dynamics in this electronic manifold. The low-energy progression in the photoelectron band is found to have mainly been caused by the degenerate CH_2 wagging (ν_4) and ring deformation (ν_5) modes. While the LVC scheme overestimates the observed spacing in the low-energy progressions, it leads to a very good agreement with the overall shape of the observed band. The effect of quadratic coupling terms of the Hamiltonian on this low-energy progression is also discussed.

The highly diffuse nature and the absence of a bimodal intensity distribution of the second photoelectron band indicates that the JT effect in the $\widetilde{A}^2E''$ electronic manifold is not as strong as that in the $\widetilde{X}^2E'$ ground electronic manifold. Although the QVC results improve the agreement between theory and experiment when compared to the LVC results, still, the theoretical envelope does not reveal the observed structureless and diffuse nature of the band. The discussed discrepancies between the theoretical and experimental results motivated us to further examine the possible role of PJT interactions between the $\widetilde{X}^2E'$ and $\widetilde{A}^2E''$ electronic states of CP^+ and the intermode bilinear JT coupling terms. We have found that only the a_1'' and one of the three e'' vibrational modes (both of CH_2 twisting type) are PJT active. Moreover, we have also discovered low-lying crossings of the $\widetilde{X}$-$\widetilde{A}$ states occurring in the energy range of the photoelectron bands [91]. Therefore, we now here develop an extended diabatic vibronic Hamiltonian considering the intermode coupling terms, apart from the possible PJT interactions between the $\widetilde{X}^2E'$ and $\widetilde{A}^2E''$ electronic states of CP^+. The theoretical findings establish the importance of both the bilinear and the PJT couplings in the nuclear dynamics [91, 92]. The simulation of the nuclear dynamics in the coupled $\widetilde{X}^2E'$-$\widetilde{A}^2E''$ electronic states is highly involved since it requires consideration of four interacting electronic states of CP^+ and fourteen relevant vibrational degrees of freedom. Such a task is computationally impossible with the matrix diagonalization approach and is therefore carried out by a WP propagation approach using the MCTDH scheme [53–55].

Chapter 2

Theoretical Methodology

2.1 Theory of Vibronic-Coupling Effects

2.1.1 Adiabatic approximation and diabatic basis

We consider a molecule described by the Hamiltonian

$$H \;=\; T_e + T_N + U(\mathbf{r}, \mathbf{R}) \tag{2.1}$$

where T_e and T_N are the operators for the kinetic energy of the electrons and nuclei, respectively, and $U(\mathbf{r}, \mathbf{R})$ is the total potential energy of the electrons and nuclei. The vector $\mathbf{r}$ denotes the set of electronic coordinates describing the displacements from a reference configuration. For fixed nuclei, i.e., $T_N = 0$, the orthonormal electronic wave functions $\Phi_n(\mathbf{r},\, \mathbf{R})$ and energies $V_n(\mathbf{R})$ defined by

$$\left[\underbrace{T_e + U(\mathbf{r}, \mathbf{R})}_{H_e} - V_n(\mathbf{R})\right] \Phi_n(\mathbf{r}, \mathbf{R}) \;=\; 0 \tag{2.2}$$

depend parametrically on the nuclear geometry. They are known as the BO electronic states and PESs [93], respectively. The exact eigenstates of the system

can be expanded in the BO electronic states

$$\Psi(\mathbf{r},\mathbf{R}) \;=\; \sum_n \chi_n(\mathbf{R})\Phi_n(\mathbf{r},\mathbf{R}). \tag{2.3}$$

Inserting this ansatz into the Schrödinger equation

$$(H-E)\Psi(\mathbf{r},\mathbf{R}) \;=\; 0 \tag{2.4}$$

one readily obtains [93] the following set of coupled equations for the expansion coefficients in Eq. (2.3)

$$\left[T_N + V_n(\mathbf{R}) - E\right]\chi_n(\mathbf{R}) \;=\; \sum_m \hat{\Lambda}_{nm}\chi_m(\mathbf{R}). \tag{2.5}$$

The operators Λ_{nm} are known as the nonadiabatic operators, given by [41]

$$\hat{\Lambda}_{nm} \;=\; -\int d\mathbf{r}\Phi_n^\star(\mathbf{r},\mathbf{R})[T_N,\Phi_m(\mathbf{r},\mathbf{R})]. \tag{2.6}$$

If we rewrite the fundamental set of equations given in Eq. (2.5) as a matrix Schrödinger equation, we have

$$\left(\underbrace{T_N\mathbf{1}+\mathbf{V}(\mathbf{R})-\hat{\mathbf{\Lambda}}}_{\mathcal{H}} - E\mathbf{1}\right)\chi = 0. \tag{2.7}$$

The matrix Hamiltonian $\mathcal{H}$ describes the nuclear motion in the manifold of electronic states. χ is the column vector with elements χ_n; $\mathbf{1}$ is the unit matrix, and $\mathbf{V}(\mathbf{R}) = V_n(\mathbf{R})\delta_{nm}$ is the diagonal matrix of electronic energies.

The adiabatic approximation is obtained by neglecting the nonadiabatic operator $\hat{\mathbf{\Lambda}}$ in Eq. (2.7). This approximation is based on the assumption that the kinetic-energy operator of the nuclei can be considered as a small perturbation of the electronic Hamiltonian. In the adiabatic approximation the matrix Hamiltonian $\mathcal{H}$ becomes diagonal and the total wave function (Eq. 2.3) becomes a product

of a nuclear and electronic wave function

$$\Psi(\mathbf{r},\mathbf{R}) \;=\; \chi_n(\mathbf{R})\Phi_n(\mathbf{r},\mathbf{R}). \tag{2.8}$$

The nuclear motion can be thought of as proceeding on the PES $V_n(\mathbf{R})$ of a given electronic state characterized by the index n.

Although the adiabatic approximation is often a very useful approach, it may fail in cases where the PESs of different electronic states are energetically close. In these cases the nonadiabatic operators $\hat{\mathbf{\Lambda}}$ cannot be neglected in the Hamiltonian $\mathcal{H}$ for those electronic indices n and m which belong to the manifold of closely lying electronic states. These electronic states are now vibronically coupled via $\hat{\Lambda}_{nm}$. In terms of the first- and second-order derivative couplings, $\hat{\Lambda}_{nm}$ in Cartesian coordinates can be written as [17, 94, 95]

$$\hat{\Lambda}_{nm} \;=\; -\sum_k \frac{\hbar^2}{M_k} F_{nm}\frac{\partial}{\partial R_k} - \sum_k \frac{\hbar^2}{2M_k} G_{nm}, \tag{2.9}$$

where M_k are nuclear masses and

$$F_{nm} \;=\; \langle\Phi_n(\mathbf{r})|\Delta_k|\Phi_m(\mathbf{r})\rangle, \tag{2.10}$$

$$G_{nm} \;=\; \langle\Phi_n(\mathbf{r})|\Delta_k^2|\Phi_m(\mathbf{r})\rangle, \tag{2.11}$$

in which $\Delta_k \equiv \partial/\partial R_k$. The matrix elements F_{nm} can be written according to the Hellmann-Feynmann type of relation as [17, 43]

$$F_{nm} \;=\; \frac{\langle\Phi_n(\mathbf{r})|\Delta_k\mathcal{H}_{el}(\mathbf{r},\mathbf{R})|\Phi_m(\mathbf{r})\rangle}{V_n(\mathbf{R}) - V_m(\mathbf{R})}, \tag{2.12}$$

where $\mathcal{H}_{el}$ defines the electronic Hamiltonian for fixed nuclear coordinates. When

the two surfaces are degenerate, $V_n(\mathbf{R}) = V_m(\mathbf{R})$ and the F_{nm} exhibit singular behavior [17]. As a result, both the electronic wave function and energy become discontinuous at the seam of CIs which makes the adiabatic electronic representation unsuitable for dynamical studies.

To overcome this problem the adiabatic wave functions $\Phi_n(\mathbf{r},\mathbf{R})$ are replaced by smooth and slowly varying functions $\phi_n(\mathbf{r},\mathbf{R})$ of the nuclear coordinates and correspond to PESs that may cross at the CIs of the adiabatic PESs. These slow-varying functions represent the diabatic basis [44]. The latter can be obtained through a suitable unitary transformation of the adiabatic Hamiltonian

$$\mathcal{H}^d = \mathbf{S}\mathcal{H}^{ad}\mathbf{S}^\dagger = T_n\mathbf{1} + \mathbf{W}. \tag{2.13}$$

Here $\mathbf{S}$ defines the orthogonal transformation matrix. For a 2×2 Hamiltonian, $\mathbf{S}$ is given by

$$\mathbf{S} \;=\; \begin{pmatrix} cos\ \theta & sin\ \theta \\ -sin\ \theta & cos\ \theta \end{pmatrix}, \tag{2.14}$$

where θ represents the adiabatic-to-diabatic transformation angle and $\Psi^d = \mathbf{S}\Psi^{ad}$. With this transformation, the diverging kinetic couplings of Eq. (2.12) are transformed into the smooth potential coupling [off-diagonal elements of $\mathbf{W}$ in Eq. (2.13)] and thereby the discontinuity of the adiabatic representation is avoided. The concept of diabatic electronic basis was introduced quite early in the literature in the context of describing the electron-nuclear coupling in atomic collision processes [44] as well as in molecular spectroscopy [11, 96]. However, construction of the latter for polyatomic molecular systems is a tedious and difficult problem since it is a matter of multi-coordinate problem rather than a single nuclear coordinate. Therefore, various approximate mathematical schemes have been proposed in the literature [97–106] to accomplish this task.

2.1.2 Normal Coordinates

Following the traditional approach [4–6, 11], we introduce normal coordinates [107] to describe small vibrations around the equilibrium geometry of the electronic ground state. We assume here that we are dealing with a closed-shell molecular system. The normal coordinates are defined by

$$\mathbf{q} = \mathbf{L}^{-1}\delta\mathbf{R} \tag{2.15}$$

where $\delta\mathbf{R}$ is the $3N-6$ ($3N-5$ for linear molecules) dimensional vector of internal displacement coordinates (changes of bond lengths and bond angles) for an N atomic molecule, and $\mathbf{L}$ is the L-matrix of the well-known Wilson FG-matrix method [107]. It is convenient to introduce dimensionless normal coordinates via

$$Q_i = (\omega_i/\hbar)^{1/2} q_i \tag{2.16}$$

where ω_i is the harmonic vibrational frequency of the ith normal mode. In the harmonic approximation, the kinetic-energy and potential-energy operators of the electronic ground state take the simple form (let us consider that $\hbar = 1$)

$$T_N = -\frac{1}{2}\sum_i \omega_i \frac{\partial^2}{\partial Q_i^2} \tag{2.17}$$

$$V_0 = \frac{1}{2}\sum_i \omega_i Q_i^2 \tag{2.18}$$

In the following sections, we proceed by expanding the diabatic excited-state potential-energy functions and coupling elements in terms of normal mode displacement coordinate Q_i.

2.1.3 Linear Vibronic Coupling Scheme

Let us assume that a diabatic basis has been obtained for a given set of vibronically interacting electronic states. In this basis the matrix Hamiltonian is given by [17]

$$\mathcal{H} = T_N \mathbf{1} + \mathbf{W}(\mathbf{Q}). \tag{2.19}$$

The matrix elements of the potential matrix $\mathbf{W}(\mathbf{Q})$ read

$$W_{nm}(\mathbf{Q}) \;=\; \int d\mathbf{r} \phi_n^\star(\mathbf{r}, \mathbf{Q}) H_e \phi_m(\mathbf{r}, \mathbf{Q}). \tag{2.20}$$

The $\phi_n(\mathbf{r},\mathbf{Q})$ are the diabatic wave functions for an electronic state of index n. For a polyatomic molecule, the accurate solution of the matrix Hamiltonian (Eq. 2.19) is very tedious and often impracticable. Therefore, an approximate form of the matrix Hamiltonian is often considered for which the Schrödinger equation can be accurately solved. The simplest, yet elegant approximation is to expand the potential-energy matrix $\mathbf{W}(\mathbf{Q})$ about a reference nuclear configuration $\mathbf{Q}_0$ and retaining the terms linear in $\mathbf{Q}$ for the off-diagonal terms. This method is known as the LVC scheme [17, 94]. The linear approximation is often sufficient since the elements of the $\mathbf{W}(\mathbf{Q})$ matrix are, by definition, slowly varying functions of $\mathbf{Q}$. Without any loss of generality it is assumed that the diabatic and adiabatic states are identical at the reference geometry $\mathbf{Q}_0$.

For the interacting electronic states n and m, the elements of the matrix Hamiltonian in the linear approximation are

$$\mathcal{H}_{nn} \;=\; T_N + V_0(\mathbf{Q}) + E_n + \sum_s \kappa_s^{(n)} Q_s \tag{2.21}$$

$$\mathcal{H}_{nm} \;=\; \sum_s \lambda_s^{(n,m)} Q_s. \tag{2.22}$$

The energies E_n which appear in the diagonal of $\mathcal{H}$ are constants given by

$W_{nn}(\mathbf{Q_0})$. The quantities $\kappa_s^{(n)}$ and $\lambda_s^{(n,m)}$ are known as *intrastate* and *interstate* electron-vibrational coupling constants, respectively, given by [17]

$$\kappa_s^{(n)} = \left(\frac{\partial V_n(\mathbf{Q})}{\partial Q_s}\right)_{\mathbf{Q_0}}, \tag{2.23}$$

$$\lambda_s^{(n,m)} = \left(\frac{\partial V_{nm}(\mathbf{Q})}{\partial Q_s}\right)_{\mathbf{Q_0}}. \tag{2.24}$$

The non-vanishing interstate coupling constants $\lambda_s^{(n,m)}$ are those for which the product of the irreducible representations of electronic states ϕ_n and ϕ_m, and of the nuclear coordinate Q_s contains the totally symmetric representation Γ_A, i.e. [17],

$$\Gamma_n \times \Gamma_{Q_s} \times \Gamma_m \supset \Gamma_A. \tag{2.25}$$

The analogous condition for the intrastate coupling constants $\kappa_s^{(n)}$ is

$$\Gamma_n \times \Gamma_{Q_s} \times \Gamma_n \supset \Gamma_A. \tag{2.26}$$

Certainly all totally symmetric modes can couple to the electronic motion which emphasize the important role of these modes in the VC problem. From the above symmetry selection rules (Eqs. 2.25 and 2.26), we can say that, only the totally symmetric modes give rise to nonzero intrastate coupling constants and only nontotally symmetric modes to nonzero interstate coupling constants.

2.1.4 Vibronic coupling involving degenerate vibrational modes and degenerate electronic states

The degenerate electronic states are well-known for the failure of the adiabatic or BO approximation. In the case of linear molecules the VC problem is known

as the RT effect [51]; otherwise, it is known as the JT effect [1]. Starting with the JT effect, which is the essential ingredient of this thesis, nearly all (nonlinear) molecules with degenerate electronic states possess several degenerate modes which can vibronically couple the components of these states. It is thus clear that we have to solve the multimode JT problem in order to arrive at an understanding of the interactions that occur in actual molecules.

2.1.4.1 The Jahn-Teller Effect

All non-linear molecules which fall under the *non-Abelian* point groups (the *Abelian* point groups are C_n, S_n, C_{2v}, D_2, and D_{2h}) possess degenerate electronic states and degenerate vibrational modes. For degenerate electronic states in non-linear molecules, Jahn and Teller have shown that there always exists a nontotally symmetric vibrational mode that can lift the orbital degeneracy in first order [1,108]. Considering a two-fold degenerate (E) electronic state, the symmetry of the desired vibrational mode for VC should be such that it is contained in the decomposition of the symmetrized product $(E)^2$. It is then found that in all but seven molecular-point groups (with two-fold and four-fold principal rotational axes of symmetry, e.g., D_{2d}, D_{4h}, C_{4v}, etc., where non-degenerate vibrational modes participate in the JT activity, the so-called ($E \times b$)-JT effect) degenerate vibrations can be JT active, leading to the ($E \times e$)-JT effect [2,5,6,13,17].

Let us consider a system with a doubly degenerate electronic state and three-fold principal rotational axis of symmetry C_3. The doubly degenerate JT active vibrational mode in Cartesian coordinates be represented as (Q_x, Q_y). In polar coordinates (ρ, ϕ), the x and y components of the degenerate vibrational mode can be written as

$$Q_x = \rho\ cos\phi \quad Q_y = \rho\ sin\phi. \tag{2.27}$$

Let us define

$$Q_{\pm} = Q_x \pm iQ_y = \rho e^{\pm i\phi}. \tag{2.28}$$

The transformation properties of $Q_{\pm}$ under C_3 are

$$C_3 Q_{\pm} = exp\left(\pm\frac{2\pi i}{3}\right) Q_{\pm}. \tag{2.29}$$

The doubly degenerate electronic states can be expressed by the diabatic wave functions in the Cartesian coordinate as (ψ_x, ψ_y). The linear combinations

$$\psi_{\pm} = \frac{1}{\sqrt{2}} \left(\psi_x \pm i\psi_y\right), \tag{2.30}$$

have the following transformation properties under C_3 operation

$$C_3 \psi_{\pm} = exp\left(\pm\frac{2\pi i}{3}\right) \psi_{\pm}. \tag{2.31}$$

By expanding the electronic part of the Hamiltonian (Eq. 2.19) in a Taylor series up to first order in $Q_{\pm}$ and evaluating matrix elements with the diabatic basis states (Eq. 2.30), taking into account the symmetry properties of Eqs. (2.29) and (2.31), one obtains [2, 5, 11]

$$H_{JT} = (T_N + V_0)\mathbf{1_2} + \begin{pmatrix} 0 & \lambda\rho e^{i\phi} \\ \lambda\rho e^{i\phi} & 0 \end{pmatrix}, \tag{2.32}$$

where $V_0 = \frac{\omega}{2}\rho^2$ and

$$T_N = -\frac{\omega}{2}\left(\frac{\partial^2}{\partial\rho^2} + \frac{1}{\rho}\frac{\partial}{\partial\rho} + \frac{1}{\rho^2}\partial^2\partial\phi^2\right). \tag{2.33}$$

ω is the vibrational frequency associated with the degenerate mode and λ is known as linear JT coupling constant. The corresponding adiabatic potential functions

obtained by diagonalizing the JT Hamiltonian at a fixed-nuclear geometry, i.e., $T_N = 0$,

$$\mathcal{V}_{\pm} = \frac{\omega}{2}\rho^2 \pm \lambda\rho, \tag{2.34}$$

are the well-known "Mexican hat" potentials [2, 5, 11, 17].

It is to be noted that most molecules have at least two vibrational modes of the same e-type symmetry (the exception are triatomic systems, such as H_3, Li_3, B_3, etc.), giving rise to the $E \times (e + e + ...)$-JT effect. The nonseparability of the JT active modes makes it necessary to sum over all contributions $\mathcal{H}_j$ of the individual modes

$$\mathcal{H} \;=\; \sum_{j}^{M} \mathcal{H}_j \tag{2.35}$$

and treat the total matrix Hamiltonian $\mathcal{H}$ as a whole rather than the individual terms separately. As a consequence, the vibronic symmetries are reduced considerably. The individual vibronic angular momenta

$$\mathbf{J}_j \;=\; \frac{1}{i}\frac{\partial}{\partial\phi_j}\mathbf{1_2} + \frac{1}{2}\begin{pmatrix} 1 & 0 \\ 0 & -1 \end{pmatrix} \tag{2.36}$$

are no longer constants of the motion. It is only the total vibronic angular momentum

$$\mathbf{J} \;=\; \sum_{j}^{M} \frac{1}{i}\frac{\partial}{\partial\phi_j}\mathbf{1_2} + \frac{1}{2}\begin{pmatrix} 1 & 0 \\ 0 & -1 \end{pmatrix} \tag{2.37}$$

that commutes with $\mathcal{H}$ [17]. In the adiabatic PESs this manifests itself in a dependence of $\mathcal{V}_{\pm}$ on the azimuthal angles ϕ_j of the individual modes. The potentials are invariant only under a common change of the angles of all vibrational modes otherwise of a very complicated shape. In addition, the locus of intersection is

no longer a single point in coordinate space, but rather a subspace of dimension $2M$ - 2. It must be evident from these remarks that the multimode JT problem leads to much more complicated nuclear dynamics than the single-mode problem. We note that it is important to take these multimode effects into consideration in order to arrive at a realistic treatment of actual molecules [17].

2.1.5 Inclusion of totally symmetric vibrational modes

From Eq. (2.21) it is clear that displacements along totally symmetric modes *tune* the energy gap ($|E_2 - E_1|$) between two electronic states and generally lead to intersections of the potential-energy functions, which are allowed by symmetry. These vibrational modes have therefore been termed *tuning modes* [17]. On the other hand, the nontotally symmetric modes satisfying Eq. (2.25) describe the coupling between two electronic states. Therefore, they are termed as *coupling modes* [17]. Within the LVC approach, the tuning modes contribute only to the diagonal elements of the electronic Hamiltonian matrix, see Eq. (2.21). Therefore, the inclusion of these modes to the VC models described earlier becomes straightforward.

In the $(E \times e)$-JT case the N_t tuning modes are represented by

$$H_{JT}^{t} = \sum_{i=1}^{N_t} \left[\left(\frac{\partial^2}{\partial Q_i^2} + Q_i^2 \right) \mathbf{1_2} + \begin{pmatrix} \kappa_i^E & 0 \\ 0 & \kappa_i^E \end{pmatrix} Q_i \right], \tag{2.38}$$

where the normal coordinates Q_i, $i = 1...N_t$, are the totally symmetric modes and the κ_i^E are the gradients of the adiabatic potential-energy functions of the E state with respect to the ith tuning mode.

From Eqs. (2.32) and (2.38), we have

$$\left[H_{JT}, H_{JT}^{t} \right] = 0 \tag{2.39}$$

2.2 Calculation of Spectra

The photoelectron spectrum for a transition to the coupled manifold of electronic states is described by the Fermi's Golden rule. According to this rule, the photoelectron intensity is given by

$$P(E) = \sum_v \left| \langle \Psi_v | \hat{T} | \Psi_0 \rangle \right|^2 \delta(E - E_v + E_0), \tag{2.40}$$

where $|\Psi_0\rangle$ is the initial electronic and vibrational ground state of the molecule with energy E_0. $|\Psi_v\rangle$ is the final vibronic state in the coupled electronic manifold and E_v is the vibronic energy. The quantity $\hat{T}$ is the transition operator that describes the interaction of the electron with the external radiation of energy E. The initial and final states are given by

$$|\Psi_0\rangle = |\Phi^0\rangle|\chi_0^0\rangle, \tag{2.41}$$

$$|\Psi_v\rangle = |\Phi^1\rangle|\chi_v^1\rangle + |\Phi^2\rangle|\chi_v^2\rangle, \tag{2.42}$$

where $|\Psi\rangle$ and $|\chi\rangle$ represent the diabatic electronic and vibrational part of the wave function, respectively. The superscripts 0, 1, and 2 refer to the ground and the two interacting diabatic electronic states, respectively. With the use of Eqs. (2.41-2.42), the excitation function of Eq. 2.40 can be rewritten as [17]

$$P(E) = \sum_v \left| \tau^1 \langle \chi_v^1 | \chi_0^0 \rangle + \tau^2 \langle \chi_v^2 | \chi_0^0 \rangle \right|^2 \delta(E - E_v + E_0), \tag{2.43}$$

where

$$\tau^m = \langle \Phi^m | \hat{T} | \Phi^0 \rangle, \tag{2.44}$$

represent the matrix elements of the transition dipole operator of the final electronic state m. Upon rewriting Eq. (2.43), the matrix elements of the transition dipole operator are treated to be independent of nuclear coordinates. These el-

ements are not calculated and are treated as constants, in accordance with the applicability of the generalized Condon approximation in a diabatic electronic basis [109].

2.2.1 Time-Independent Approach

In a time-independent quantum mechanical approach the photoelectron spectrum is calculated by solving the eigenvalue equation

$$\mathcal{H}|\Psi_v\rangle = E_v|\Psi_v\rangle \tag{2.45}$$

numerically, by representing the vibronic Hamiltonian $\mathcal{H}$ in a direct product basis of harmonic oscillator eigenstates of $\mathcal{H}_0$. In this basis, $|\chi_v^m\rangle$ takes the following form [17]:

$$|\chi_v^m\rangle \;=\; \sum_{n_1,n_2,\ldots,n_k} a^m_{v,n_1,n_2,\ldots,n_k}|n_1\rangle|n_2\rangle\ldots|n_k\rangle. \tag{2.46}$$

Here m is the electronic state index, n_l is the quantum number associated with the l^{th} vibrational mode, and k is the total number of such modes. The summation runs over all possible combinations of quantum numbers associated with each mode. For each vibrational mode, the oscillator basis is suitably truncated in the numerical calculations. The maximum level of excitation for each mode is approximately estimated from the corresponding Poisson parameter $[\frac{1}{2}\,(\frac{\kappa or \lambda}{\omega})^2]$. The Hamiltonian matrix written in such a direct product basis is usually highly sparse, and is tridiagonalized using the Lanczos algorithm prior to diagonalization [56]. The diagonal elements of the resulting eigenvalue matrix give the eigenenergies of the vibronic energy levels and the relative intensities of the vibronic lines are obtained from the squared first components of the Lanczos eigenvectors [39, 56]. A brief overview of the Lanczos algorithm is given in Appendix A.

Finally, the spectral envelope is calculated by convoluting the line spectrum

with a suitable Lorentzian line-shape function of appropriate width of the following:

$$\mathcal{L}(E) = \frac{1}{\pi}\frac{\Gamma/2}{E^2 + (\Gamma/2)^2}. \tag{2.47}$$

The quantity Γ represents the full width at the half maximum (fwhm) of the Lorentzian.

2.2.2 Time-Dependent Approach

First of all we note that the time-dependent calculations in this thesis are done only for the CP^+. In a time-dependent picture, the Fourier transform representation of the delta function is used in the above Golden rule formula. The resulting expression for the spectral intensity then rearranges to the Fourier transform of the time autocorrelation function of the wave packet [27]

$$P(E) \sim 2Re \int_0^\infty e^{iEt/\hbar} \langle 0|\boldsymbol{\tau}^\dagger e^{-i\mathcal{H}t/\hbar}\boldsymbol{\tau}|0\rangle dt, \tag{2.48}$$

$$\sim 2Re \int_0^\infty e^{iEt/\hbar} C^m(t) dt. \tag{2.49}$$

The quantity, $C^m(t) = \langle \Psi_m(0)|\Psi_m(t)\rangle$, is the time autocorrelation function of the wave packet initially prepared on m^{th} electronic state. $\boldsymbol{\tau}$ refers to the transition dipole matrix; $\boldsymbol{\tau}^\dagger = \left(\tau^{E'_x},\ \tau^{E'_y},\ \tau^{E''_x},\ \tau^{E''_y}\right)$ with τ^m given by Eq. (2.44) and, $\Psi_m(t) = e^{-i\mathcal{H}t/\hbar}\tau^m|0\rangle$. Note that Ψ possesses components on each of the vibronically coupled four diabatic electronic states (E'_x, E'_y, E''_x and E''_y), and therefore the composite photoelectron spectrum is written as a sum of the resulting four partial spectra, calculated by propagating wave packets for four different initial conditions. Finally, only terms $|\tau^m|^2$ contribute to the spectrum, after using a vibronic symmetry in Eq. (2.49), while the mixed terms $\tau^m\tau^{n^\star}$, still present in

Eq. (2.43) of the following form of CP^+,

$$P(E) = \sum_v \left| \tau^{E'_x} \langle \chi_v^{E'_x} | \chi_0^0 \rangle + \tau^{E'_y} \langle \chi_v^{E'_y} | \chi_0^0 \rangle + \tau^{E''_x} \langle \chi_v^{E''_x} | \chi_0^0 \rangle + \tau^{E''_y} \langle \chi_v^{E''_y} | \chi_0^0 \rangle \right|^2 \delta(E - E_v + E_0) \quad (2.50)$$

will vanish [17].

In time-dependent approach, the eigenvalue spectrum of the four-state (or 4 $\times$ 4) matrix Hamiltonian $\mathcal{H}$ of Eq. (5.4) are calculated by numerically solving the time-dependent Schrödinger (TDSE) equation

$$i\hbar \frac{\partial |\Psi\rangle}{\partial t} = \mathcal{H} |\Psi\rangle \quad (2.51)$$

using the MCTDH scheme. The latter provides an efficient algorithm in propagating the wave packets rather effectively with much less computational overheads. Since the details of this method have been extensively discussed in the literature [54, 55, 110], we highlight only the essentials here. The basis of the method is to use a multiconfigurational ansatz for the wave function, with each configuration being expressed as a Hartree product of time-dependent basis functions, known as Single Particle Functions (SPFs). For the nonadiabatic problem examined here, a *multiset* formulation is much more appropriate and the corresponding wave function can be expanded as:

$$\begin{aligned} \Psi(Q_1, Q_2, ..., Q_f, t) &= \Psi(q_1, q_2, ..., q_p, t) \\ &= \sum_{\alpha=1}^{4} \sum_{j_1=1}^{n_1^{(\alpha)}} ... \sum_{j_p=1}^{n_p^{(\alpha)}} A^{(\alpha)}_{j_1 ... j_p}(t) \\ &\quad \times \prod_{k=1}^{p} \phi^{(\alpha,k)}_{j_k}(q_k, t) |\alpha\rangle \quad (2.52) \\ &= \sum_{\alpha} \sum_{J} A^{(\alpha)}_J \Phi^{(\alpha)}_J |\alpha\rangle, \quad (2.53) \end{aligned}$$

where, f and p represent the number of vibrational degrees of freedom, and

MCTDH *particles* (also called *combined* modes), respectively. $A^{(\alpha)}_{j_1 \ldots j_p}$ denote the MCTDH expansion coefficients and the $\phi^{(\alpha,k)}_{j_k}$ are the one-dimensional expansion functions, known as SPFs. The labels $\{\alpha\}$ are indices denoting the discrete set of electronic states considered in the calculation. Thus, the WP, $\Psi^{(\alpha)}$ ($= \sum_J A^{(\alpha)}_J \Phi^{(\alpha)}_J$) associated with each electronic state is described using a different set of SPFs, $\{\phi^{(\alpha,k)}_{j_k}\}$. Here the multiindex, $J = j_1 \ldots j_p$ depends implicitly on the state α as the maximum number of SPFs may differ for different states. The summation $\sum_J$ is a shorthand notation for summation over all possible index combinations for the relevant electronic state. The variables for the p sets of SPFs are defined in terms of one or multidimensional coordinates of a particle.

The equations of motion for the expansion coefficients, $A^{(\alpha)}_J$ and SPFs, $\phi^{(\alpha,k)}_{j_k}$ have been derived using the Dirac-Frankel variational principle [111, 112]. The resulting equations of motion are coupled differential equations for the coefficients and the SPFs. For k degrees of freedom there are n_k SPFs, and these SPFs are represented by N_k primitive basis functions or grid points. The efficiency of the MCTDH algorithm grows with increasing N_k/n_k [110]. The use of the variational principle ensures that the SPFs evolve so as to optimally describe the true WP; i.e., the time-dependent basis moves with the WP. This provides the efficiency of the method by keeping the basis optimally small.

In general, for the present type of nonadiabatic problems, MCTDH is quite capable of handling 20-30 vibrational degrees of freedom. CP has 21 vibrational degrees of freedom (seven nondegenerate and seven doubly degenerate) and we find that only 14 of them are relevant and need to be considered in the nuclear dynamics treated here. So, the physical system is described by a set of $f = 14$ coordinates, Q_1,...,Q_f. For large systems, let say, for $f \geq 6$, it is important to combine degrees of freedom in order to make the calculation computationally feasible. The collection of combined degrees of freedom is called a " particle " [110]. Thus, a particle coordinate is chosen to be a set of coordinates: i.e., $q_k = [Q_1, Q_2,...]$. The SPFs are then multidimensional functions of the set of system coordinates

and the number of particles $p < f$. By doing so, the computational resources can be significantly reduced and high-dimensional systems can be treated without affecting the variational nature of the method. However, the multimode problems remain an open challenge since the exponential growth in the computational resources restricts a calculation up to 6-8 particles.

To set up an MCTDH calculation one needs to choose a set of primitive basis functions in the first step. The SPFs, their time derivatives and the Hamiltonian are then represented in this basis at each point in time. A combination scheme for the degrees of freedom is then selected to reduce the computational requirements and finally, a set of SPFs is specified in order to accurately represent the evolving WP. The primitive basis chosen is a harmonic oscillator discrete variable representation (DVR). The initial SPFs used are sets of ortho-normalized harmonic oscillator functions in the mass-frequency scaled coordinates used. In the multiset formalism, one set is required for each particle for each electronic state. The initial wave function is the vibrational wave function of CP in its ground electronic state, which is simply expressed as a product of the first SPFs in each set, and assumes the form of a Gaussian wave packet. The various mode combination schemes, the sizes of the primitive and SPF bases used in the present calculations are given in Tables 5.6 and 5.7.

Chapter 3

The JT and PJT effects in the anion photoelectron spectroscopy of B_3 cluster

3.1 Introduction

This chapter deals with the fate of the B_3 cluster in its orbitally degenerate $\widetilde{C}^2E'$ electronic manifold which is probed in a photodetachment experiment from its anion B_3^- [67]. Both B_3^- and its neutral counterpart B_3 possess D_{3h} equilibrium geometry in their electronic ground state. Within the D_{3h} point group, the ground state ($\widetilde{X}^1A_1'$) molecular orbital sequence of B_3^- can be written as [67, 113]

$$(1a_1')^2(1e')^4(1a_2'')^2(2a_1')^2.$$

Electron detachment from the $1e'$ orbital of B_3^- produces B_3 in its final degenerate $\widetilde{C}^2E'$ electronic state, which is prone to the JT distortion. The vibrational modes of B_3^- belong to the following symmetry species of the D_{3h} point group:

$$\Gamma_{vib} = a_1' + e'. \tag{3.1}$$

The symmetric direct product of the E' representation in the D_{3h} point group yields,

$$(E')^2 \;=\; a_1' + e'. \tag{3.2}$$

Similarly, the direct product of E' and A_1' representations in the same point group yields,

$$E' \times A_1' \;=\; e'. \tag{3.3}$$

The totally symmetric vibrational mode ν_1 of a_1' symmetry is Condon active and cannot lift the electronic degeneracy [17]. The degenerate vibrational mode ν_2 of e' symmetry on the other hand, can lift the degeneracy of the $\widetilde{C}^2E'$ electronic manifold and can participate in the $(E \otimes e)$-JT activity. Moreover, the symmetry selection rule of Eq. (3.3) permit a PJT coupling of the $\widetilde{X}^2A_1'$ and the $\widetilde{C}^2E'$ electronic states of B_3 via the e' vibrational mode. The existence of different types of coupling lead to the formation of multiple CIs of electronic states and the nuclear dynamics proceeds via highly complex nonadiabatic paths. As noted in chapter 2, this represent the $(E \times e)$-JT system which possesses only one JT active e' vibrational mode.

The details of the experimental photodetachment of spectrum of B_3^- and the available electronic structure results are already given in section 1.3. In this chapter, we construct a model vibronic Hamiltonian of the final $\widetilde{X}^2A_1'$ -$\widetilde{C}^2E'$ coupled electronic manifold of B_3 in terms of the dimensionless normal coordinates of the electronic ground state of B_3^- in a diabatic electronic representation and simulate the nuclear dynamics in this manifold to calculate the photodetachment spectrum [17, 44]. The theoretical results are in good accord with the experimental data [67]. We find that the higher order JT and PJT interactions, in particular, have no impact on the vibronic structure of the photoelectron bands.

The observed sharp and discernible splitting of $\sim 1100\ cm^{-1}$ in the experimental $\widetilde{C}^2E'$ band is found to be due to a progression along the JT active vibrational mode ν_2 [68].

3.2 The Vibronic Hamiltonian

The photodetachment process is delineated as a FC transition from the electronic ground state of B_3^- ($\widetilde{X}^1A_1'$) to the coupled $\widetilde{X}^2A_1'$-$\widetilde{C}^2E'$ electronic manifold of B_3. Ionization of electrons from the valence $2a_1'$ and $1e'$ molecular orbitals of B_3^- produces B_3 in its ground $\widetilde{X}^2A_1'$ and excited $\widetilde{C}^2E'$ electronic states, respectively. The latter is prone to the JT instability when distorted along the degenerate vibrational mode ν_2. The JT split components of the $\widetilde{C}^2E'$ electronic manifold are allowed (by symmetry selection rule) to undergo crossings with the $\widetilde{X}^2A_1'$ electronic state, and therefore, can exhibit PJT activity. These multiple crossings of electronic states lead to intricate mixing of electronic and nuclear motions [17, 43, 114].

A model diabatic vibronic Hamiltonian [17] is constructed in terms of the dimensionless normal coordinates of the ground electronic state of B_3^- in order to simulate the nuclear dynamics in the coupled $\widetilde{X}^2A_1'$-$\widetilde{C}^2E'$ electronic manifold of B_3. In what follows, we define Q_i as the dimensionless normal coordinate of B_3^- associated with the vibrational mode ν_i. The vibrational mode ν_1 of a_1' symmetry is Condon active and ν_2 of e' symmetry is JT and PJT active. In this description the Hamiltonian assumes the form [17]

$$\mathcal{H} \;=\; \mathcal{H}_0\mathbf{1_3} + \begin{pmatrix} \mathcal{U}_{11} & \mathcal{U}_{12} & \mathcal{U}_{13} \\ & \mathcal{U}_{22} & \mathcal{U}_{23} \\ h.c. & & \mathcal{U}_{33} \end{pmatrix}. \tag{3.4}$$

Where $\mathcal{H}_0 = \mathcal{T}_N + \mathcal{V}_0$, with

$$\mathcal{T}_N = -\frac{1}{2}\omega_1\frac{\partial^2}{\partial Q_1^2} - \frac{1}{2}\omega_2\left(\frac{\partial^2}{\partial Q_{x2}^2} + \frac{\partial^2}{\partial Q_{y2}^2}\right), \tag{3.5}$$

$$\mathcal{V}_0 = \frac{1}{2}\omega_1 Q_1^2 + \frac{1}{2}\omega_2\left(Q_{x2}^2 + Q_{y2}^2\right), \tag{3.6}$$

is the Hamiltonian matrix associated with the electronic ground state of B_3^-, and is defined in terms of unperturbed harmonic oscillators with frequencies ω_i. The elements of the electronic Hamiltonian matrix ($\mathcal{U}_{ij}$) are expanded in a second-order Taylor series around the equilibrium geometry of the electronic ground state of B_3^- occurring at $\mathbf{Q}$=0, as follows

$$\begin{aligned}\mathcal{U}_{11} = {} & E_{E'}^0 + \kappa_1 Q_1 + \lambda_2 Q_{x2} + \frac{1}{2}[\gamma_1 Q_1^2 \\ & + \gamma_2(Q_{x2}^2 + Q_{y2}^2) + \eta_2(Q_{x2}^2 - Q_{y2}^2) + \gamma_{12} Q_1 Q_{x2}],\end{aligned} \tag{3.7a}$$

$$\mathcal{U}_{22} = E_{A_1'}^0 + \kappa_1' Q_1 + \frac{1}{2}\gamma_1' Q_1^2 + \frac{1}{2}\gamma_2'(Q_{x2}^2 + Q_{y2}^2), \tag{3.7b}$$

$$\begin{aligned}\mathcal{U}_{33} = {} & E_{E'}^0 + \kappa_1 Q_1 - \lambda_2 Q_{x2} + \frac{1}{2}[\gamma_1 Q_1^2 \\ & + \gamma_2(Q_{x2}^2 + Q_{y2}^2) - \eta_2(Q_{x2}^2 - Q_{y2}^2) - \gamma_{12} Q_1 Q_{x2}],\end{aligned} \tag{3.7c}$$

$$\mathcal{U}_{12} = \lambda_2' Q_{x2}, \tag{3.7d}$$

$$\mathcal{U}_{13} = \lambda_2 Q_{y2} - \eta_2 Q_{x2} Q_{y2} + \frac{1}{2}\gamma_{12} Q_1 Q_{y2}, \tag{3.7e}$$

$$\mathcal{U}_{23} = -\lambda_2' Q_{y2}. \tag{3.7f}$$

The parameters in the above equations have the following identities. The vertical ionization energies of the $\widetilde{C}^2E'$ and $\widetilde{X}^2A_1'$ electronic states of B_3 are defined as $E^0_{E'}$ and $E^0_{A_1'}$, respectively. The linear *intrastate* coupling constant [17] for the totally symmetric vibrational mode ν_1 is given by κ_1 and κ_1' in the $\widetilde{C}^2E'$ and $\widetilde{X}^2A_1'$ electronic states, respectively. The linear and quadratic JT coupling parameters for the degenerate vibrational mode ν_2 within the $\widetilde{C}^2E'$ electronic manifold are denoted by λ_2 and η_2, respectively. The quantities γ_i and γ_i' describe the diagonal second-order coupling parameters for the $\widetilde{C}^2E'$ and $\widetilde{X}^2A_1'$ electronic states, respectively. The bilinear JT (a_1'-e') coupling parameter is given by γ_{12}. The normal coordinates of the x and y components of the degenerate vibrational mode ν_2 is denoted by Q_{x2} and Q_{y2}, respectively. The quantity λ_2' describes the linear PJT coupling parameter between the $\widetilde{X}^2A_1'$-$\widetilde{C}^2E'$ electronic states. All these parameters are determined by performing extensive *ab initio* calculations which are discussed in detail in section 3.3.

3.3 Electronic Structure Calculations

3.3.1 Optimized geometry, harmonic vibrational frequencies, and normal coordinates of B_3^- in the ground electronic state

The geometry optimization and the calculation of harmonic vibrational frequencies of B_3^- in its ground electronic state ($\widetilde{X}^1A_1'$) are carried out at the Møller-Plesset perturbation theory (MP2) level employing the correlation-consistent polarized valence triple-ζ (cc-pVTZ) Gaussian basis set of Dunning [115]. The electronic structure calculations were performed using the Gaussian03 program package [116]. The *ab initio* force constant matrix for the ground electronic state of B_3^- is obtained with the cc-pVTZ basis set at the MP2 level. On diagonalization of this force constant matrix, the harmonic vibrational frequencies (ω_i)

Table 3.1: Equilibrium geometry parameters and harmonic vibrational frequencies of B_3^- in its $\widetilde{X}^1A_1'$ electronic state along with experimental and other theoretical results. We note that the experiment describes the fundamental vibrational frequencies.

Level	Reference	R(B-B) Å	∠ B1-B2-B3 deg	$\omega_1(a_1')$ cm^{-1}	$\omega_2(e')$ cm^{-1}
MP2/cc-pVTZ	This work	1.555	60	1298	952
B3LYP/6-311+G*	[67]	1.542	-	1239	959
RCCSD(T)/6-311+G*	[67]	1.576	-	1190	897
CAS-MRCI/6-311+G*	[67]	1.552	-	a	a
Experimental	[67]	-	-	1230 ± 40	1100 ± 80
Description				Symmetric stretch (breathing)	Asymmetric stretch (bending)

[a] Properties were not reported at this level of the theory.

are obtained. Along with the latter, the transformation matrix from the symmetry coordinates to the mass-weighted normal coordinates is obtained. The dimensionless normal coordinates (Q_i) are then obtained by multiplying the latter with $\sqrt{\omega_i}$ (in atomic units) [107]. The equilibrium geometry parameters and harmonic vibrational frequencies of B_3^- in its electronic ground state along with the available theoretical and experimental results [67] are given in Table 3.1.

3.3.2 Coupling Parameters of the Hamiltonian

The coupling parameters of the Hamiltonian in Eqs. (3.7a-3.7f) represent the derivatives of the adiabatic potential energy of B_3 of appropriate order with respect to the dimensionless normal coordinates (Q_i), calculated at the equilibrium geometry of B_3^- ($\mathbf{Q}$=0) [94]. The linear coupling parameters κ_1, κ_1', λ_2, and the second-order coupling parameters γ_1, γ_2, γ_1', and η_2 are obtained by fitting the adiabatic form of the diabatic electronic Hamiltonian of Eqs. (3.7a-3.7f). The bilinear γ_{12} and the linear λ_2' PJT coupling parameters are obtained by suitable numerical finite difference schemes. These are defined as

$$\gamma_{12} = \left(\frac{\partial^2 V_{E'}}{\partial Q_1 \partial Q_2}\right)\Bigg|_{\mathbf{Q}=\mathbf{0}}, \tag{3.8}$$

$$\lambda_2' = \frac{1}{2}\sqrt{\left(\frac{\partial^2 \Delta E}{\partial Q_2^2}\right)}\Bigg|_{\mathbf{Q}=\mathbf{0}}, \tag{3.9}$$

where ΔE is the difference of squares of the adiabatic potential energy difference between the $\widetilde{C}^2E'$ and $\widetilde{X}^2A_1'$ ionic states for normal coordinate displacement Q_2 and the same for the equilibrium configuration, $\mathbf{Q}$=0.

To estimate these coupling parameters, direct calculations of vertical ionization energies of B_3^- were performed by the OVGF method [117, 118] employing the cc-pVTZ basis set. The electronic structure calculations were carried out as a function of the dimensionless normal mode displacement (from $\mathbf{Q}$=0) coordinates, Q_i (i = 1-2) = -1.5 (0.25) 1.5, using the Gaussian-03 program package [116]. The adiabatic PESs of the $\widetilde{X}^2A_1'$ and $\widetilde{C}^2E'$ electronic states of B_3 along Q_1 and Q_2 are obtained from the calculated vertical ionization energies. These energies are then fitted to the adiabatic form of the diabatic Hamiltonian described in Eqs. (3.7a-3.7f) by a least-square fit and thereby the coupling parameters are derived. We note that, the coupling parameters are also estimated by numerical finite difference scheme and the identity of the results is confirmed. However, the bilinear (γ_{12}) and the linear PJT (λ_2') coupling parameters are estimated only by a suitable finite difference method.

In Fig. 3.1, the adiabatic potential energy values of the $\widetilde{X}^2A_1'$ (panel a) and $\widetilde{C}^2E'$ (panel b) electronic states of B_3 measured relative to the $\widetilde{X}^1A_1'$ ground electronic state of B_3^- (these are the vertical ionization energy values obtained from the OVGF calculations), along the dimensionless normal coordinate Q_1 of the symmetric (ν_1) vibrational mode is plotted. The asterisks in each panel

represent the computed *ab initio* data and a quadratic fit to these data is shown by the solid lines. The vibrational mode ν_1 represents the breathing vibration of B_3. The linear κ_1', κ_1, and quadratic γ_1', γ_1 coupling parameters of the Hamiltonian [Eqs. (3.7a-3.7c)] for ν_1 derived from the above fits are given in Table 3.2.

The degenerate vibrational mode ν_2 consists of asymmetric stretch and bending vibrations. It represents the ring deformation of B_3. The linear and quadratic JT coupling parameters for this mode is estimated by fitting the (signed) difference of the JT split PESs along this mode. In Fig. 3.2(a), this energy difference is plotted along the dimensionless normal coordinate of the x component, Q_{2x} of this mode. The asterisks in the panel denote the computed *ab initio* energies and the solid line superimposed on them represents the quadratic fit. The value of the linear (λ_2) and the quadratic (η_2) JT parameters of the Hamiltonian [Eqs. (3.7a, 3.7c-3.7f)] obtained from the above fit are included in Table 3.2. The value of the diagonal second-order coupling parameter γ_2 for ν_2 is extracted from a fit of the mean of the JT split PESs. This fit along with the *ab initio* data is shown in Fig. 3.2(b), and the value of γ_2 is included in Table 3.2.

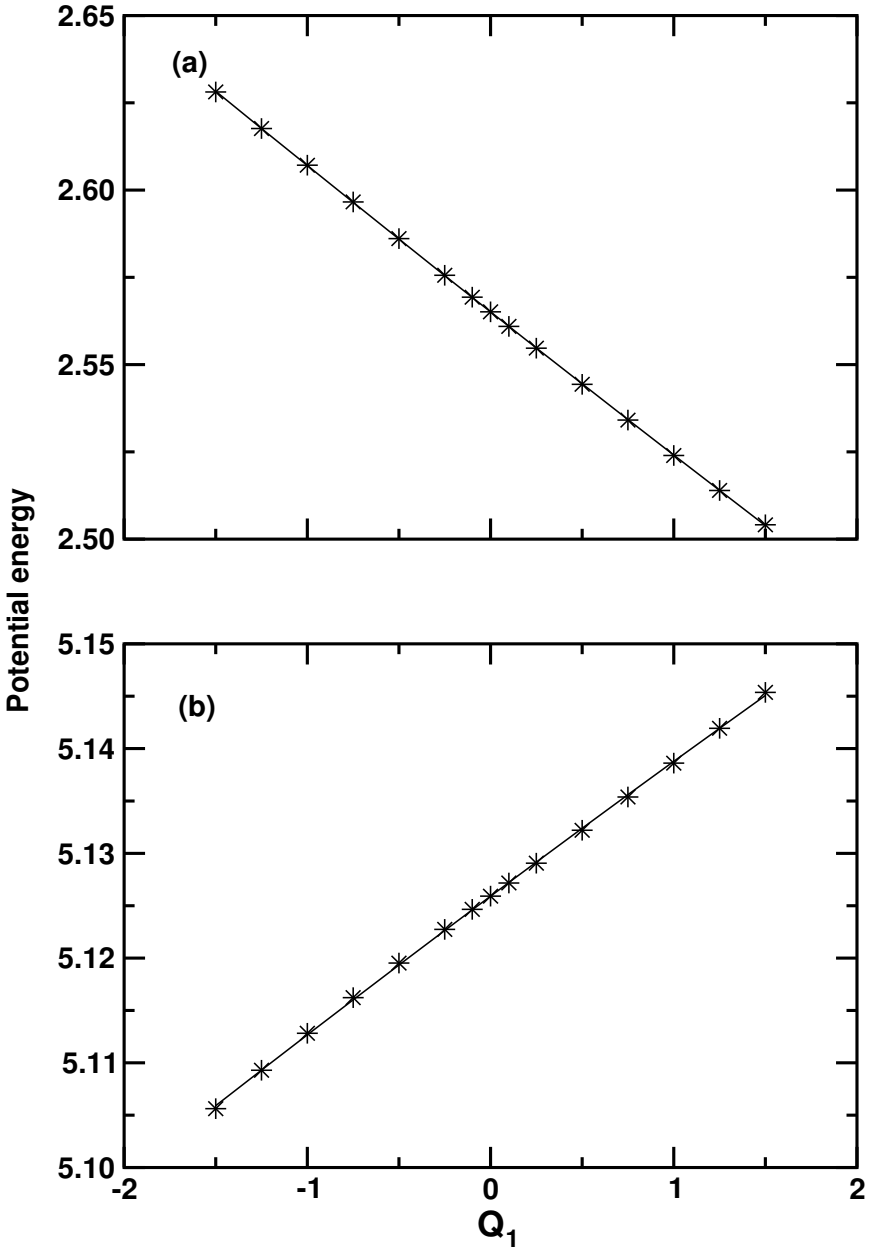

Figure 3.1: Vertical ionization energy of B_3^- pertinent to the first ($\widetilde{X}^2A_1'$) and third ($\widetilde{C}^2E'$) photoelectron bands, plotted along the dimensionless normal coordinate of the symmetric vibrational mode ν_1 are shown in panel (a) and (b), respectively. The *ab initio* OVGF energy values are shown by the asterisks, and a quadratic fit to these points is shown by the solid line. The linear (κ_1 and κ_1') and the diagonal (γ_1 and γ_1') quadratic coupling parameters listed in Table 3.2 are obtained from the above fits.

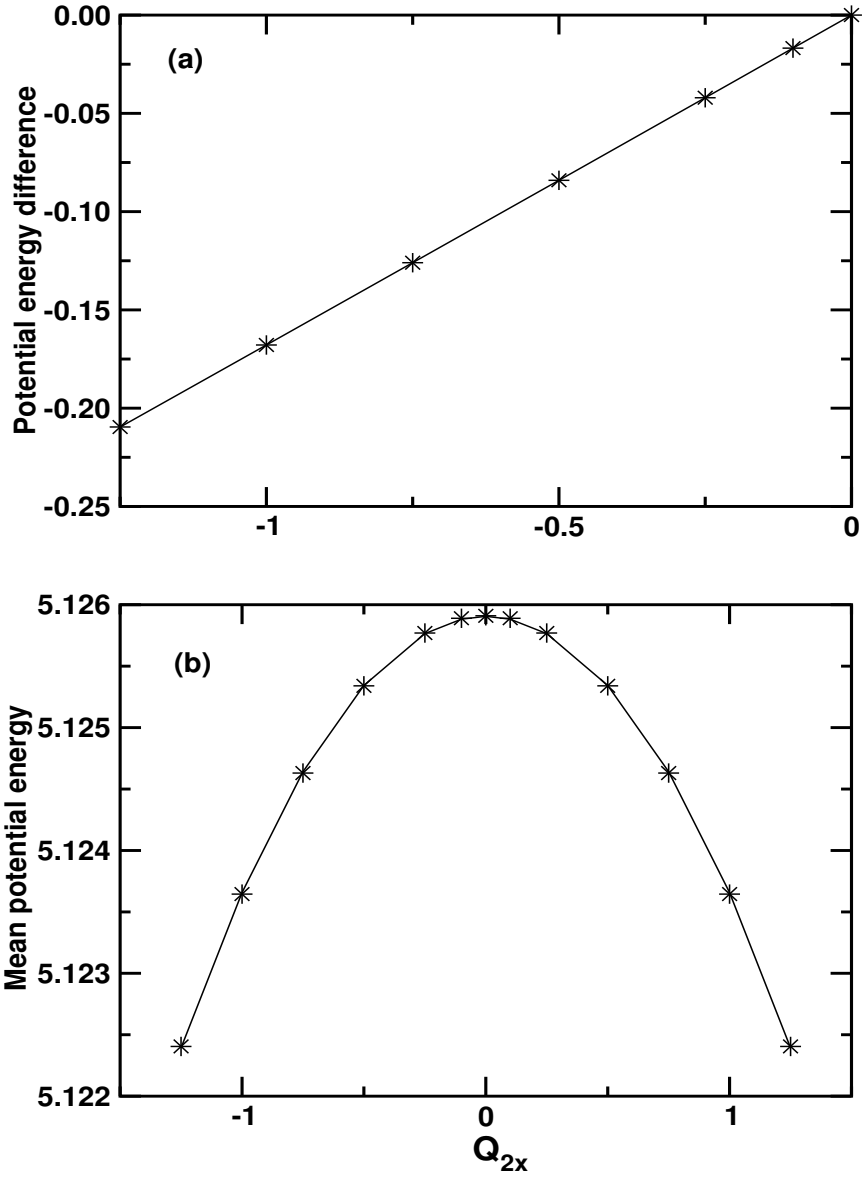

Figure 3.2: (a) The potential energy difference and (b) the mean of the JT split adiabatic sheets of the $\widetilde{C}^2E'$ electronic manifold of B_3 plotted along the dimensionless normal coordinate of the degenerate vibrational mode ν_2. The *ab initio* OVGF data are shown by the asterisks; a quadratic and a parabolic fit to these data are shown by the solid lines, in both panel (a) and (b). The linear (λ_2), quadratic (η_2) JT and diagonal quadratic (γ_2) coupling parameters for this mode derived from the above fits are listed in Table 3.2.

Table 3.2: Coupling parameters of the Hamiltonian [Eqs. (3.7a-3.7f)] of the $\widetilde{X}^2A_1'$ and $\widetilde{C}^2E'$ electronic states of B_3 derived from the computed OVGF data. All quantities are in eV if not otherwise stated. The dimensionless excitation strengths ($\kappa^2 or \lambda^2/2\omega^2$) are included in the parentheses.

Modes	κ or λ	κ'	λ'	γ	γ'	η	γ_{12}
(Sym.)	$\widetilde{C}^2E'$	$\widetilde{X}^2A_1'$	$\widetilde{X}^2A_1' \otimes \widetilde{C}^2E'$	$\widetilde{C}^2E'$	$\widetilde{X}^2A_1'$	$\widetilde{C}^2E'$	$\widetilde{C}^2E'$
$\nu_1(a_1')$	0.013 (0.003)	-4.147 $\times 10^{-2}$ (0.033)	-	-3.717 $\times 10^{-4}$	4.347 $\times 10^{-4}$	-	-
$\nu_2(e_1')$	0.169 (1.019)	-	3.974 $\times 10^{-2}$ (0.057)	-4.496 $\times 10^{-3}$	-6.044 $\times 10^{-3}$	1.253 $\times 10^{-3}$	a

$a = 6.34 \times 10^{-3}$.

$E^0_{E'}$ 5.13 - MP2/cc-pVTZ; 5.31 - [b]ROVGF/6-311+G(2df); 5.43 - [c]ADC(3)/6-311+G(2df).

$E^0_{A_1'}$ 2.57 - MP2/cc-pVTZ; 2.72 - [b]ROVGF/6-311+G(2df);2.68 - [c]ADC(3)/6-311+G(2df);

$E^0_{A_1'}$ 2.88 - [c]RCCSD(T)/6-311+G(2df).

[b] Data from Ref. [113].

[c] Data from Ref. [67].

3.4 Results and Discussion

3.4.1 Adiabatic Potential Energy Surfaces

The adiabatic PESs of the $\widetilde{C}^2E'$ electronic manifold of B_3 are given by the eigenvalues of the diabatic electronic Hamiltonian matrix of Eq. (3.4) [17]. Setting the linear PJT coupling parameter λ_2 to zero one obtains the following eigenvalues:

$$\mathcal{V}^{A_1'}(Q) = \mathcal{V}_0(Q) + E^0_{A_1'} + \kappa_1' Q_1 + \frac{1}{2}\gamma_1' Q_1^2 + \frac{1}{2}\gamma_2'(Q_{x2}^2 + Q_{y2}^2), \quad (3.10)$$

$$\mathcal{V}_{\mp}(Q) = \mathcal{V}_0(Q) + E^0_{E'} + \kappa_1 Q_1 + \frac{1}{2}\gamma_1 Q_1^2 + \frac{1}{2}\gamma_2(Q_{x2}^2 + Q_{y2}^2) \mp \sqrt{[\lambda_2 Q_{x2} + \frac{1}{2}\eta_2(Q_{x2}^2 - Q_{y2}^2) + \frac{1}{2}\gamma_{12} Q_1 Q_{x2}]^2 + [\lambda_2 Q_{y2} - \eta_2 Q_{x2} Q_{y2} + \frac{1}{2}\gamma_{12} Q_1 Q_{y2}]^2}, \quad (3.11)$$

where, $\mathcal{V}^{A_1'}(Q)$ represents the adiabatic PES of the $\widetilde{X}^2A_1'$ electronic state and $\mathcal{V}_-$ and $\mathcal{V}_+$ denote the lower and upper adiabatic sheets of the JT split $\widetilde{C}^2E'$ electronic manifold of B_3, respectively. The quantity $\mathcal{V}_0$(Q) is given by Eq. (3.6). The analytic form of the argument of the square root in Eq. (3.11) refers to a cusp in the vicinity of the JT undistorted configuration at $\mathbf{Q}$=0.

The cuts of the adiabatic PESs described by Eq. (3.11) (without the bilinear γ_{12} JT coupling term) along the normal coordinates of the vibrational modes ν_1 and ν_2 are shown by the solid lines in Figs. 3.3(a) and 3.3(b), respectively. The dashed lines in panel *a* and *b* refer to the cut of the $\widetilde{X}^2A_1'$ electronic state along ν_1 and ν_2, respectively (Eq. 3.10). The totally symmetric mode ν_1 cannot lift the degeneracy of the $\widetilde{C}^2E'$ electronic state of B_3. However, depending on its excitation strength (cf. Table 3.2) it can shift the potential energy minimum of the $\widetilde{C}^2E'$ state away from the equilibrium geometry of the anion ($\mathbf{Q}$=0) and display Condon activity in the photoelectron band. The computed *ab initio* energies are superimposed on the model PESs, and are shown by the filled triangles in the

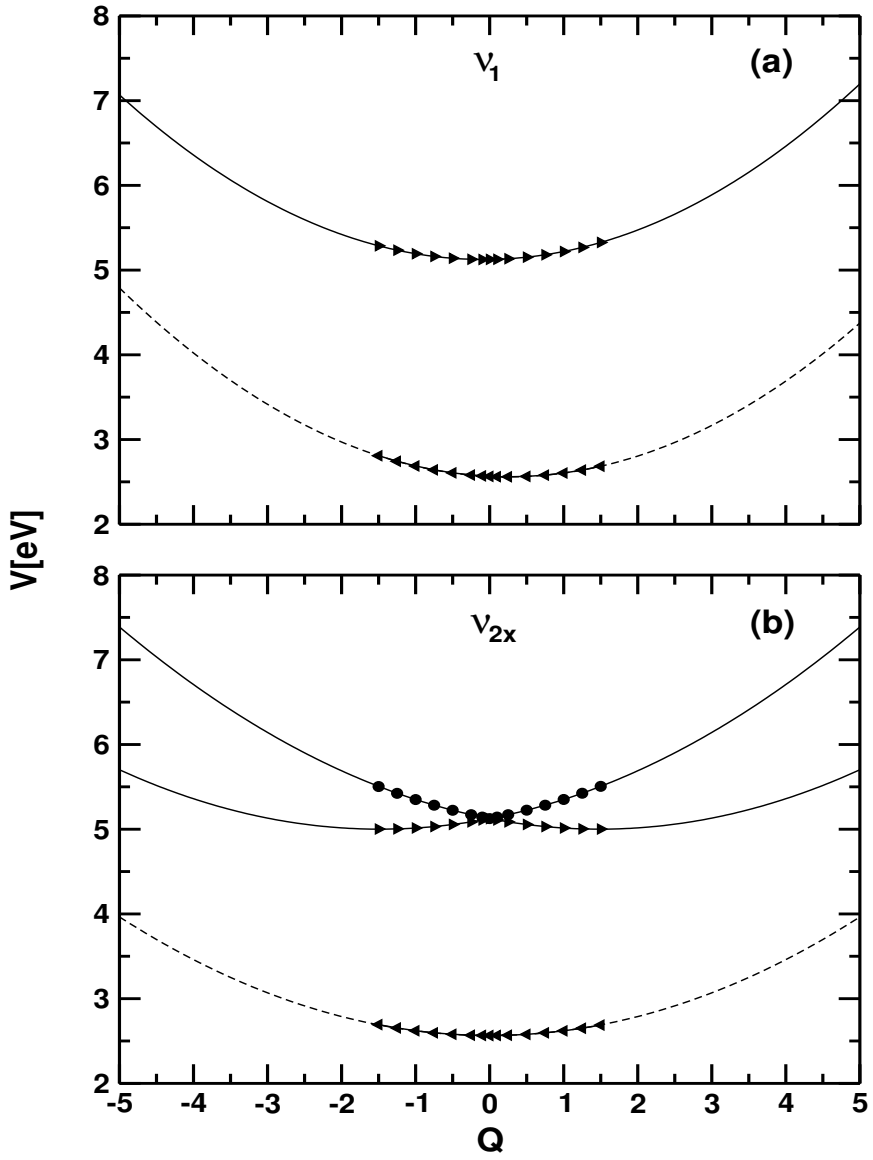

Figure 3.3: Adiabatic potential energy cuts of the $\widetilde{X}^2A_1'$ (dashed lines) and $\widetilde{C}^2E'$ (solid lines) electronic states of B_3 as a function of the dimensionless normal coordinates of the symmetric vibrational mode ν_1 (panel a) and the x component of the degenerate vibrational mode ν_2 (panel b). The PESs obtained from Eqs. (3.10-3.11) without the bilinear JT contributions are shown by the dashed and solid lines, respectively, whereas, the computed *ab initio* points are shown by the filled triangles/circles in the two panels. The equilibrium geometry of B_3^- in its electronic ground state ($\widetilde{X}^1A_1'$) corresponds to $\mathbf{Q}$=0.

figure. It can be seen that the computed *ab initio* energies are well reproduced by the model. Because of its very small excitation strength, the minimum of the $\widetilde{C}^2E'$ state shifts only slightly relative to the equilibrium geometry of the anion at $\mathbf{Q}$=0. However, the minimum of the $\widetilde{X}^2A_1'$ state shifts to a somewhat larger distance in the opposite direction.

The adiabatic PESs along the normal coordinate of the x component of the degenerate vibrational mode ν_2 obtained from Eqs. 3.10 and 3.11 are shown in Fig. 3.3(b). The solid lines in the figure refer to the potential energies of the $\widetilde{C}^2E'$ electronic states, whereas, the dashed lines refer to those of the $\widetilde{X}^2A_1'$ electronic state of B_3. The computed *ab initio* energies (filled triangles and circles) are also superimposed on the figure. It can be seen that the *ab initio* data are very well reproduced by the model. The degeneracy of the $\widetilde{C}^2E'$ electronic manifold is split upon displacements from the D_{3h} equilibrium geometry along this vibrational mode. It can be seen from Table 3.2 that the excitation strength of this mode is much larger than that of ν_1 and therefore, a considerable splitting of the degeneracy can be observed from Fig. 3.3(b). As a result, the two sheets of the JT split PESs form CIs at the D_{3h} equilibrium configuration. Upon distortion along Q_{2x} the D_{3h} symmetry of the system breaks and the system moves to the new energetic minima (here C_{2v}) of lower symmetry [17]. In three dimensions, three nearly equivalent minima separated by three saddle points appear on the lower adiabatic sheet and along with the cusp at the D_{3h} configuration it exhibits a "Mexican hat" type of topography of the PESs and such an image is shown in Fig. 3.4 plotted as a function of the dimensionless normal coordinates of the x and y components of the degenerate vibrational mode ν_2.

We now proceed to discuss the various stationary points of these PESs [cf. Eq. (3.11)]. The minimum of the seam of CIs of the two JT split PESs occur for $Q_1^0 = -\kappa_1/(\omega_1 + \gamma_1)$, along the symmetric vibrational mode ν_1 and the energy at this

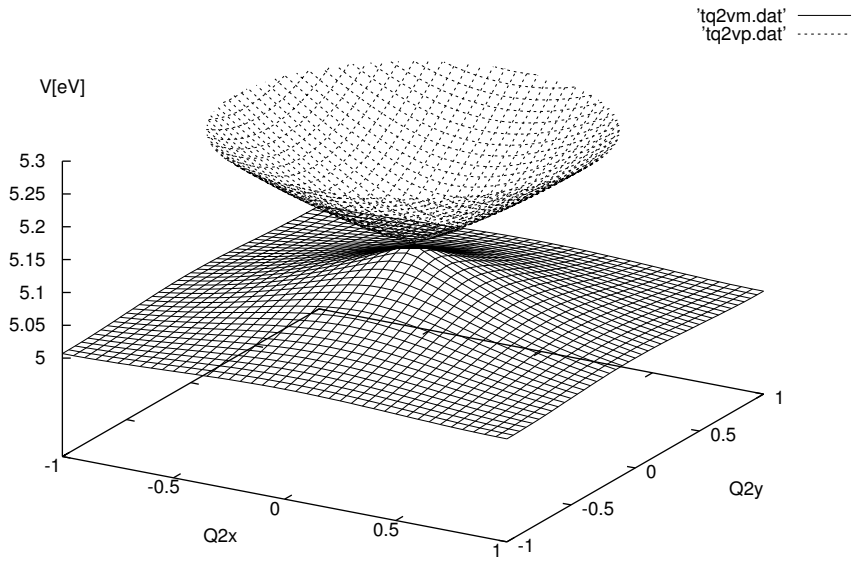

Figure 3.4: The $(E \times e)$-JT conical intersection of the $\widetilde{C}^2E'$ electronic manifold of B_3. This resembles the shape of the "Mexican hat" type of topography with the lower PES comprising three equivalent minima and three equivalent saddle points linking pairs of minima and the upper one resembles a conical shape with its vertex touching the lower one at the point of 3-fold-symmetry.

minimum is given by [17]

$$\mathcal{V}_{min}^{(c)} = E_{E'}^{0} - \frac{1}{2}\frac{\kappa_1^2}{(\omega_1+\gamma_1)}. \tag{3.12}$$

Along the degenerate mode ν_2, two solutions, $Q_{x2} = \pm\lambda_2/(\omega_2+\gamma_2 \mp \eta_2)$, are obtained with energies [17]

$$\mathcal{V}_{-}^{0} = E_{E'}^{0} - \frac{1}{2}\frac{\kappa_1^2}{(\omega_1+\gamma_1)} - \frac{1}{2}\frac{\lambda_2^2}{(\omega_2+\gamma_2-\eta_2)} \tag{3.13}$$

and

$$\mathcal{V}_{-}^{sp} = E_{E'}^{0} - \frac{1}{2}\frac{\kappa_1^2}{(\omega_1+\gamma_1)} - \frac{1}{2}\frac{\lambda_2^2}{(\omega_2+\gamma_2+\eta_2)}, \tag{3.14}$$

where, $\mathcal{V}_{-}^{0}$ and $\mathcal{V}_{-}^{sp}$ refer to the energy of the minimum and the saddle point, respectively, on the lower adiabatic sheet for the signs of the coupling constants as given in Table 3.2. With the data listed in the table, one obtains $\mathcal{V}_{min}^{(c)} = 5.125$ eV at Q_1^0 = -0.081. The new minima on $\mathcal{V}_{-}$ for the JT distorted geometry occur at $Q_{2x}^0 = 1.501$, with energy $\mathcal{V}_{-}^{0} = 5.0005$ eV. The saddle point occurs at Q_{2x}^{sp} = -1.468, with energy $\mathcal{V}_{-}^{sp} = 5.0017$ eV. The JT stabilization energy amounts to $\sim$ 0.125 eV.

3.4.2 Photodetachment Spectrum

In this section we show the results obtained using the above theoretical formalism along with the parameters of Table 3.2 and discuss and compare them with the available experimental results [67].

The final theoretical results are shown in Figs. 3.5(b) and 3.5(d) along with the experimental results in Figs. 3.5(a) and 3.5(c) reproduced from Ref. [67]. The intensity in arbitrary units is plotted as a function of the energy of the final vibronic state. The experimental bands in Figs. 3.5(a) and 3.5(c) correspond to the

355 *nm* and 193 *nm* recordings, respectively, of Ref. [67]. It is to be noted that the $\widetilde{C}^2E'$ electronic manifold of B_3 could be probed only at a very high photon energy (6.424 eV). Therefore, the energy resolution in the experimental band in Fig. 3.5(c) is quite poor. The theoretical stick eigenvalue spectra (in Figs. 3.5(b) and 3.5(d)) are convoluted with a Lorentzian line-shape function of 40 meV fwhm to generate the spectral envelopes. It can be seen that the theoretical envelopes agree reasonably well with the experimental band shapes. While the theoretical results show clear vibrational progressions for the $\widetilde{C}^2E'$ band, they are blurred in the experimental recording due to poor energy resolution.

The experimental results are reported at three different photon energies. At 355 *nm* (3.496 eV) only the $\widetilde{X}^2A_1'$ electronic state of B_3 could be probed and the vibronic structures of the $\widetilde{C}^2E'$ electronic manifold is observed only at 193 *nm* (6.424 eV). The hot band contribution is not revealed in the theoretical results which correspond to zero temperature calculations. We mention that we have examined the theoretical spectra shown in Figs. 3.5(b) and 3.5(d) under various situations viz., (1) within the LVC scheme, with and without the PJT coupling; (2) within the quadratic JT coupling scheme, excluding the bilinear contribution and with the full second-order Hamiltonian [Eqs. (3.4-3.7f)]. Our observations revealed insignificant contribution from the PJT, quadratic JT, and the bilinear JT couplings in the photodetachment spectrum [this is also revealed by the substantially low magnitude of their coupling parameters (cf. Table 3.2)].

The photoelectron band of the $\widetilde{X}^2A_1'$ electronic state of B_3 (cf. Fig. 3.5(b)) appears at $\sim$ 2.56 eV energy. Also, the adiabatic and the vertical ionization energies are nearly same in this case. This band reveals a progression along the ν_1 vibrational mode, an energy spacing of $\sim$ 1299 cm^{-1} can be observed from the theoretical stick spectrum. We note that the intensities of the second and the third peaks are drastically lower than that of the origin 0-0 peak. They are, respectively, $\sim 10^{-2}$ and $\sim 10^{-4}$ times lower than that of the 0-0 peak. As a

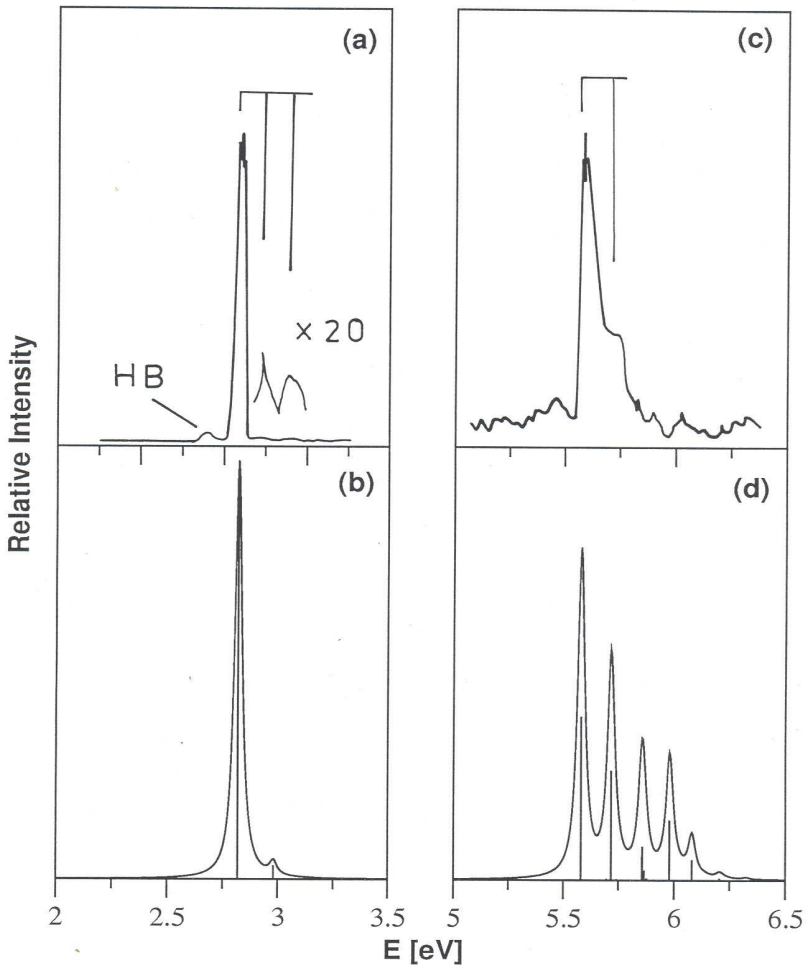

Figure 3.5: The final theoretical photoelectron band of the $\widetilde{X}^2A_1'$ (panel b) and $\widetilde{C}^2E'$ (panel d) electronic states of B_3 computed with the full second-order Hamiltonian [Eqs. (3.4-3.7f)] are shown along with the available experimental results in panels (a) and (c), respectively. The theoretical spectra are shifted by 0.26 eV and 0.62 eV, respectively to the higher energy along the abscissa to reproduce the adiabatic ionization positions of the bands at their experimental values. Both the theoretical spectra are convoluted with a Lorentzian function of 40 meV fwhm to calculate the spectral envelope.

result, the third peak is not at all visible in Fig. 3.5(b). An energy spacing of $\sim 1020 \pm 50\ cm^{-1}$ is reported for the experimental band. However, we observe a spacing of $\sim 1299\ cm^{-1}$ in the theoretical spectrum which is also consistent with the frequency of the ν_1 vibrational mode in the $\widetilde{X}^2A_1'$ state of B_3 [67].

The theoretical band of the $\widetilde{C}^2E'$ electronic manifold of B_3 in Fig. 3.5(d) shows nicely resolved structures. This band originates at ~ 4.96 eV and exhibits a dominant progression along the JT active vibrational mode ν_2. The lines are $\sim 1103\ cm^{-1}$ spaced in energy, and is in excellent agreement with the observed splitting of $1100 \pm 80\ cm^{-1}$ in the experimental band [67]. This also confirms that the splitting observed in the experimental band indeed represents a vibrational structure. The symmetric vibrational mode ν_1 is very weakly excited in this band, which is also revealed by the extremely small coupling strength of this mode (cf. Table 3.2). We note here that, essentially the same result (cf. Fig. 3.5(d)) is obtained by ignoring the quadratic JT coupling and also with and without the PJT coupling. This shows that a linear JT model is good enough to reproduce the observed features of the experiment in this case. The $\widetilde{X}^2A_1'$ and the $\widetilde{C}^2E'$ electronic states are vertically separated by ~ 2.561 eV in energy. The PJT interactions between these electronic states is very weak, and therefore do not have any impact on the vibronic structures of the photoelectron bands. The JT coupling within the $\widetilde{C}^2E'$ electronic manifold is also weak compared to similar strong $(E \otimes e)$-JT coupling cases treated in the literature [26, 90, 119].

To conclude, we mention that photodetachment experiments for the smallest boron clusters are reported to be quite delicate because of weak cluster intensities and low photodetachment cross sections [67]. The resolution of the apparatus was ~ 30 meV for 1 eV electrons [67]. The highest binding energy feature in the 193 nm (6.424 eV) recording (reproduced in Fig. 3.5(c)) is reported at 5.58 eV [67]. Beyond this energy, the experimental resolution and detection are expected to be very poor because of a loss of electrons with low kinetic energy, and also keeping in mind the low photodetachment cross sections of B_3^-. Furthermore, the vibronic

structures beyond 6 eV are not expected to be resolved by the 6.424 eV laser photon. These are some of the possible reasons for the observed disagreement between the experiment and theory in Figs. 3.5(c) and 3.5(d), respectively.

3.5 Summary and Outlook

In this chapter, we have presented a theoretical account on the anion photoelectron spectroscopy of triatomic boron cluster. The impact of static and dynamic aspects of the JT and PJT interactions in the $\widetilde{X}^2A_1'$-$\widetilde{C}^2E'$ electronic states of B_3 on the vibronic structure of the photodetachment spectrum is examined. A diabatic electronic Hamiltonian is constructed, and the nuclear dynamics is simulated by a Lanczos based quantum mechanical approach. The theoretical findings are compared with the experimental recordings of Zhai *et al.* [67].

The elements of the model diabatic Hamiltonian are expanded in a second-order Taylor series in terms of the dimensionless normal coordinates of the electronic ground state of B_3^-. The equilibrium geometry of B_3^- in its ground electronic state is optimized at the MP2 level of theory, and the harmonic force field and dimensionless normal coordinates are calculated. The vertical detachment energies of B_3^- are calculated as a function of the normal mode displacements from the equilibrium geometry by the OVGF method. These energies are equated with the adiabatic potential energies of the $\widetilde{X}^2A_1'$-$\widetilde{C}^2E'$ electronic manifold of B_3 and the parameters of the Hamiltonian are derived.

The theoretical results reproduced the observed shape of the photodetachment bands very well. For the $\widetilde{X}^2A_1'$ band of B_3, a progression along the symmetric ν_1 vibrational mode is found. The successive lines are 1299 cm^{-1} apart in energy, which compares well with the vibrational frequency of ν_1 in the $\widetilde{X}^2A_1'$ electronic state of B_3. However, an energy spacing of $\sim 1020 \pm 50$ cm^{-1} of this progression is reported in the experiment. The vibronic structure of the $\widetilde{C}^2E'$ band, on the other hand, showed a dominant and extended progression along the degenerate

ν_2 vibrational mode. The spacing between the successive lines is $\sim 1103\ cm^{-1}$, this is in very good agreement with the observed sharp splitting of $\sim 1100 \pm 80\ cm^{-1}$; in the experimental recording. This provides an unambiguous evidence that the observed splitting of the band recorded in the experiment is due to the vibrational progression along the JT active mode ν_2. Our explicit theoretical analysis indicates that the linear PJT, quadratic, and bilinear JT couplings have practically no impact on the vibronic structure of the $\widetilde{X}^2A_1'$-$\widetilde{C}^2E'$ photoelectron band of B_3. The JT effect in the $\widetilde{C}^2E'$ electronic manifold is also quite weak when compared to the similar other examples treated in the literature [26, 90, 119].

Chapter 4

The JT and PJT interactions in the ethane radical cation

4.1 Introduction

The present chapter deals with the static and dynamic aspects of the JT and PJT interactions in the photoionization spectrum of ET. The equilibrium geometry of neutral ET corresponds to a staggered conformation belonging to the D_{3d} point group in its electronic ground state ($\widetilde{X}^1A_{1g}$). Using the D_{3d} symmetry, the ground-state molecular orbital sequence of ET can be written as [69]

$$(1a_{1g})^2(1a_{2u})^2(2a_{1g})^2(2a_{2u})^2(1e_u)^4(3a_{1g})^2(1e_g)^4$$

Ionizations from the last three outer valence molecular orbitals of neutral ET produce ET^+ in the ^2E_g, $^2A_{1g}$, and ^2E_u electronic states, respectively. Ethane is a prototypical saturated hydrocarbon and its 18 vibrational degrees of freedom belong to the following irreducible representations of the D_{3d} point group:

$$\Gamma_{vib} = 3a_{1g} + 3e_g + a_{1u} + 2a_{2u} + 3e_u. \quad (4.1)$$

The symmetrized direct product of two E_g or E_u representation in the D_{3d} point group yields [107],

$$(E_g)^2 = (E_u)^2 = a_{1g} + e_g \tag{4.2}$$

The symmetry selection rule stated above implies that the degenerate e_g vibrational modes (the symmetry species of normal modes are designated by the lower case symbols) can split the degeneracy of the $\widetilde{X}^2E_g$ and $\widetilde{B}^2E_u$ electronic states and therefore may exhibit $(E \otimes e_g)$-JT activity. The a_{1g} vibrational modes, on the other hand, cannot lift the degeneracy of these two electronic states but they can exhibit tuning activity [17] by shifting their energetic minimum relative to the ground electronic state of ET. Similarly, the direct products of E_g, A_{1g}, and E_u states in the D_{3d} point group yield

$$E_g \times A_{1g} = e_g \tag{4.3a}$$

$$E_u \times A_{1g} = e_u \tag{4.3b}$$

$$E_g \times E_u = e_u \tag{4.3c}$$

From Eq. (4.3a), it can be seen that the same e_g vibrational mode can also cause PJT coupling between the E_g and A_{1g} electronic states. This pattern generally holds true for molecules possessing a three-fold principal rotational axis of symmetry [7, 17, 45–47]. The degenerate e_u vibrational modes, on the other hand, involved in the PJT coupling of $\widetilde{B}^2E_u$ electronic manifold with the neighboring $\widetilde{X}^2E_g$ and $\widetilde{A}^2A_{1g}$ electronic states [cf. Eqs. (4.3b-4.3c)].

For a brief account of the photoelectron spectrum of ET and the available electronic structure results we refer to section 1.3. In this chapter, we consider

the first photoelectron band observed in the 11.5-14.5 eV ionization energy range pertinent to the vibronic structure of the *gerade (g)*, $\widetilde{X}^2E_g$ -$\widetilde{A}^2A_{1g}$ electronic manifold of ET^+. The $\widetilde{A}^2A_{1g}$ state is estimated to be $\sim$ 0.345 eV above the $\widetilde{X}^2E_g$ state and $\sim$ 2.405 eV below the $\widetilde{B}^2E_u$ state at the vertical configuration. The JT and PJT interactions in the excited $\widetilde{A}^2A_{1g}$ -$\widetilde{B}^2E_u$ interacting electronic manifold of the ET^+ have been studied by Kumar *et al.* and those results are not included in this thesis [120]. A model diabatic Hamiltonian is constructed where the effect of the Condon active tuning vibrational modes (a_{1g} symmetry) is considered up to the second order, whereas only linear terms are considered for the JT and PJT active degenerate (e_g symmetry) coupling modes. The various coupling parameters of the Hamiltonian are calculated by *ab initio* methods at the MP2 level of theory using the cc-pVTZ basis set [115]. The photoelectron band is computed by solving the eigenvalue equation using Lanczos algorithm [56]. Our findings reveal that the CH_3 deformation modes of a_{1g} and e_g symmetries, particularly, play crucial roles in the nuclear dynamics in the ^2E_g - $^2A_{1g}$ electronic manifold of ET^+. They form the dominant progressions in the photoelectron band at low energies and the more diffuse structure at high energies results from the PJT interactions of the ^2E_g and $^2A_{1g}$ electronic states mainly through the degenerate bending and CH_3 deformation modes.

4.2 The Vibronic Hamiltonian

The photoionization process is described as a FC transition from the electronic ground state ($\widetilde{X}^1A_{1g}$) of ET to the interacting $\widetilde{X}^2E_g$ -$\widetilde{A}^2A_{1g}$ electronic manifold of ET^+. The nuclear motion in the latter electronic manifold is monitored with the aid of a model Hamiltonian constructed in a diabatic electronic representation [17, 38] in terms of the dimensionless normal coordinates pertinent to the equilibrium configuration of the ground electronic state of ET. The nuclear vibrations in this initial electronic state is treated as harmonic. The use of a

diabatic electronic basis is facilitated by the weak dependence of the elements of the vibronic Hamiltonian with the nuclear coordinates. This justifies the use of the Condon approximation in the photoionization process [109]. Moreover, in this electronic basis the states are coupled through the electronic part of the Hamiltonian, rather than the nuclear part as in an adiabatic electronic basis [44]. In the latter case, the elements of the nonadiabatic coupling matrix exhibit a singularity at the seam of intersections of the electronic states.

Within a LVC scheme, the nuclear dynamics in the $\widetilde{X}^2E_g$ -$\widetilde{A}^2A_{1g}$ electronic manifold is governed by the vibrational modes of g symmetry only [cf. Eqs. (4.2-4.3a)]. These vibrational modes ν_j of ET are sketched in Fig. 4.1. In this section we define Q_j as the displacement from the ground state equilibrium geometry of ET along the dimensionless normal coordinates of the vibrational mode ν_j. These coordinates are more clearly defined in section 4.3 below. The three totally symmetric a_{1g} vibrational modes, j = 1-3, act as the tuning modes (Condon active) in both the $\widetilde{X}^2E_g$ and $\widetilde{A}^2A_{1g}$ ionic states. The three degenerate e_g vibrational modes, j = 4-6, on the other hand, act as the JT coupling modes within the $\widetilde{X}^2E_g$ electronic manifold and as the PJT coupling modes in the coupled $\widetilde{X}^2E_g$-$\widetilde{A}^2A_{1g}$ electronic states.

Our goal here is to examine the vibronic structures of the first photoelectron band of ET using a $(E_g + A_{1g}) \otimes e$ coupling scheme [17, 45–47]. The interactions with the E_u electronic state of the radical cation is not considered, primarily because it is energetically well separated by $\sim$ 2.750 eV from the E_g state and $\sim$ 2.405 eV from the A_{1g} state. Throughout this study, a LVC scheme is assumed for the degenerate vibrational modes. However, the second-order coupling effects due to the totally symmetric vibrational modes are also discussed. The full second-order treatment of the coupling modes is more involved and, in addition, the vibrational modes of e_u symmetry are also to be considered. Such a study is computationally not viable with the matrix diagonalization approach due to the huge increase in the size of the secular matrix by considering additional

vibrational degrees of freedom. Alternatively, it can be carried out by a WP propagation approach using the MCTDH scheme.

The Hamiltonian described below represents the $(E \otimes e_g)$-JT interactions in the $\widetilde{X}^2E_g$ electronic manifold and $(E + A) \otimes e_g$-PJT interactions in the $\widetilde{X}^2E_g$-$\widetilde{A}^2A_{1g}$ electronic states in addition to the Condon activity of the totally symmetric a_{1g} vibrational modes. The diabatic Hamiltonian for this interacting electronic manifold can be expressed as [17],

$$\mathcal{H} \;=\; \mathcal{H}_0\mathbf{1_3} + \Delta\mathcal{H} \tag{4.4}$$

Here $\mathcal{H}_0 = \mathcal{T}_N + \mathcal{V}_0$, with

$$\mathcal{T}_N \;=\; -\frac{1}{2}\sum_{j=1}^{3}\omega_j\frac{\partial^2}{\partial Q_j^2} - \frac{1}{2}\sum_{j=4}^{6}\omega_j\left(\frac{\partial^2}{\partial Q_{jx}^2} + \frac{\partial^2}{\partial Q_{jy}^2}\right), \tag{4.5}$$

$$\mathcal{V}_0 \;=\; \frac{1}{2}\sum_{j=1}^{3}\omega_j Q_j^2 + \frac{1}{2}\sum_{j=4}^{7}\omega_j\left(Q_{jx}^2 + Q_{jy}^2\right), \tag{4.6}$$

and

$$\Delta\mathcal{H} \;=\; \begin{pmatrix} \mathcal{H}_{11} & \mathcal{H}_{12} & \mathcal{H}_{13} \\ & \mathcal{H}_{22} & \mathcal{H}_{23} \\ h.c. & & \mathcal{H}_{33} \end{pmatrix}. \tag{4.7}$$

$\mathcal{H}_0$ is the Hamiltonian matrix associated with the electronic ground state of ET and is defined in terms of unperturbed harmonic oscillators with frequencies ω_j. $\mathbf{1}_3$ is a 3×3 unit matrix. The quantity $\Delta\mathcal{H}$ describes the change in electronic energy upon ionization from the electronic ground state of ET. This is a non-diagonal (3×3) matrix, the elements of which represent the diabatic potential energies of the $\widetilde{X}^2E_g$ -$\widetilde{A}^2A_{1g}$ interacting electronic states of the ET^+. These elements are expanded in a Taylor series around the D_{3d} equilibrium geometry

of ET (**Q**=0) along each of the normal mode displacement coordinates and in conjunction with the symmetry selection rules given in the introduction. Within the coupling scheme stated above the matrix Hamiltonian $\Delta\mathcal{H}$ can be expressed as [17, 45–47]

$$\mathcal{H}_{11} = E^0_{E_g} + \sum_{j=1}^{3} \kappa_j Q_j + \sum_{j=4}^{6} \lambda_j Q_{jx} + \frac{1}{2}\sum_{j=1}^{3} \gamma_j Q_j^2, \tag{4.8a}$$

$$\mathcal{H}_{22} = E^0_{A_{1g}} + \sum_{j=1}^{3} \kappa'_j Q_j + \frac{1}{2}\sum_{j=1}^{3} \gamma'_j Q_j^2, \tag{4.8b}$$

$$\mathcal{H}_{33} = E^0_{E_g} + \sum_{j=1}^{3} \kappa_j Q_j - \sum_{j=4}^{6} \lambda_j Q_{jx} + \frac{1}{2}\sum_{j=1}^{3} \gamma_j Q_j^2, \tag{4.8c}$$

$$\mathcal{H}_{12} = \sum_{j=4}^{6} \lambda'_j Q_{jx}, \tag{4.8d}$$

$$\mathcal{H}_{13} = \sum_{j=4}^{6} \lambda_j Q_{jy}, \tag{4.8e}$$

$$\mathcal{H}_{23} = -\sum_{j=4}^{6} \lambda'_j Q_{jy}. \tag{4.8f}$$

The parameters of the Hamiltonian stated above have the following physical meaning. The quantities $E^0_{E_g}$ and $E^0_{A_{1g}}$ are the vertical ionization energies of the $\widetilde{X}^2E_g$ and $\widetilde{A}^2A_{1g}$ electronic states of ET^+, respectively. The intrastate linear coupling constants for the totally symmetric vibrational modes are given by κ_j

and κ'_j in the E_g and A_{1g} electronic states, respectively. The linear JT coupling constants for the degenerate vibrational modes in the E_g electronic manifold are denoted by λ_j. The quantities λ'_j define the linear PJT coupling constants for the degenerate vibrational modes. The second-order coupling parameters for the totally symmetric modes are denoted by γ_j and γ'_j in the E_g and A_{1g} electronic states, respectively. A similar vibronic Hamiltonian has been used in the literature [28, 47, 121] in order to describe the interaction of nondegenerate and two-fold degenerate electronic states. In the present application as stated above, the Hamiltonian describes the JT interaction in the $\widetilde{X}^2E_g$ state and PJT interactions between the $\widetilde{X}^2E_g$ -$\widetilde{A}^2A_{1g}$ states of ET^+.

4.3 Electronic Structure Calculations

The geometry optimization, calculations of harmonic vibrational frequencies, and normal coordinates of ET in its $\widetilde{X}^1A_{1g}$ ground electronic state are carried out at the MP2 level of theory employing the cc-pVTZ Gaussian basis set. The *ab initio* calculations were performed using the Gaussian03 program package [116]. The optimized geometry parameters for the ground-state equilibrium geometry of ET are presented in Table 4.1 along with the available experimental results [122]. It can be seen from Table 4.1 that the MP2 equilibrium geometry parameters correspond well with the available experimental data. The dimensionless normal coordinates are obtained as we discussed in section 3.3.1.

The normal vibrational modes of g symmetry of ET are schematically represented in Fig. 4.1. The nature of these vibrational modes, their symmetry properties, and harmonic vibrational frequencies are reported in Table 4.2, along with the available experimental results [70] for comparison. Despite a relatively large discrepancy for the C-H stretching frequencies (ν_3 and ν_6), the theoretical data are in good accord with the experimental results [70]. Furthermore, the apparent deviation between the two can be attributed to the fundamental nature

Table 4.1: Equilibrium geometry of ethane in its ground electronic state ($\widetilde{X}^1A_{1g}$) along with the experimental results [122].

	∠ H-C-H (deg)	∠ C-C-H (deg)	C-H (Å)	C-C (Å)
MP2/cc-pVTZ	107.64	111.24	1.088	1.523
Expt [122]	107.07	111.75	1.096	1.532

Table 4.2: Symmetry, frequency, and description of the vibrational modes of g symmetry of the electronic ground state of ethane. The experimental results are reproduced from Ref. [70]. Note that, the theoretical frequencies are harmonic, whereas the experimental ones are fundamental.

		Vibrational frequency (ω_i)/eV		
Symmetry	Mode	MP2/cc-pVTZ	Experiment	Description
a_{1g}	ν_1	0.1278	0.1157	C-C Stretching
	ν_2	0.1775	0.1705	CH_3 deformation
	ν_3	0.3819	0.3594	C-H Stretching
e_g	ν_4	0.1525	0.1432	Bending
	ν_5	0.1888	0.1810	CH_3 deformation
	ν_6	0.3910	0.3674	C-H Stretching

of the experimental vibrational frequencies.

4.3.1 Coupling Parameters of the Hamiltonian

In order to calculate the coupling parameters of the Hamiltonian [Eqs. (4.8a-4.8f)], we perform direct calculations of vertical ionization energies of ET by the OVGF method [117, 118] employing the cc-pVTZ basis set [115]. The electronic structure calculations are carried out as a function of the dimensionless normal coordinates Q_j (j = 1-6) = $\pm$0.10, $\pm$0.25 ($\pm$0.25) $\pm$1.50 using the Gaussian03 program package [116]. The vertical ionization energies thus obtained are equated with the adiabatic potential energy of the electronic states of ET^+ relative to the electronic ground state of ET.

The coupling parameters of the Hamiltonian matrix represent the derivatives of the adiabatic potential-energy function of the radical cation (of appropriate

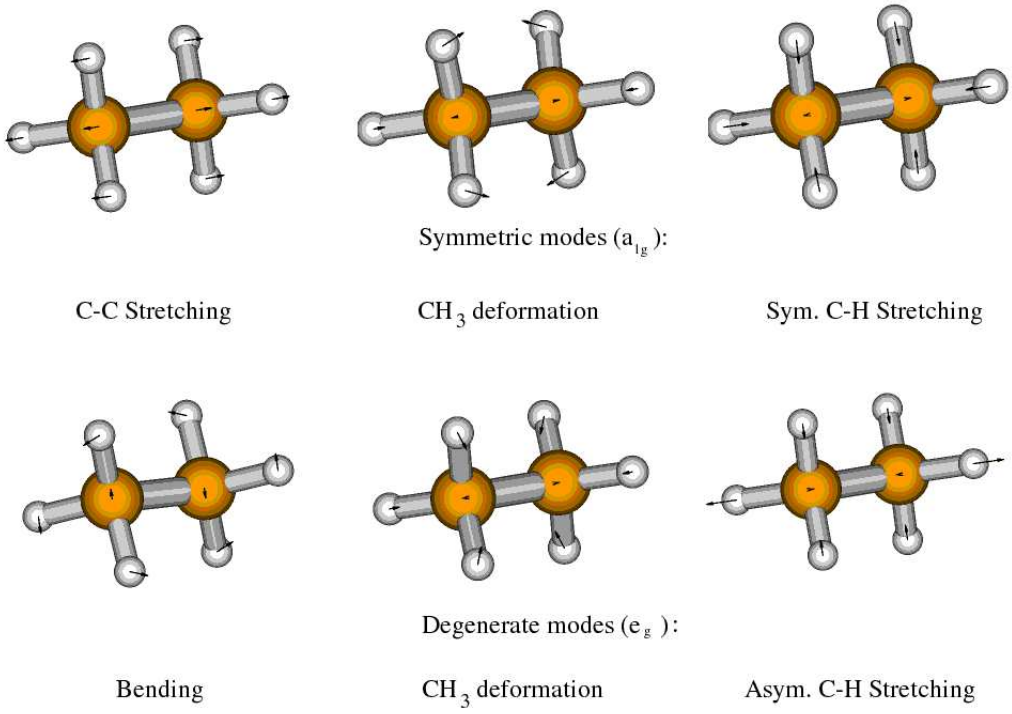

Figure 4.1: Schematic representation of the normal vibrational modes of g symmetry of the electronic ground state of ethane.

order) with respect to the dimensionless normal coordinate Q_j of the vibrational mode ν_j evaluated at the equilibrium geometry of the neutral at $\mathbf{Q}$=0 [123]. The linear intrastate (κ_j) and the JT coupling parameters (λ_j) are defined as the gradients of the adiabatic potential energy of the $\widetilde{X}^2E_g$ state of ET^+ with respect to the dimensionless normal coordinate of the vibrational mode ν_j, evaluated at the ground state equilibrium geometry of ET ($\mathbf{Q}$=0) [17, 123],

$$\kappa_j = \left(\frac{\partial V_{E_g}}{\partial Q_j}\right)\Bigg|_{\mathbf{Q=0}}, \qquad j = 1-3, \tag{4.9}$$

$$\lambda_j = \frac{1}{2}\left(\frac{\partial \Delta V_{E_g}}{\partial Q_j}\right)\Bigg|_{\mathbf{Q=0}}, \qquad j = 4-6, \tag{4.10}$$

where V_{E_g} denotes the adiabatic potential energy of the degenerate $\widetilde{X}^2E_g$ electronic state of ET^+. The quantity ΔV_{E_g} is the (signed) difference of the JT split PESs of the $\widetilde{X}^2E_g$ electronic manifold. An analogous definition holds for κ'_j, where V_{E_g} in Eq. (4.9) is replaced by the adiabatic potential energy $V_{A_{1g}}$ of the $\widetilde{A}^2A_{1g}$ electronic state of the radical cation. The PJT coupling parameters λ'_j for the degenerate vibrational modes ν_4-ν_6 can be obtained using Eq. (3.9) in which ΔE is the difference of squares of the adiabatic potential-energy difference between the $\widetilde{A}^2A_{1g}$ and $\widetilde{X}^2E_g$ ionic states for normal coordinate displacement Q_j and the same for the equilibrium configuration, $\mathbf{Q}$=0. Coupling parameters described by the above equations can be obtained by a suitable finite difference scheme (given in Appendix B) using small normal coordinate displacements from the ground-state equilibrium geometry of ET.

The second-order coupling parameters of the Hamiltonian in Eqs. (4.8a-4.8c)

are defined as follows [17, 123]:

$$\gamma_j = \left(\frac{\partial V_{E_g}}{\partial Q_j}\right)\Bigg|_{\mathbf{Q=0}}, \qquad j = 1-3, \tag{4.11}$$

$$\gamma'_j = \left(\frac{\partial V_{A_{1g}}}{\partial Q_j}\right)\Bigg|_{\mathbf{Q=0}}, \qquad j = 1-3. \tag{4.12}$$

For a given symmetric mode, the linear and the quadratic coupling parameters can be obtained in a straight forward way by a two-parameter least-square fit of the mode specific contribution

$$E^0 + \frac{1}{2}\omega_j Q_j^2 + \kappa_j Q_j + \gamma_j Q_j^2 \tag{4.13}$$

to the adiabatic potential-energy function, keeping ω_j constant. We note that these parameters are calculated both by a numerical finite difference scheme and also by a least-square fitting procedure and the identity of the results is confirmed.

For the degenerate vibrational modes, the linear JT coupling parameters λ_j are calculated both by a numerical finite difference scheme and by fitting the adiabatic potential-energy difference of the JT split surfaces by a least-square method. Identical results are obtained by both these procedures. Finally, the PJT coupling parameters are also determined by a numerical finite difference scheme as well as by fitting the eigenvalues of the coupling matrix

$$\mathcal{V} = \begin{pmatrix} E^0_{E_g} + \lambda_j Q_{jx} & \lambda'_j Q_{jx} \\ \lambda'_j Q_{jx} & E^0_{A_{1g}} \end{pmatrix} \tag{4.14}$$

along each degenerate vibrational mode j. We note that the value obtained by these two procedures typically show a difference of $\sim \pm$ 0.03 eV. The difference being somewhat more for the mode ν_6. However, this is a high-frequency mode (C-H stretch) and does not have a significant contribution to the nuclear dynamics

Table 4.3: *Ab initio* calculated coupling parameters of the Hamiltonian [Eqs. (4.4-4.8f)]. The excitation strength of each mode estimated by the Poisson parameters $(\kappa_j/\omega_j)^2/2$, $(\lambda_j/\omega_j)^2/2$, and $(\kappa'_j/\omega_j)^2/2$ are given in parentheses. All coupling parameters and energies are in eV.

Mode (symmetry)	κ_j or λ_j $\widetilde{X}^2E_g$	κ'_j $\widetilde{A}^2A_{1g}$	γ_j $\widetilde{X}^2E_g$	γ'_j $\widetilde{A}^2A_{1g}$	λ'_j $\widetilde{X}^2E_g \times \widetilde{A}^2A_{1g}$
$\nu_1(a_{1g})$	0.135(0.560)	-0.256(2.008)	-1.956 $\times 10^{-2}$	3.013 $\times 10^{-3}$	–
$\nu_2(a_{1g})$	0.167(0.443)	-0.643(6.554)	-6.042 $\times 10^{-2}$	2.124 $\times 10^{-2}$	–
$\nu_3(a_{1g})$	0.290(0.289)	0.013(0.046)	1.327 $\times 10^{-2}$	-3.778 $\times 10^{-3}$	–
$\nu_4(e_g)$	0.194(0.806)	–	–	–	0.3317
$\nu_5(e_g)$	0.303(1.288)	–	–	–	0.2721
$\nu_6(e_g)$	0.233(0.177)	–	–	–	0.0370
$E^0_{E_g}$ 12.711					
$E^0_{A_{1g}}$ 13.056					

as illustrated below.

In Fig. 4.2(a-f) the adiabatic potential-energy values of the $\widetilde{X}^2E_g$ and $\widetilde{A}^2A_{1g}$ electronic states of ET^+ measured relative to the electronic ground state of ET (these are the vertical ionization energies obtained from the OVGF calculations) along the dimensionless normal coordinate of the a_{1g} vibrational modes, ν_1, ν_2, and ν_3 are plotted. The asterisks and the filled circles represent the computed data for the $\widetilde{X}^2E_g$ and $\widetilde{A}^2A_{1g}$ electronic states, respectively, and a quadratic fit to these data is shown by the solid line in each panel. The modes ν_1, ν_2, and ν_3 represent the C-C stretching, CH_3 deformation, and C-H stretching vibrations, respectively. It can be seen that the degeneracy of the $\widetilde{X}^2E_g$ electronic state of ET^+ is not split on displacements along these modes. The linear κ_j and κ'_j and the second-order γ_j and γ'_j coupling parameters for these modes resulting from the above fits are given in Table 4.3.

The linear JT coupling parameters (λ_j) for the e_g vibrational modes ν_4-ν_6 in the $\widetilde{X}^2E_g$ electronic manifold are calculated by fitting the signed difference of the JT split PESs along these modes. In Figs. 4.3(a-c), we have shown the JT split potential energy differences plotted along the dimensionless normal coordinates of

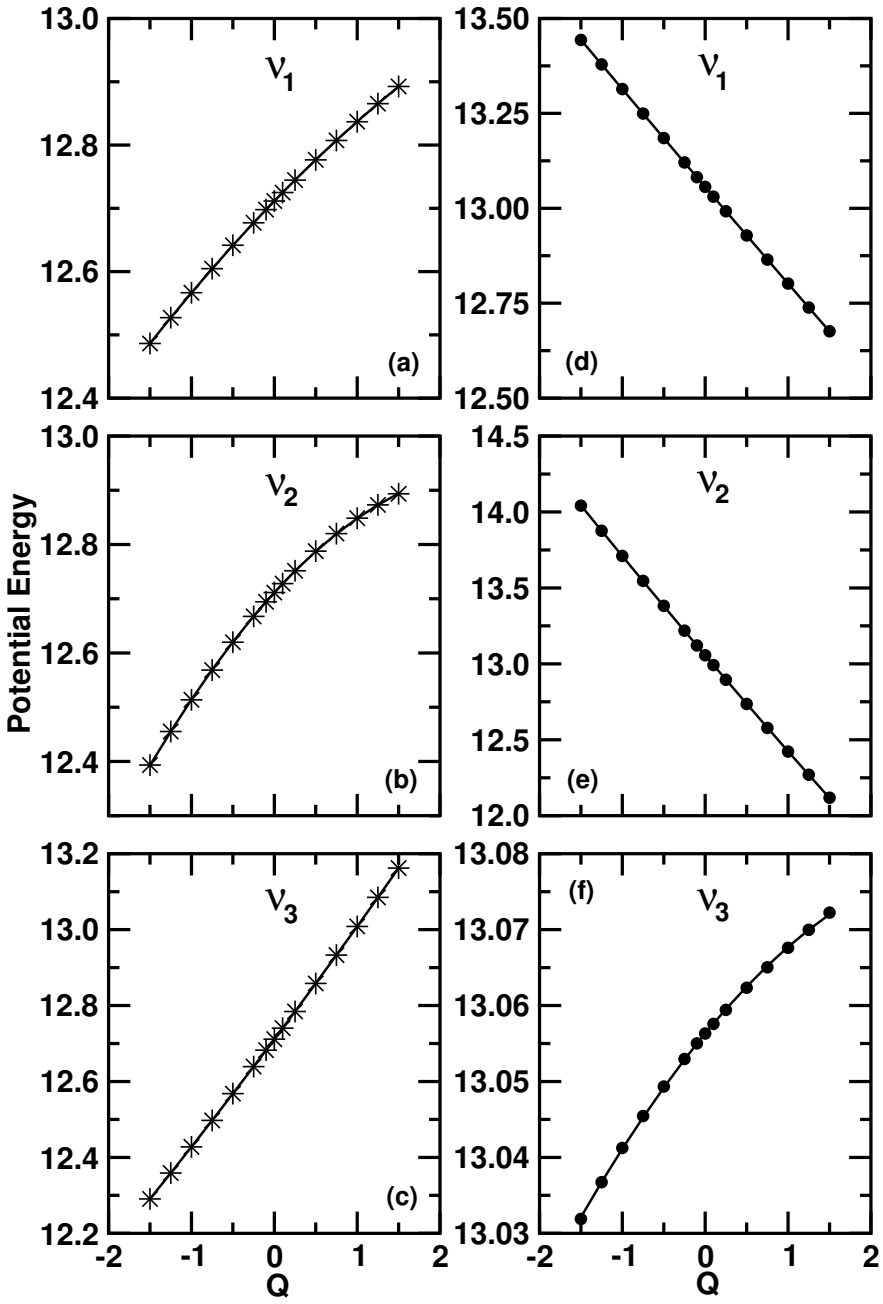

Figure 4.2: Adiabatic potential energies of the $\widetilde{X}^2E_g$ (panels: a-c) and $\widetilde{A}^2A_{1g}$ (panels: d-f) electronic states of ET^+ measured relative to the electronic ground state of ET along the dimensionless normal coordinates of the symmetric vibrational modes ν_1, ν_2, and ν_3. The asterisks and filled circles represent the computed data for the $\widetilde{X}^2E_g$ and $\widetilde{A}^2A_{1g}$ electronic states respectively, and a quadratic fit to these data is shown by the solid line in each panel. The linear (κ_j and κ'_j) and diagonal quadratic coupling (γ_j and γ'_j) parameters listed in Table 4.3 are obtained from the above fits.

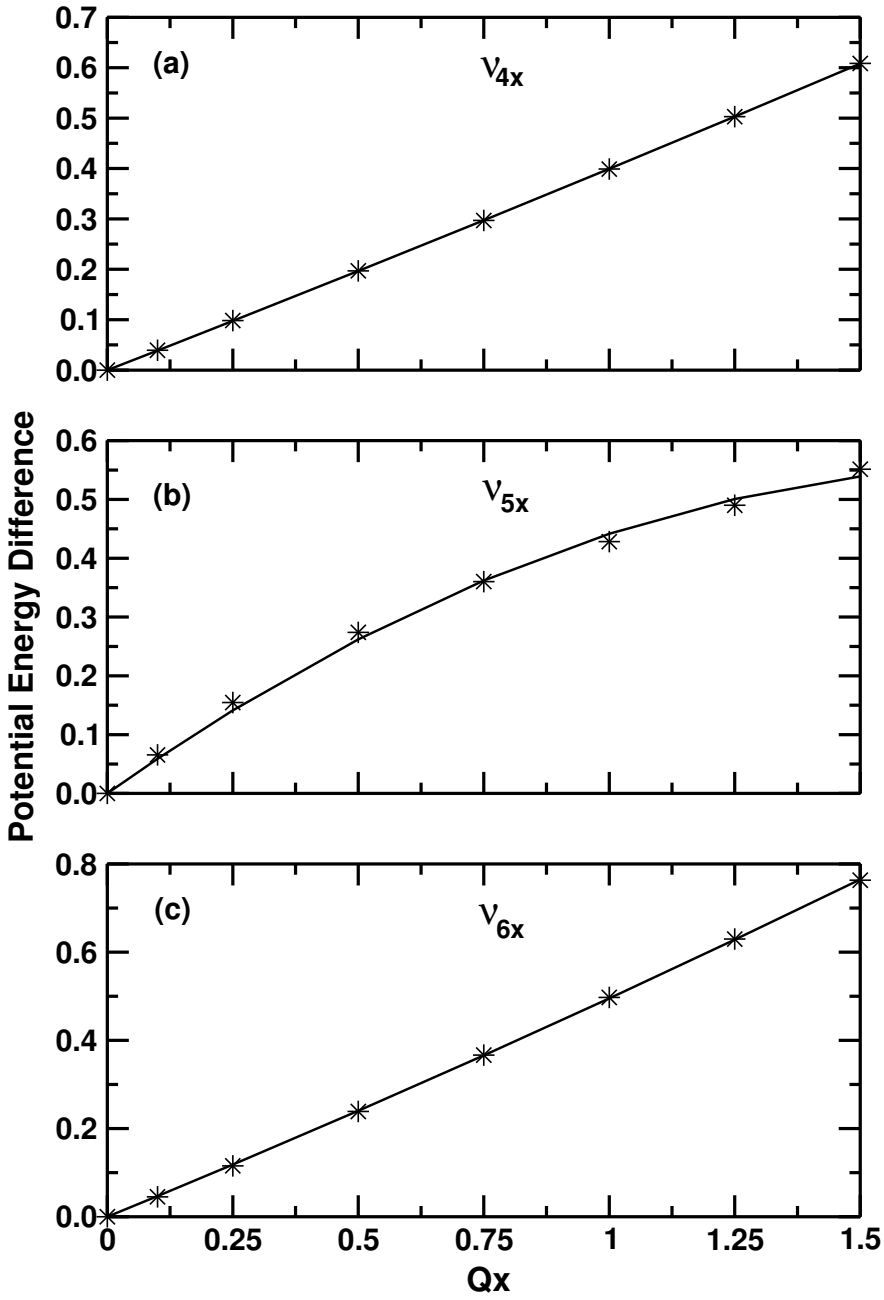

Figure 4.3: Potential energy difference (signed) of the JT split adiabatic sheets of the $\widetilde{X}^2E_g$ electronic manifold of ET^+ plotted along the dimensionless normal coordinate of the x component of the degenerate vibrational modes ν_4, ν_5, and ν_6 are shown in panels a, b, and c, respectively. The computed data are shown by the asterisks and a quadratic fit to these data is shown by the solid lines. The linear JT coupling parameters λ_j extracted from these fits are documented in Table 4.3

the x components of the degenerate vibrational modes ν_4, ν_5, and ν_6. These modes represent the C-H bending, CH_3 deformation, and C-H Stretching vibrations, respectively. Again the asterisks denote the computed energies and the solid line represents a quadratic fit to these data in each panel.

The numerical values of all coupling parameters discussed above are given in Table 4.3. In the last two rows of the Table 4.3, the vertical ionization energies of the $\widetilde{X}^2E_g$ and $\widetilde{A}^2A_{1g}$ electronic states of the radical cation are listed. We use these parameters below to calculate the photoelectron band.

4.4 Results and Discussion

4.4.1 Adiabatic Potential Energy Surfaces

The topography of the adiabatic PESs of the $\widetilde{X}^2E_g$ and $\widetilde{A}^2A_{1g}$ electronic states of ET^+ using the coupling parameters of Table 4.3 is discussed here. At first, we consider the electronic Hamiltonian matrix within the LVC scheme [i.e., excluding the second-order contributions γ_j and γ'_j of totally symmetric vibrational modes a_{1g} in Eqs. (4.8a-4.8c)], whereby the adiabatic PESs of the $\widetilde{X}^2E_g$ and $\widetilde{A}^2A_{1g}$ electronic states of the radical cation are obtained by diagonalizing the diabatic electronic Hamiltonian matrix of Eq. (4.4) [17].

In Figs. 4.4(a-c) we show the one dimensional cuts of the adiabatic PESs of the radical cation along the dimensionless normal coordinates of the three totally symmetric vibrational modes ν_1, ν_2, and ν_3, respectively. They are obtained by keeping the other vibrational modes fixed at their equilibrium value ($\mathbf{Q}$=0). The potential energies of the $\widetilde{X}^2E_g$ and $\widetilde{A}^2A_{1g}$ electronic states are shown by the solid and dashed lines, respectively. The computed ionization energies added with the harmonic ground state potential are shown by the points in the diagram. It can be seen that the computed *ab initio* energies are well represented by the linear coupling model. Since the dimensionless normal coordinates are used here,

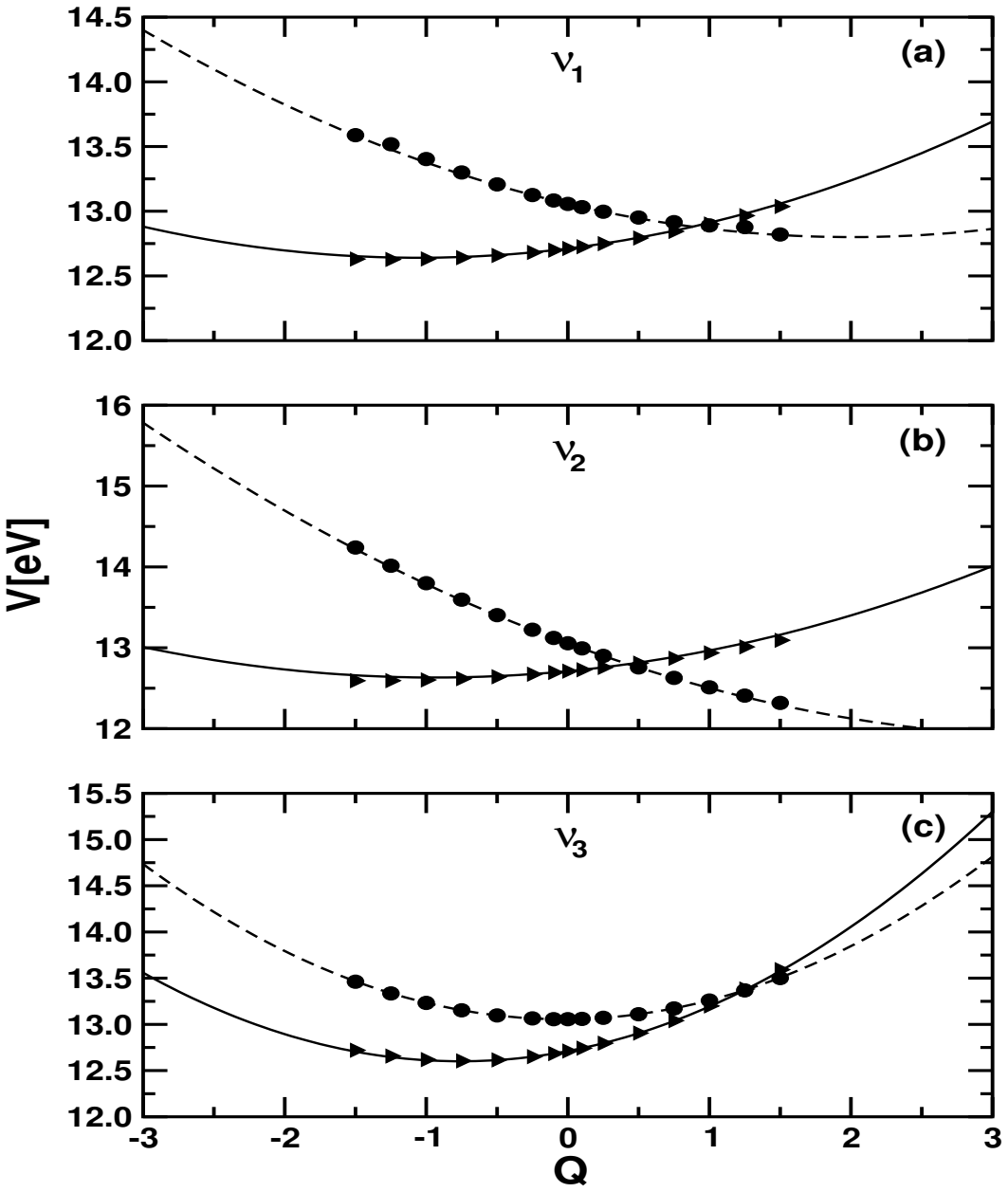

Figure 4.4: The adiabatic potential-energy curves of the $\widetilde{X}^2E_g$ (solid lines) and $\widetilde{A}^2A_{1g}$ (dashed lines) electronic states of ET^+ along the dimensionless normal displacement coordinates for the totally symmetric (a) ν_1, C-C stretching, (b) ν_2, CH_3 deformation, and (c) ν_3, C-H stretching vibrational modes. Each curve in the figure represents a cut along the multidimensional potential-energy hypersurface of the respective electronic state. The equilibrium geometry of ET in its electronic ground state ($^1A_{1g}$) corresponds to $\mathbf{Q}$=0. The *ab initio* potential energies with a harmonic contribution from the neutral ground electronic state are shown by the points on the diagram.

the PESs up to $Q_j = \pm$ 1.5 are expected to represent well the large amplitude vibrations in the internal coordinates. The agreement between the computed energies and the model would describe fairly well the vibronic states in the energy range of the first photoelectron band. The totally symmetric vibrational modes cannot lift the degeneracy of the $\widetilde{X}^2E_g$ electronic manifold, however, they shift the potential energy minimum considerably away from the equilibrium geometry of the neutral ET (**Q**=0) and therefore display the tuning activity. This shift amounts to -κ_j/ω_j for the vibrational mode ν_j [17]. The data listed in Table 4.3 reveal opposite signs for the coupling constants (κ and κ') for the vibrational modes ν_1 and ν_2 in the E_g and A_{1g} electronic states. Therefore, the minimum of these states shifts in the opposite direction relative to the equilibrium position of the ground electronic state of ET along these vibrational modes. As a result of this shift the $\widetilde{X}^2E_g$ and $\widetilde{A}^2A_{1g}$ electronic states of the radical cation undergo PJT crossing. The ν_1 and ν_2 vibrational modes are expected to be significantly excited in the photoelectron band. The excitation strength (cf. Table 4.3) of the CH_3 deformation mode ν_2 is very large in the $\widetilde{A}^2A_{1g}$ electronic state, and, therefore, it is expected to have a major role in the nuclear dynamics of this state.

The vibrational modes of e_g symmetry are both JT and PJT active in ET^+. In order to calculate the adiabatic potential energy curves of the radical cation along these vibrational modes, we consider one component (say the x component) of these degenerate vibrations keeping the others fixed at their equilibrium value at **Q**=0. The electronic Hamiltonian matrix (excluding the γ_j and γ'_j terms) of Eqs. (4.8a-4.8f) then assumes a block-diagonal structure. For a vibrational mode j the eigenvalues of this block-diagonal matrix

$$\mathcal{V}_{1,2}(Q_{jx}) = \mathcal{V}_0(Q_{jx}) + \frac{E^0_{E_g} + E^0_{A_{1g}}}{2} + \frac{\lambda_j}{2}Q_{jx} \mp \sqrt{\Big((E^0_{E_g} + \lambda_j Q_{jx} - E^0_{A_{1g}})/2\Big)^2 + (\lambda'_j Q_{jx})^2}, \tag{4.15a}$$

$$\mathcal{V}_3(Q_{jx}) \;=\; \mathcal{V}_0(Q_{jx}) + E^0_{E_g} - \lambda_j Q_{jx}, \tag{4.15b}$$

describe the adiabatic potential energies of the $\widetilde{X}^2E_g$ -$\widetilde{A}^2A_{1g}$ electronic states of the radical cation.

The adiabatic PESs of the $\widetilde{X}^2E_g$ and $\widetilde{A}^2A_{1g}$ electronic states of the ET^+ are plotted along the x component of the degenerate vibrational modes ν_4, ν_5, and ν_6 in Figs. 4.5(a-c), respectively. The solid and the dotted curve represent the two components of the JT split $\widetilde{X}^2E_g$ electronic manifold and the dashed curve represents the potential energy of the $\widetilde{A}^2A_{1g}$ electronic state. As in the case of Fig. 4.4, the computed *ab initio* energies are also included in Fig. 4.5 and shown as points. It can be seen that the present linear JT-PJT coupling scheme represents well the *ab initio* potentials in the FC zone and beyond up to $Q_j \approx 1.5$. Inspection of the adiabatic potential-energy curves above reveals substantial JT splitting of the $\widetilde{X}^2E_g$ electronic manifold due to the ν_4 and ν_5 vibrational modes. The JT activity of the CH_3 deformation mode ν_5 is somewhat stronger. The PJT repulsions between the upper adiabatic sheet of the $\widetilde{X}^2E_g$ electronic manifold and the $\widetilde{A}^2A_{1g}$ state are almost similar in magnitude for both the ν_4 and ν_5 vibrational modes. It can be seen from panel *c* that both the JT and PJT effects due to ν_6 are weaker compared to that due to ν_4 and ν_5.

We now examine some static aspects of the discussed PESs. In doing so, we first focus on the $(E \otimes e)$-JT part. Within the linear coupling scheme, the eigenvalues of the respective electronic Hamiltonian are given by [17]

$$\mathcal{V}_{\mp}(Q) \;=\; \mathcal{V}_0(Q) + E^0_{E_g} + \kappa_j Q_j \mp \sqrt{(\lambda_j Q_{jx})^2 + (\lambda_j Q_{jy})^2}. \tag{4.16}$$

The quantities $\mathcal{V}_-$ and $\mathcal{V}_+$ refer to the lower and upper adiabatic sheets of the JT split $\widetilde{X}^2E_g$ electronic manifold of ET^+, respectively. In the absence of any

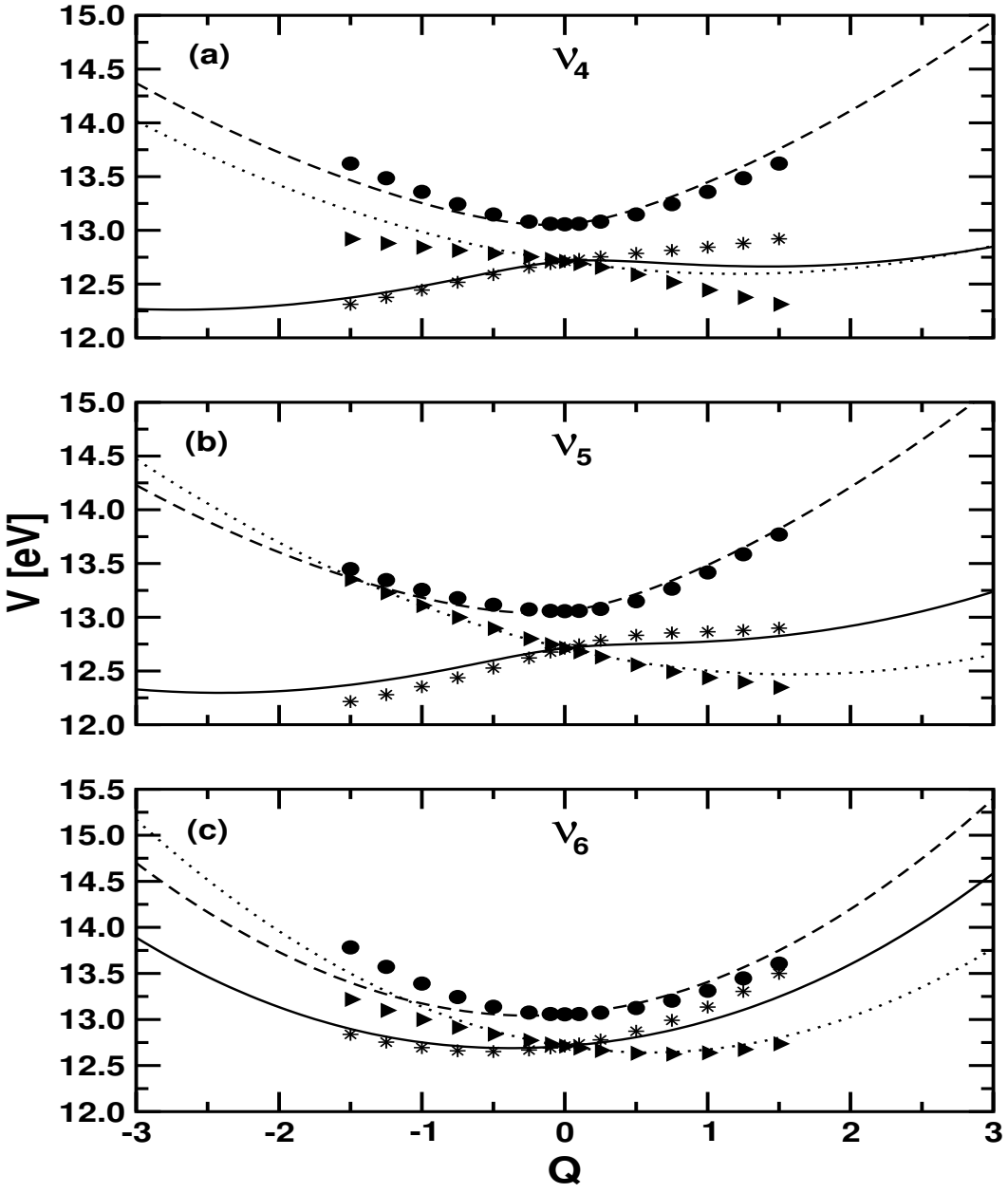

Figure 4.5: Adiabatic potential-energy curves of the JT split $\widetilde{X}^2E_g$ (solid and dotted lines) and the $\widetilde{A}^2A_{1g}$ (dashed lines) electronic states of ET^+ plotted as a function of the dimensionless normal coordinates of the x component of the degenerate (e_g) vibrational modes: (a) ν_4, the bending vibrational mode, (b) ν_5, the CH_3 deformation mode, and (c) ν_6, the C-H stretching mode. The *ab initio* potential energies with a harmonic contribution from the neutral ground electronic state are shown by the points on the diagram.

JT distortion, i.e., Q_j (j=4-6) = 0, the two sheets $\mathcal{V}_-$ and $\mathcal{V}_+$ remain degenerate. This degeneracy is lifted for Q_j (j=4-6) $\neq$ 0 and the resulting two sheets form CIs [cf. Figs. 4.5(a)-4.5(c)]. The two sheets remain degenerate in the coordinate space of the symmetric a_{1g} vibrational modes. The locus of this degeneracy defines the seam of CIs and the energetic minimum on this seam is given by [17]

$$\mathcal{V}_{min}^{(c)} = E_{E_g}^0 - \frac{1}{2}\sum_{j=1}^{3}\frac{\kappa_j^2}{\omega_j} \tag{4.17}$$

occurs for Q_j^0 (j = 1-3) = -κ_j/ω_j within the linear coupling scheme.

The global minimum on $\mathcal{V}_-$ at the D_{3d} equilibrium geometry becomes a cusp when distorted along any of the two components of a degenerate vibrational mode which is revealed by the analytic argument of the square root in Eq. (4.16). The minimum of $\mathcal{V}_+$ remains at the minimum of the seam of CIs and new minima appear on $\mathcal{V}_-$ at Q_j^0 (j = 1-3) = -κ_j/ω_j and Q_{pj}^0 ($p = x/y$, j = 4-6) = $\pm$ λ_{pj} / ω_{pj} with an energy

$$\mathcal{V}_-^0 = E_{E_g}^0 - \frac{1}{2}\sum_{j=1}^{3}\frac{\kappa_j^2}{\omega_j} - \frac{1}{2}\sum_{j=4}^{6}\frac{\lambda_{pj}^2}{\omega_{pj}}. \tag{4.18}$$

In multidimensional space this results into a "Mexican hat" type of topography of the JT split PESs. The JT stabilization energy amounts to $\sum_{j=4}^{6}\lambda_{pj}^2/2\omega_{pj}$. From the data collected in Table 4.3, one can see that the $\mathcal{V}_{min}^{(c)}$ = 12.45 eV occurs at Q_1^0 = -1.059, Q_2^0 = -0.941, and Q_3^0 = -0.760. The new minima on $\mathcal{V}_-^0$ [Eq. (4.18)] for the JT distorted geometry occurs at Q_{4x}^0 = 1.201, Q_{5x}^0 = 1.605, and Q_{6x}^0 = 0.595 with an energy $\mathcal{V}_-^0$ = 12.022 eV. The JT stabilization energy amounts to $\sim$ 0.43 eV.

We now provide an approximate estimate of the energetic minimum of the PJT crossings. In this example the same degenerate vibrational mode acts both as the JT and PJT coupling modes. Along the x component of the degenerate

vibrational modes, the $(E + A) \otimes e$ coupling matrix is given by

$$\mathcal{H}_{el}^{PJT} = \mathcal{V}_0\mathbf{1} + \begin{pmatrix} E_{E_g}^0 + \sum_{j=1}^{3}\kappa_j Q_j + \sum_{j=4}^{6}\lambda_j Q_{jx} & \sum_{j=4}^{6}\lambda_j' Q_{jx} \\ \sum_{j=4}^{6}\lambda_j' Q_{jx} & E_{A_{1g}}^0 + \sum_{j=1}^{3}\kappa_j' Q_j \end{pmatrix}. \quad (4.19)$$

Defining $\Sigma = (E_{E_g}^0 + E_{A_{1g}}^0)/2$, $\Delta = (E_{A_{1g}}^0 - E_{E_g}^0)/2$, $\sigma_j = (\kappa_j + \kappa_j')/2$, $\delta_j = (\kappa_j' - \kappa_j)/2$, $\sigma_j' = \lambda_j/2$, and $\delta_j' = -\lambda_j/2$, the eigenvalues of the Hamiltonian in Eq. (4.19) are given by [17]

$$\mathcal{V}_{E_g,A_{1g}}(Q) = \mathcal{V}_0(Q) + \Sigma + \sigma_j Q_j + \sigma_j' Q_{jx} \mp \mathcal{W} \quad (4.20)$$

where $\mathcal{V}_{A_{1g}}$ refers to the adiabatic potential energy of the $\widetilde{A}^2A_{1g}$ electronic state of the radical cation. The quantity $\mathcal{W}$ in the above equation is given by [17]

$$\mathcal{W} = \sqrt{d^2 + c^2}, \quad (4.21)$$

with

$$d = \Delta + \delta_j Q_j + \delta_j' Q_{jx}, \quad (4.22)$$

$$c = \lambda_j' Q_{jx}. \quad (4.23)$$

The energetic minimum of the seam of CIs between the above two adiabatic electronic states occurs at [17]

$$\mathcal{V}_{min}^{(c)} = \Sigma + \frac{(F - \Delta)^2}{2D} - \frac{1}{2}\sum_{j=1}^{3}\frac{\sigma_j^2}{\omega_j} - \frac{1}{2}\sum_{j=4}^{6}\frac{\sigma_j'^2}{\omega_j}, \quad (4.24)$$

where

$$F = \sum_{j=1}^{3} \frac{\delta_j \sigma_j}{\omega_j} + \sum_{j=4}^{6} \frac{\delta'_j \sigma'_j}{\omega_j}, \tag{4.25}$$

$$D = \sum_{j=1}^{3} \frac{\delta_j^2}{\omega_j} + \sum_{j=4}^{6} \frac{\delta_j'^2}{\omega_j}. \tag{4.26}$$

In the present case considering the values of the parameters mentioned in Table 4.3, $\mathcal{V}_{min}^{(c)}$ occurs at ~ 12.99 eV. This minimum occurs well within the energetic range of the first photoelectron band of ET^+ and only ~ 0.54 eV above the minimum of the JT conical intersections. Therefore, the PJT crossings are expected to play a crucial role in the photoionization of ET.

4.4.2 Photoelectron Spectrum

In this section we report the first photoelectron band of ET^+ theoretically calculated by employing the diabatic Hamiltonian of Eqs. (4.4-4.8f) developed above. The theoretical results are compared with the available experimental results [69]. In the following discussions, we proceed systematically to treat the JT interactions within the $\widetilde{X}^2E_g$ electronic manifold of ET^+ first and then consider the PJT coupling with its $\widetilde{A}^2A_{1g}$ electronic state to unambiguously establish the importance of the latter in the nuclear dynamics.

In the absence of any bilinear coupling term in the Hamiltonian, the Condon activity of the totally symmetric a_{1g} vibrational modes and the JT activity of the degenerate e_g vibrational modes within the $\widetilde{X}^2E_g$ electronic manifold of ET^+ is separable, i.e., $H^{a_{1g}}$ and H^{e_g} commute with each other. Therefore, we calculate two partial spectra for the a_{1g} and e_g vibrational modes separately and finally convolute them to generate the complete spectrum. This reduces the computational effort by effectively reducing the dimensionality of the secular matrix in each calculation. All theoretical stick spectra presented below are convoluted with a Lorentzian line shape function of 40 meV fwhm to generate the respective

Table 4.4: The number of harmonic-oscillator (HO) basis functions along each vibrational mode, the dimension of the secular matrix, and the number of Lanczos iterations used to calculate the converged theoretical stick spectrum shown in various figures.

No. of HO basis functions						Dimension of the secular matrix	Lanczos iterations	Figure(s)
ν_1	ν_2	ν_3	ν_4	ν_5	ν_6			
17	13	9	-	-	-	2520	2000	4.6(a) & 4.7(a)
35	28	18	-	-	-	19,836	5000	4.8(a)
-	-	-	22	40	5	4,990,356	10^4	4.6(b), 4.7(a), & 4.8(a)
16	52	4	-	-	-	4505	5000	4.7(b) & 4.8(b)
5	20	3	7	13	2	11,430,720	10^4	4.9 & 4.11

spectral envelopes. The number of basis functions, size of the secular matrix, and the number of Lanczos iterations used in generating the numerically converged spectra presented below are documented in Table 4.4.

In Fig. 4.6(a), the spectrum obtained with the three a_{1g} vibrational modes, ν_1, ν_2, and ν_3 within the LVC scheme is shown. The spectral intensity in arbitrary units is plotted as a function of the energy of the final vibronic state. The symmetric spectrum reveals dominant excitations of ν_1 and ν_2 vibrational modes, the first two peaks from the 0-0 line. These peaks are ~ 0.128 and ~ 0.177 eV spaced in energy, corresponding to the frequency of ν_1 and ν_2 modes, respectively. The next four peaks corresponds to the excitation of $2\nu_1$, $\nu_1+\nu_2$, $2\nu_2$, and ν_3, respectively. The excitation of ν_3 mode is relatively weak (the intensity is 100 times less than the 0-0 line) in accord with its low coupling strength. The remaining high energy peaks mostly correspond to the excitation of higher quanta of ν_1 and ν_2 and their combinations. The peaks in the spectrum are weighed by the coupling strength, $\kappa_j^2/2\omega_j^2$ (Poisson parameter), of the respective vibrational mode, which yields the intensity of the fundamental relative to the 0-0 line.

The partial spectrum obtained with the three e_g vibrational modes is shown in Fig. 4.6(b). The convergence of the stick spectrum has been explicitly checked with respect to the size of the basis set as well as the number of Lanczos iter-

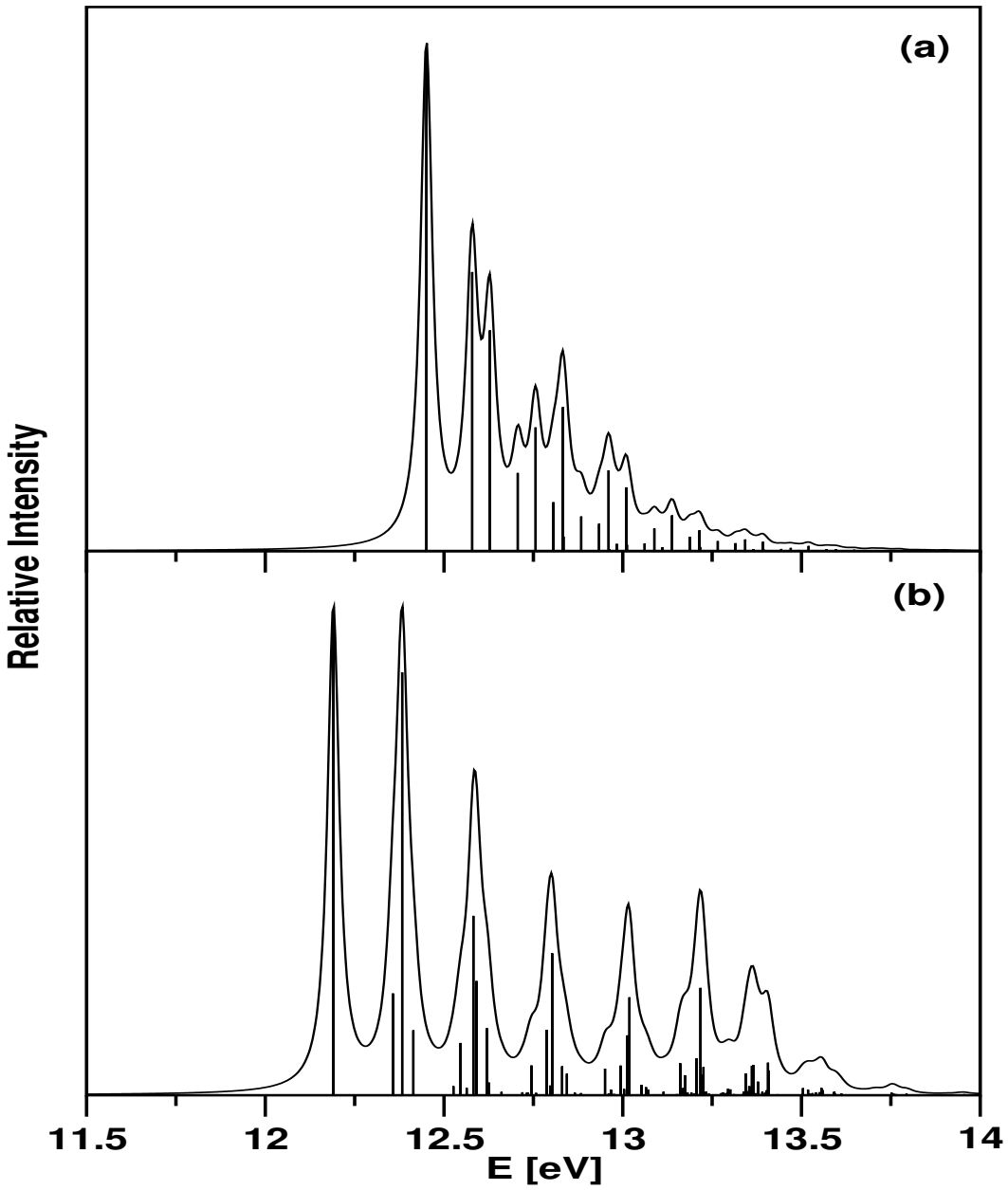

Figure 4.6: The first photoelectron band of ET pertaining to a transition to the $\widetilde{X}^2E_g$ electronic manifold of ET^+: (a) partial spectrum computed with the three totally symmetric a_{1g} vibrational modes ν_1-ν_3 and (b) partial spectrum computed with the three JT active degenerate e_g vibrational modes ν_4-ν_6. The spectra above are calculated within the LVC scheme. Each theoretical stick spectrum is convoluted with a Lorentzian function of 40 meV fwhm to calculate the spectral envelope.

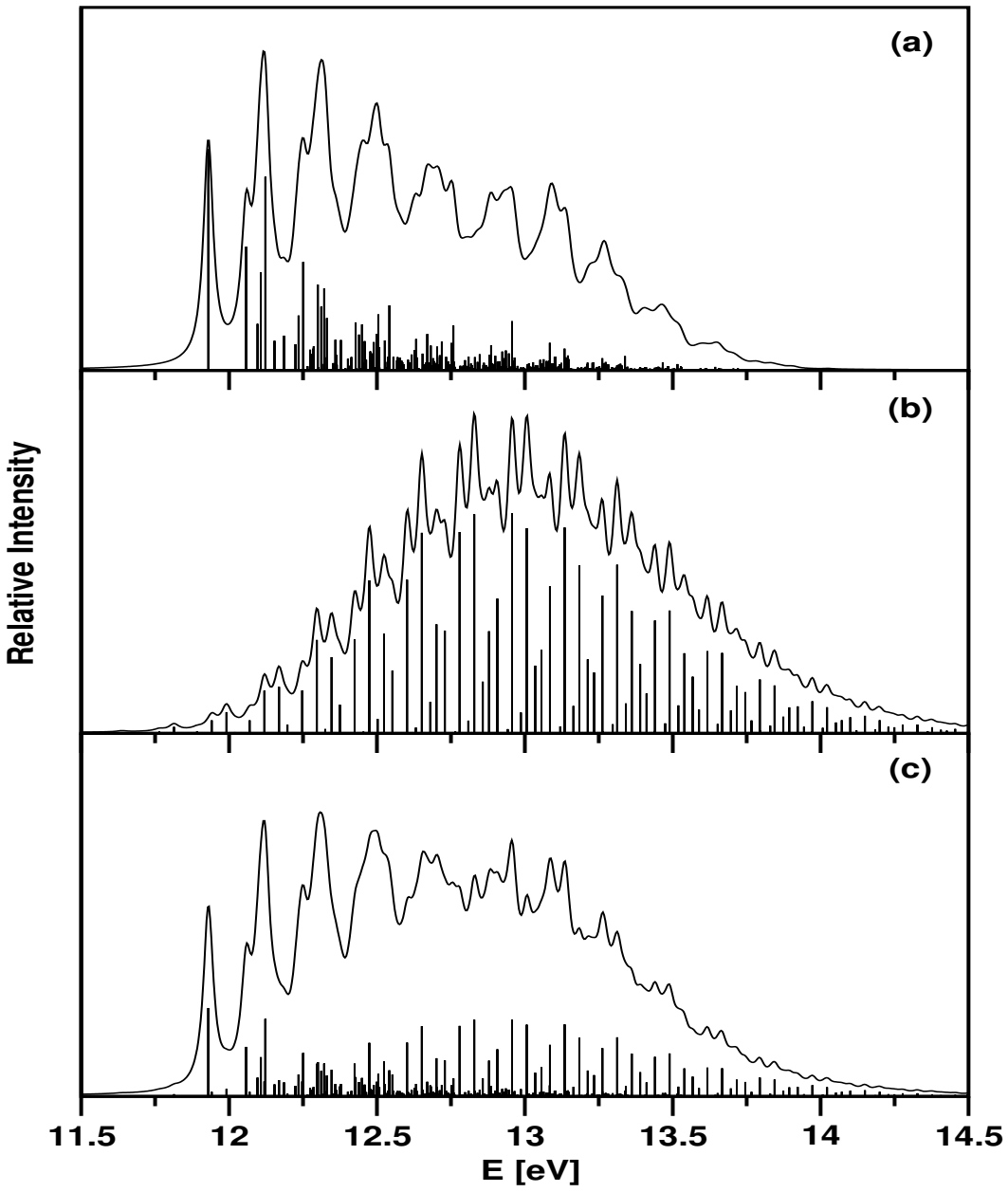

Figure 4.7: The first photoelectron band of ET^+: (a) the spectrum of the $\widetilde{X}^2E_g$ electronic manifold of ET^+, obtained by convoluting two partial spectra due to the a_{1g} and e_g vibrational modes (see text), (b) the spectrum of $\widetilde{A}^2A_{1g}$ electronic state of ET^+, and (c) the composite photoelectron band obtained by superimposing the spectra in panel a and b. The spectra are calculated within the LVC scheme.

ative steps. The spectrum is dominated by the 0-0 line, followed by a number of irregular lines. It reveals progression along all the three ν_4, ν_5, and ν_6 vibrational modes, however, the dominant progression is formed by the degenerate CH_3 deformation mode ν_5 alone. The ν_4 and ν_6 vibrational modes on the other hand are only weakly excited. The line spacings, ~ 0.166, ~ 0.193, and ~ 0.392 eV, corresponding to the excitation of ν_4, ν_5, and ν_6 vibrational modes can be observed from the spectrum. The irregular spacings of the stick spectra are due to multimode JT interactions [17] in the ground state of ET^+.

In Figs. 4.7(a)-4.7(c) we show the final convoluted vibronic spectrum of the $\widetilde{X}^2E_g$ electronic manifold of ET^+ (panel a), the vibrational spectrum of the $\widetilde{A}^2A_{1g}$ electronic state of ET^+ (panel b), and the superposition of the two (panel c) within a linear coupling scheme [setting γ_j and γ'_j in Eqs. (4.8a-4.8c) to zero]. A convolution of the two partial stick spectra due to the a_{1g} and e_g vibrational modes (Figs.4.6(a-b)) is presented in Fig. 4.7(a). The resulting convoluted stick spectrum is then convoluted again with a Lorentzian function with a fwhm of 40 meV to generate the spectral envelope. The progression in the spectrum in Fig. 4.7(a) is mostly formed by the ν_1, ν_2, and ν_5 vibrational modes. A close look at this spectrum reveals that the JT effect is not very strong in the $\widetilde{X}^2E_g$ electronic manifold of ET^+. A strong $(E \otimes e)$-JT interaction would have resulted in a characteristic bimodal distribution of the spectral intensities and more clumping of the spectral lines under the envelope as revealed in other examples in the literature [90, 119].

The spectrum of the uncoupled $\widetilde{A}^2A_{1g}$ electronic state of ET^+ is shown in Fig. 4.7(b). The vibronic structure of this spectrum reveals a dominant excitation of the ν_2 vibrational mode. The other two vibrational modes ν_1 and ν_3 are only weakly excited. The superposition of the two spectra of panel (a) and (b) is shown in Fig. 4.7(c). We again note that the PJT coupling between the $\widetilde{X}^2E_g$ - $\widetilde{A}^2A_{1g}$ electronic state is ignored in generating this spectrum. It can be seen that the spectrum in Fig. 4.7(c) does not compare well with the experimental

recording shown below in Fig. 4.10(a).

Analogous results are obtained when the diagonal second-order coupling terms γ_j and γ'_j for the a_{1g} vibrational modes are included in the dynamical simulations. The resulting spectra are shown in Figs. 4.8(a)-4.8(c). When compared with the similar spectra in Figs. 4.7(a)-4.7(c), it can be seen that these diagonal coupling terms result into a more clumping of the spectral lines and also the irregular structure of the envelopes becomes more regular. This results from a change in the curvature of the adiabatic electronic states of ET^+ along the normal coordinates of these vibrational modes when the second-order coupling terms are included. It can be seen from both Figs. 4.7 and 4.8 that the $\widetilde{A}^2A_{1g}$ electronic state contributes to the spectral intensity significantly only beyond $\sim$ 13.0 eV. As in the case of the spectrum in Fig. 4.7(c), the similar one in Fig. 4.8(c) also does not agree well with the experimental results.

We will now proceed to discuss on the change in the spectra shown above when the PJT interactions between the $\widetilde{X}^2E_g$ -$\widetilde{A}^2A_{1g}$ electronic states of ET^+ are considered. Our estimation as shown in Eq. 4.24 reveals that the minimum of the PJT crossing seam occurs at $\sim$ 12.99 eV, which is near to the minimum of the JT crossing seam in the $\widetilde{X}^2E_g$ electronic manifold occurring at $\sim$ 12.45 eV. Also, the PJT coupling constant λ'_j is quite large for the vibrational modes ν_4 and ν_5 (cf. Table 4.3). Therefore, one can expect significant PJT effects due to these two vibrational modes in the photoelectron spectrum of ET.

In Fig. 4.9, we show the photoelectron spectrum of E (panel a) and A_1 (panel b) vibronic symmetries obtained by including the PJT interactions between $\widetilde{X}^2E_g$ -$\widetilde{A}^2A_{1g}$ electronic states within a linear coupling scheme. The above two spectra are to be compared with the corresponding ones in Figs. 4.7(a) and 4.7(b), respectively, obtained by excluding these PJT interactions. A comparison of the two reveals that both the spectra become structureless and more diffuse at high energies on inclusion of the PJT coupling terms. The latter cause a huge increase in the line density in the spectra at high energies beyond the minimum of

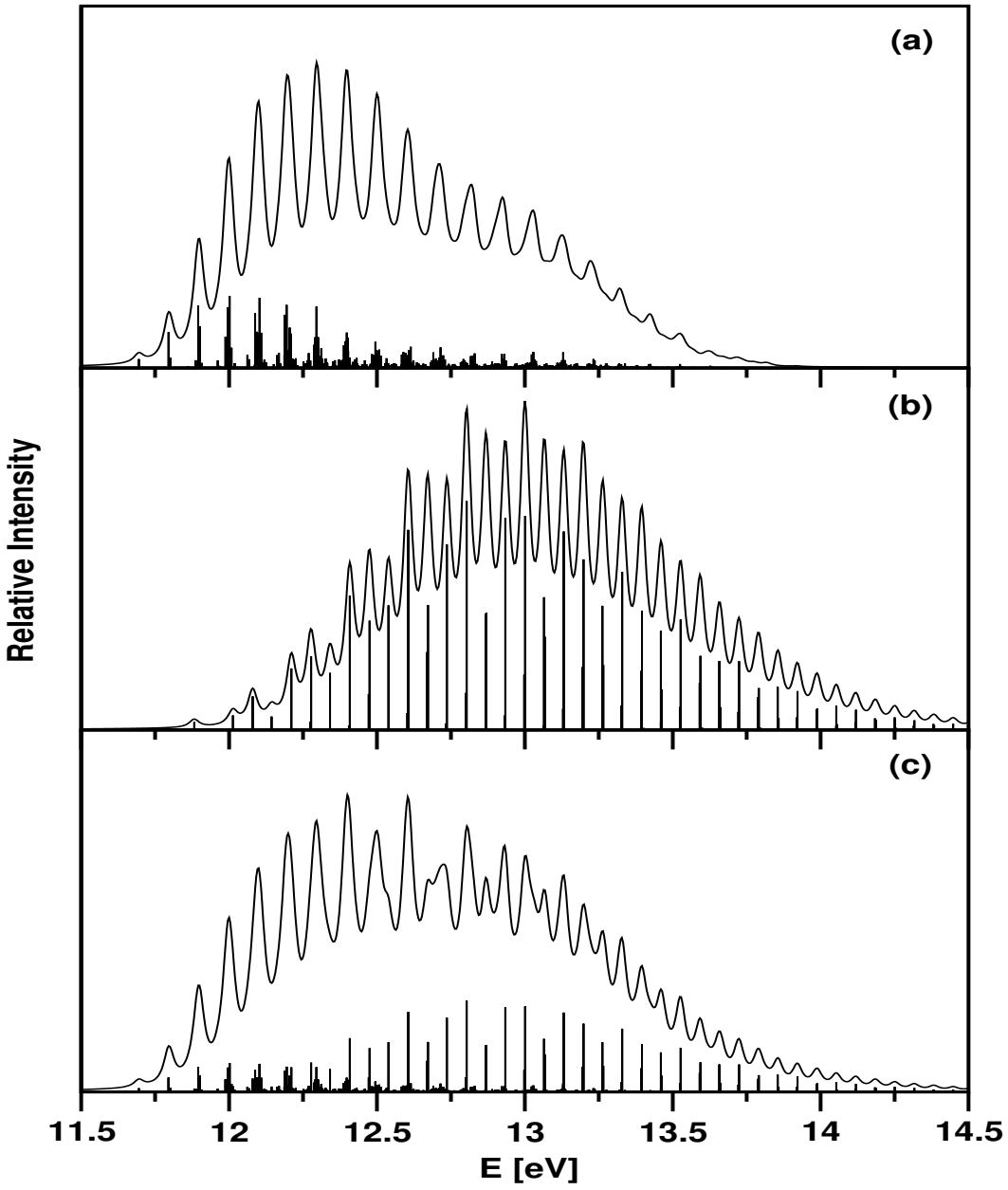

Figure 4.8: The same as in Fig. 4.7, obtained by considering the second-order coupling parameters γ_j and γ'_j for the totally symmetric vibrational modes ν_1-ν_3.

the seam of PJT conical intersections at $\sim$ 12.99 eV. The higher vibronic levels of E_g manifold are strongly mixed with the low-lying vibronic levels of the A_{1g} electronic state and due to this mixing, the discrete vibronic levels are clumped into quasi-bound resonances. The spectrum of E vibronic symmetry in Fig. 4.9(a) is dominated by progressions along the ν_2 and ν_5 vibrational modes, whereas, the spectrum in Fig. 4.9(b) is dominated by the progression along the ν_2 vibrational mode at low energies. The ν_1 vibrational mode also has a comparable contribution to the progression in both the spectra. The average spacing of the clump of lines in both the spectra in panel a and b is $\sim$ 0.20 eV. A careful inspection of the two spectra of E vibronic symmetry shown in Fig. 4.7(a) and 4.9(a) reveals a significant improvement of the excitation pattern at low energies on inclusion of the PJT coupling which compares much better with the experimental findings.

The composite $(E+A)\otimes e$ vibronic spectrum of ET^+ obtained within the linear coupling scheme is shown in Fig. 4.10(b) along with the experimental results in Fig. 4.10(a), reproduced from Ref. [69]. The theoretical spectrum in panel b is to be compared with a similar one in Fig. 4.7(c), obtained without the PJT coupling. The comparison reveals a very significant and extremely important contribution of the $E - A$ PJT interactions in the first photoelectron band of ET. It can be seen that the progression in the low-energy wing of the spectrum is in very good accord with the experiment when PJT coupling is considered in the nuclear dynamics. The progression is formed mainly by the ν_1, ν_2, and ν_5 vibrational modes. Moreover, the diffuseness of the band at high energies is in good accord with the experiment. A close look at the stick spectrum underneath the envelopes in Figs. 4.7(c) and 4.10(b) clearly indicates a huge increase in the line density at high energies when the PJT coupling is included. The three band maxima in the ionization region of the first photoelectron band can be seen from Fig. 4.10(b) to occur at $\sim$ 12.25, $\sim$ 12.75, and $\sim$ 13.50 eV which is in good accord with the experimental results [69]. In conjunction with the static properties of the PESs described in the previous section, these three maxima can be unambiguously

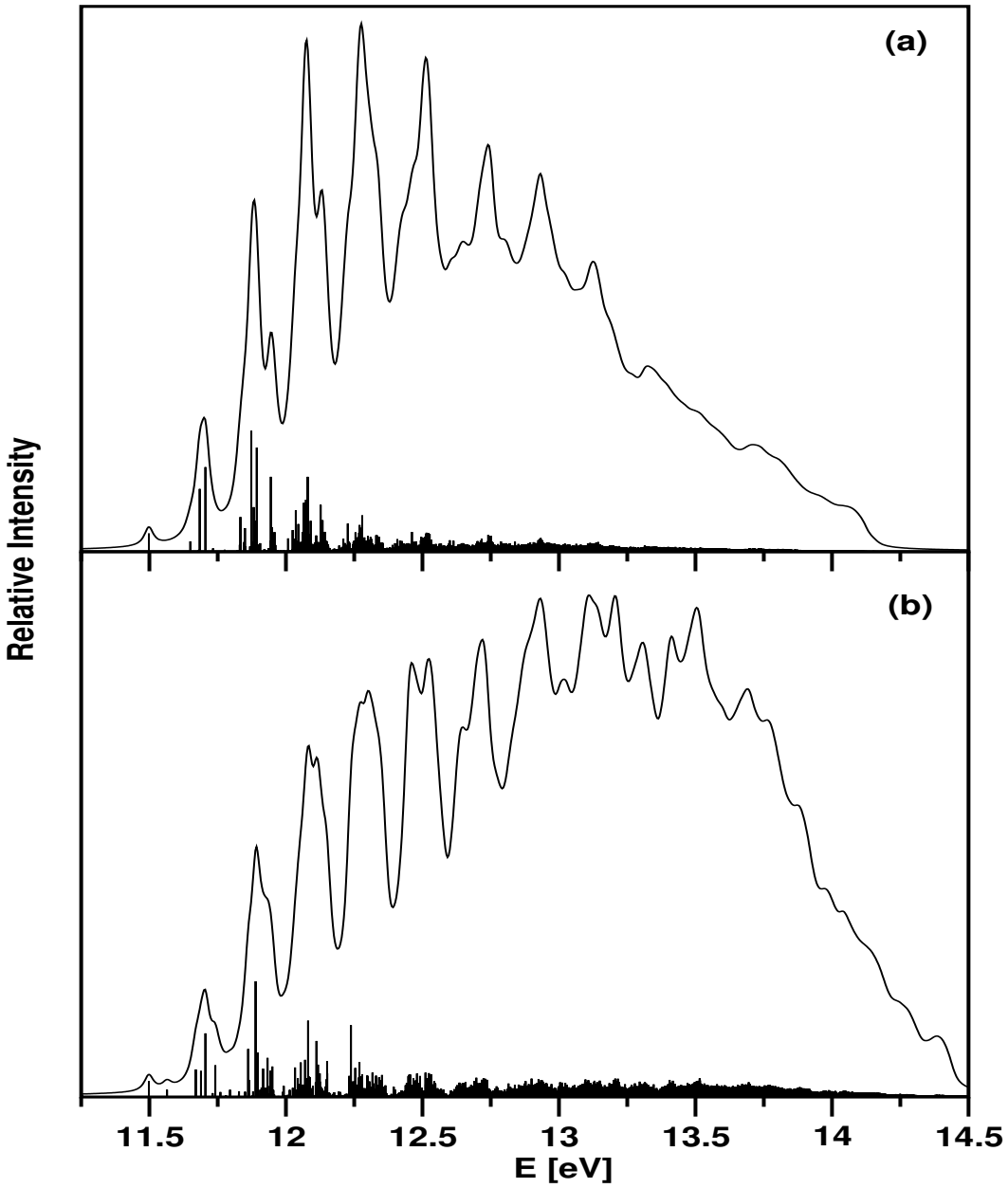

Figure 4.9: The first photoelectron band of ET^+ of E (panel a) and A_1 (panel b) vibronic symmetries computed by including the PJT interactions between the $\widetilde{X}^2E_g$ -$\widetilde{A}^2A_{1g}$ electronic states and a LVC scheme. The stick spectra are convoluted with a Lorentzian function of 40 meV fwhm to generate the spectral envelope.

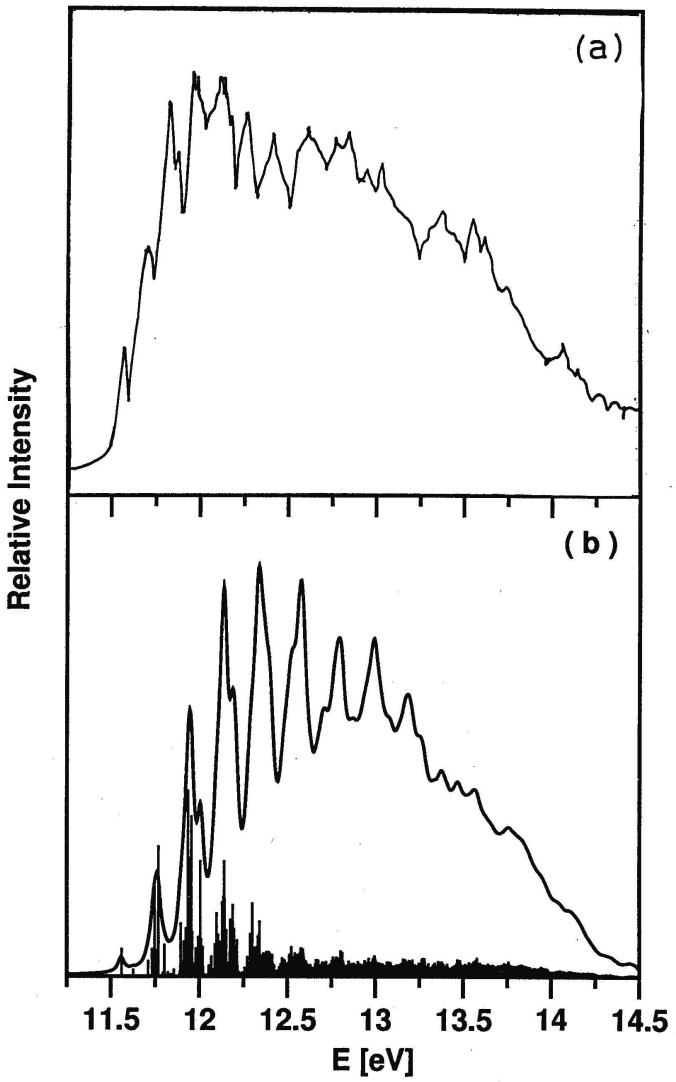

Figure 4.10: Comparison of the experimental (panel a) [Ref. [69]] and theoretical (panel b) (considering linear JT and PJT coupling in the $\widetilde{X}^2E_g$ -$\widetilde{A}^2A_{1g}$ electronic manifold) spectra for the first photoelectron band of ET^+. The two stick spectra in Figs. 4.9(a) and 4.9(b) are combined in 2:1 statistical ratio to generate the composite stick theoretical spectrum in panel *b*. The latter is finally convoluted with a Lorentzian of 40 meV fwhm to obtain the spectral envelope. The theoretical spectrum is shifted by 0.06 eV along the energy axis to reproduce the observed adiabatic ionization position of the band. For a clearer representation, the stick theoretical spectrum in panel *b* is magnified by a factor of 5.

attributed to be due to the JT split $\widetilde{X}^2E_g$ component and the $\widetilde{A}^2A_{1g}$ electronic states of ET^+. Despite these agreements, the broadening of the spectral envelope in Fig. 4.10(b) is somewhat less when compared to the experiment.

The remaining differences between the theoretical and experimental results may be associated with the possible effects of the higher-order coupling terms of the Hamiltonian. It is to be noted that the vibrational modes of u symmetry also enter in the dynamics when a second-order coupling model is considered. Although the ^2E_u ionic state is energetically well separated from the low-lying ^2E_g (by ~ 2.75 eV) and $^2A_{1g}$ (by ~ 2.40 eV) electronic states, the e_u vibrational modes may still couple the A_{1g}-E_u and E_g-E_u ionic states. These interactions will lead to additional PJT conical intersections.

In order to examine the role of the second-order coupling terms due to the totally symmetric vibrational modes, we have shown in Figs. 4.11 and 4.12 the spectra obtained by considering the γ_j and γ'_j parameters in the Hamiltonian of Eqs. (4.8a-4.8c). We note that the linear coupling scheme is retained in treating the JT and PJT interactions of the degenerate vibrational modes in the above spectra. In Figs. 4.11(a) and 4.11(b), respectively, the spectra of E and A_1 vibronic symmetries are shown. When compared with the similar spectra in Figs. 4.9(a) and 4.9(b), it can be seen that these second-order coupling terms make the spectrum more broad and diffuse, particularly at high energies. The agreement between the theory and experiment as shown in Figs. 4.12(a) and 4.12(b) improves to some extent when the overall structure of the envelope is considered. It is to be noted that we have examined the effects of the second-order coupling terms due to the degenerate e_g vibrational modes also. However, the agreement between the theory and experiment deteriorates when the vibrational modes of g symmetry are considered alone. We therefore strongly anticipate the role of the vibrational modes of u symmetry, possible bilinear coupling terms, and the PJT interactions with the E_u electronic states which may further improve the agreement between the theory and the experiment.

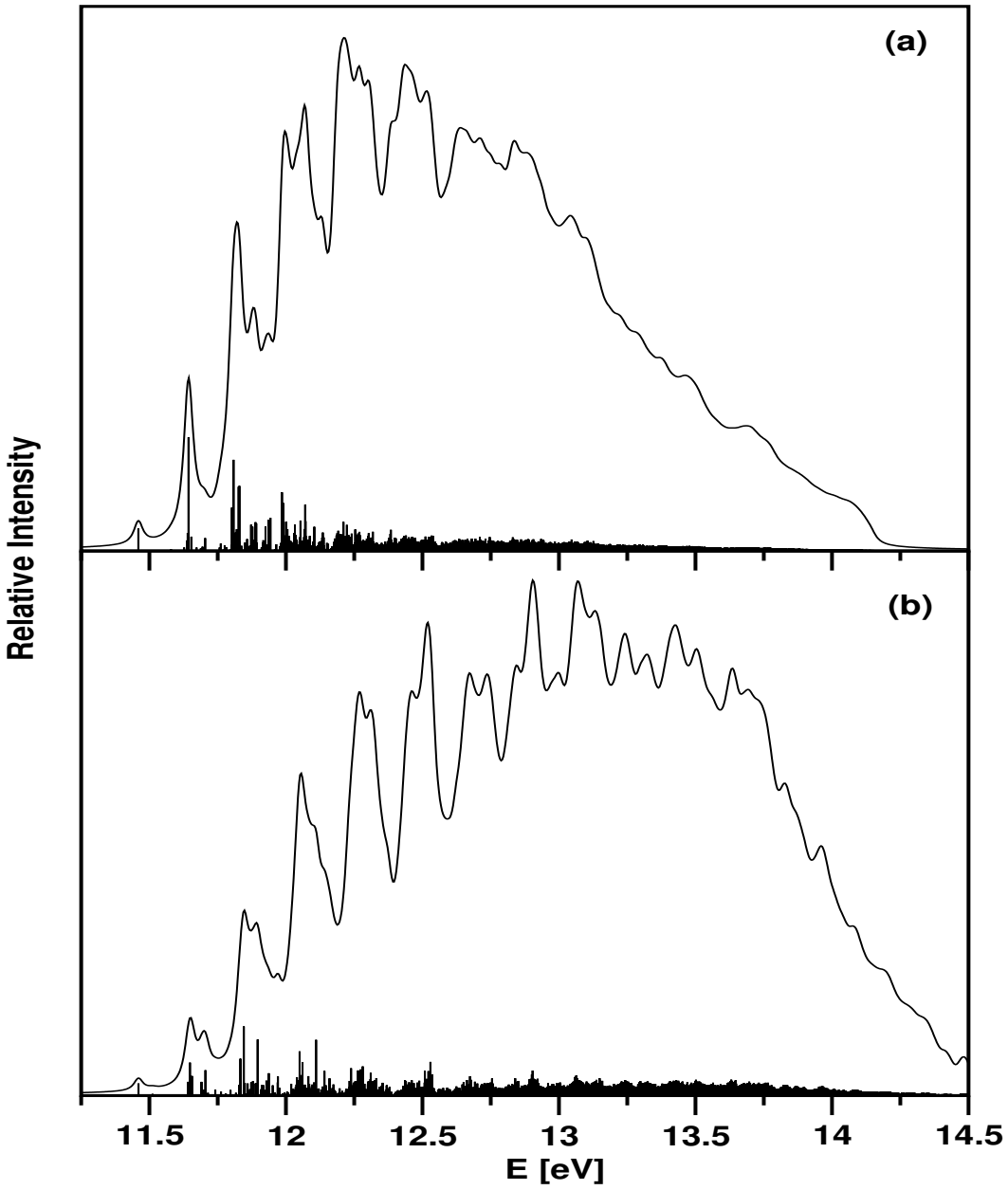

Figure 4.11: The same as in Figs. 4.9(a) and 4.9(b), obtained by including the second-order coupling parameters γ_j and γ'_j due to the totally symmetric vibrational modes, ν_1-ν_3.

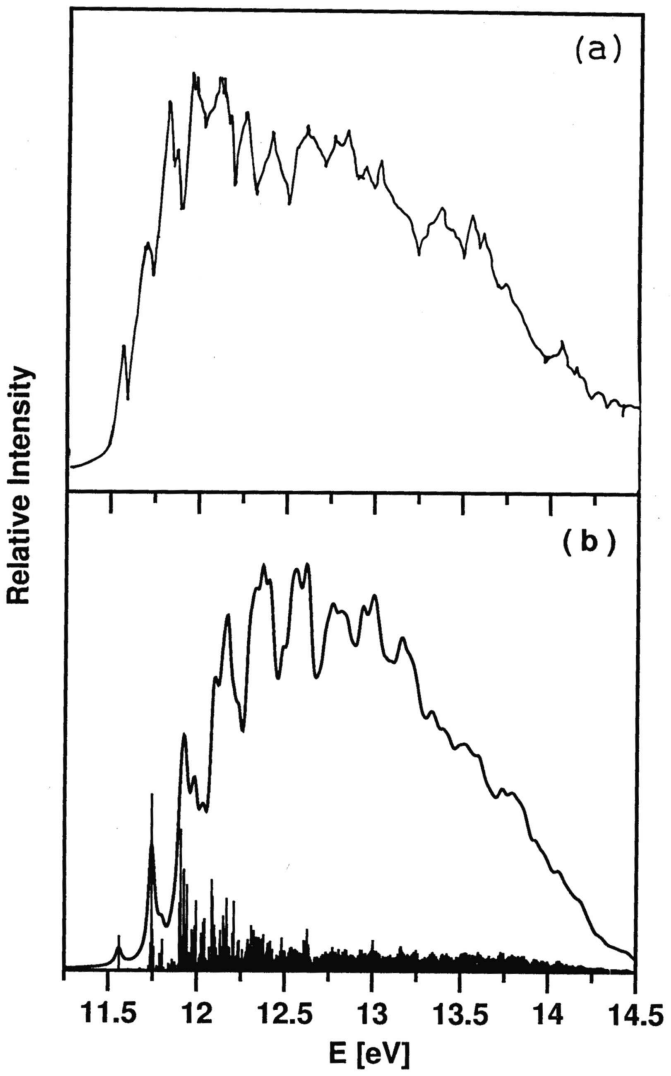

Figure 4.12: The same as in Figs. 4.10(a) and 4.10(b), obtained by including the second-order coupling parameters γ_j and γ'_j due to the totally symmetric vibrational modes, ν_1-ν_3. The theoretical spectrum is shifted by 0.1 eV along the energy axis to reproduce the observed adiabatic ionization position of the band. The stick theoretical spectrum in panel *b* is magnified by a factor of 5 in order to have a clearer representation.

4.5 Summary and Outlook

In the foregoing discussion, we have presented a detailed theoretical account on the JT and PJT coupling effects in the $\widetilde{X}^2E_g$ -$\widetilde{A}^2A_{1g}$ electronic states of ET^+, with the aid of an *ab initio* based quantum dynamical approach. Both the static and dynamic aspects of these effects are discussed. These interactions lead to multiple multidimensional CIs of electronic states which drive the nuclear dynamics through highly complex nonadiabatic paths. The present theoretical results compare well with the He I excited experimental photoelectron bands of ET [69]. Our theoretical approach is based on a model diabatic Hamiltonian where the degenerate vibrational modes (ν_4-ν_6) are considered only till the first-order and the totally symmetric vibrational modes (ν_1-ν_3) are considered up to the second-order. The theoretical results for both the $(E\otimes e)$-JT and $(E+A)\otimes e$ JT-PJT coupling schemes are presented in order to establish unambiguously the importance of the PJT interactions between the $\widetilde{X}^2E_g$ -$\widetilde{A}^2A_{1g}$ electronic states of ET^+.

The equilibrium geometry of ET in its ground electronic state is optimized at the MP2 level of theory employing a cc-pVTZ basis set and then the harmonic force field and the dimensionless normal coordinates are calculated. The equilibrium geometry parameters and the harmonic vibrational frequencies thus obtained are in good accord with the available experimental data [70]. The vertical ionization potentials of ET are calculated as a function of the normal-mode displacement coordinates Q_j by the OVGF method. The ionization energies are then equated with the adiabatic potential energies of the $\widetilde{X}^2E_g$ and $\widetilde{A}^2A_{1g}$ electronic states of ET^+. The coupling parameters of the Hamiltonian [Eqs. 4.4-4.8f] are then derived from these potential-energy functions.

In the nuclear dynamical simulations, we systematically examined the vibronic structure of the $\widetilde{X}^2E_g$ -$\widetilde{A}^2A_{1g}$ electronic states of ET^+ first by considering the JT interactions alone within the $\widetilde{X}^2E_g$ ionic manifold and then by including

the PJT interactions with the $\widetilde{A}^2A_{1g}$ electronic state. Three totally symmetric vibrational modes (ν_1-ν_3) and three degenerate JT active vibrational modes (ν_4-ν_6) of g symmetry are considered in the present dynamical study. This makes the vibronic Hamiltonian a nine-dimensional one involving three electronic states. The coupling parameters for the vibrational modes and the subsequent dynamical results reveal that the symmetric vibrational modes ν_1 (C-C stretching) and ν_2 (CH_3 deformation) are strongly excited in the $\widetilde{X}^2E_g$ state and ν_2 is the crucial vibrational mode contributing to the progressions in the vibronic structure of the $\widetilde{A}^2A_{1g}$ state. The progression of all three JT active vibrational modes are observed in the overall structure of the photoelectron band. However, the vibrational mode ν_5 (CH_3 deformation) is found to be strongly excited. The theoretical findings in conjunction with the experimental observations unambiguously establish the very crucial role of the PJT interactions in the first photoelectron band of ET.

The experimental photoelectron band of ET^+ shows irregular vibrational progressions, with its numerous shoulders and small peaks below 12.55 eV that are attributed to the dynamic $(E \otimes e)$-JT effect within the $\widetilde{X}^2E_g$ state. The three maxima obtained in the first photoelectron band at $\sim$ 12.25, $\sim$ 12.75, and $\sim$ 13.50 eV, due to the JT split $\widetilde{X}^2E_g$ component states and the $\widetilde{A}^2A_{1g}$ electronic state, compare well with the experimental observations [69]. However, the overall diffuseness of the experimental photoelectron band is not very well reproduced by the present theoretical model.

Chapter 5

The JT and PJT interactions in the cyclopropane radical cation

5.1 Introduction

In the present chapter, we focus on the static and dynamic aspects of the JT and PJT interactions in the two low-lying degenerate electronic states of CP^+. CP molecule belongs to the D_{3h} symmetry point group in its equilibrium configuration. In the D_{3h} symmetry configuration, the ground state ($\widetilde{X}^1A_1'$) molecular orbital sequence of CP can be written as [82–86, 88]

$$(1a_1')^2(1e')^4(2a_1')^2(2e')^4(1a_2'')^2(3a_1')^2(1e'')^4(3e')^4.$$

Ionization of an electron from its two highest occupied $3e'$ and $1e''$ molecular orbitals forms CP^+ in the ground $\widetilde{X}^2E'$ and first excited $\widetilde{A}^2E''$ electronic states, respectively. CP is a nonlinear molecule and its 21 vibrational modes belong to the following symmetry species in the D_{3h} symmetry point group:

$$\Gamma_{vib} = 3a_1' + a_2' + 4e' + a_1'' + 2a_2'' + 3e''. \tag{5.1}$$

The symmetrized direct product of two E' or E'' representations in the D_{3h} point group yields

$$(E')^2 = (E'')^2 = a_1' + e'. \tag{5.2}$$

Similarly, the direct product of E' and E'' irreducible representations in the D_{3h} point group yields

$$E' \times E'' \;\; = \;\; a_1'' + a_2'' + e''. \tag{5.3}$$

The above elementary symmetry selection rules [Eqs. (5.2-5.3)] suggest that the degenerate $\widetilde{X}^2E'$ and $\widetilde{A}^2E''$ electronic states of CP^+ would undergo JT splitting in first order when distorted along the degenerate vibrational modes of e' symmetry. These two degenerate electronic states may also undergo PJT-type interactions along the vibrational modes of a_1'', a_2'', and e'' symmetries. However, by analyzing their coupling strengths extracted from our extensive *ab initio* electronic structure data, we note that only one of the three e'' vibrational modes and one a_1'' vibrational mode are found to be PJT active. Although the $\widetilde{X}^2E'$ and $\widetilde{A}^2E''$ electronic states are separated by ~ 2.428 eV in energy at the equilibrium configuration of neutral CP, such interactions are found to be important in the energy range of its photoelectron bands considered in this chapter. The PJT coupling of two JT split degenerate electronic states is expected to yield a series of CIs and consequently the nuclear motion may become highly nonadiabatic owing to the possibility of nonradiative transitions to four component electronic states.

In this chapter we have undertaken a detailed *ab initio* dynamical study of the photoionization spectrum of CP (cf. Fig. 5.1). The latter is already discussed

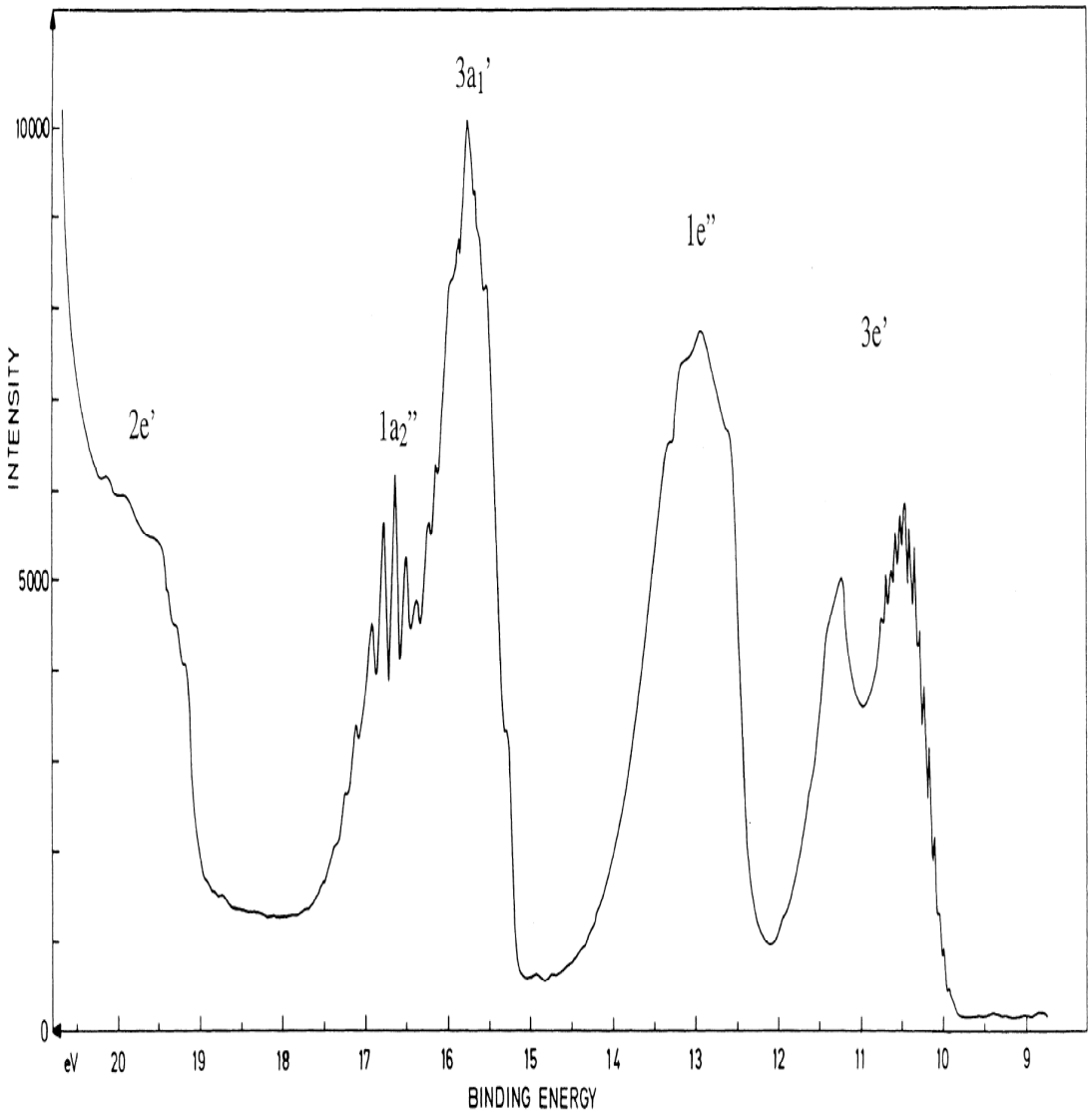

Figure 5.1: The He I experimental photoelectron spectrum of cyclopropane reproduced from Ref. [75].

in section 1.3 along with the available electronic structure results. At first, we have treated the JT interactions in the $\widetilde{X}^2E'$ electronic manifold of CP^+ by constructing a two-states and eleven-modes model vibronic Hamiltonian up to a QVC scheme by an *ab initio* quantum dynamical approach [90]. Our results were shown to compare well with the high-resolution He I excited recording of Holland *et al.* [75] (cf. Fig. 5.1). The strong JT interactions within this state lead to the observed bimodal intensity distribution of the first photoelectron band. The separation between the two maxima of the bimodal profile of ~ 0.80 eV was in good agreement with the experimental value of ~ 0.78 eV. Two Condon active (a_1') and three JT active (e') vibrational modes were found to contribute mostly to the nuclear dynamics in this electronic manifold [90]. In addition, it was found that the progressions in the low-energy wing of the envelope are mainly formed by the JT active ν_4 (CH_2 wagging) and ν_5 (ring deformation) vibrational modes. The average spacing between the successive peaks was found to be in agreement with the experimental value of ~ 60 meV [75]. However, in contrast to the experimental results, highly irregular vibronic structures in the low-energy wing of the theoretical spectrum was found. Also, the second maximum of the bimodal spectral profile revealed more structures than that observed in the experimental envelope [90].

The second photoelectron band of CP^+, attributed to the vibronic structure of $\widetilde{A}^2E''$ electronic manifold, is highly diffuse and broad [75]. In order to reveal the coupling effects of various vibrational modes on the vibronic fine structure of this band, we first examined the nuclear dynamics employing a quadratic coupling scheme in the $\widetilde{A}^2E''$ electronic manifold [91]. Dominant excitation of the ν_2, ν_3, ν_4 and ν_6 vibrational modes was found in the photoelectron band [91]. However, we note that the JT activity of the e' vibrational modes is relatively weak in the $\widetilde{A}^2E''$ electronic manifold when compared to the same in the $\widetilde{X}^2E'$ electronic manifold. Although the quadratic vibronic coupling results compare well with the experimental data, still, the theoretical envelope does not reveal the observed

structureless and diffuse nature of the band.

The discussed discrepancies between the theoretical and experimental results motivated us to further examine the possible role of PJT interactions between the $\widetilde{X}^2E'$ and $\widetilde{A}^2E''$ electronic states of CP^+ and the intermode bilinear JT coupling terms. Therefore, we now here develop an extended diabatic vibronic Hamiltonian considering the intermode coupling terms, apart from the possible PJT interactions between the $\widetilde{X}^2E'$ and $\widetilde{A}^2E''$ electronic states of CP^+. In what follows, a QVC scheme is employed for the JT active e' vibrational modes and the Condon active a_1' vibrational modes, whereas the PJT active a_1'' and e'' vibrational modes are treated within a LVC scheme. Therefore, the complete theoretical model developed here consists of four interacting electronic states and fourteen nuclear degrees of freedom. We mention that VC in CP^+ represents a unique example in which degenerate vibrational modes of two different symmetries are involved in the JT and PJT activities.

Detailed *ab initio* electronic structure calculations are carried out to derive the relevant coupling parameters of the vibronic Hamiltonian. A time-independent matrix diagonalization approach to treat the nuclear dynamics on four interacting electronic states including fourteen vibrational degrees of freedom is computationally impracticable. This task is therefore accomplished with a time-dependent WP propagation approach within the MCTDH scheme [53–55] which has been very successful, in particular, treating the multistate and multimode VC problems of large dimensions. The details of the MCTDH method is documented in a recent review article by Beck et al. [110]. In the recent past, this method has been successfully applied to treat very complex VC in $C_6H_6^+$ [27] and $C_5H_4^+$ [124]. The final results of this chapter are obtained by this method, and comparison calculations are carried out in reduced dimensions by the time-independent matrix diagonalization approach, to check the consistencies of various results and also to examine the detailed vibrational progressions in the photoelectron bands. A systematic treatment of the nuclear dynamics revealed that PJT interactions

between the $\widetilde{X}^2E'$ and $\widetilde{A}^2E''$ electronic states of CP^+ play an important role in the detailed structure of the photoelectron bands. The minimum of the seam of PJT conical intersections is found to occur ~ 1.475 eV above and ~ 0.638 eV below the minimum of the JT conical intersections of the $\widetilde{X}^2E'$ and $\widetilde{A}^2E''$ electronic states, respectively. The PJT couplings due to a_1'' and e'' vibrational modes cause a huge increase in the spectral line density. As a result, the second maxima of the first photoelectron band and the entire second photoelectron band, exhibit a structureless pattern. The theoretical findings also establish the importance of the bilinear coupling terms in the nuclear dynamics. They are found to be in excellent agreement with the experimental data.

5.2 The Vibronic Hamiltonian

The photoionization to the two low-lying degenerate $\widetilde{X}^2E'$ and $\widetilde{A}^2E''$ electronic states of CP^+ is theoretically examined here. As stated in the introduction, each of these two electronic states undergo JT splitting when CP^+ is perturbed along the degenerate vibrational modes of e' symmetry. The symmetry selection rule [Eq. 5.3] allows the JT split component states of the two degenerate electronic states to exhibit PJT-type interactions via the vibrational modes of a_1'' and e'' symmetries. In addition, there are three totally symmetric a_1' vibrational modes that are Condon active in each of these two electronic states. The nuclear dynamical simulations on the resulting four coupled electronic states includes 14 vibrational degrees of freedom. The latter are selected from the set of 21 vibrational degrees of freedom of CP^+ by analyzing their coupling strengths extracted from our extensive electronic structure data. In the following, we first resort to a diabatic electronic basis [44] to treat this VC problem. This is to avoid the numerical difficulties [17] that arise due to the singular nature of the nonadiabatic coupling terms in an adiabatic electronic basis. The diabatic vibronic Hamiltonian is constructed in terms of the dimensionless normal coordinates of the

electronic ground state of neutral CP. To a good approximation, the vibrational motion in the latter is treated as harmonic. Here, we refer to Q_i as the dimensionless normal coordinate of the vibrational mode ν_i with a harmonic vibrational frequency ω_i. Actually, each Q_i represents the normal displacement coordinate from the equilibrium configuration of the electronic ground state of CP at $\mathbf{Q}$=0. In the present chapter, the three a_1' vibrational modes are numbered as ν_1, ν_2, and ν_3, the four e' vibrational modes as ν_4, ν_5, ν_6, and ν_7, and one a_1'' and one of three e'' vibrational modes as ν_8 and ν_9, respectively. Following the well-known VC theory [17], we represent the diabatic vibronic Hamiltonian of the coupled manifold of four interacting electronic states as

$$\mathcal{H} = \mathcal{H}_0\mathbf{1_4} + \begin{pmatrix} \mathcal{W}_{11} & \mathcal{W}_{12} & \mathcal{W}_{13} & \mathcal{W}_{14} \\ & \mathcal{W}_{22} & \mathcal{W}_{23} & \mathcal{W}_{24} \\ h.c. & & \mathcal{W}_{33} & \mathcal{W}_{34} \\ & & & \mathcal{W}_{44} \end{pmatrix}. \tag{5.4}$$

Here $\mathcal{H}_0 = \mathcal{T}_N + \mathcal{V}_0$, with

$$\mathcal{T}_N = -\frac{1}{2}\sum_{i=1}^{3}\omega_i\frac{\partial^2}{\partial Q_i^2} - \frac{1}{2}\sum_{i=4}^{7}\omega_i\left(\frac{\partial^2}{\partial Q_{xi}^2} + \frac{\partial^2}{\partial Q_{yi}^2}\right) - \frac{1}{2}\omega_8\frac{\partial^2}{\partial Q_8^2} - \frac{1}{2}\omega_9\left(\frac{\partial^2}{\partial Q_{x9}^2} + \frac{\partial^2}{\partial Q_{y9}^2}\right) \tag{5.5}$$

and

$$\mathcal{V}_0 = \frac{1}{2}\sum_{i=1}^{3}\omega_i Q_i^2 + \frac{1}{2}\sum_{i=4}^{7}\omega_i\left(Q_{xi}^2 + Q_{yi}^2\right) + \frac{1}{2}\omega_8 Q_8^2 + \frac{1}{2}\omega_9\left(Q_{x9}^2 + Q_{y9}^2\right) \tag{5.6}$$

is the Hamiltonian matrix associated with the ground electronic state of CP and is defined in terms of unperturbed harmonic oscillators with frequencies ω_i. The matrix Hamiltonian with elements $\mathcal{W}_{ij}$ in Eq. (5.4) describes the change in the electronic energy upon ionization from the electronic ground state of CP. These elements are expanded in a Taylor series around the D_{3h} equilibrium geometry

of CP along each of the normal mode displacement coordinates. The series is truncated after the second-order terms for the symmetric a_1' and JT active e' vibrational modes, whereas up to the first-order terms are retained only for the PJT active a_1'' and e'' vibrational modes. Including the various bilinear (a_1'-a_1', e'-e', and a_1'-e') coupling terms, the following results are obtained in conjunction with the elementary symmetry selection rules (as stated above) and a rigorous group theoretical analysis (given in Appendix C) [17]:

$$\begin{aligned}\mathcal{W}_{11} &= E^0_{E'} + \sum_{i=1}^{3}\kappa_i' Q_i + \frac{1}{2}\sum_{i=1}^{3}\sum_{j=1}^{3}\gamma_{ij}' Q_i Q_j + \sum_{i=4}^{7}\lambda_i' Q_{xi} + \frac{1}{2}\sum_{i=1}^{3}\sum_{j=4}^{7} b_{ij}' Q_i Q_{xj} \\ &\quad \frac{1}{2}\sum_{i=4}^{7}\sum_{j=4}^{7}\left[\gamma_{ij}'(Q_{xi}Q_{xj}+Q_{yi}Q_{yj}) + \eta_{ij}'(Q_{xi}Q_{xj}-Q_{yi}Q_{yj})\right], \end{aligned} \tag{5.7a}$$

$$\begin{aligned}\mathcal{W}_{22} &= E^0_{E'} + \sum_{i=1}^{3}\kappa_i' Q_i + \frac{1}{2}\sum_{i=1}^{3}\sum_{j=1}^{3}\gamma_{ij}' Q_i Q_j - \sum_{i=4}^{7}\lambda_i' Q_{xi} - \frac{1}{2}\sum_{i=1}^{3}\sum_{j=4}^{7} b_{ij}' Q_i Q_{xj} \\ &\quad \frac{1}{2}\sum_{i=4}^{7}\sum_{j=4}^{7}\left[\gamma_{ij}'(Q_{xi}Q_{xj}+Q_{yi}Q_{yj}) - \eta_{ij}'(Q_{xi}Q_{xj}-Q_{yi}Q_{yj})\right], \end{aligned} \tag{5.7b}$$

$$\begin{aligned}\mathcal{W}_{33} &= E^0_{E''} + \sum_{i=1}^{3}\kappa_i'' Q_i + \frac{1}{2}\sum_{i=1}^{3}\sum_{j=1}^{3}\gamma_{ij}'' Q_i Q_j + \sum_{i=4}^{7}\lambda_i'' Q_{xi} + \frac{1}{2}\sum_{i=1}^{3}\sum_{j=4}^{7} b_{ij}'' Q_i Q_{xj} \\ &\quad \frac{1}{2}\sum_{i=4}^{7}\sum_{j=4}^{7}\left[\gamma_{ij}''(Q_{xi}Q_{xj}+Q_{yi}Q_{yj}) + \eta_{ij}''(Q_{xi}Q_{xj}-Q_{yi}Q_{yj})\right], \end{aligned} \tag{5.7c}$$

$$\begin{aligned}\mathcal{W}_{44} &= E^0_{E''} + \sum_{i=1}^{3}\kappa_i'' Q_i + \frac{1}{2}\sum_{i=1}^{3}\sum_{j=1}^{3}\gamma_{ij}'' Q_i Q_j - \sum_{i=4}^{7}\lambda_i'' Q_{xi} - \frac{1}{2}\sum_{i=1}^{3}\sum_{j=4}^{7} b_{ij}'' Q_i Q_{xj} \\ &\quad \frac{1}{2}\sum_{i=4}^{7}\sum_{j=4}^{7}\left[\gamma_{ij}''(Q_{xi}Q_{xj}+Q_{yi}Q_{yj}) - \eta_{ij}''(Q_{xi}Q_{xj}-Q_{yi}Q_{yj})\right], \end{aligned} \tag{5.7d}$$

$$\mathcal{W}_{12} = \sum_{i=4}^{7}\lambda_i' Q_{yi} - \sum_{i=4}^{7}\sum_{j=4}^{7}\eta_{ij}' Q_{xi}Q_{yj} + \frac{1}{2}\sum_{i=1}^{3}\sum_{j=4}^{7} b_{ij}' Q_i Q_{yj}, \tag{5.7e}$$

$$\mathcal{W}_{13} = \lambda_9 Q_{x9}, \tag{5.7f}$$

$$\mathcal{W}_{14} = \lambda_8 Q_8 + \lambda_9 Q_{y9}, \tag{5.7g}$$

$$\mathcal{W}_{23} = -\lambda_8 Q_8 + \lambda_9 Q_{y9}, \tag{5.7h}$$

$$\mathcal{W}_{24} = -\lambda_9 Q_{x9}, \tag{5.7i}$$

$$\mathcal{W}_{34} = \sum_{i=4}^{7}\lambda_i'' Q_{yi} - \sum_{i=4}^{7}\sum_{j=4}^{7}\eta_{ij}'' Q_{xi}Q_{yj} + \frac{1}{2}\sum_{i=1}^{3}\sum_{j=4}^{7} b_{ij}'' Q_i Q_{yj}. \tag{5.7j}$$

Here $E^0_{E'}$ and $E^0_{E''}$ are the vertical ionization potentials of the $\widetilde{X}^2E'$ and $\widetilde{A}^2E''$ electronic states of CP^+, respectively. The quantities κ_i' and κ_i'' are the linear intrastate coupling constants for the totally symmetric vibrational modes (i = 1-3). The parameters λ_i' and λ_i'' are the linear JT coupling constants for the JT active degenerate vibrational modes (i = 4-7). The quantities γ_{ij}' and γ_{ij}'' (i, j = 1-7, $i = j$) denote the diagonal second-order coupling parameters which account for the change of vibrational frequencies upon ionization from the electronic ground state of CP. The coefficients γ_{ij}' and γ_{ij}'' pertain to the intermode a_1'-a_1' (i, j = 1-3, $i \neq j$) and e'-e' (i, j = 4-7, $i \neq j$) couplings for the a_1' and e' vibrational modes, whereas η_{ij}' and η_{ij}'', i, j = 4-7, denote the crossed quadratic JT terms. The b_{ij}, i = 1-3, j = 4-7 are the bilinear JT coupling parameters related to the

mixing of the vibrational modes of the a_1' and e' symmetries. The linear PJT coupling parameters for the a_1'' and e'' vibrational modes are designated as λ_8 and λ_9, respectively. Here, we note that the primed and doubly primed parameters are associated with the $\widetilde{X}^2E'$ and $\widetilde{A}^2E''$ electronic states, respectively. The calculations of these parameters are discussed in section 5.3.1 below, and their numerical values are given in Tables 5.3 and 5.4.

5.3 Electronic Structure Calculations

For the dynamical study, the various coupling parameters of the vibronic Hamiltonian of Eqs. (5.7a-5.7j), need to be determined first. We therefore perform detailed *ab initio* calculations of the electronic PESs of the $\widetilde{X}^2E'$ and $\widetilde{A}^2E''$ electronic states of CP^+ along the dimensionless normal coordinates of all 21 vibrational degrees of freedom. The latter are obtained as we discussed in section 3.3.1. The important and most relevant vibrational modes are then selected and included in the dynamical calculations based on their coupling strength. The geometry optimization and the calculation of harmonic vibrational frequencies (ω_i) of CP in its ground electronic state ($\widetilde{X}^1A_1'$) are carried out at the MP2 level of theory employing the cc-pVTZ basis set. The electronic structure calculations were performed using the Gaussian03 program package [116]. The optimized geometry parameters of CP in its ground electronic state are documented in Table 5.1 along with the available experimental results [125]. It can be seen from Table 5.1 that MP2 equilibrium geometry parameters correspond well with the corresponding experimental values, except the $\angle$ H-C-H angle, which is $\sim 2^\circ$ smaller than the experimental value.

The relevant normal vibrational modes of CP are schematically represented in Fig. 5.2. The nature of these vibrational modes, their symmetry properties, and harmonic vibrational frequencies are reported in Table 5.2, along with the available experimental results [126]. The apparent deviations between the two can

Table 5.1: Equilibrium geometry of CP in its ground electronic state ($\widetilde{X}^1A_1'$) along with the experimental results of Ref. [125].

	∠ H-C-H (deg)	∠ C-C-C (deg)	C-H (Å)	C-C (Å)
MP2/cc-pVTZ	115.08	60	1.078	1.503
Expt [125]	117.08	59.98	1.074	1.499

Table 5.2: Symmetry, frequency, and description of the relevant vibrational modes of the electronic ground state of CP. The experimental results are reproduced from Ref. [126]. Note that, theoretical frequencies are harmonic, whereas, experimental ones are fundamental.

		Vibrational frequency (ω_i)/eV		
Symmetry	Mode	MP2/cc-pVTZ	Experiment	Description
a_1'	ν_1	0.1531	0.1473	C-C stretching
	ν_2	0.1902	0.1829	CH_2 scissoring
	ν_3	0.3965	0.3744	Symmetric C-H stretching
e'	ν_4	0.1129	0.1074	CH_2 wagging
	ν_5	0.1309	0.1270	Ring deformation
	ν_6	0.1841	0.1778	CH_2 scissoring
	ν_7	0.3954	0.3743	Asymmetric C-H stretching
a_1''	ν_8	0.1449	-	CH_2 twisting
e''	ν_9	0.1514	-	CH_2 twisting

be attributed to the fact that the experimental results represent the fundamental vibrational frequencies.

5.3.1 Coupling Parameters of the Hamiltonian

The coupling parameters of the Hamiltonian [Eqs. (5.4-5.7j)] represent derivatives of the adiabatic potential-energy function of CP^+ of appropriate order with respect to the dimensionless normal coordinates Q_i of the vibrational mode ν_i calculated at the equilibrium geometry of neutral CP (**Q=0**) [94]. The linear intrastate (κ_i' and κ_i''; i = 1-3) and the JT (λ_i' and λ_i''; i = 4-7) coupling parameters are obtained using Eqs. (4.9) and (4.10), respectively, given in section 4.3.1. The diagonal second-order coupling parameters (γ_i' and γ_i''; i = 1-3) for the to-

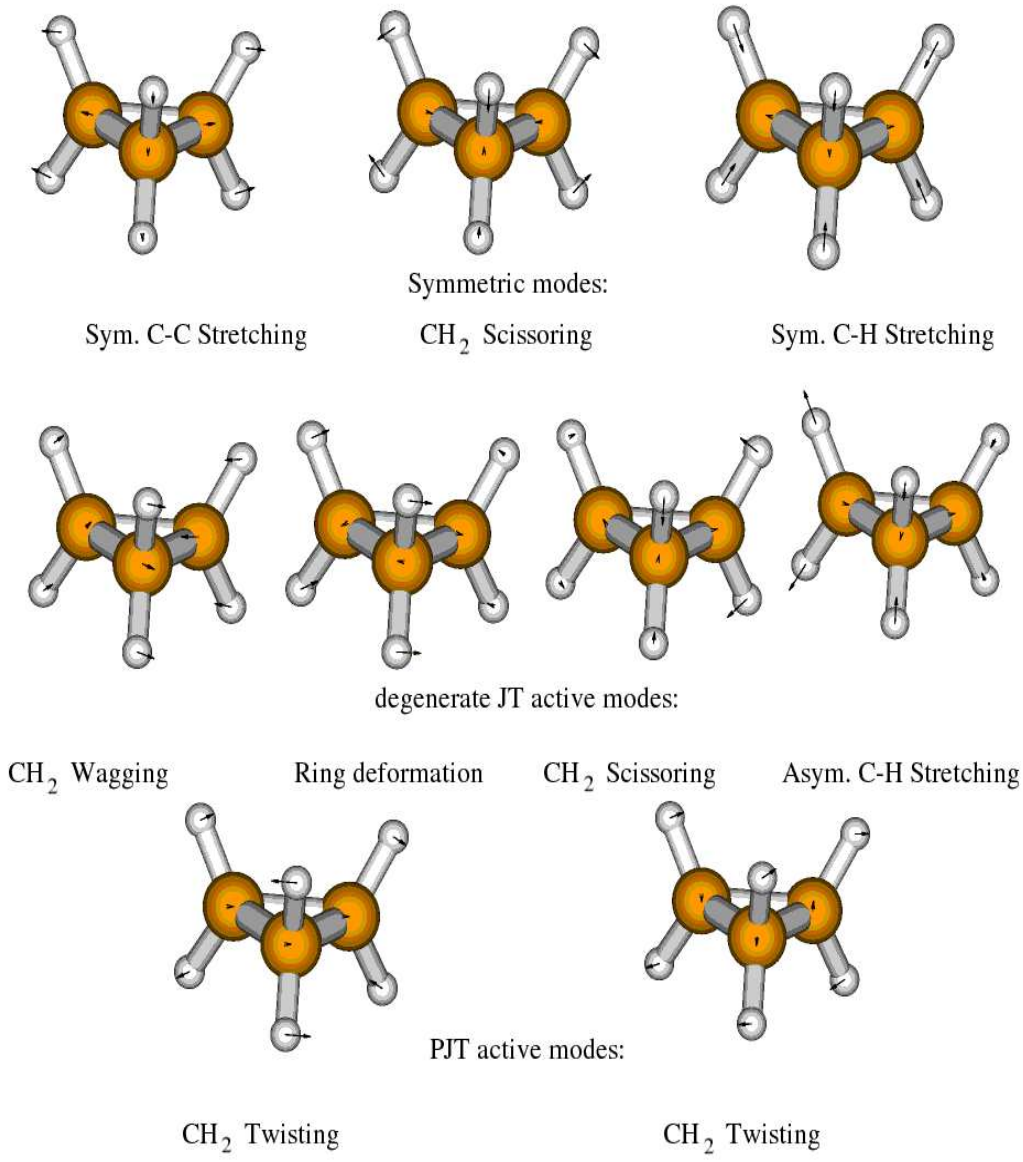

Figure 5.2: Schematic representation of the relevant normal vibrational modes of CP in its ground electronic state ($\widetilde{X}^1A_1'$).

tally symmetric a_1' vibrational modes are obtained from Eq. (4.11). Similarly, the second-order coupling parameters (γ_i'; i = 4-7) for the degenerate e' vibrational modes are obtained from the following expression,

$$\gamma_i' = \left(\frac{\partial^2 \overline{V}_{E'}}{\partial Q_i^2}\right)\Bigg|_{\mathbf{Q=0}}, \qquad i = 4-7. \tag{5.8}$$

where $\overline{V}_{E'}$ is the mean of the JT split PESs of the $\widetilde{X}^2E'$ electronic state of CP^+. An analogous definition holds for γ_i'' (i = 4-7), where $\overline{V}_{E'}$ in Eq. (5.8) is replaced by $\overline{V}_{E''}$ energies respectively, of the $\widetilde{A}^2E''$ electronic manifold.

The quadratic JT (η_i') coupling parameters of the $\widetilde{X}^2E'$ electronic manifold are calculated from the corresponding (signed) difference of the JT split PESs:

$$\eta_i' = \frac{1}{2}\left(\frac{\partial^2 \Delta E'}{\partial Q_i^2}\right)\Bigg|_{\mathbf{Q=0}}, \qquad i = 4-7. \tag{5.9}$$

Similarly one can obtain η_i'' of e' vibrational modes (i = 4-7) by replacing $\Delta E''$ energies of the $\widetilde{A}^2E''$ electronic manifold.

In order to estimate these coupling parameters we performed direct calculations of vertical ionization energies of CP by the OVGF method [117, 118] employing the cc-pVTZ basis set. The electronic structure calculations are carried out as a function of the dimensionless normal mode displacement (from **Q=0**) coordinates and for Q_i (i = 1-7) = ± 0.10, ± 0.25 (± 0.25) ± 1.50, using the Gaussian03 program package [116]. The vertical ionization energies thus obtained are equated with the adiabatic potential energies of the $\widetilde{X}^2E'$ and $\widetilde{A}^2E''$ electronic states of CP^+ and $\widetilde{X}^1A_1'$ electronic state of CP along the respective normal modes of vibration. These energies are then fitted to the adiabatic form of the diabatic Hamiltonian described in Eqs. (5.7a-5.7j) by a nonlinear least-square fit procedure and thereby the coupling parameters are derived. The various fitting diagrams are shown in Figs. 5.3-5.6 for the $\widetilde{X}^2E'$ and $\widetilde{A}^2E''$ electronic manifold of CP^+. We note that, the coupling parameters are also estimated by numerical finite dif-

ference scheme (given in Appendix B) and the identity of the results is confirmed.

The $\widetilde{X}^2E'$-$\widetilde{A}^2E''$ PJT coupling parameters for the a_1'' and e'' vibrational modes can be obtained from

$$\lambda_i = \frac{1}{2}\sqrt{\left(\frac{\partial^2 \Delta E}{\partial Q_i^2}\right)}\Bigg|_{\mathbf{Q=0}}, \qquad i = 8, 9. \tag{5.10}$$

Here $\Delta E = \Delta V_{Q_i}^2$ - ΔV_0^2, where $\Delta V_{Q_i}^2$ and ΔV_0^2 are the potential energy differences between the $\widetilde{A}^2E''$ and $\widetilde{X}^2E'$ electronic states for the normal mode displacement Q_i, and for the equilibrium configuration ($\mathbf{Q}$=0), respectively. In order to estimate these parameters, additional electronic structure calculations are performed along the a_1'' and e'' vibrational modes as a function of the dimensionless normal mode displacement (from $\mathbf{Q=0}$) coordinates and for Q_i (i = 8, 9) = ± 0.10, ± 0.25 (± 0.25) ± 1.50, using the Gaussian03 program package [116]. The PJT coupling parameters are then obtained by a suitable numerical finite difference scheme.

The a_1'-a_1' bilinear coupling parameters of the $\widetilde{X}^2E'$ electronic manifold are given by

$$\gamma_{ij}' = \left(\frac{\partial^2 V_{E'}}{\partial Q_i \partial Q_j}\right)\Bigg|_{\mathbf{Q=0}}, \qquad i, j = 1-3; \quad i \neq j \tag{5.11}$$

An analogous definition holds for γ_{ij}'', where $V_{E'}$ in Eq. (5.11) is replaced by the adiabatic potential energy $V_{E''}$ of the $\widetilde{A}^2E''$ electronic manifold. In a similar manner, we have also estimated the a_1'-e' (i = 1-3; j = 4-7; $i \neq j$) and e'-e' (i, j = 4-7; $i \neq j$) bilinear coupling parameters b_{ij}', b_{ij}'', and γ_{ij}' and γ_{ij}'', respectively, of the $\widetilde{X}^2E'$ and $\widetilde{A}^2E''$ electronic manifold of CP^+. In order to estimate these parameters, we have performed extensive electronic structure calculations by small normal mode displacement coordinates along two vibrational modes simultaneously and for Q_{ij} (i, j = 1-7; $i \neq j$) = ± 0.10, ± 0.25 (± 0.25) ± 1.0, using the Gaussian03 program package [116]. Then the parameters are calculated by suit-

able numerical finite difference schemes (cf. Appendix B). The numerical values of these intermode bilinear coupling parameters are given in Table 5.4. We note that, the limitation to maximum distortions of 1.0 here does not seem to be a rigorous, but a useful one. This is due to the fact that we displace along two normal coordinates at the same time, their combined effect is bigger and may thus reach the limitations of the coupling model more easily than with the linear coupling constants (single mode displacements alone) [17].

In Figs. 5.3(a-f) the adiabatic potential energy values of the $\widetilde{X}^2E'$ and $\widetilde{A}^2E''$ electronic states of CP^+ measured relative to the $\widetilde{X}^1A_1'$ electronic state of CP (these are the vertical ionization energy values obtained from the OVGF calculations) along the dimensionless normal coordinate of the a_1' vibrational modes ν_1, ν_2, and ν_3 are plotted. The asterisks and the filled circles represent the computed *ab initio* data for the $\widetilde{X}^2E'$ and $\widetilde{A}^2E''$ electronic states, respectively, and a quadratic fit to these data is shown by the solid line in each panel. The vibrational modes ν_1, ν_2, and ν_3 represent the C-C stretching, CH_2 scissoring, and symmetric C-H stretching motion, respectively [126]. It can be seen that the degeneracy of the $\widetilde{X}^2E'$ and $\widetilde{A}^2E''$ electronic states of CP^+ is not lifted when displacing along these vibrational modes. The linear (κ_i' and κ_i'') and the second-order (γ_i' and γ_i'') coupling parameters for these modes resulting from the above fits are given in Table 5.3.

The mean of the JT split PESs of the $\widetilde{X}^2E'$ and $\widetilde{A}^2E''$ electronic states of CP^+ for displacements along the x-component of the degenerate e' vibrational modes ν_4, ν_5, ν_6, and ν_7 is plotted in Figs. 5.4(a-d) and 5.5(a-d), respectively, as a function of their dimensionless normal coordinates. These modes represent the CH_2 wagging, ring deformation, CH_2 scissoring, and asymmetric C-H stretching motion, respectively, in that order [126]. The computed *ab initio* points in each panel of Fig. 5.4(a-d) and Fig. 5.5(a-d) are shown by the asterisks and a quadratic fit to these points is shown by the solid line. It can be seen, from Eqs. (5.7a-5.7j) that, in absence of the bilinear coupling, the above fits yield the diagonal second-

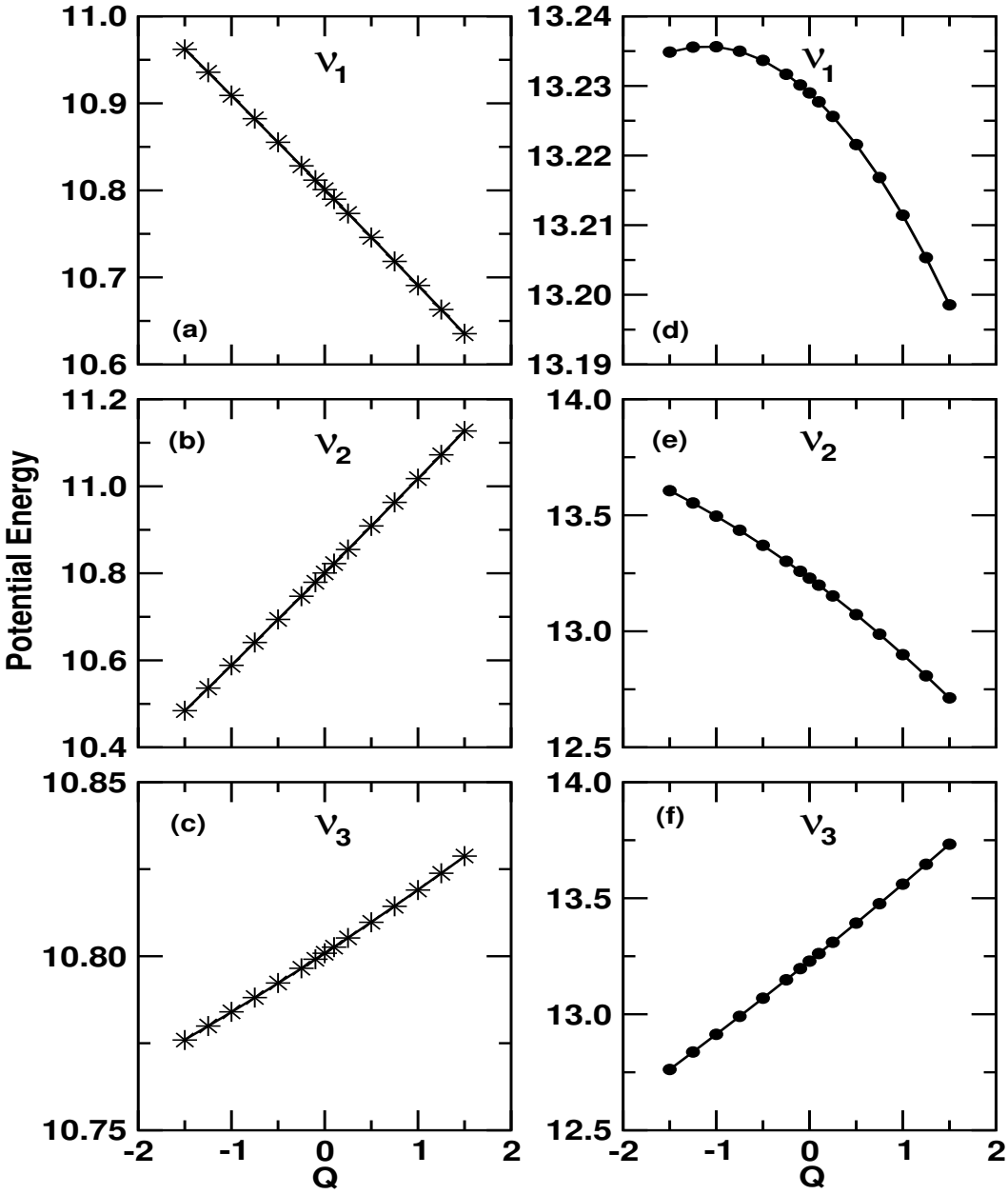

Figure 5.3: Adiabatic potential energies of the $\widetilde{X}^2E'$ (panels: a-c) and $\widetilde{A}^2E''$ (panels: d-f) electronic states of CP^+ measured relative to the electronic ground state of CP along the dimensionless normal coordinates of the symmetric vibrational modes ν_1, ν_2, and ν_3. The asterisks and filled circles represent the computed data for the $\widetilde{X}^2E'$ and $\widetilde{A}^2E''$ electronic states respectively, and a quadratic fit to these data is shown by the solid line in each panel. The linear (κ_i and κ_i') and diagonal quadratic coupling (γ_i and γ_i') parameters listed in Table 5.3 are obtained from the above fits.

order coupling parameters γ_i' and γ_i'' for the i^{th} vibrational mode of $\widetilde{X}^2E'$ and $\widetilde{A}^2E''$ electronic states, respectively. The value of these parameters obtained from the above fits are included in Table 5.3.

The linear and quadratic JT coupling parameters of the $\widetilde{X}^2E'$ and $\widetilde{A}^2E''$ electronic states of CP^+ for the degenerate vibrational modes ν_4-ν_7 are evaluated by fitting the (signed) difference of the JT split PESs along these modes. In Fig. 5.6(a-h) this energy difference is plotted along the dimensionless normal coordinates of the x component of the respective mode. The asterisks and the filled circles denote the computed *ab initio* energies for the $\widetilde{X}^2E'$ and $\widetilde{A}^2E''$ electronic states, respectively, and the solid line superimposed on them in each panel represents the quadratic fit (excluding bilinear coupling terms). The value of the linear (λ_i' and λ_i'') and quadratic (η_i' and η_i'') JT coupling parameters thus obtained from the above fits are included in Table 5.3.

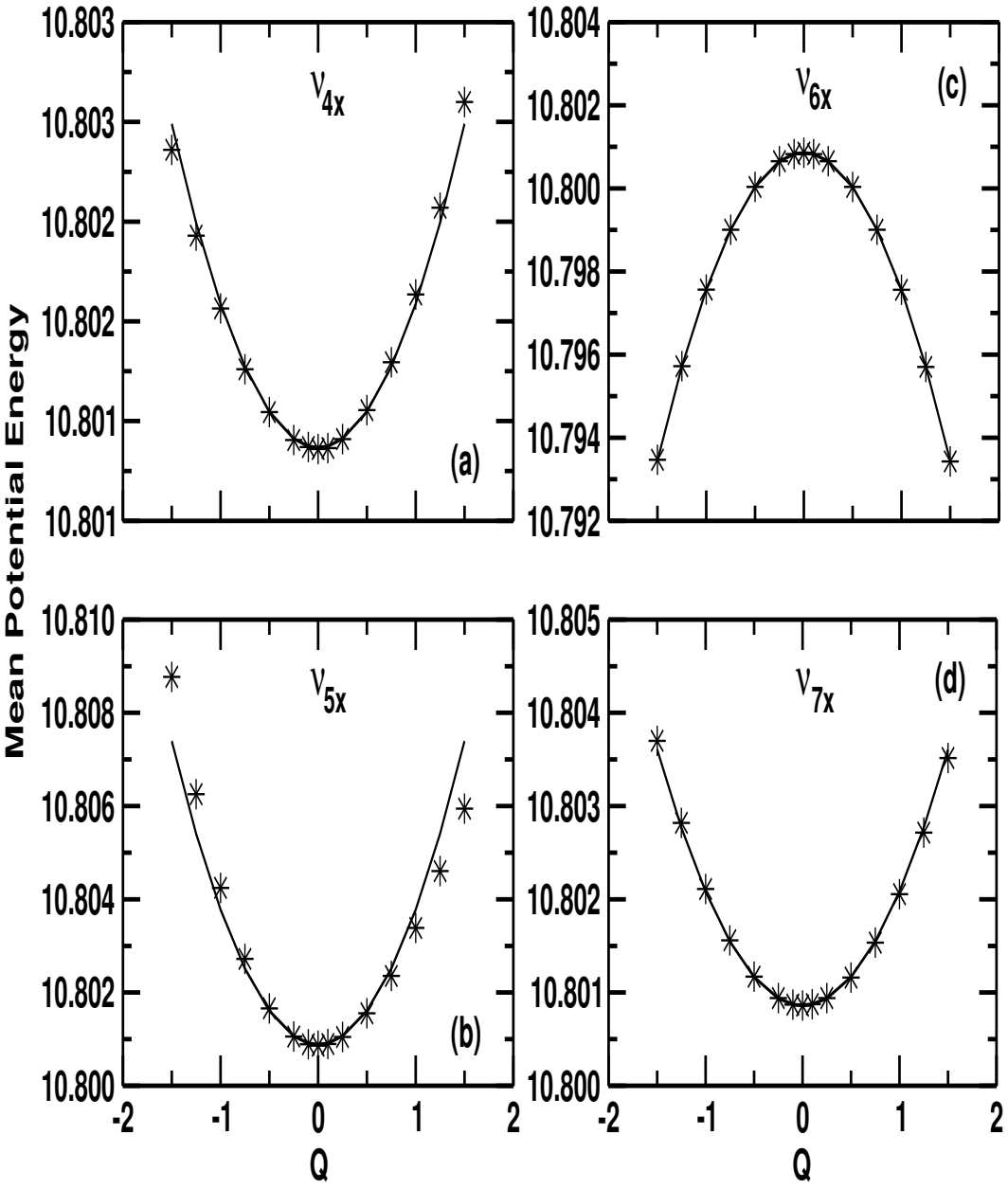

Figure 5.4: The mean potential energy of the JT split adiabatic sheets of the $\widetilde{X}^2E'$ electronic manifold of CP^+ plotted along the dimensionless normal coordinates of the x components of the degenerate vibrational modes ν_4, ν_5, ν_6, and ν_7 in panel a, b, c, and d, respectively. The *ab initio* OVGF data are shown by the asterisks and a parabolic fit to these data is shown by the solid lines. The diagonal quadratic coupling constants for the JT modes (γ_i') listed in Table 5.3 are derived from the above fits.

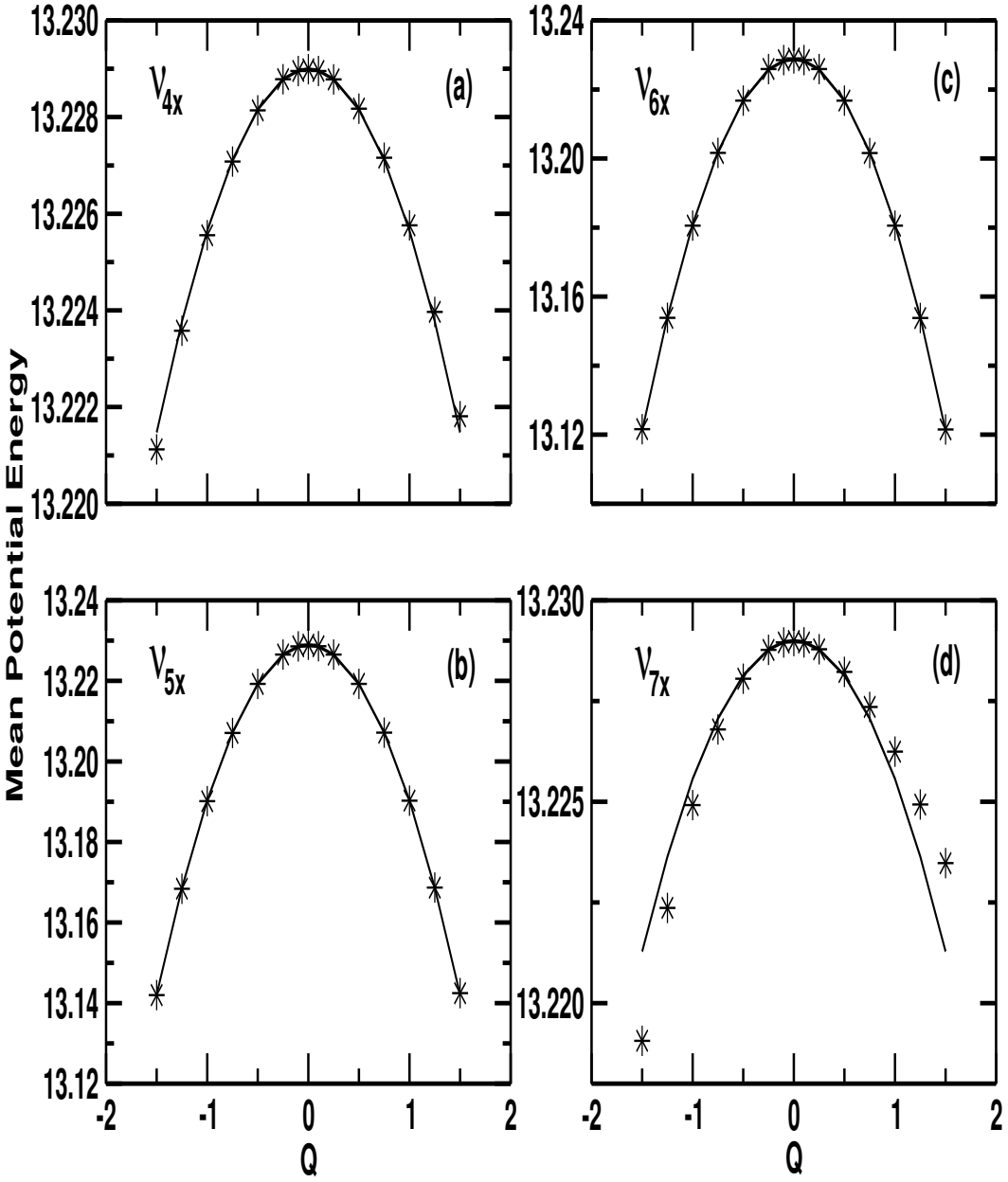

Figure 5.5: The same as in Fig. 5.4 of the $\widetilde{A}^2E''$ electronic manifold of CP^+. The diagonal quadratic coupling constants for the JT modes (γ_i'') documented in Table 5.3 are derived from the above fits.

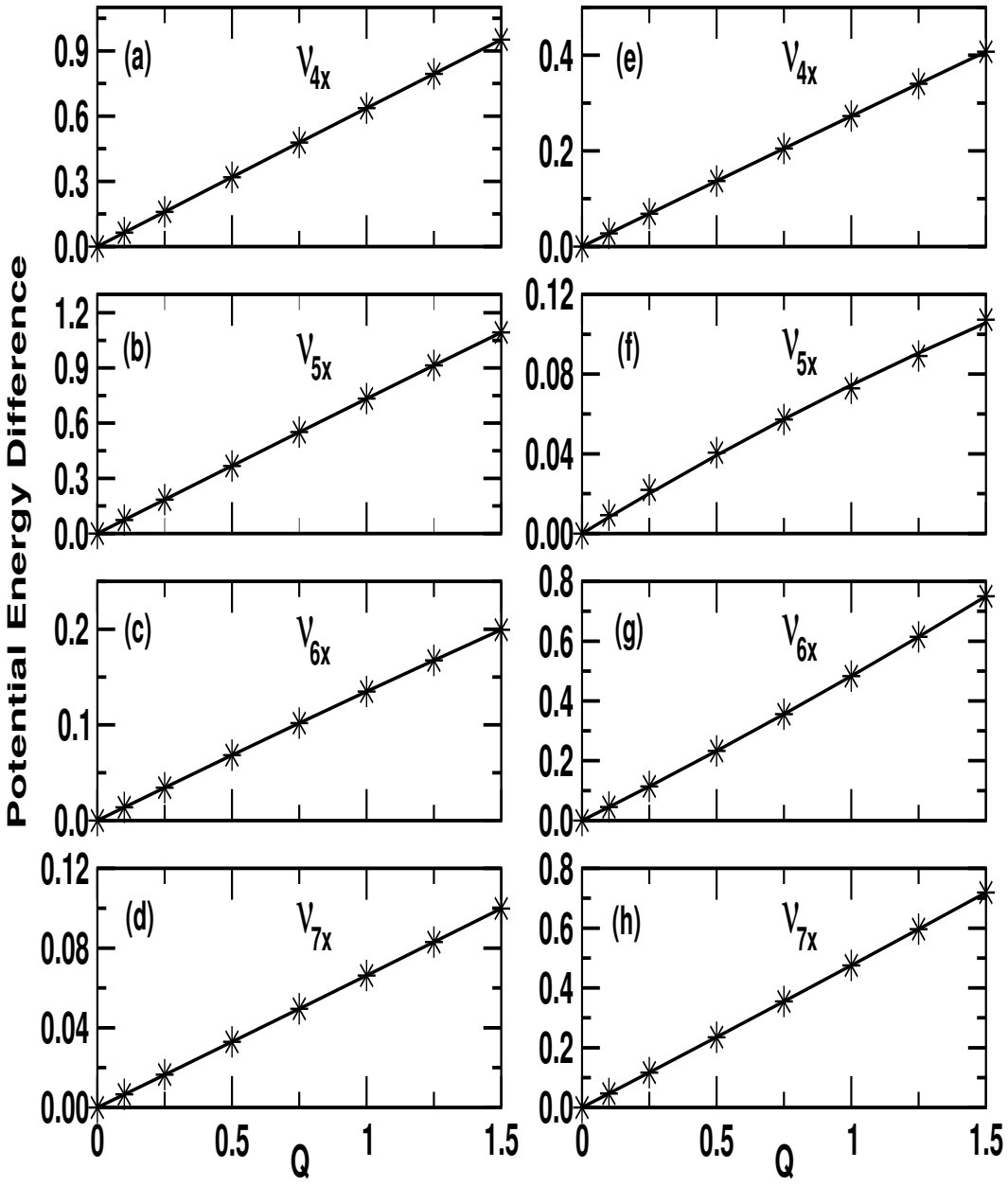

Figure 5.6: The potential energy difference of the JT split adiabatic sheets of the $\widetilde{X}^2E'$ (panel: a-d) and $\widetilde{A}^2E''$ (panel: e-h) electronic states of CP^+ plotted along the dimensionless normal coordinates of the x components of the degenerate vibrational modes ν_4-ν_7 . The *ab initio* OVGF data are shown by the asterisks and filled circles for the $\widetilde{X}^2E'$ and $\widetilde{A}^2E''$ electronic states, respectively, and a quadratic fit to these data is shown by the solid line. The linear (λ_i' and λ_i'') and the quadratic (η_i' and η_i'') JT coupling parameters listed in Table 5.3 are derived from the above fits.

Table 5.3: *Ab initio* calculated linear and quadratic coupling constants for the $\widetilde{X}^2E'$ and $\widetilde{A}^2E''$ electronic states of CP^+. The vertical ionization energies of these two electronic states are also given in the table. All quantities are in eV. The dimensionless Poisson parameters $(\kappa_i'/\omega_i)^2/2$, $(\lambda_i'/\omega_i)^2/2$, $(\kappa_i''/\omega_i)^2/2$ and $(\lambda_i''/\omega_i)^2/2$ are given in parentheses.

Mode (symmetry)	κ_i' or λ_i' $\widetilde{X}^2E'$	κ_i'' or λ_i'' $\widetilde{A}^2E''$	γ_i' $\widetilde{X}^2E'$	γ_i'' $\widetilde{A}^2E''$	η_i' $\widetilde{X}^2E'$	η_i'' $\widetilde{A}^2E''$	λ_i $\widetilde{X}^2E' \otimes \widetilde{A}^2E''$
$\nu_1(a_1')$	-0.109(0.254)	-0.012(0.003)	-1.902 $\times 10^{-3}$	-1.092 $\times 10^{-2}$	–	–	
$\nu_2(a_1')$	0.214(0.635)	-0.298(1.228)	4.350 $\times 10^{-3}$	-6.176 $\times 10^{-2}$	–	–	
$\nu_3(a_1')$	0.018(0.001)	0.324(0.333)	1.324 $\times 10^{-3}$	1.635 $\times 10^{-2}$	–	–	
$\nu_4(e')$	0.320(4.019)	0.138(0.743)	1.442 $\times 10^{-3}$	-6.685 $\times 10^{-3}$	-3.772 $\times 10^{-3}$[a]	-2.494 $\times 10^{-3}$	
$\nu_5(e')$	0.370(3.997)	0.041(0.050)	5.784 $\times 10^{-3}$	-7.716 $\times 10^{-2}$	-7.410 $\times 10^{-3}$[a]	-8.052 $\times 10^{-3}$	
$\nu_6(e')$	0.069(0.071)	0.224(0.741)	-6.586 $\times 10^{-3}$	-9.558 $\times 10^{-2}$	-3.648 $\times 10^{-3}$[a]	3.456 $\times 10^{-2}$	
$\nu_7(e')$	0.033(0.003)	0.233(0.174)	2.441 $\times 10^{-3}$	-6.858 $\times 10^{-3}$	6.692 $\times 10^{-4}$[a]	8.833 $\times 10^{-3}$	
$\nu_8(a_1'')$							0.3280
$\nu_9(e'')$							0.1836
$E^0_{E'}$	10.801						
$E^0_{E''}$	13.229						

5.4 Results and Discussion

5.4.1 Adiabatic Potential Energy Surfaces

The adiabatic PESs of the $\widetilde{X}^2E'$ and $\widetilde{A}^2E''$ electronic states are obtained by diagonalizing the diabatic electronic Hamiltonian matrix given in Eqs. (5.4-5.7j). In absence of the PJT coupling of the a_1'' and e'' vibrational modes, the eigenvalues of the $\widetilde{X}^2E'$ and $\widetilde{A}^2E''$ electronic states are given by

$$\mathcal{V}_{1,2}(\mathbf{Q}) = \mathcal{V}_0(\mathbf{Q}) + E^0_{E'} + \sum_{i=1}^{3}\kappa_i' Q_i + \frac{1}{2}\sum_{i=1}^{3}\gamma_i' Q_i^2 + \frac{1}{2}\sum_{i=4}^{7}\gamma_i'\left(Q_{xi}^2 + Q_{yi}^2\right) \mp \sqrt{\left[\sum_{i=4}^{7}\left(\lambda_i' Q_{xi} + \frac{1}{2}\eta_i'(Q_{xi}^2 - Q_{yi}^2)\right)\right]^2 + \left[\sum_{i=4}^{7}(\lambda_i' Q_{yi} - \eta_i' Q_{xi}Q_{yi})\right]^2} \quad (5.12a)$$

$$\mathcal{V}_{3,4}(\mathbf{Q}) = \mathcal{V}_0(\mathbf{Q}) + E^0_{E''} + \sum_{i=1}^{3}\kappa_i'' Q_i + \frac{1}{2}\sum_{i=1}^{3}\gamma_i'' Q_i^2 + \frac{1}{2}\sum_{i=4}^{7}\gamma_i''\left(Q_{xi}^2 + Q_{yi}^2\right) \mp \sqrt{\left[\sum_{i=4}^{7}\left(\lambda_i'' Q_{xi} + \frac{1}{2}\eta_i''(Q_{xi}^2 - Q_{yi}^2)\right)\right]^2 + \left[\sum_{i=4}^{7}(\lambda_i'' Q_{yi} - \eta_i'' Q_{xi}Q_{yi})\right]^2} \quad (5.12b)$$

where $\mathcal{V}_1$ and $\mathcal{V}_2$ refer to the lower and upper adiabatic sheets of the $\widetilde{X}^2E'$ electronic manifold and $\mathcal{V}_3$ and $\mathcal{V}_4$ to the lower and upper adiabatic sheets of the $\widetilde{A}^2E''$ electronic manifold, respectively. With the aid of the parameters of Table 5.3, the adiabatic PESs of the quadratic vibronic model are obtained. In Figs. 5.7(a-c), we show one dimensional cuts of these multidimensional potential energy hypersurfaces along the totally symmetric vibrational modes ν_1, ν_2, and ν_3. In the figure the potential energy values obtained from the above quadratic vibronic model are shown by the solid and dashed lines for the $\widetilde{X}^2E'$ and $\widetilde{A}^2E''$ electronic states, respectively, and the corresponding *ab initio* computed energies are superimposed on them and indicated by the filled circles. The electronic degeneracy of these states is restored upon displacements along the symmetric vibrational modes. It can be seen that the model reproduces the computed energies very well.

Table 5.4: *Ab initio* calculated intermode coupling parameters of the Hamiltonian. All quantities are in eV.

Intermode couplings i,j	$\widetilde{X^2E'}$	Intermode couplings i,j	$\widetilde{A^2E''}$
a_1'-a_1'		a_1'-a_1'	
γ'_{12}	-4.61 $\times 10^{-3}$	γ''_{12}	-1.18 $\times 10^{-2}$
γ'_{13}	8.15 $\times 10^{-4}$	γ''_{13}	-6.99 $\times 10^{-3}$
γ'_{23}	3.35 $\times 10^{-3}$	γ''_{23}	-2.63 $\times 10^{-2}$
a_1'-e'		a_1'-e'	
b'_{14}	1.28 $\times 10^{-2}$	b''_{14}	1.28 $\times 10^{-2}$
b'_{24}	-1.73 $\times 10^{-2}$	b''_{24}	-3.38 $\times 10^{-3}$
b'_{34}	2.60 $\times 10^{-3}$	b''_{34}	-1.15 $\times 10^{-3}$
b'_{15}	1.21 $\times 10^{-2}$	b''_{15}	2.20 $\times 10^{-3}$
b'_{25}	-1.13 $\times 10^{-2}$	b''_{25}	6.30 $\times 10^{-3}$
b'_{35}	-9.19 $\times 10^{-3}$	b''_{35}	-2.18 $\times 10^{-3}$
b'_{16}	2.49 $\times 10^{-3}$	b''_{16}	-1.40 $\times 10^{-2}$
b'_{26}	3.10 $\times 10^{-3}$	b''_{26}	-4.63 $\times 10^{-2}$
b'_{36}	-6.05 $\times 10^{-3}$	b''_{36}	-2.05 $\times 10^{-2}$
b'_{17}	1.96 $\times 10^{-3}$	b''_{17}	5.87 $\times 10^{-3}$
b'_{27}	-7.91 $\times 10^{-3}$	b''_{27}	1.73 $\times 10^{-2}$
b'_{37}	2.19 $\times 10^{-3}$	b''_{37}	-9.75 $\times 10^{-3}$
e'-e'		e'-e'	
γ'_{45}	-6.54 $\times 10^{-3}$	γ''_{45}	-9.15 $\times 10^{-3}$
γ'_{46}	4.05 $\times 10^{-3}$	γ''_{46}	-4.52 $\times 10^{-3}$
γ'_{47}	2.95 $\times 10^{-4}$	γ''_{47}	6.89 $\times 10^{-4}$
γ'_{56}	-9.36 $\times 10^{-3}$	γ''_{56}	1.34 $\times 10^{-3}$
γ'_{57}	-1.64 $\times 10^{-4}$	γ''_{57}	-1.20 $\times 10^{-4}$
γ'_{67}	8.36 $\times 10^{-4}$	γ''_{67}	-7.18 $\times 10^{-4}$
η'_{45}	3.80 $\times 10^{-5}$	η''_{45}	5.09 $\times 10^{-5}$
η'_{46}	1.71 $\times 10^{-3}$	η''_{46}	-1.91 $\times 10^{-3}$
η'_{47}	-4.94 $\times 10^{-3}$	η''_{47}	-1.19 $\times 10^{-2}$
η'_{56}	-4.01 $\times 10^{-3}$	η''_{56}	5.83 $\times 10^{-4}$
η'_{57}	3.13 $\times 10^{-3}$	η''_{57}	2.26 $\times 10^{-3}$
η'_{67}	-1.70 $\times 10^{-3}$	η''_{67}	1.42 $\times 10^{-3}$

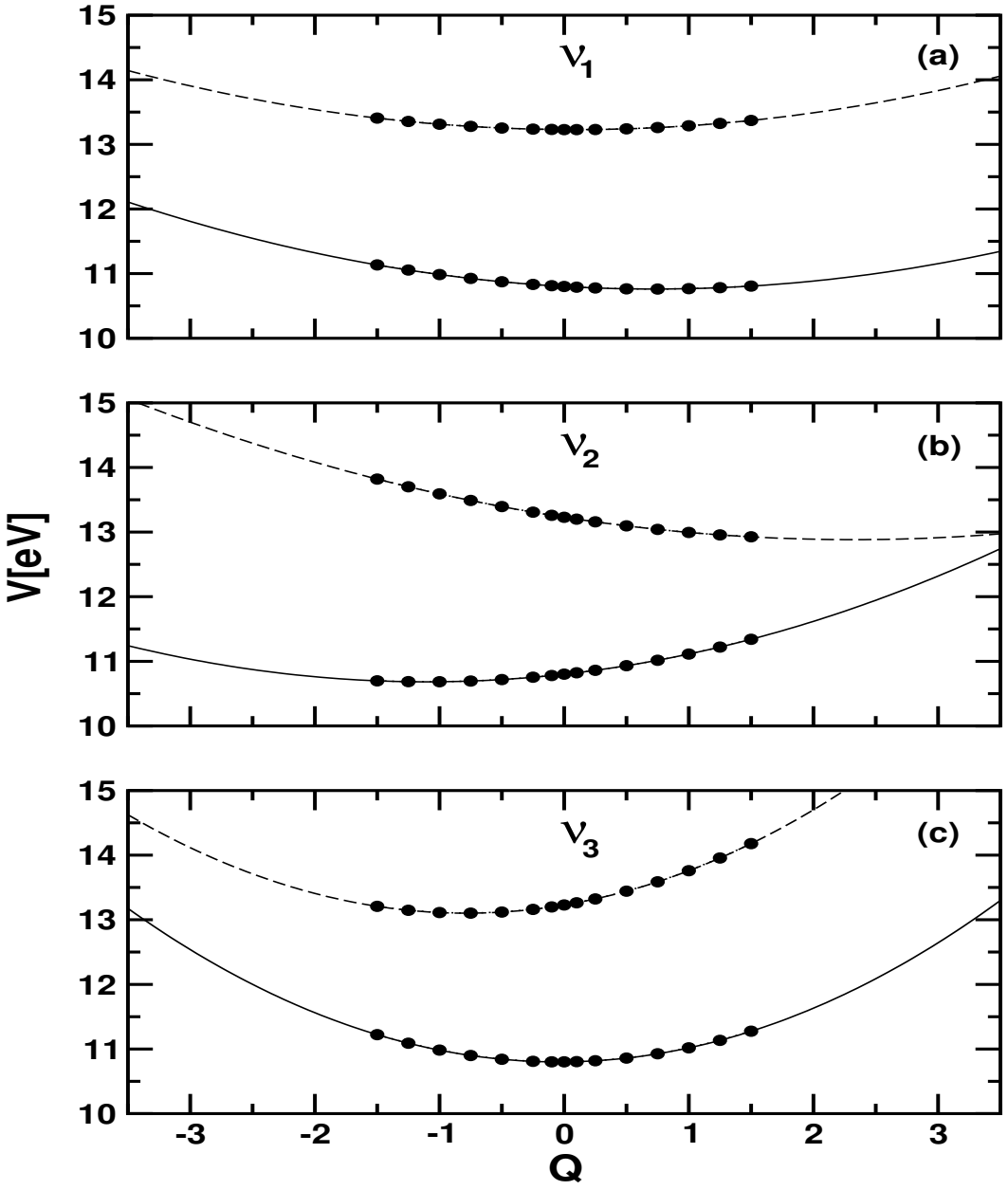

Figure 5.7: The adiabatic potential energy curves of the $\widetilde{X}^2E'$ (solid lines) and $\widetilde{A}^2E''$ (dashed lines) electronic states of CP^+ along the dimensionless normal coordinates for the totally symmetric (a_1'): (a) ν_1 (C-C stretching), (b) ν_2 (CH_2 scissoring) and (c) ν_3 (symmetric C-H stretching) vibrational modes. Each curve in the figure represents a cut along the multidimensional potential energy hypersurface of the respective electronic states. The equilibrium geometry of CP in its electronic ground state ($^1A_1'$) corresponds to $\mathbf{Q}$=0. The *ab initio* ionization energies with a harmonic contribution from the neutral ground electronic state are shown by the filled circles on the diagram.

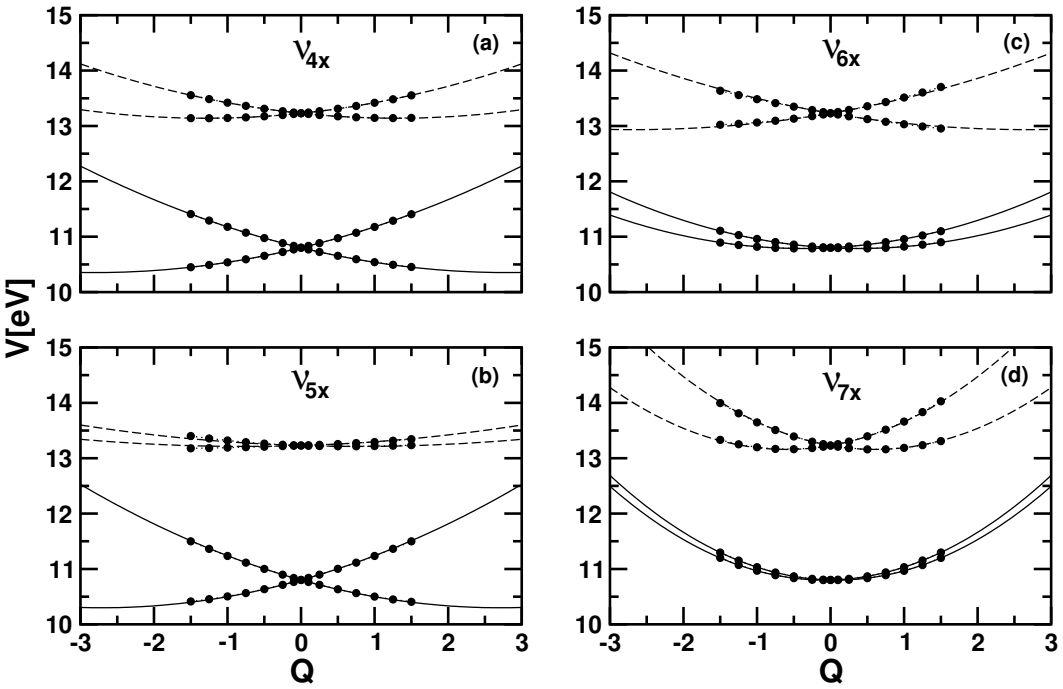

Figure 5.8: Adiabatic potential energy curves of the JT split $\widetilde{X}^2E'$ (solid lines) and the $\widetilde{A}^2E''$ (dashed lines) electronic states of CP^+ plotted as a function of the x component of the dimensionless normal coordinates of the degenerate (e'): (a) ν_4 (CH_2 wagging mode) (b) ν_5 (ring deformation), (c) ν_6 (CH_2 scissoring) and (d) ν_7 (asymmetric C-H stretching) vibrational modes. The *ab initio* ionization energies with a harmonic contribution from the neutral ground electronic state are shown by the filled circles on the diagram.

One-dimensional cuts of the above two electronic states along the x-component of the JT active vibrational modes ν_4, ν_5, ν_6, and ν_7 are plotted in Figs. 5.8(a-d). As above, the solid and dashed lines describe the energy values obtained from the model for the $\widetilde{X}^2E'$ and $\widetilde{A}^2E''$ electronic states, respectively, and the points superimposed on them represent the corresponding computed energies. It can be seen that the degeneracy of the $\widetilde{X}^2E'$ and $\widetilde{A}^2E''$ electronic states is split upon displacements along these modes. It is noteworthy that the degenerate vibrational modes ν_4 and ν_5 cause a large JT splitting in the $\widetilde{X}^2E'$ electronic manifold compared to that in the $\widetilde{A}^2E''$ electronic manifold. On the other hand, the vibrational modes ν_4 and ν_6 cause a relatively large splitting of the degeneracy of the $\widetilde{A}^2E''$ electronic manifold when compared to that of the $\widetilde{X}^2E'$ electronic manifold. It is apparent from Fig. 5.8 that the JT coupling in the $\widetilde{X}^2E'$ electronic manifold is stronger than in the $\widetilde{A}^2E''$ electronic manifold, which is also revealed by the magnitude of the coupling strengths given in Table 5.3. The curve crossings at the origin in the above figures represent the CIs associated with the $(E \times e)$-JT effect. In addition, there are curve crossings between the upper sheet of the $\widetilde{X}^2E'$ and the lower sheet of the $\widetilde{A}^2E''$ electronic states, which will be shown and discussed below.

At this point it is useful to examine a few stationary points of the PESs discussed above. To begin with let us examine the stationary points of the $(E\times e)$-JT split PESs of the $\widetilde{X}^2E'$ electronic manifold within the LVC scheme. The two sheets of the latter manifold remain degenerate [Eq. (5.12a); consider that γ_i' and η_i' are zero] in absence of any JT distortion, that is, Q_i (i = 4-7) = 0. These two sheets form CIs and the minimum of this intersection seam occurs at Q_i^0 (i = 1-3) = -κ_i'/ω_i, in the space of a_1' vibrational modes with an energy [17, 90]

$$\mathcal{V}^{(c)}_{min,JT} \;=\; E^0_{E'} - \frac{1}{2}\sum_{i=1}^{3}\frac{\kappa_i'^2}{\omega_i} \tag{5.13}$$

This global minimum on $\mathcal{V}_1$ at the D_{3h} equilibrium geometry becomes a cusp when distorted along any of the two components of the degenerate vibrational modes. The minimum of $\mathcal{V}_2$ remains at the minimum of the seam of CIs and new minima appear on $\mathcal{V}_1$ at, Q_i^0 (i = 1-3) = -κ_i'/ω_i and Q_{pi}^0 ($p = x/y$, i = 4-7) = $\pm$ λ_{pi}' / ω_{pi} with an energy [90]

$$\mathcal{V}_1^0 \;=\; E_{E'}^0 - \frac{1}{2}\sum_{i=1}^{3}\frac{\kappa_i'^2}{\omega_i} - \frac{1}{2}\sum_{i=4}^{7}\frac{\lambda_{pi}'^2}{\omega_{pi}} \tag{5.14}$$

In multidimensional space this results into a "Mexican hat" topography of the JT split PESs. The JT stabilization energy amounts to $\sum_{i=4}^{7}\lambda_{pi}'^2$ / $2\omega_{pi}$.

Considering the data collected in Table 5.3, one can see that the $\mathcal{V}_{min}^{(c)}$ = 10.6408 eV, occurs at Q_1^0 = 0.7126, Q_2^0 = -1.1272 and Q_3^0 = -0.444. The new minima on $\mathcal{V}_1^0$ [Eq. (5.14)] for the JT distorted geometry occurs at Q_{4x}^0 = 2.8351, Q_{5x}^0 = 2.827, Q_{6x}^0 = 0.3759, and Q_{7x}^0 = 0.0829 with an energy $\mathcal{V}_1^0$ = 9.6495 eV. The JT stabilization energy amounts to $\sim$ 0.991 eV.

The above stationary points of the PESs are further modified when the quadratic coupling terms γ_i' and η_i' in Eq. (5.12a) are considered. In the space of a_1' vibrational modes the minimum of the seam of CIs now occurs at Q_i^0 (i = 1-3) = -$\kappa_i'/(\omega_i + \gamma_i')$, and the energy at the minimum is given by [90]

$$\mathcal{V}_{min,JT}^{(c)} \;=\; E_{E'}^0 - \frac{1}{2}\sum_{i=1}^{3}\frac{\kappa_i'^2}{(\omega_i + \gamma_i')} \tag{5.15}$$

Along the JT active e' vibrational modes, this energetic minimum changes to a cusp and the new minima and saddle points appear on the lower adiabatic component of the JT split $\widetilde{X}^2E'$ electronic manifold. When we distort along one component (say x) of these doubly degenerate vibrational modes, two solutions

are obtained for $Q_{xi} = \mp\lambda_i'/(\omega_i + \gamma_i' \pm \eta_i')$ (i = 4 -7), with energies [90]

$$\mathcal{V}_1^0 = E_{E'}^0 - \frac{1}{2}\sum_{i=1}^{3}\frac{\kappa_i'^2}{(\omega_i + \gamma_i')} - \frac{1}{2}\sum_{i=4}^{7}\frac{\lambda_i'^2}{(\omega_i + \gamma_i' + \eta_i')} \tag{5.16}$$

and

$$\mathcal{V}_1^{sp} = E_{E'}^0 - \frac{1}{2}\sum_{i=1}^{3}\frac{\kappa_i'^2}{(\omega_i + \gamma_i')} - \frac{1}{2}\sum_{i=4}^{7}\frac{\lambda_i'^2}{(\omega_i + \gamma_i' - \eta_i')} \tag{5.17}$$

where $\mathcal{V}_1^0$ and $\mathcal{V}_1^{sp}$ refer to the energy of the minimum and the saddle point, respectively for the signs of the coupling constants as given in Table 5.3. With the data listed in Table 5.3 one obtains $\mathcal{V}_{min}^{(c)}$ = 10.6419 eV at Q_1^0 = 0.7171, Q_2^0 = -1.1145 and Q_3^0 = -0.0443. The new minima on $\mathcal{V}_1$ for the JT distorted geometry occur at $Q_{4x}^0 = 2.7541$, $Q_{5x}^0 = 2.6363$, $Q_{6x}^0 = 0.3859$, and $Q_{7x}^0 = 0.0825$, with energy $\mathcal{V}_1^0$ = 9.6563 eV. The saddle point occurs at Q_{4x}^{sp} = -2.8464, Q_{5x}^{sp} = -2.7831, Q_{6x}^{sp} = -0.3939, and Q_{7x}^{sp} = -0.0824, with energy $\mathcal{V}_1^{sp}$ = 9.6985 eV. The JT stabilization energy amounts to $\sim$ 0.924 eV. A comparison with the linear coupling results (discussed above) reveals that when the quadratic couplings are considered both $\mathcal{V}_{min}^{(c)}$ and $\mathcal{V}_1^0$ shifts to slightly higher energy value. The shift in the value of $\mathcal{V}_1^0$ is relatively greater than that in $\mathcal{V}_{min}^{(c)}$. As a result, the JT stabilization energy also decreases slightly [90].

Let us now consider the $(E \times e)$-JT PESs of the $\widetilde{A}^2E''$ electronic manifold and also its PJT coupling with the $\widetilde{X}^2E'$ electronic manifold. In the space of a_1' vibrational modes, the minimum of the seam of CIs now occurs at Q_i^0 (i = 1-3) = -$\kappa_i''/(\omega_i + \gamma_i'')$, and the energy at the minimum is given by [91]

$$\mathcal{V}_{min,JT}^{(c)} = E_{E''}^0 - \frac{1}{2}\sum_{i=1}^{3}\frac{\kappa_i''^2}{(\omega_i + \gamma_i'')} \tag{5.18}$$

When distorted along the JT active e' vibrational modes, this energetic minimum changes to a cusp and new minima and saddle points appear on the lower

adiabatic component of the JT split $\widetilde{A}^2E''$ electronic manifold. Along one component (say x) of these doubly degenerate vibrational modes, two solutions are obtained for $Q_{xi} = \mp\lambda_i''/(\omega_i + \gamma_i'' \pm \eta_i'')$ (i = 4 -7), with energies [91]

$$\mathcal{V}_3^0 = E_{E''}^0 - \frac{1}{2}\sum_{i=1}^{3}\frac{\kappa_i''^2}{(\omega_i + \gamma_i'')} - \frac{1}{2}\sum_{i=4}^{7}\frac{\lambda_i''^2}{(\omega_i + \gamma_i'' - \eta_i'')} \tag{5.19}$$

and

$$\mathcal{V}_3^{sp} = E_{E''}^0 - \frac{1}{2}\sum_{i=1}^{3}\frac{\kappa_i''^2}{(\omega_i + \gamma_i'')} - \frac{1}{2}\sum_{i=4}^{7}\frac{\lambda_i''^2}{(\omega_i + \gamma_i'' + \eta_i'')} \tag{5.20}$$

where $\mathcal{V}_3^0$ and $\mathcal{V}_3^{sp}$ refer to the energy of the new minima and the saddle points, respectively. Using the parameters given in Table 5.3, we obtain $\mathcal{V}_{min,JT}^{(c)} = 12.756$ eV occurring at Q_1^0 = 0.085, Q_2^0 = 2.320 and Q_3^0 = -0.784; $\mathcal{V}_3^0$ = 12.118 eV occurring at Q_{4x}^0 = 1.266, Q_{5x}^0 = 0.668, Q_{6x}^0 = 4.155 and Q_{7x}^0 = 0.668 and $\mathcal{V}_3^{sp}$ = 12.374 eV occurring at Q_{4x}^{sp} = -1.327, Q_{5x}^{sp} = -0.904, Q_{6x}^{sp} = -1.822 and Q_{4x}^{sp} = -0.587 for the $\widetilde{A}^2E''$ electronic manifold. The JT stabilization energy of the latter amounts to $\sim$ 0.638 eV [91].

We now provide an approximate estimate of the energetic minimum of the PJT crossings of the $\widetilde{X}^2E'$ and $\widetilde{A}^2E''$ electronic states. We repeat that the PJT active modes here are of a_1'' and e'' symmetries, and only two such modes ν_8 (a_1'') and ν_9 (e'') are relevant in the present situation. Defining $\Sigma = (E_{E'}^0 + E_{E''}^0)/2$, $\Delta = (E_{E''}^0 - E_{E'}^0)/2$, $\sigma_i = (\kappa_i' + \kappa_i'')/2$, $\delta_i = (\kappa_i'' - \kappa_i')/2$, $\sigma_i' = (\lambda_i' + \lambda_i'')/2$, $\delta_i' = (\lambda_i'' - \lambda_i')/2$ and setting Q_{yi}, Q_8, Q_{9x}, Q_{9y} = 0, the energetic minimum of the seam of CIs between the JT split components of the $\widetilde{X}^2E'$ and $\widetilde{A}^2E''$ electronic states occurs at [17]

$$\mathcal{V}_{min,PJT}^{(c)} = \Sigma + \frac{(F-\Delta)^2}{2D} - \frac{1}{2}\sum_{i=1}^{3}\frac{\sigma_i^2}{\omega_i} - \frac{1}{2}\sum_{i=4}^{7}\frac{\sigma_i'^2}{\omega_i}, \tag{5.21}$$

where

$$F = \sum_{i=1}^{3} \frac{\delta_i \sigma_i}{\omega_i} + \sum_{i=4}^{7} \frac{\delta_i' \sigma_i'}{\omega_i}, \tag{5.22}$$

$$D = \sum_{i=1}^{3} \frac{\delta_i^2}{\omega_i} + \sum_{i=4}^{7} \frac{\delta_i'^2}{\omega_i}. \tag{5.23}$$

At this point it is necessary to discuss a few technical points. The determination of the energetic minimum of the PJT crossing using Eq. (5.21) requires the knowledge of a definite relative sign of the JT coupling parameters λ_i' and λ_i'' in the $\widetilde{X}^2E'$ and $\widetilde{A}^2E''$ electronic states, respectively. In principle, there may be four different possibilities for this relative sign: (i) $\lambda_i' > 0$, $\lambda_i'' > 0$; (ii) $\lambda_i' > 0$, $\lambda_i'' < 0$; (iii) $\lambda_i' < 0$, $\lambda_i'' < 0$; (iv) $\lambda_i' < 0$, $\lambda_i'' > 0$. The last two possibilities do not yield any new results when compared to the first two. Using the parameters given in Table 5.3 one finds that $\mathcal{V}_{min,PJT}^{(c)}$ occurs at 12.878 eV in case of (i) and at 12.118 eV in case of (ii). The first value is $\sim$ 0.123 eV above and the second one is $\sim$ 0.638 eV below the minimum of the JT conical intersections in the $\widetilde{A}^2E''$ electronic manifold. In practice, the relative signs of these two JT parameters is fixed by examining the invariance property of the Hamiltonian matrix with respect to the symmetry operations of the D_{3h} point group. Such an exercise is detailed in Appendix C. This shows that (ii) is the correct option in this case. Therefore, the minimum of the PJT crossing in the present situation occurs $\sim$ 1.475 eV above the minimum of the $\widetilde{X}^2E'$ and $\sim$ 0.638 eV below the minimum of the $\widetilde{A}^2E''$ JT conical intersections in CP^+.

Interestingly, these relative signs of the JT coupling parameters (λ_i' and λ_i'') can be determined from energy calculations alone. We note that, the relative JT signs do not matter at all for the PJT active e'' vibrational mode. However, they do matter when we incorporate the PJT active a_1'' vibrational mode in the dynamical calculations. Therefore, we have estimated some more *ab initio* data points by simultaneously distorting the JT active and a_1'' vibrational modes. The

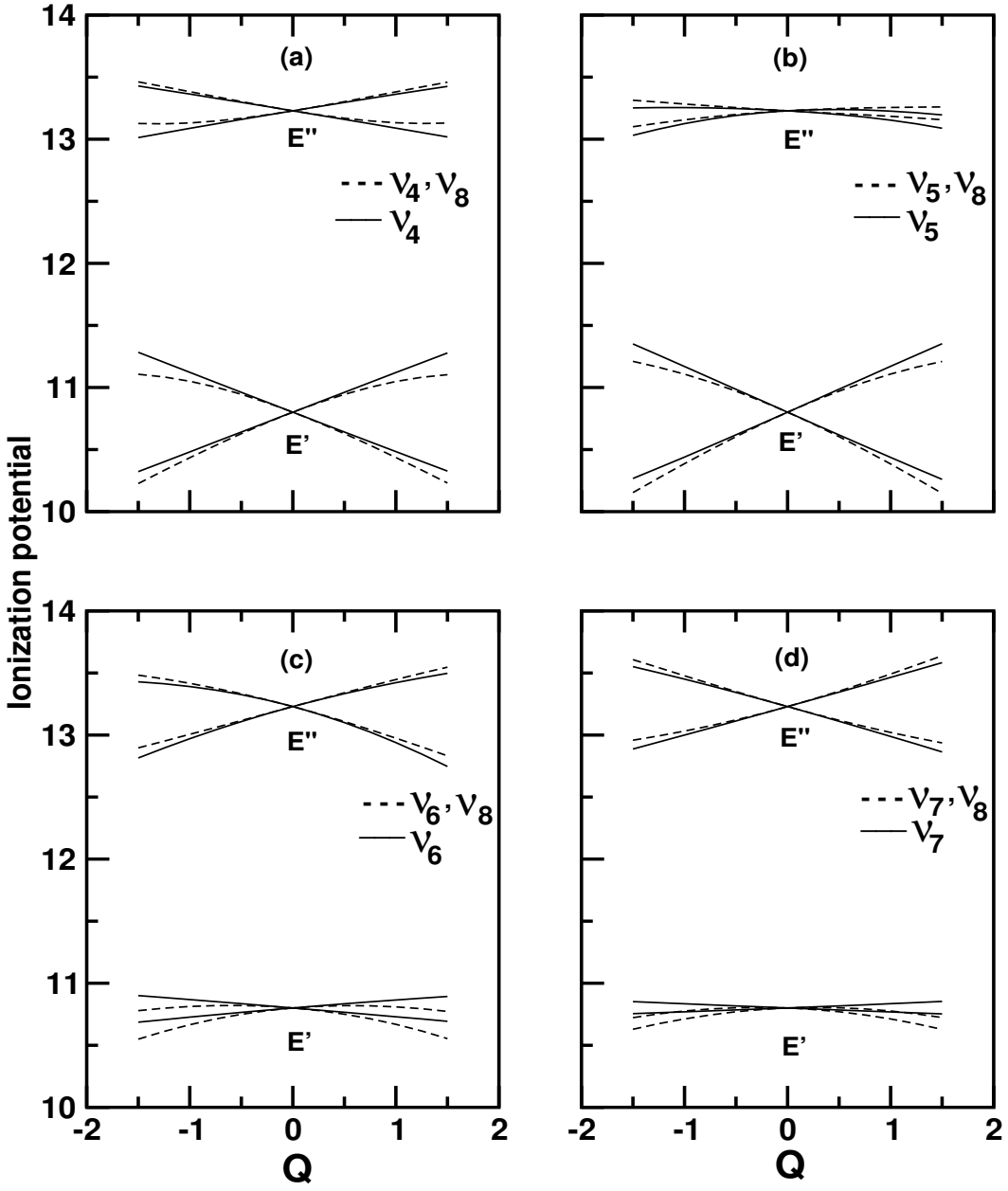

Figure 5.9: The adiabatic potential energies of the JT split $\widetilde{X}^2E'$ and $\widetilde{A}^2E''$ electronic states of CP^+ plotted along the dimensionless normal coordinates of the x components of the degenerate vibrational vibrational modes ν_4, ν_5, ν_6, and ν_7 in panel a, b, c, and d, respectively. The solid lines represent the *ab initio* data points for displacement along the degenerate e' vibrational modes, whereas the dashed lines represent the *ab initio* data points obtained by simultaneous distortion of e' and a_1'' vibrational modes. In order to have a clearer representation, the a_1'' displacements are kept as constants in these calculations.

relative JT signs can then be extracted from the observation, whether the two upper (as well as the two lower) JT sheets repel each other, or whether the upper E' sheet repels from the lower E'' sheet (and the lower E' sheet repels from the upper E'' sheet). In order to guide the eye properly, the a_1'' mode displacements are kept constant and then the *ab initio* data points are estimated. In Fig. 5.9(a-d), we have shown these data points by dashed lines superimposed on the JT active (ν_4-ν_7) potential energy curves by solid lines of the $\widetilde{X}^2E'$ and $\widetilde{A}^2E''$ electronic manifold of CP^+.

Given the above, we could identify a *clear* relative sign of the JT coupling constants only for the mode ν_4 (panel *a*), where it is *negative*, since the upper E' curve repels from the lower E'' curve and the lower E' repels from the upper E'' curve. For the other modes, the situation is less clear to us and it is difficult to extract a clear repulsion pattern from the curves.

5.4.2 Photoelectron Spectrum

In this section we report on the photoelectron bands revealing the vibronic energy level structure of the $\widetilde{X}^2E'$ and $\widetilde{A}^2E''$ electronic states of CP^+. These photoelectron bands are calculated by the time-independent and time-dependent quantum mechanical methods described above and using the parameters of Table 5.3 and Table 5.4. Consistencies of various theoretical results are explicitly checked whenever possible and the final theoretical results are compared with the experimental data [75]. The final theoretical results of this paper are, however, obtained by propagating wave packets using the MCTDH algorithm [53–55]. In the following, we start with various reduced dimensional models and systematically approach the full simulation of nuclear dynamics using the four states and fourteen modes Hamiltonian of Eqs. (5.4-5.7j).

5.4.2.1 The $\widetilde{X}^2E'$ photoelectron band

Here we report on the photoelectron band of the $\widetilde{X}^2E'$ electronic manifold of CP^+. The theoretical results are compared with the most recent experimental results of Holland *et al.* [75]. The experimental photoelectron band revealed a characteristic bimodal structure indicating a strong first-order JT splitting in the $\widetilde{X}^2E'$ electronic manifold of CP^+. The energetic separation between the two maxima in the bimodal profile is reported to be ~ 0.78 eV [75], which amounts to this JT splitting. A fairly resolved vibrational progression is observed in the low-energy wing of the bimodal spectral envelope, which becomes extremely diffuse with increasing energy. An average spacing of 60 meV is reported for the resolved structure at low-energies, which is mainly attributed to the progression of the degenerate vibrational mode ν_4 [75].

We in the following discuss this $\widetilde{X}^2E'$ photoelectron band of CP^+ calculated with the linear and QVC schemes. We again note that in absence of the bilinear and PJT coupling terms, the Hamiltonian is decoupled in terms of the symmetric (a_1') and degenerate (e') vibrational modes. We utilize this property of the Hamiltonian in our numerical calculations and calculate two partial spectra by considering the totally symmetric and degenerate vibrational modes separately in the nuclear dynamics. Finally, these two partial spectra are convoluted to generate the complete spectrum. This substantially reduces the effective dimensionality of the secular matrix in each calculation. Furthermore, we did not consider the degenerate vibrational mode ν_7 in the dynamics, as it has a very low coupling strength and causes only negligible splitting in the $\widetilde{X}^2E'$ electronic manifold (cf. Fig.5.8 (d)).

In Fig. 5.10(a) the spectrum obtained with three totally symmetric modes ν_1, ν_2, and ν_3 within the LVC scheme is shown. The spectral intensity in arbitrary units is plotted as a function of the energy of the final vibronic state (E'). For the symmetric modes, all nuclear motions decouple and the spectrum is obtained

Table 5.5: The number of harmonic oscillator (HO) basis functions along each vibrational mode, the dimension of the secular matrix, and the number of Lanczos iterations used to calculate the converged theoretical stick spectrum shown in various figures noted below.

No. of HO basis functions							Dimension of the secular matrix	Lanczos iterations	Figure(s)
ν_1	ν_2	ν_3	ν_4	ν_5	ν_6	ν_7			
8	20	3	-	-	-	-	960	1,500	5.10(a) & 5.12(a)
-	-	-	40	40	8	-	33,359,445	15,000	5.10(b), 5.12(b), & 5.13(b)
4	38	10	-	-	-	-	3,040	1,500	5.17(a) & 5.18(a)
-	-	-	23	2	22	5	51,207,200	15,000	5.17(b) & 5.18(b)

by convoluting the spectra of the individual one-dimensional oscillators. Each of the latter spectra can be expressed analytically and follow a Poisson distribution of intensity [17]. The resulting stick eigenvalue spectrum thus obtained is again convoluted with a Lorentzian line shape function of 20 meV fwhm to generate the spectral envelope. The same Lorentzian function is used to convolute all time-independent stick spectra shown below. In Table 5.5, the number of harmonic oscillator basis functions along the considered vibrational modes, the size of the secular matrix, and the number of Lanczos iterations used in computing the numerically converged spectra are given.

The spectrum reveals a dominant excitation of ν_1 and ν_2 modes, the first two peaks from the 0-0 line. These peaks are ~ 153 and ~ 190 meV spaced in energy, corresponding to the frequency of ν_1 and ν_2 modes, respectively, in the cationic ground state. The next three peaks correspond to the excitation $2\nu_1$, $\nu_1 + \nu_2$, and $2\nu_2$, respectively. The remaining high-energy peaks correspond to the excitation of higher quanta of ν_1 and ν_2 and to combination modes. The excitation of the ν_3 vibrational mode is negligibly small (the intensity is 10^3 times less than the 0-0 line) and is not visible in the spectrum. The peaks in the spectrum are weighted by the coupling strength, $\kappa_i'^2/2\omega_i^2$ (Poisson parameter), of the respective vibrational mode, which yields the intensity of the fundamental relative to the

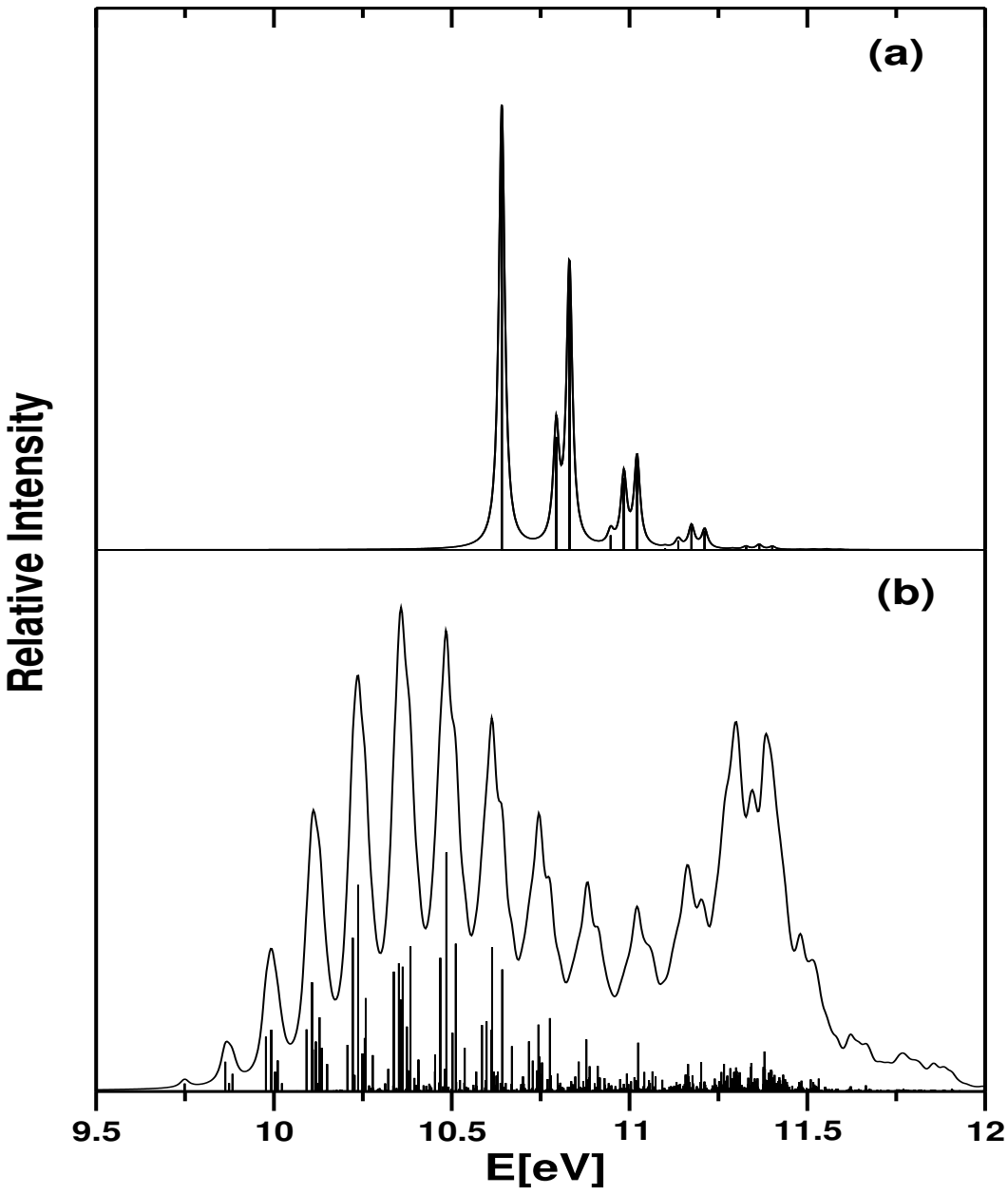

Figure 5.10: The photoelectron band of the $\widetilde{X}^2E'$ electronic manifold of CP^+ computed with three totally symmetric modes (ν_1-ν_3) and three degenerate (ν_4-ν_6) modes alone, within the LVC scheme, is shown in panel (a) and (b), respectively. Each theoretical stick spectrum is convoluted with the Lorentzian function of 20 meV fwhm to calculate the spectral envelope.

0-0 line.

In Fig. 5.10(b) the spectrum obtained with the degenerate vibrational modes ν_4, ν_5, and ν_6 and a LVC scheme is shown. The convergence of the stick spectrum is explicitly checked with respect to the size of the basis set as well as the number of Lanczos iteration steps. A careful inspection of the spectral intensity and the coupling strengths of the vibrational modes ν_4, ν_5, and ν_6 reveals dominant excitations of ν_4 and ν_5 modes in the spectrum. Line spacings of ~ 114, ~ 134, and ~ 184 meV corresponding to the excitation of ν_4, ν_5, and ν_6 vibrational modes can be observed from the spectrum. The latter is very weakly excited, which is also indicated by its extremely small coupling strength. The clumping of spectral lines under each peak and a huge line density is indicative of strong coupling JT effects due to the vibrational modes ν_4 and ν_5. This increases the line density in the spectrum, and for energies below ~ 11 eV leads to a long series of resonances corresponding to vibrational motion on the lower JT sheet $\mathcal{V}_1$. For energies above ~ 11 eV also $\mathcal{V}_2$ plays a role. The strong nonadiabatic effects, however, mix the discrete vibrational levels of $\mathcal{V}_2$ with the quasi-continuum levels of $\mathcal{V}_1$, and therefore, the nuclei undergo simultaneous transitions to both sheets of the JT split PES. The occurrence of higher energy maxima in the spectral envelope is thus explained to be due to the metastable resonances of the upper potential well. The latter is very narrow and extremely anharmonic and as a result its lowest levels are widely spaced in energy. These are showing up in the spectral envelope of Fig. 5.10(b) in the energy range above 11 eV: between $\sim$ 11 and 11.5 eV the resonance corresponds to the ground vibrational level of $\mathcal{V}_2$ while around 11.8 eV another structure becomes visible which represents the first excited vibrational level of $\mathcal{V}_2$. The broadening mechanisms are just the strong nonadiabatic coupling effects characteristic for JT intersections [38]. These are referred to as Slonczewski resonances and the existence of these resonances was demonstrated in several model $(E \times e)$-JT problems [6, 127, 128].

The complete photoelectron band of the electronic ground state of CP^+ ob-

tained with the LVC scheme is shown in Fig. 5.11(b) along with the experimental result of Holland *et al.* in Fig.5.11(a). The theoretical stick spectrum in Fig.5.11(b) is obtained by convoluting the two partial stick spectra in Figs. 5.10(a) and 5.10(b). Because of this convolution, the progression of the symmetric mode spectrum is represented on each JT line of Fig. 5.10(b). The resulting convoluted stick spectrum is then convoluted again with a Lorentzian function of 20 meV fwhm to generate the spectral envelope shown in Fig. 5.11(b). A comparison of this theoretical envelope with the experimental one in Fig. 5.11(a) reveals a very good overall agreement between the two. The overall width of the theoretical spectrum is in good accord with the experimental one. The splitting between the two maxima of the theoretical spectrum of ~ 0.80 eV compares well with its experimental value of ~ 0.78 eV. The progression in the low-energy wing of the envelope is mainly formed by the JT active ν_4 and ν_5 vibrational modes. The spacing between the successive peaks in the theoretical envelope is ~ 40 meV higher than its experimentally reported average value of ~ 60 meV. We, however, note that the experimental band is smoothed and it is not clear at this point if the line spacings are affected in this smoothening procedure. In fact, the structure present in the second maximum of the theoretical envelope is not seen in the experimental result. Apart from these discrepancies, the regularity in the low-energy progression is nicely reproduced by the theoretical result. When compared with the pure JT spectrum of Fig. 5.10(b), it can be seen that the symmetric vibrational modes cause additional broadening of the spectral envelope and some of the low-energy structures are quenched.

We now discuss the effect of second-order coupling on the above theoretical spectra. In Fig. 5.12 we show the two partial spectra obtained with the symmetric (panel a) and JT active (panel b) vibrational modes. The complete spectrum obtained by convoluting these two partial spectra is shown in Fig. 5.12(c). A close look at the quadratic symmetric mode spectrum in Fig. 5.12(a) reveals essentially no difference with that obtained with the linear coupling scheme (cf. Fig. 5.10(a)).

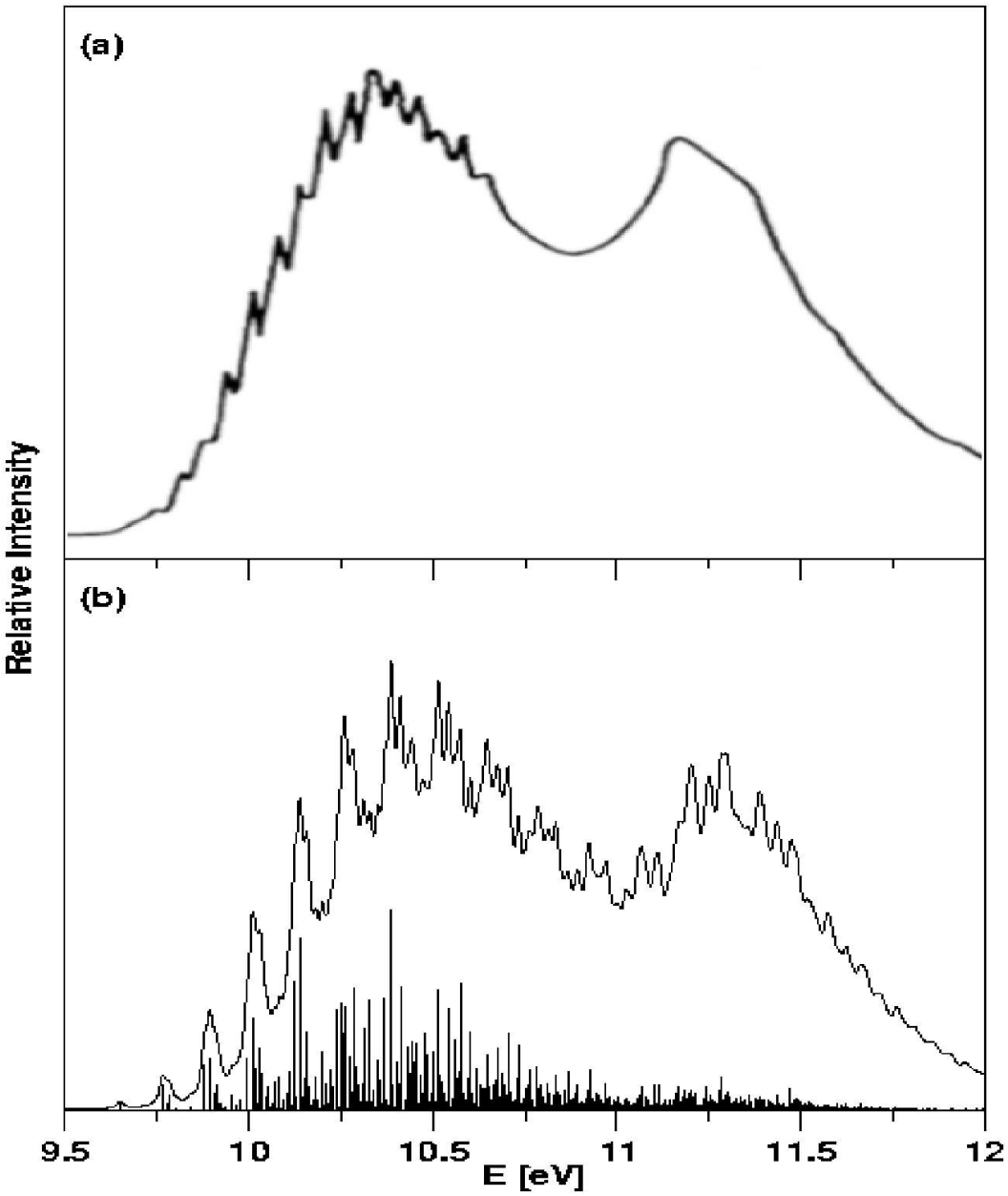

Figure 5.11: A comparison of the experimental [Ref. [75]] and final theoretical (of the LVC model) results for the $\widetilde{X}^2E'$ photoelectron band of CP^+. The theoretical stick spectrum is obtained by convoluting the two partial spectra of Figs. 5.10(a) and5.10(b). The resulting complete stick spectrum is again convoluted with a Lorentzian of 20 meV fwhm to calculate the spectral envelope. The theoretical spectrum is shifted by 0.062 eV to the higher energy along the abscissa in order to reproduce the adiabatic ionization position of the band at its experimental value.

The peaks are $\sim$ 152 and $\sim$ 192 meV spaced in energy corresponding to the frequencies of ν_1 and ν_2 vibrational modes modified by the respective second-order coupling terms (cf. Table 5.3).

The quadratic JT mode spectrum in Fig. 5.12(b), on the other hand, differs considerably from the linear one (cf. Fig. 5.10(b)). Each peak of the linear spectrum is further split in the quadratic coupling scheme. Because of the increase of the line density, the quadratic JT spectrum is somewhat more diffuse. The apparent regularity in the low-energy progression is lost in the quadratic JT spectrum. The higher-energy maxima appearing at 11.3 and 11.8 eV in Fig. 5.12(b), however, survive in the quadratic model. As discussed in relation to Fig. 5.10(b), these represent the first and second Slonczewski resonances. The above symmetric and the JT mode spectra are convoluted and the resulting composite spectrum is shown in Fig. 5.12(c). The overall appearance of the composite spectrum looks similar to the one obtained with the LVC scheme (cf. Fig. 5.11(b)).

In both cases, in particular, the second Slonczewski resonance at 11.8 eV is blurred by the convolution (cf. Fig. 5.11(b) with 5.10(b) and Fig. 5.12(c) with 5.12(b)) while the first one at 11.3 eV becomes broadened but still dominates the high-energy spectral profile. Thus, the first photoelectron band of CP represents a prominent example of such a resonance in an actual molecular JT spectrum. However, a more detailed analysis of the spectrum in Fig. 5.12(c) reveals a dramatic effect of the quadratic JT coupling parameters on the vibronic fine structure of the photoelectron band. To reveal this more clearly, we present in Fig. 5.13 an enlarged view of the low-energy part of Fig. 5.12(c) (in panel b) along with the experimental data (in panel a). A comparison of the two results indicates that the quadratic JT coupling does account for a lower value ($<$ 100 meV) of the average spacing of this low-energy progression. An average spacing of the order of $\sim$ 60 meV can be estimated from the QVC result.

To optimize various numerical parameters in the time-dependent WP calculations using the MCTDH scheme, we have simulated the $\widetilde{X}^2E'$ photoelectron band

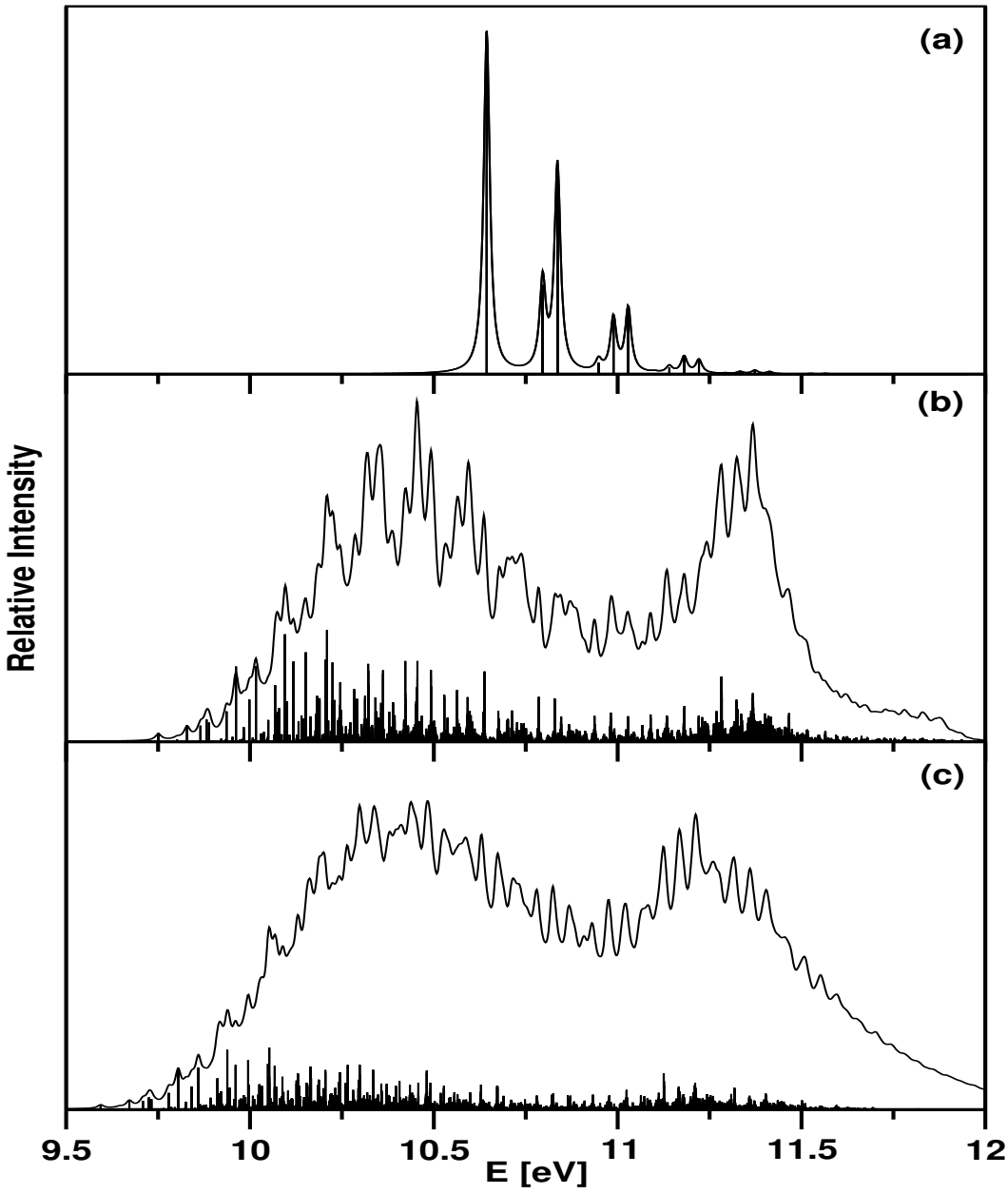

Figure 5.12: The photoelectron band of the $\widetilde{X}^2E'$ electronic manifold of CP^+ calculated with the quadratic coupling scheme (see text for details). The intensity in arbitrary units is plotted as a function of the energy of the final vibronic states. The spectrum calculated with the symmetric (ν_1-ν_3) modes and the JT (ν_4 - ν_7) modes alone is shown in panel (a) and (b), respectively. These two partial spectra of panels (a) and (b) are convoluted to generate the complete spectrum of panel (c). The theoretical stick spectrum of each panel is convoluted with the Lorentzian function of 20 meV fwhm to generate the corresponding spectral envelope. In order to have a clearer representation the stick spectra in panel (b) and (c) are magnified by a factor of 3.

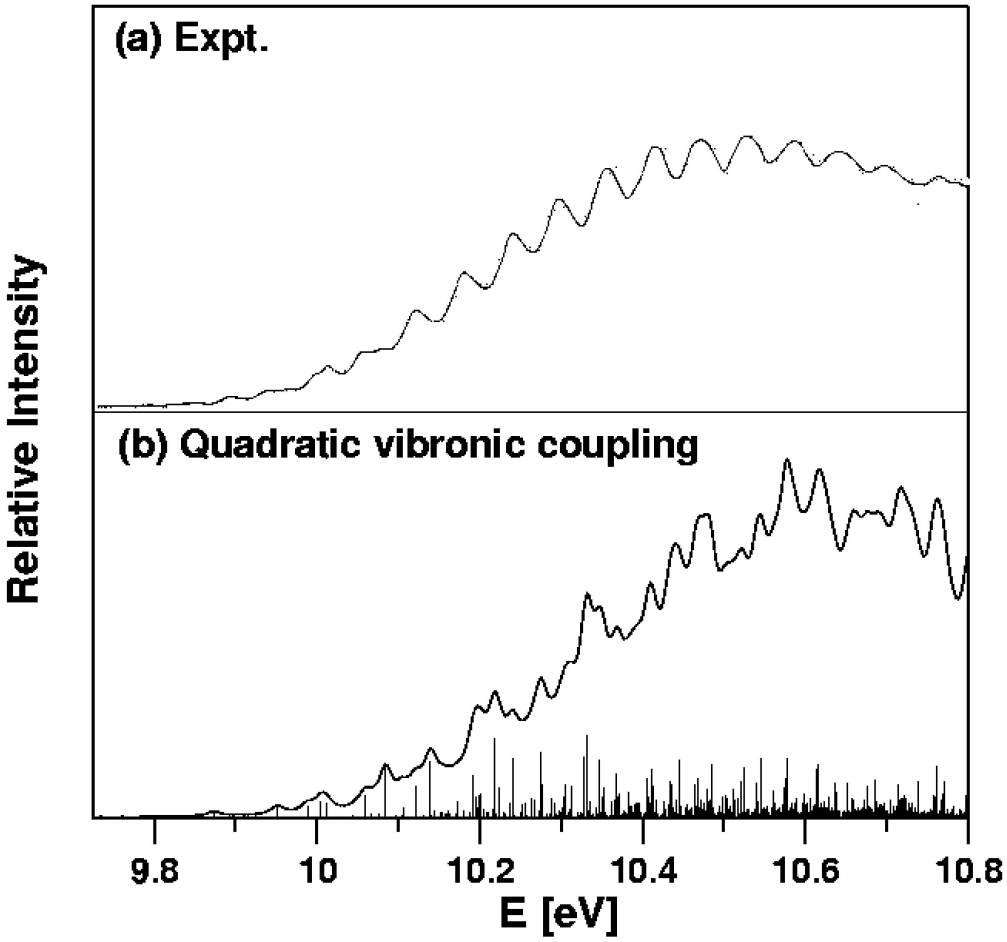

Figure 5.13: The low-energy wing of the $\widetilde{X}^2E'$ photoelectron band of CP^+. The experimental result of Holland *et al.* [75] is shown in panel (a). The theoretical result of Fig. 5.12(c) is reproduced in panel (b) in order to clearly reveal the impact of quadratic coupling terms on the low-energy progression in the band.

once again using the Hamiltonian developed in section 5.2 and compare the same with the time-independent results. In the time-dependent simulations, the linear vibronic Hamiltonian for the $\widetilde{X}^2E'$ electronic manifold is used considering the three totally symmetric Condon active (ν_1, ν_2 and ν_3) and three degenerate JT active (ν_4, ν_5 and ν_6) vibrational modes as it was done with the time-independent simulations [90]. These modes are found to be primarily important, and form the major progressions in the vibronic structure of the $\widetilde{X}^2E'$ photoelectron band. The combination of normal modes, the sizes of the primitive and SPF bases used for these calculations are given in the upper part of Table 5.6. A total of four multidimensional particles are used: Of these, particle 1 is three-dimensional and combines ν_1, ν_2, and ν_3 vibrational modes. The remaining three particles are two-dimensional and combine the x and y components of ν_4, ν_5, and ν_6 vibrational modes, respectively. The sizes of the primitive and SPF bases are selected in such a way that the calculations are converged with respect to the vibronic structure of the photoelectron band.

The photoelectron band thus obtained is shown in Fig. 5.14(a) along with the corresponding time-independent results in Fig. 5.14(b). The latter is essentially reproduced from Fig. 5.11(b). The theoretical spectrum in panel *a* represents a sum of contributions from the two JT split components (x and y) of the degenerate $\widetilde{X}^2E'$ electronic manifold. Each of these contributions is the Fourier transform of the time-autocorrelation function $C^m(t)$ computed with an initial WP located on the m^{th} electronic state (cf. Eq. (2.49)). The WP in each calculation is propagated for 150 fs, which effectively yields $C^m(t)$ up to 300 fs, using the prescription, $C^m(t) = \langle \Psi^m(t/2)^\star | \Psi^m(t/2) \rangle$, for a real initial WP [129]. This prescription helps to increase the energy resolution, $\Delta E = 2\pi\ \hbar/T$, in the spectrum by effectively doubling the propagation time T. A constant energy shift of -0.743 eV was applied while plotting the photoelectron band in Fig. 5.14(a) in order to match the energy ranges covered by the time-independent "stick" spectrum (cf. Fig. 5.14(b)). This, in turn, reproduces the adiabatic ionization position of

Table 5.6: The normal mode combinations, sizes of the primitive and the single particle basis used in the WP propagation using the MCTDH algorithm on the (a) $\widetilde{X}^2E'$ electronic manifold within the LVC scheme, (b) $\widetilde{A}^2E''$ electronic manifold within the QVC scheme and (c) $\widetilde{X}^2E'$-$\widetilde{A}^2E''$ coupled electronic manifold within the quadratic JT plus linear PJT coupling scheme. The CPU time required for each run is also given.

Normal modes[a]	Primitive basis[b]	SPF basis[c]	CPU time	Figure
		(a)		
		$[E'_x, E'_y]$[d]		
(ν_1, ν_2, ν_3)	(8, 20, 3)	[8, 8]	E'_x: 13h 41m 12s	
(ν_{4x}, ν_{4y})	(40, 40)	[30, 30]	E'_y: 13h 28m 21s	Fig. 5.14(a)
(ν_{5x}, ν_{5y})	(40, 40)	[30, 30]		
(ν_{6x}, ν_{6y})	(8, 8)	[10, 10]		
		(b)[e]		
		$[E''_x, E''_y]$		
(ν_1, ν_2, ν_3)	(4, 21, 7)	[8, 8]	E''_x: 14h 44m 50s	
(ν_{4x}, ν_{4y})	(23, 23)	[22, 22]	E''_y: 15h 06m 16s	Fig. 5.18(d)
(ν_{5x}, ν_{5y})	(6, 6)	[12, 12]		
(ν_{6x}, ν_{6y})	(22, 22)	[22, 22]		
(ν_{7x}, ν_{7y})	(8, 8)	[10, 10]		
		(c)[f]		
		$[E'_x, E'_y, E''_x, E''_y]$		
(ν_1, ν_2, ν_3)	(7, 23, 9)	[10, 10, 5, 5]	E'_x: 126h 15m 26s	
(ν_{4x}, ν_{4y})	(40, 40)	[22, 22, 17, 17]	E'_y: 136h 03m 02s	Fig. 5.20(b)
(ν_{5x}, ν_{5y})	(40, 40)	[22, 22, 16, 16]	E''_x: 82h 14m 32s	
$(\nu_{6x}, \nu_{6y}, \nu_8)$	(12, 12, 19)	[14, 14, 15, 15]	E''_y: 116h 31m 02s	
$(\nu_{7x}, \nu_{7y}, \nu_{9x}, \nu_{9y})$	(5, 5, 8, 8)	[13, 13, 11, 11]		

The calculations were converged with respect to the spectrum. [a]Vibrational modes bracketed together were treated as a single particle, e.g., particle 1 is a 3-dimensional particle including modes ν_1, ν_2, and ν_3. [b] The primitive basis is the number of harmonic oscillator DVR functions, in the dimensionless coordinate system required to represent the system dynamics along the relevant mode. Here we note that the number of basis functions are identical in both the time-independent (cf. Table 5.5) and time-dependent calculations. The primitive basis for each particle is the product of the one-dimensional bases; e.g for particle 2 in (a), the primitive basis was 40 × 40 = 1600 functions. The full primitive basis consists of a total of 7.86 $\times 10^{10}$ functions. [c] The SPF basis is the number of single-particle functions used, one set for each of the two electronic (component) states. Here they are same in numbers in order to give equal weight for the x and y components of the degenerate electronic states. [d] The total number of configurations is 144 000. [e] The full primitive basis consists of a total of 3.46 $\times 10^{11}$ functions and there are 929 280 configurations altogether. [f] The full primitive basis consists of a total of 1.62 $\times 10^{16}$ functions and there are 2 210 560 configurations altogether.

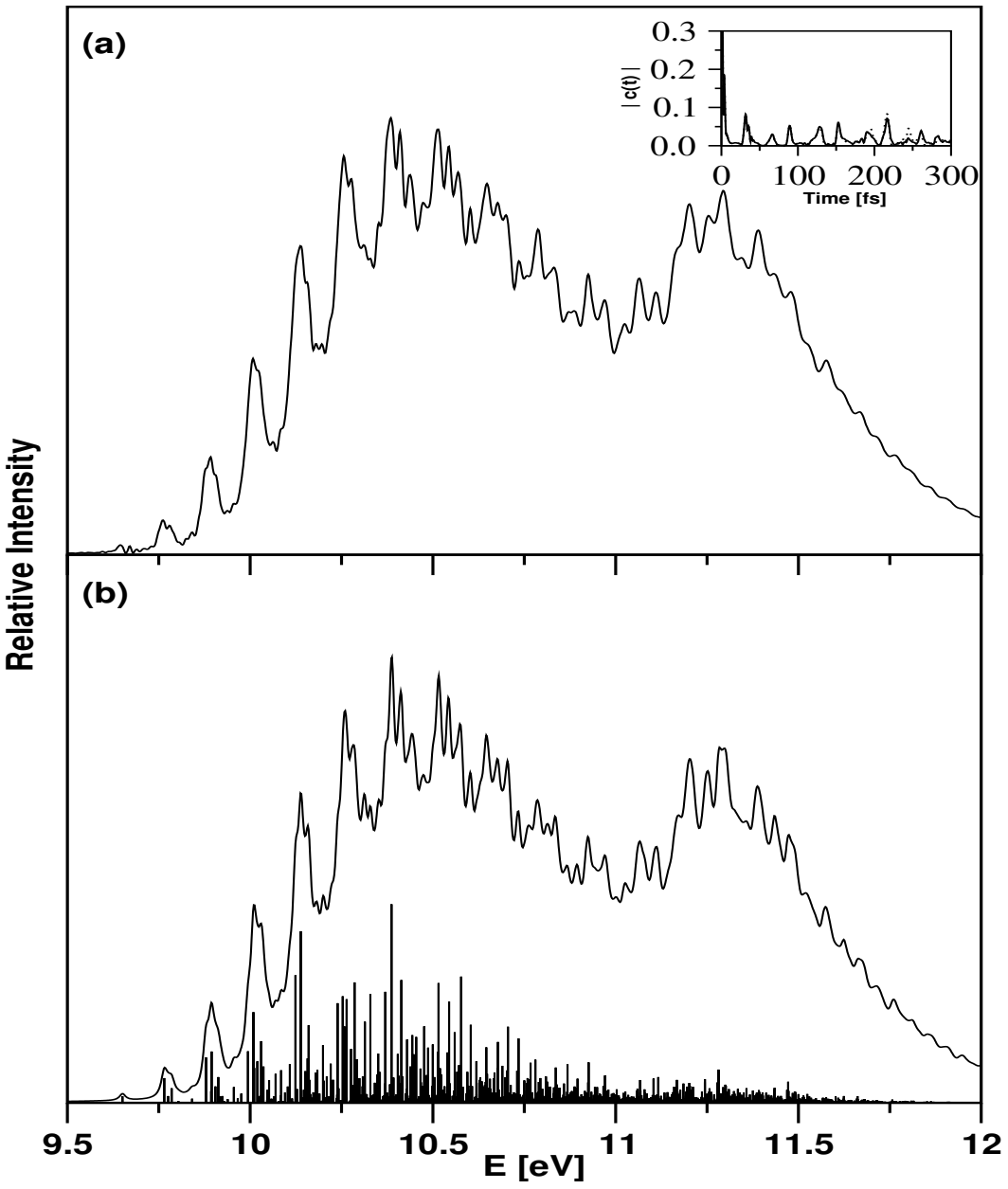

Figure 5.14: The first photoelectron band of CP revealing the vibronic level structure of the $\widetilde{X}^2E'$ electronic manifold of CP^+. The intensity in arbitrary units is plotted as a function of the energy of the final vibronic state. The energy is measured relative to the zero-point level of the electronic ground state of CP. The photoelectron band obtained by the wave packet propagation method within the MCTDH scheme considering a two-state six-mode model is shown in panel *a*. The absolute values of the time autocorrelation functions $|C(t)|$ computed by locating the initial wave packet separately on the two component states of the $\widetilde{X}^2E'$ electronic manifold are plotted in the insert of panel *a* and are shown by the solid and dotted lines. The corresponding results obtained by the time-independent matrix diagonalization method are essentially reproduced from Ref. [90] (see text) and shown in panel *b*.

the band at its experimental value along the abscissa [90]. The overall width and the tiny structures of both the spectral envelopes are in very good agreement with each other over the entire energy range. The splitting between the two maxima in the bimodal intensity distribution in Fig. 5.14(a) is ~ 0.81 eV and compares well with the time-independent (cf. Fig. 5.14(b)) and experimental results of ~ 0.80 eV and ~ 0.78 eV, respectively.

To account for the finite broadening of the experimental spectra due to poor energy resolution of the spectrometer and also due to the possible role of additional degrees of freedom (like rotation) not considered here, the stick vibronic spectrum is convoluted with a suitable line-shape function of appropriate width. In the time-dependent picture, the latter is equivalent to damping the autocorrelation function by a time-dependent function. By a careful choice of this function, one can minimize the artifacts due to the finite length of propagation time. In the following, all spectra resulting from the time-dependent calculations are obtained by damping the corresponding autocorrelation functions by the time-dependent function

$$F(t) \;=\; cos\left(\frac{\pi t}{2T}\right), \tag{5.24}$$

with T being the total length of the time propagation. As t $\rightarrow T$, $F(t)C(t) \rightarrow 0$ and therefore the artifacts due to finite time Fourier transformation are reduced. Multiplying $C(t)$ with $F(t)$ is equivalent to convoluting the spectrum with the Fourier transform of $F(t)$, which in this case reads [110]

$$\widetilde{F}(\omega) \;=\; \frac{4\pi T}{\pi^2 - (2\omega T)^2} cos(\omega T), \tag{5.25}$$

with a fwhm of $\Gamma = 3.4/\mathrm{T}$. Further phenomenological broadening, due to the spectral resolution and neglect of the other degrees of freedom, is added by the

function

$$G(t) \;=\; exp\left(\frac{-t}{\tau_r}\right), \tag{5.26}$$

with τ_r being the relaxation time. This leads to a Lorentzian broadening of the spectrum with fwhm $\Gamma = 2/\tau_r$. In Fig. 5.14(a) the vibronic spectrum of the $\widetilde{X}^2E'$ electronic manifold is obtained by damping the autocorrelation function with $\tau_r = 66\ fs$ ($\Gamma \approx 20$ meV). The same damping is used in all later spectra presented here.

In Figs. 5.15(a-c) the photoelectron band for the $\widetilde{X}^2E'$ electronic manifold up to the QVC scheme is shown at different levels of approximation. The photoelectron band of panel *a* is reproduced from Fig. 5.12(c), which was obtained by a time-independent matrix diagonalization approach using the Lanczos algorithm and without the bilinear coupling terms of Table 5.4. This is included here in order to check the consistency of the present WP propagation results using the MCTDH algorithm [53–55]. The latter are shown in panel *b* (without the bilinear coupling terms) and panel *c* (with the bilinear coupling terms). The details of the mode combinations, sizes of the primitive and SPF bases used in the MCTDH simulations are given in Table 5.7(a). The theoretical spectrum shown in panels *b* and *c* represents a sum of contributions from the two JT split components (x and y) of the degenerate $\widetilde{X}^2E'$ electronic manifold. Each of these contributions is the Fourier transform of the corresponding time autocorrelation function $C^m(t)$ computed with an initial WP located on the respective electronic (component) states and propagated up to 150 fs.

A constant energy shift of -0.793 eV was applied while plotting the photoelectron bands in Figs. 5.15(b) and 5.15(c) in order to match the energy ranges covered by the time-independent "stick" spectrum (cf. Fig. 5.15(a)). This in turn reproduces the adiabatic ionization position of the band at its experimental value along the abscissa [90]. It can be seen from Fig. 5.15 that the WP results of panel

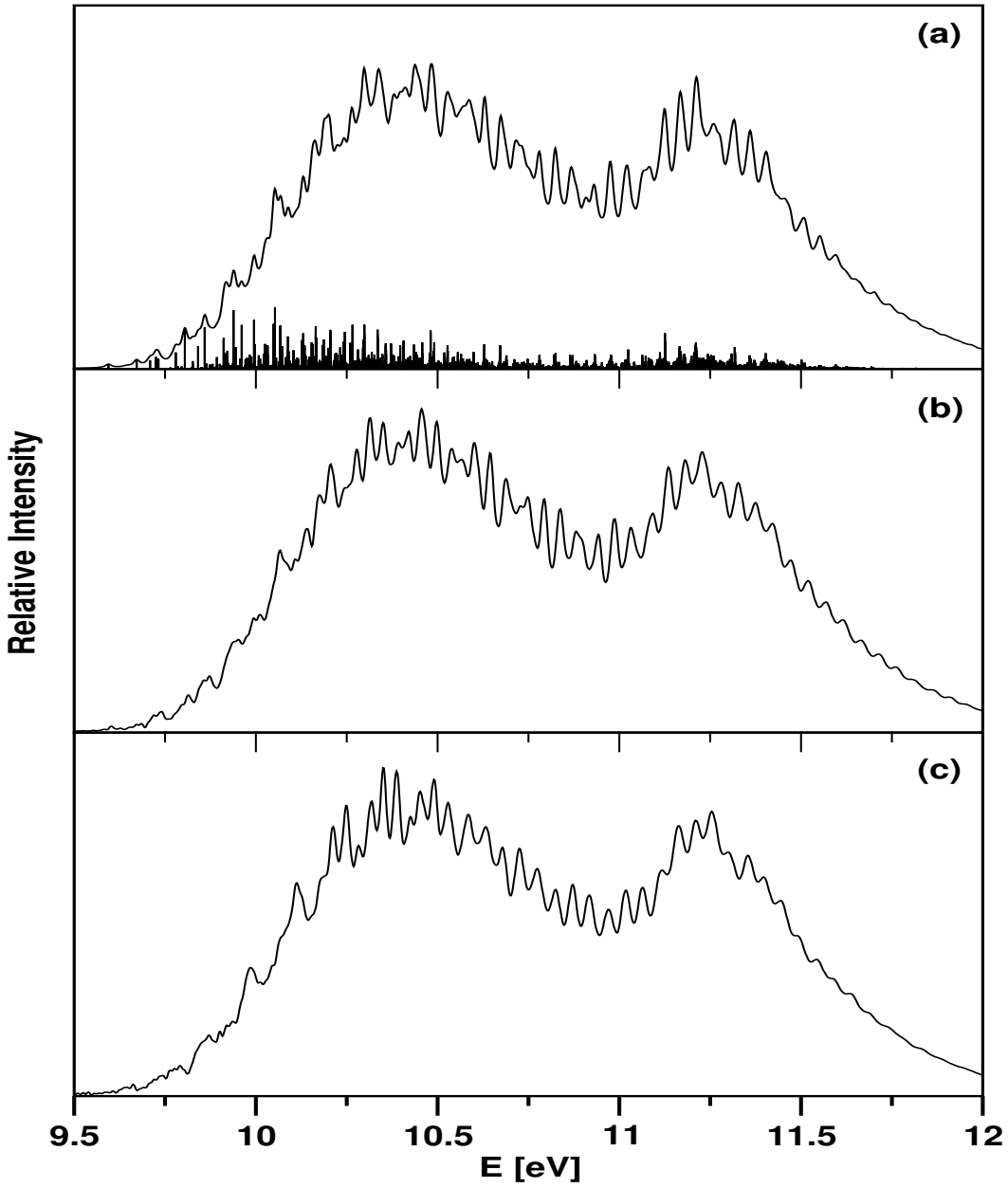

Figure 5.15: The first photoelectron band of CP, pertaining to an ionization to the $\widetilde{X}^2E'$ electronic manifold of CP^+, calculated with the quadratic vibronic coupling model. The results obtained from the time-independent matrix diagonalization approach are reproduced from Fig. 5.12(c) and shown in panel *a*. The present WP dynamical results without and with the intermode bilinear coupling terms are shown in panels *b* and *c*, respectively.

b are in very good accord with the time-independent results of panel a. There is an important difference immediately noticed between the two spectra in panels b and c: the vibronic structure in the low-energy wing is substantially modified by the bilinear intermode (particularly the bilinear a_1'-e' JT coupling) terms. Such an effect of the bilinear JT coupling terms has been discovered recently in other $(E\otimes e)$-JT systems [130,131]. The e'-e' bilinear coupling terms on the other hand are of the order of 10^{-3} or less (cf. Table 5.4). These are not expected to contribute noticeably to the spectrum and therefore are not included in the present calculations.

5.4.2.2 The $\widetilde{A}^2E''$ photoelectron band

To unravel the complex vibronic structure of the second photoelectron band of CP, we here treat the nuclear dynamics systematically in the isolated $\widetilde{A}^2E''$ electronic manifold first and then finally for the coupled $\widetilde{X}^2E'$-$\widetilde{A}^2E''$ electronic states of CP^+. The second photoelectron band at ~ 13 eV, attributed to the vibronic structure of $\widetilde{A}^2E''$ electronic manifold of CP^+, is essentially structureless (cf. Fig. 5.1). To reveal the coupling effects of various vibrational modes on the vibronic fine structure of this band, we first examine the nuclear dynamics employing the linear and the quadratic coupling scheme, separately in the $\widetilde{A}^2E''$ electronic manifold alone. For this purpose we used the time-independent matrix diagonalization scheme to solve the eigenvalue equation (cf. Eq. (2.45)) in order to find the precise locations of the vibronic energy levels. The simulation of the nuclear dynamics in the coupled $\widetilde{X}^2E'$-$\widetilde{A}^2E''$ electronic states is more involved and computationally unfeasible with the matrix diagonalization approach and is therefore carried out by the WP propagation approach using the MCTDH scheme.

It is mentioned in Sec. 5.1 that the $\widetilde{X}^2E'$ and $\widetilde{A}^2E''$ electronic states can couple together via the PJT active a_1'' and e'' vibrational modes. The minimum of the seam of PJT crossings occurs below/above the minimum of the JT conical intersections in the $\widetilde{A}^2E''/\widetilde{X}^2E'$ electronic states. The intersections of JT split

Table 5.7: The normal mode combinations, sizes of the primitive and the SPFs used in the WP propagation using the MCTDH algorithm on the (a) $\widetilde{X}^2E'$ electronic manifold with (Fig. 5.15(c)) and without (Fig. 5.15(b)) the intermode coupling terms, (b) $\widetilde{A}^2E''$ electronic manifold with the intermode coupling terms and (c) $\widetilde{X}^2E'$-$\widetilde{A}^2E''$ coupled electronic manifold within the full second-order JT (including intermode) plus linear PJT coupling scheme. The CPU time required for each run is also given.

Normal modes	Primitive basis	SPF basis	CPU time	Figure(s)
	(a)[d]			
		[E'_x, E'_y]		
(ν_1, ν_2, ν_3)	(8, 20, 3)	[8, 8]	E'_x: 17h 13m 35s[g]	
(ν_{4x}, ν_{4y})	(40, 40)	[30, 30]	E'_y: 17h 12m 41s[g]	5.15(b) & (c)
(ν_{5x}, ν_{5y})	(40, 40)	[30, 30]		
(ν_{6x}, ν_{6y})	(8, 8)	[10, 10]		
	(b)[e]			
		[E''_x, E''_y]		
(ν_1, ν_2, ν_3)	(4, 21, 7)	[8, 8]	E''_x: 37h 01m 44s[g]	
(ν_{4x}, ν_{4y})	(23, 23)	[22, 22]	E''_y: 39h 03m 40s[g]	5.19
(ν_{5x}, ν_{5y})	(6, 6)	[12, 12]		
(ν_{6x}, ν_{6y})	(22, 22)	[22, 22]		
(ν_{7x}, ν_{7y})	(8, 8)	[10, 10]		
	(c)[f]			
		[E'_x, E'_y,E''_x, E''_y]		
(ν_1, ν_2, ν_3)	(6, 21, 8)	[8, 8, 5, 5]	E'_x: 73h 25m 58s[g]	
(ν_{4x}, ν_{4y})	(38, 38)	[20, 20, 14, 14]	E'_y: 19h 46m 05s[h]	5.21(b)
(ν_{5x}, ν_{5y})	(38, 38)	[20, 20, 14, 14]	E''_x: 32h 01m 32s[h]	
(ν_{6x}, ν_{6y}, ν_8)	(12, 12, 19)	[8, 8, 10, 10]	E''_y: 42h 31m 19s[h]	
(ν_{7x}, ν_{7y}, ν_{9x}, ν_{9y})	(5, 5, 8, 8)	[11, 11, 9, 10]		

[d] The full primitive basis consists of a total of 7.86 $\times 10^{10}$ functions. The total number of configurations is 144 000. [e] The full primitive basis consists of a total of 3.46 $\times 10^{11}$ functions and there are 929 280 configurations altogether. [f] The full primitive basis consists of a total of 9.20 $\times 10^{15}$ functions and there are 749 400 configurations altogether. [g] Calculations are done on a 3.00 GHz processor Linux machine. [h] Calculations are done on a 3.20 GHz processor Linux machine.

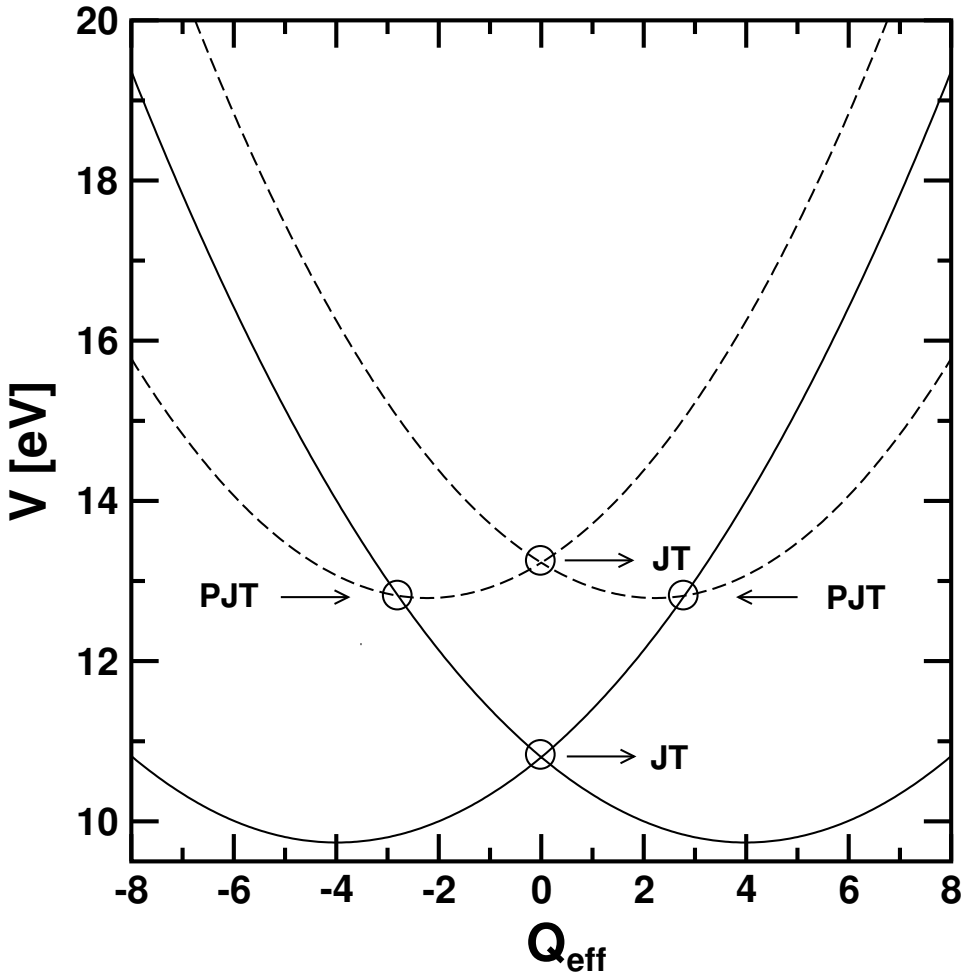

Figure 5.16: Schematic drawing of the JT and PJT conical intersections in the $\widetilde{X}^2E'$-$\widetilde{A}^2E''$ coupled electronic manifold of CP. The potential energies of the JT split components of the $\widetilde{X}^2E'$ (solid lines) and $\widetilde{A}^2E''$ (dashed lines) are plotted along the dimensionless normal coordinate of an effective vibrational mode (see text for further details). They appear as curve crossings and are marked by open circles in the diagram.

components of the $\widetilde{X}^2E'$-$\widetilde{A}^2E''$ electronic manifold are schematically shown in Fig. 5.16. In this drawing, the potential energies of these component electronic states are plotted as a function of the dimensionless normal coordinates of an effective vibrational mode. The latter is constructed individually for the $\widetilde{X}^2E'$ and $\widetilde{A}^2E''$ electronic states by combining the highly excited a_1' and e' vibrational modes in those states. From Table 5.3 it can be seen that the coupling strengths of the ν_2, ν_4, and ν_5 vibrational modes in the $\widetilde{X}^2E'$ electronic manifold and that of the ν_2, ν_4, and ν_6 vibrational modes in the $\widetilde{A}^2E''$ electronic manifold are significant. Therefore, the mentioned vibrational modes are considered within the respective electronic states and the effective first-order coupling constant, $\kappa_{eff} = \sqrt{\sum_i \kappa_i^2}$, and effective vibrational frequency, $\omega_{eff} = \sum_i \omega_i \kappa_i^2 \ / \kappa_{eff}^2$, for the effective mode are calculated. Therefore, in the schematic diagram of Fig. 5.16, the effective mode for the $\widetilde{X}^2E'$ electronic manifold consists of ν_2, ν_4, and ν_5 and that for the $\widetilde{A}^2E''$ electronic manifold consists of ν_2, ν_4, and ν_6 vibrational modes. The crossings of the PESs in Fig. 5.16, become multidimensional CIs in the multidimensional space of a_1' and e' vibrational modes. Therefore, a WP initially excited to one component of the $\widetilde{A}^2E''$ electronic manifold would approach these multiple multidimensional CIs and the resulting nuclear motion is expected to be highly nonadiabatic. In the following, we save some space to discuss this nonadiabatic transition of the nuclear WP to the component electronic states of the $\widetilde{X}^2E'$-$\widetilde{A}^2E''$ electronic manifold by examining the time evolution of a WP initially prepared on the $\widetilde{A}^2E''$ electronic manifold.

The $\widetilde{A}^2E''$ photoelectron band is calculated with the linear and also the QVC scheme in absence of the PJT coupling with the $\widetilde{X}^2E'$ electronic manifold. In Fig. 5.17(a) the partial spectrum obtained with the three totally symmetric a_1' vibrational modes ν_1, ν_2, and ν_3 within the LVC scheme is shown. The spectral intensity in arbitrary units is plotted as a function of the energy of the final vibronic state. A careful analysis of the spectrum reveals dominant excitation of the ν_2 vibrational mode. The excitation of the ν_3 vibrational mode is weaker. The

vibrational mode ν_1 on the other hand does not reveal any noticeable excitation. Relatively strong excitation of the ν_2 vibrational mode compared to ν_1 and ν_3 was also observed in the $\widetilde{X}^2E'$ photoelectron band [90]. However, ν_1 is the weakest mode in the $\widetilde{A}^2E''$ electronic manifold in contrast to ν_3 in the $\widetilde{X}^2E'$ electronic manifold. The peaks in the spectrum in Fig. 5.17(a) are $\sim$ 190 meV and $\sim$ 396 meV spaced in energy and correspond to the frequency of the ν_2 and ν_3 vibrational modes, respectively. In Table 5.5, the number of harmonic oscillator basis functions along the considered vibrational modes, the size of the secular matrix and the number of Lanczos iterations used in computing the numerically converged spectra are given.

The spectrum obtained with the JT active vibrational modes ν_4, ν_5, ν_6 and ν_7 within the linear coupling scheme is shown in Fig. 5.17(b). A convolution of the symmetric mode spectrum of Fig. 5.17(a) and the JT spectrum of Fig. 5.17(b) is presented in Fig. 5.17(c). The JT spectrum in Fig. 5.17(b) reveals dominant excitation of the ν_4 and ν_6 vibrational modes. The excitation strength of these two vibrational modes are almost the same (cf. Table 5.3). Peak spacings of $\sim$ 122, $\sim$ 137, $\sim$ 187, and $\sim$ 397 meV can be observed in the spectrum and they correlate with the frequencies of the ν_4, ν_5, ν_6, and ν_7 vibrational modes, respectively. The excitation of the ν_5 and ν_7 vibrational modes, however, is much weaker compared to that for ν_4 and ν_6. We note that the JT coupling strengths of the e' vibrational modes in the $\widetilde{A}^2E''$ electronic manifold are much weaker compared to those in the $\widetilde{X}^2E'$ electronic manifold. The JT coupling of the ν_4 and ν_5 vibrational modes in the latter electronic manifold is quite strong, and therefore, a distinct bimodal intensity distribution is observed for the first photoelectron band of CP. The dominant excitations in the convoluted composite spectrum of Fig. 5.17(c) are therefore due to the ν_2, ν_3, ν_4, and ν_6 vibrational modes. When compared with the experimental band shown in Fig. 5.1, it can be seen that the linear coupling approach is not at all adequate to reproduce the highly diffuse structure of the second photoelectron band of CP.

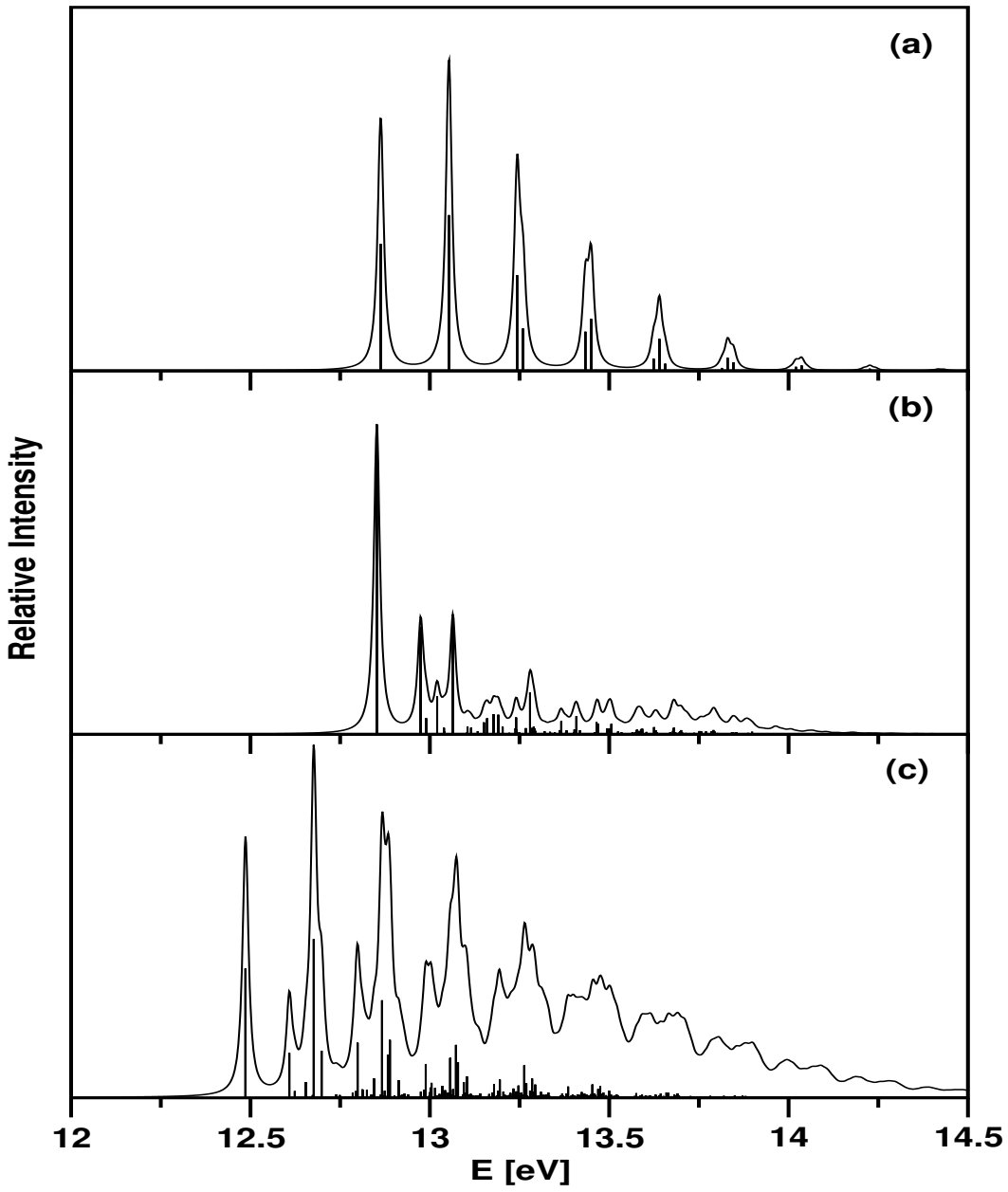

Figure 5.17: The second photoelectron band of CP pertaining to an ionization to the $\widetilde{A}^2E''$ electronic manifold of CP^+ calculated within the LVC scheme: (a) partial spectrum obtained with the three symmetric a_1' vibrational modes ν_1-ν_3, (b) partial spectrum obtained with the four JT active degenerate e' vibrational modes ν_4-ν_7 and (c) the composite theoretical spectrum obtained by convoluting the above two partial spectra. The stick vibronic spectrum of each panel is convoluted with a Lorentzian function of 20 meV fwhm to generate the spectral envelope.

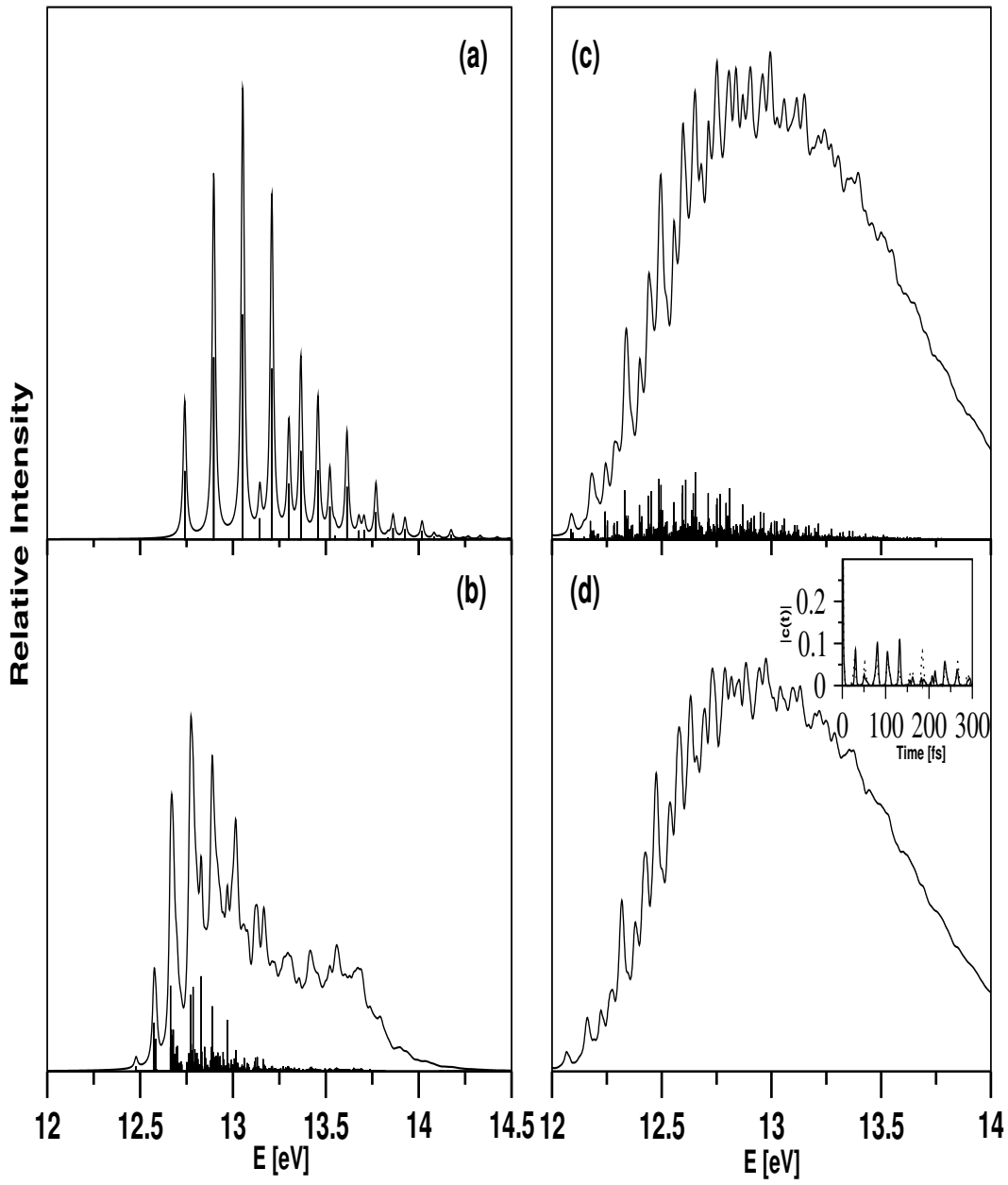

Figure 5.18: Panels (a-c): same as in Figs. 5.17(a-c), obtained with the QVC model. Panel (d): the results obtained by the wave packet propagation method within the MCTDH scheme, using the same quadratic vibronic Hamiltonian for the $\widetilde{A}^2E''$ electronic manifold as employed above. The absolute value of the time autocorrelation function, $|C(t)|$, computed by locating the initial wave packet separately on the two component states of this degenerate electronic manifold is shown by the solid and dotted lines in the insert.

The effect of the second-order coupling terms of the Hamiltonian on the vibronic structure of the above photoelectron band is shown in Fig. 5.18(a-c). The two partial spectra computed separately with the a_1' and e' vibrational modes are shown in panels a and b, respectively, and a convolution of the two is shown in panel c. In comparison with the linear coupling spectra of Figs. 5.17(a-c), the second-order coupling terms, in general, cause an increase of the spectral line density. The dominant progression in the composite spectrum of Fig. 5.18(c) is mainly caused by the ν_2, ν_4, and ν_6 vibrational modes. It can be seen that the quadratic JT coupling terms significantly increase the spectral line density and, as a result, the spectral envelope becomes broad and diffuse and it resembles more closely the experimental envelope (cf. Fig. 5.1) when compared to the linear coupling results (cf. Fig. 5.17(c) and Fig. 5.18(c)). In Fig. 5.18(d) the same photoelectron band is shown as obtained by propagating wave packets within the MCTDH scheme. The spectrum in Fig. 5.18(d) is obtained by combining two partial spectra calculated by locating the initial WP on the x and y component of the $\widetilde{A}^2E''$ electronic manifold separately. The time dependence of the autocorrelation function, $|C(t)|$, for these two initial conditions are shown as an inset in Fig. 5.18(d), by the solid and dotted lines. The details of the mode combinations and the size of various bases used in the WP propagation are given in Table 5.6(b). It can be seen from the inset of Fig. 5.18(d) that the time period of the quasi-periodic oscillations in $|C(t)|$ remains the same; however, their amplitude differs for the two initial conditions. The damping time (66 fs) of autocorrelation function in Fig. 5.18(d) corresponds to the convolution width (20 meV fwhm Lorentzian function) of the spectrum in Fig. 5.18(c). The vibronic fine structure of the time-dependent spectrum of panel d is virtually in perfect accord with the time-independent results of panel c.

In Fig. 5.19 the photoelectron band for the $\widetilde{A}^2E''$ electronic manifold considering the full quadratic vibronic Hamiltonian including the bilinear a_1'-a_1' and a_1'-e' coupling terms is shown. The WP propagation is carried out using the

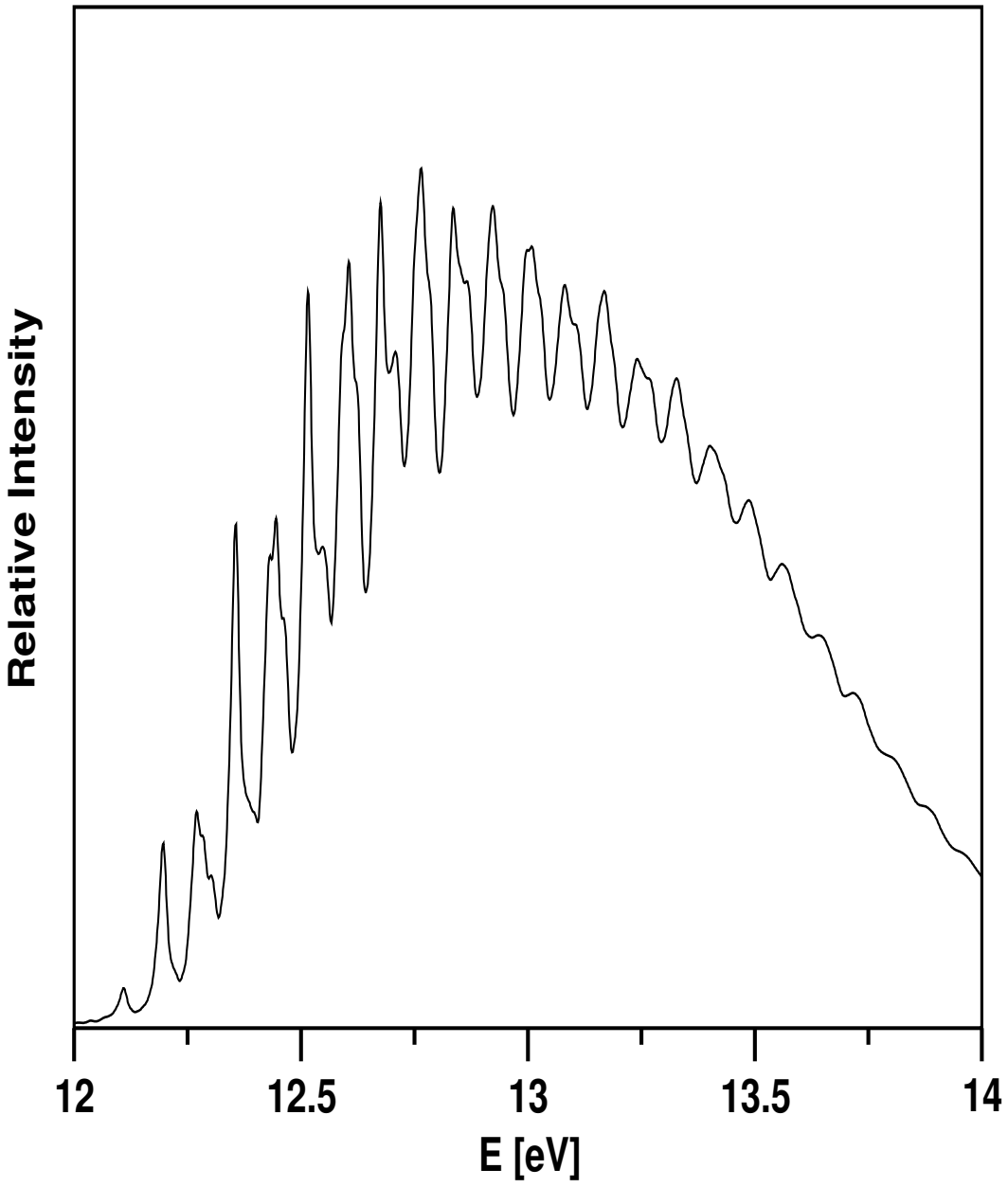

Figure 5.19: The second photoelectron band of CP, pertaining to an ionization to the $\widetilde{A}^2E''$ electronic manifold of CP^+, calculated in the same way as in Fig. 5.15(c).

MCTDH algorithm, and the details of the primitive and SPF bases are given in Table 5.7(b). Other numerical details of the calculations are the same as described above. In contrast to the experimental results (cf. Fig. 5.1), the theoretical band in Fig. 5.19 contains too many resolved vibronic structures. Therefore, the PJT coupling between the $\widetilde{X}$-$\widetilde{A}$ electronic states is considered in the final theoretical simulations.

5.4.2.3 The coupled $\widetilde{X}^2E'$-$\widetilde{A}^2E''$ photoelectron band

So far we did not include the PJT coupling due to the a_1'' and e'' vibrational modes in the calculations. When these coupling terms are considered in the Hamiltonian, the separability of the Hamiltonian in terms of the symmetric and degenerate vibrational modes as explored above no longer exists. It is therefore necessary to simulate the nuclear dynamics on four component electronic states of the coupled $\widetilde{X}^2E'$-$\widetilde{A}^2E''$ electronic manifold simultaneously including all relevant vibrational degrees of freedom. As mentioned before, this task is computationally impracticable by the time-independent matrix diagonalization approach.

The complete photoelectron band that represents the final results is therefore simulated by propagating wave packets using the MCTDH program package [53], including four electronic states and fourteen relevant vibrational degrees of freedom. Four WP propagations are carried out separately by locating the initial WP on each of the component electronic states of the coupled $\widetilde{X}^2E'$-$\widetilde{A}^2E''$ electronic manifold. The fourteen vibrational degrees of freedom are grouped into five particles, out of which one is four dimensional, two are three-dimensional, and the remaining two are two-dimensional. The detailed combination scheme of the vibrational modes is given in Table 5.6(c) along with the sizes of the primitive and SPF bases. These parameters are optimally chosen to ensure the numerical convergence of the photoelectron band. The WP for each initial location is propagated for 150 fs, which leads to $\sim$ 13.7 meV energy resolution in the photoelectron band. The final theoretical results are shown in panel b of Fig. 5.20

along with the experimental results in panel *a*. The final theoretical spectrum of panel *b* represents a combination of the partial spectra obtained for four different initial conditions stated above. The relative intensity in arbitrary units is plotted as a function of the energy of the final vibronic state. It can be seen from Fig. 5.20 that the theoretical results compare extremely well with the experiment. We note that to generate the partial spectra the autocorrelation functions are damped with $\tau_r = 66\ fs$ (≈ 20 meV) before Fourier transformation.

The theoretical results in Fig. 5.20(b) when compared with the results of Fig. 5.18(c-d) discussed above immediately reveal the strong impact of the PJT coupling on the vibronic structure of both the photoelectron bands. The vibronic structure of the second band is perturbed starting from its origin. This is because the minimum of the seam of PJT conical intersections occurs ~ 0.638 eV below that of the $\widetilde{A}^2E''$ JT conical intersections. The PJT coupling of the two degenerate electronic states causes a huge increase in spectral line density - the almost continuum levels of the $\widetilde{X}^2E'$ electronic manifold mix with the low-lying vibronic levels of the $\widetilde{A}^2E''$ electronic manifold. This mixing of levels of two different vibronic symmetries causes the increase in the spectral line density. As a result, the second maximum due to the JT split upper adiabatic cone of the $\widetilde{X}^2E'$ electronic manifold of the first photoelectron band and the entire second photoelectron band becomes moderately and extremely diffuse and structureless, respectively. Despite a good overall agreement between theory and experiment, there are remaining minor discrepancies in the finer details of the two. For example, the overall widths of the second maximum of the first band and the second band are somewhat narrow compared to the experimental results. These minor discrepancies may be attributed to the inadequate energy resolution in the experimental recording and also to the neglect of the intermode coupling terms of the Hamiltonian in the theoretical calculations. Therefore, the impact of the latter on the vibronic structure of the photoelectron band is also analyzed and discussed below.

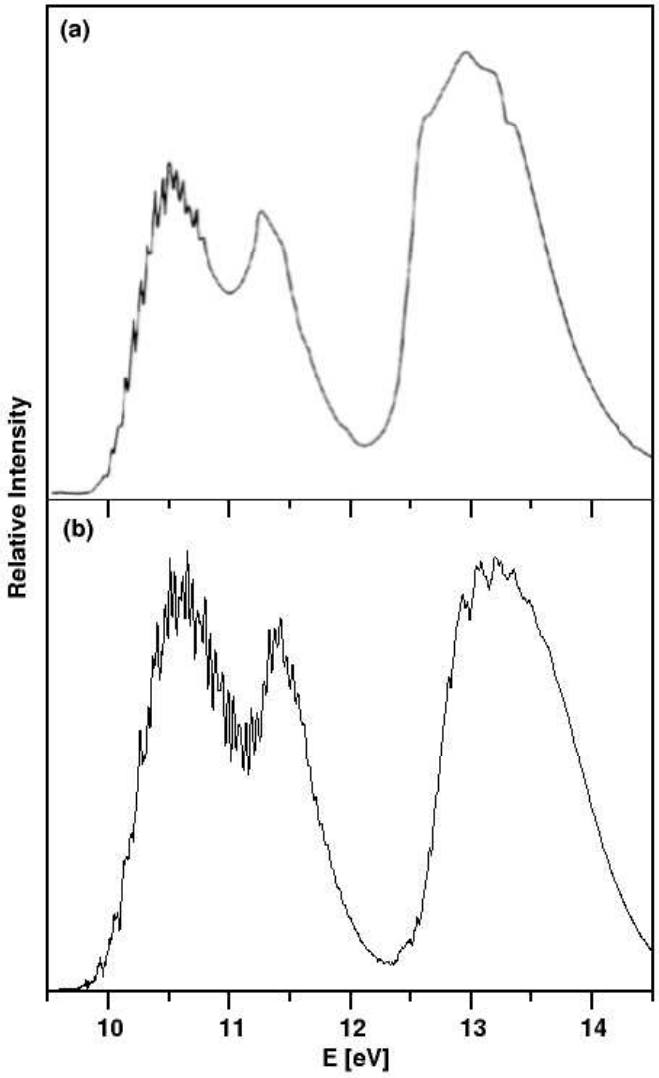

Figure 5.20: The photoelectron bands (first and second) of CP. The final theoretical results are shown in the panel *b* along with the experimental results of Holland *et al.* [75] in panel *a*. The relative intensity in arbitrary units is plotted as a function of the energy of the vibronic levels of the $\widetilde{X}^2E'$-$\widetilde{A}^2E''$ coupled electronic manifold. The zero of energy corresponds to the zero-point energy of the electronic ground state of CP. The theoretical results are obtained by the WP propagation approach using the MCTDH algorithm (see text).

In the final theoretical simulations, PJT interactions among the four JT split components of $\widetilde{X}$-$\widetilde{A}$ electronic manifold of CP^+ are considered. The full quadratic Hamiltonian (excluding the bilinear e'-e' coupling terms) including 14 relevant vibrational modes is employed in the WP propagation. The theoretical photoelectron bands are shown in Fig. 5.21(b) along with the experimental results of Ref. [75] in Fig. 5.21(a). The details of the normal mode combinations, the sizes of the primitive and SPF bases used to generate the theoretical spectra are given in Table 5.7(c). The theoretical spectra of panel *b* represent a combination of the partial spectra obtained from four different WP propagations carried out by locating the initial WP in each of the four JT split component states of the coupled $\widetilde{X}$-$\widetilde{A}$ electronic manifold. It can be seen from Fig. 5.21 that the theoretical results are in very good accord with experiment [75]. An impact of the bilinear JT coupling terms is immediately seen in the low-energy wing of the first photoelectron band when comparing Fig. 5.21(b) with Fig. 5.20(b). The progressions in this part of the spectrum are substantially modified by the bilinear (particularly a_1'-e') terms and as a result the theoretical envelope agrees much better with the experiment (when compared to Fig. 5.11(b)).

5.4.3 Time-Dependent Wave Packet Dynamics

In this section we discuss the femtosecond internal conversion dynamics of a WP initially prepared on one component of the JT split $\widetilde{A}^2E''$ electronic manifold. This WP during its evolution in time approaches all the JT and PJT conical intersections in the $\widetilde{X}^2E'$-$\widetilde{A}^2E''$ coupled electronic manifold (shown schematically in Fig. 5.16), and nonradiatively transits to all four component electronic states of this manifold. The time dependence of the diabatic electronic populations of these four electronic states is shown in Fig. 5.22. The WP is initially located on one component of the $\widetilde{A}^2E''$ electronic manifold. The population of this state starts from 1.0 at $t = 0$ and decays to a value of ~ 0.20 at longer times (dotted line).

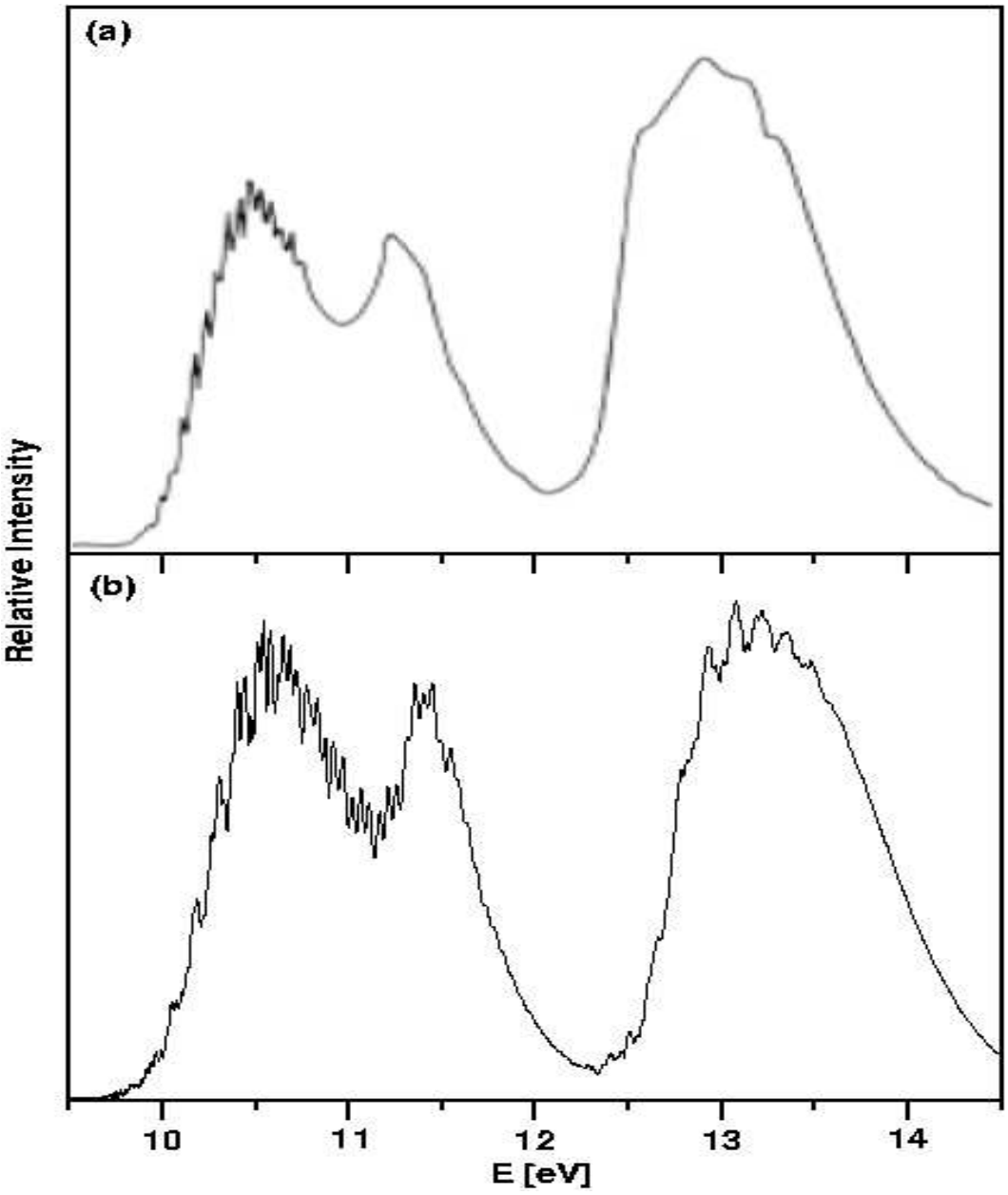

Figure 5.21: The $\widetilde{X}$-$\widetilde{A}$ photoelectron bands of CP. The final theoretical results obtained by propagating wave packets on the coupled $\widetilde{X}$-$\widetilde{A}$ electronic states (see text for details) are shown in panel *b* along with the experimental results of Holland *et al.* [75] in panel *a*. The relative intensity in arbitrary units is plotted as a function of the energy of the vibronic levels of the $\widetilde{X}^2E'$-$\widetilde{A}^2E''$ coupled electronic manifold. The zero of energy correspond to the minimum of the potential energy of the electronic ground state of CP.

The initial decay of population of this state relates to a decay rate of $\sim 10\ fs$. Companion calculations reveal a decay rate of $\sim 10\ fs$ of the second component of the $\widetilde{A}^2E''$ electronic manifold. It can be seen from Fig. 5.22 that at $t = 0$ the population of the remaining three electronic states of the $\widetilde{X}^2E'$-$\widetilde{A}^2E''$ electronic manifold is zero. At longer times the WP approaches the PJT and JT conical intersections and undergoes nonadiabatic transitions and populates these three electronic states. The population of the second component of the $\widetilde{A}^2E''$ electronic manifold and that of the x and y components of the $\widetilde{X}^2E'$ electronic manifold is shown in Fig. 5.22 by the thick solid line, solid line, and dashed line, respectively. Finally, the populations of both the components of the $\widetilde{A}^2E''$ electronic manifold saturate nearly to the same value. When the WP is initially prepared on the JT split component of the $\widetilde{X}^2E'$ electronic manifold, the population transfer to the $\widetilde{A}^2E''$ electronic manifold is found to be negligible (diagram not shown here). This WP moves back and forth between the two component electronic states only through the $\widetilde{X}^2E'$ JT conical intersections and their populations fluctuate around an average value of ~ 0.5.

In order to better understand the population dynamics of Fig. 5.22, in Fig. 5.23(a-f) we show snapshots of the WP evolving on the $\widetilde{X}^2E'$-$\widetilde{A}^2E''$ coupled electronic manifold. The probability density ($|\Psi|^2$) of the WP is superimposed on the potential energy curves along the normal coordinate of the strongest Condon active a_1' vibrational mode ν_2. The potential energy curves and the WP probability densities are shown as solid and dashed lines for the $\widetilde{X}^2E'$ and $\widetilde{A}^2E''$ electronic states, respectively. For the purpose of drawing, the zero of the WP probability densities is chosen to occur near a potential energy of ~ 13.5 eV. Since the Condon activity of ν_2 is strongest in both the electronic states, most of the significant structures in the population diagram of Fig. 5.22 can be interpreted from the WP snapshots along this mode. Again we mention that the electronic degeneracy of the two electronic states is retained along this totally symmetric vibrational mode.

Since the WP is initially (at $t = 0$) located on one component of the $\widetilde{A}^2E''$ elec-

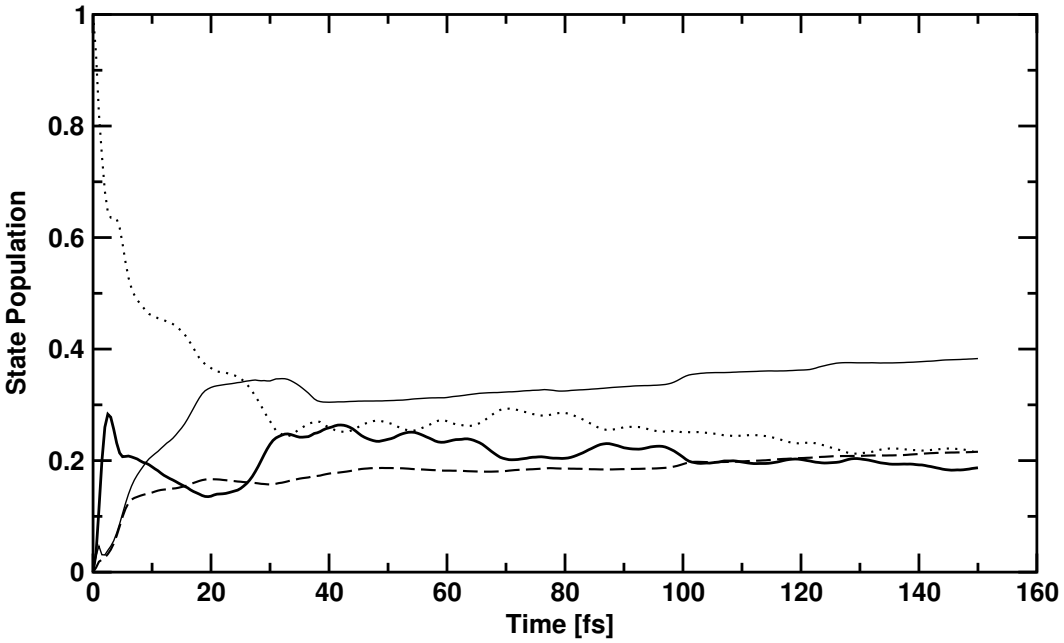

Figure 5.22: Time evolution of the diabatic electronic populations obtained by locating an initial wave packet on one component of the $\widetilde{A}^2E''$ electronic manifold of CP^+. The decay of the population of this component electronic state is shown by the dotted line and the growth of the population of the other component of the $\widetilde{A}^2E''$ electronic state and the two JT split components of the $\widetilde{X}^2E'$ electronic state is shown by the thick solid line, solid and dashed lines, respectively.

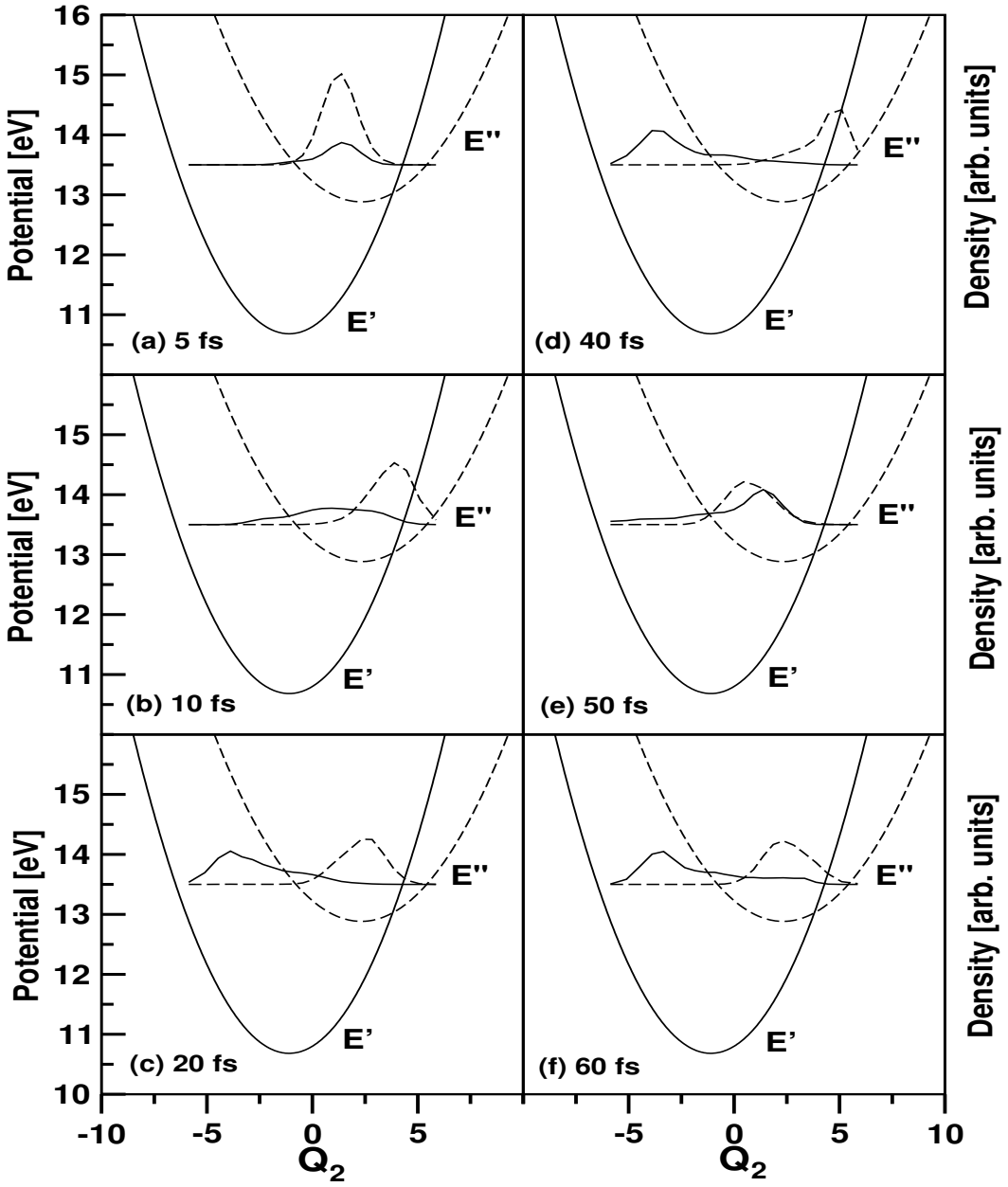

Figure 5.23: Wave packet probability densities ($|\Psi|^2$) as a function of the dimensionless normal coordinate Q_2 of the vibrational mode ν_2 integrated over all other coordinates at different times (indicated in each panel) superimposed on the potential energy curves of the $\widetilde{A}^2E''$ (dashed line) and $\widetilde{X}^2E'$ (solid line) electronic states of CP^+. The WP probability densities on these electronic states are shown by the same line types. The zero of the WP probability densities has been chosen, for graphical reasons, to occur near a potential energy of 13.5 eV. The scale for the probability density is arbitrary but identical for all $|\Psi|^2$ displayed in the figure.

tronic manifold (not shown in the figure), the population of this state starts from 1.0 (dotted line in Fig. 5.22). In about 5 fs (cf. Fig. 5.23(a)), a fraction of population ($\sim$ 42 %) transfers to the $\widetilde{X}^2E'$ electronic manifold and as a result a sharp drop in the $\widetilde{A}^2E''$ population occurs (cf. Fig. 5.22). In about 10 fs (Fig. 5.23(b)), the WP component on the $\widetilde{A}^2E''$ electronic manifold moves more towards the $\widetilde{X}-\widetilde{A}$ PJT crossing seam, and in $\sim$ 40 fs (Fig. 5.23(d)), it moves solely toward it. At longer times (Figs. 5.23(e-f)), the remaining WP component on this electronic manifold moves closer to its potential energy minimum. The WP component on the $\widetilde{X}^2E'$ electronic manifold, on the other hand, moves away from the crossing seam and mostly remains localized near its *own* potential energy minimum. This is because the minimum of the $\widetilde{X}^2E'$-$\widetilde{A}^2E''$ PJT crossing seam occurs $\sim$ 1.475 eV above the minimum of the $\widetilde{X}^2E'$ electronic manifold. Therefore, the recrossing probability of the WP component on this electronic manifold to the $\widetilde{A}^2E''$ electronic manifold is expected to be very small. We note that in addition to this crossing through the $\widetilde{X}-\widetilde{A}$ PJT conical intersections, the WP component on each degenerate electronic manifold undergoes crossing through the respective JT conical intersections. The seam of the latter occurs at the equilibrium configuration $\mathbf{Q}$=0. Therefore, motion of the WP towards the minimum of the potential energy curves in Fig. 5.23 is associated with the population exchange between the JT split components of the respective degenerate electronic manifold. This is revealed by the growth of population in time of the three JT component states in Fig. 5.22. The weak structures in the population diagram appear due to the interference of the WP components in the vicinity of various curve crossings in the $\widetilde{X}^2E'$-$\widetilde{A}^2E''$ coupled electronic manifold.

5.5 Summary and Outlook

A detailed theoretical description of the multimode JT and PJT interactions in the low-lying doubly degenerate $\widetilde{X}^2E'$ and $\widetilde{A}^2E''$ electronic states of CP^+ has

been presented. Degenerate vibrational modes of e' symmetry split the electronic degeneracy of these electronic states and the resulting JT split component states exhibit PJT interactions via the vibrational modes of a_1'' and e'' symmetries. The theoretical model here is constructed by considering interactions among these four component electronic states and fourteen relevant vibrational degrees of freedom. Quantum dynamical simulations of the nuclear motion are carried out both by a time-independent and by a time-dependent approach and the vibronic level structure of this coupled manifold of electronic states is calculated. The theoretical results are compared with the available experimental photoelectron spectrum of CP.

In the theoretical description, a model vibronic Hamiltonian of the four interacting electronic states including the fourteen vibrational degrees of freedom is constructed in terms of the dimensionless normal coordinates of the electronic ground state of CP in a diabatic electronic basis. A QVC scheme is employed to describe the Condon activity of the three a_1' vibrational modes and the JT activity of the four e' vibrational modes. The PJT activity of the a_1'' and e'' vibrational modes is treated by a LVC scheme. In addition, we have considered the a_1'-a_1' and a_1'-e' intermode bilinear coupling terms in our theoretical simulations. The coupling parameters of the Hamiltonian are determined by calculating the adiabatic PESs of the $\widetilde{X}^2E'$ and $\widetilde{A}^2E''$ electronic states along each vibrational mode by the OVGF method.

In the nuclear dynamical simulations, we systematically examined the vibronic energy level structure of the $\widetilde{X}^2E'$ and $\widetilde{A}^2E''$ electronic states of CP^+ first by considering the JT interactions alone in both these states and then by introducing the PJT interactions between the two. To start with, we reproduced the time-independent results on the first band by the time-dependent WP propagation method. Moreover, the importance of the bilinear JT coupling terms for the vibronic structures of the low-energy wing of the $\widetilde{X}^2E'$ photoelectron band is established. The $\widetilde{A}^2E''$ photoelectron band is then calculated by considering

three Condon active (ν_1-ν_3) and four JT active vibrational modes (ν_4-ν_7) within a linear coupling scheme by the time-independent method. The results obtained from this approach do not correspond well with the experiment. The effect of the second-order coupling terms of the Hamiltonian is then considered and the spectrum is calculated by both the time-independent and time-dependent approaches. The second-order coupling terms cause an increase in the spectral line density, and the spectral envelope reveals much better agreement with the experiment. The dominant progression in this band is mainly caused by the ν_2, ν_4, and ν_6 vibrational modes. The vibronic fine structure of the time-dependent spectrum of Fig. 5.18(d) is in good accord with the time-independent one of Fig. 5.18(c).

The complete photoelectron band is simulated by propagating wave packets using the MCTDH approach, including four electronic states and fourteen relevant vibrational degrees of freedom. Such a task is computationally not viable by the time-independent matrix diagonalization approach. When we compare the theoretical results with the experimental one, a strong impact of the PJT coupling on the vibronic structure of both the photoelectron bands can be observed. The impact of the PJT coupling on the second band is more than that on the first band. This is because the minimum of the seam of PJT conical intersections occurs ~ 0.638 eV below that of the $\widetilde{A}^2E''$ JT conical intersections. As a result, the continuum levels of the $\widetilde{X}^2E'$ electronic manifold mix with the low-lying vibronic levels of the $\widetilde{A}^2E''$ electronic manifold. The huge increase in the spectral line density results from this mixing of levels of two different vibronic symmetries.

The time evolution of the diabatic electronic populations reveals a nonradiative decay time of $\sim 10\ fs$ of the $\widetilde{A}^2E''$ electronic manifold of CP^+ mediated by the PJT interaction with the $\widetilde{X}^2E'$ electronic manifold through the a_1'' and e'' vibrational modes. The $\widetilde{X}^2E'$-$\widetilde{A}^2E''$ photoelectron band of CP^+ represents a unique and complex example of the interplay between the JT and PJT interactions involving two doubly degenerate electronic states.

Chapter 6

Future Directions

The static and dynamic aspects of the JT and PJT interactions in B_3, $C_2H_6^+$, and $C_3H_6^+$ are studied in this thesis. The theoretical approach is based on *ab initio* electronic structure calculations and quantum dynamical studies. With the advent of high-resolution spectroscopic techniques, advances in electronic structure calculations, and computational capabilities, better understanding of the highly complicated JT and PJT vibronic coupling effects in isolated molecules has become possible. The success of the theoretical approach lies on the adoption of simple VC model Hamiltonians. Further computational advantage is the assumption of harmonic diabatic potentials and truncation of Taylor series (around the equilibrium geometry of the neutral molecule) in low-order.

The main findings of the present work are given below.

1. (a) The vibronic structure of the $\widetilde{C}^2E'$ photoelectron band of B_3 showed a progression along the degenerate ν_2 vibrational mode. The spacing between the successive lines is $\sim$ 1103 cm^{-1} [68], this is in very good agreement with the observed sharp splitting of $\sim 1100 \pm 80$ cm^{-1}; in the experimental recording.

(b) Our explicit theoretical analysis indicates that the linear PJT, quadratic, and bilinear JT couplings have practically no impact on the vibronic structure of the $\widetilde{X}^2A_1'$-$\widetilde{C}^2E'$ photoelectron band of B_3.

(c) The JT effect in the $\widetilde{C}^2E'$ electronic manifold is also quite weak when

compared to the similar other examples treated in the literature [26, 90, 119].

2. (a) For the $\widetilde{X}^2E_g$ electronic manifold of ET^+, the irregular vibrational progressions, with its numerous shoulders and small peaks observed below 12.55 eV are attributed due to the dynamic $(E \times e)$-JT effect.

(b) Our findings revealed that the PJT activity of the degenerate vibrational modes (e_g) is particularly strong in the coupled $\widetilde{X}^2E_g$-$\widetilde{A}^2A_{1g}$ electronic manifold which leads to a broad and diffuse structure of the observed photoelectron band.

(c) The three maxima obtained in the $\widetilde{X}^2E_g$ -$\widetilde{A}^2A_{1g}$ photoelectron band of ET^+ at $\sim$ 12.25, $\sim$ 12.75, and $\sim$ 13.50 eV, due to the JT split $\widetilde{X}^2E_g$ component states and the $\widetilde{A}^2A_{1g}$ electronic state [89], compare well with the experimental observations [69].

3. (a) For the $\widetilde{X}^2E'$ electronic manifold of CP^+, the observed splitting between the two maxima in the bimodal intensity distribution was found to be $\sim$ 0.78 eV [75] and compares well with the time-independent and time-dependent results of $\sim$ 0.80 and $\sim$ 0.81 eV, respectively, within the LVC scheme [91].

(b) The minimum of the PJT crossing occurs $\sim$ 1.475 eV above the minimum of the $\widetilde{X}^2E'$ and $\sim$ 0.638 eV below the minimum of the $\widetilde{A}^2E''$ JT conical intersections in CP^+.

(c) Therefore, the vibronic structure of the coupled $\widetilde{X}$-$\widetilde{A}$ electronic manifold of CP^+ is calculated by propagating wave packets using the MCTDH algorithm considering the PJT interactions between the two electronic states through the a_1'' and e'' vibrational modes.

(d) The time evolution of the diabatic electronic populations reveals a nonradiative decay time of $\sim$ 10 *fs* of the $\widetilde{A}^2E''$ electronic manifold of CP^+ [91].

To conclude in case of B_3, we note that besides the model study presented here, which, in fact, reproduces the experimental results reasonably well, a more rigorous electronic structure calculations to establish the anionic and neutral PESs and the nonadiabatic coupling elements are to be carried out with an aim to perform wave packet dynamical simulations to study the decay of the excited

electronic states of B_3 cluster.

In case of ET^+, the overall diffuseness of the experimental photoelectron band ($\widetilde{X}^2E_g$-$\widetilde{A}^2A_{1g}$) is not very well reproduced by the present theoretical model. This can be attributed due to the neglect of the second-order coupling terms of degenerate e_g vibrational modes and the various (a_{1g}-a_{1g}, a_{1g}-e_g, and e_g-e_g) bilinear coupling terms. We note that the vibrational modes of u symmetry also enter in the dynamics when a QVC model is considered. Moreover, the PJT interaction of $\widetilde{B}^2E_u$ electronic manifold via e_u vibrational modes with the well separated low-lying states $\widetilde{X}^2E_g$ (by $\sim$ 2.75 eV) and $\widetilde{A}^2A_{1g}$ (by $\sim$ 2.40 eV) are also to be analyzed which may bring the theoretical results close to the experiment. An estimate of the feasibility of such interactions ($\widetilde{X}^2E_g$ - $\widetilde{A}^2A_{1g}$ - $\widetilde{B}^2E_u$) and the nuclear dynamics which includes the above five component states and fifteen vibrational degrees of freedom are to be carried out using the MCTDH algorithm.

To this end we mention that by studying systems of growing size (going from B_3 to $C_3H_6^+$), the scenario of the nuclear dynamics changes from single coupling mode to multi coupling modes which essentially makes the vibronic structure of the photoelectron bands highly complex to understand and the computational resources required to simulate them also grows exponentially. Therefore, we would like to learn which are the relevant prevailing coupling mechanisms and what type of modes are important in the nuclear dynamics. The outcome of the present study gives a pathway to understand more complex vibronic interactions ubiquitous in molecular systems. The understanding of the nuclear dynamics in vibronically interacting medium and large systems and the exploration of the impact of these intricate interactions in photophysical and photochemical processes, are some of the prospective directions for the future studies.

However, the study of systems of growing size is an uphill task. Because, the number of vibrational degrees of freedom increases as the number of atoms increases in a molecule. This makes the problem more difficult to access since we require a predefined PES over which the nuclei moves. Calculation of this

multidimensional PES is an impossible task. Alternatively, if we look at the on-the-fly (or direct) molecular dynamics where the PES is provided by explicit evaluation of the electronic wave function for the states of interest, the larger systems are also treated successfully [132].

Appendix A

The Lanczos Algorithm

For multi-mode VC problems, the solution of the eigenvalue problem of the Hamiltonian matrix $\mathcal{H}$ in the harmonic-oscillator basis functions is a formidable numerical task. The large dimension of the sparse-Hamiltonian matrix causes problem related to storing the matrix elements. Lanczos algorithm is used to circumvent this problem. In this method the structured sparsity of the Hamiltonian is exploited. The following is a brief description of the algorithm.

Let us consider some initial state $|p_0\rangle$ and define the state vector $|p_1\rangle$ by the relations

$$\begin{aligned} |q_1\rangle &= \mathcal{H}|p_0\rangle - \langle p_0|\mathcal{H}|p_0\rangle|p_0\rangle \\ |p_1\rangle &= q_1/\sqrt{\langle q_1|q_1\rangle}. \end{aligned} \tag{A.1}$$

Given these states, one can start the following three-term recurrence relations, also called Lanczos iteration [56, 133], as follows:

$$\begin{aligned} |q_{i+1}\rangle &= \mathcal{H}|p_i\rangle - \langle p_i|\mathcal{H}|p_i\rangle - \sqrt{\langle q_i|q_i\rangle}|p_i\rangle \\ |p_{i+1}\rangle &= |q_{i+1}\rangle/\sqrt{\langle q_{i+1}|q_{i+1}\rangle}. \end{aligned} \tag{A.2}$$

The above Lanczos iterations generate a sequence of orthonormal states $|p_0\rangle$,

$|p_1\rangle$, $|p_2\rangle$...spanning the so-called Krylov subspace of $\mathcal{H}$. In this new basis, the Hamiltonian matrix takes a tridiagonal form as follows,

$$\begin{aligned} \mathcal{T}_{ii} &= \langle p_i|\mathcal{H}|p_i\rangle \\ \mathcal{T}_{i,i+1} &= \sqrt{\langle q_{i+1}|q_{i+1}\rangle} = \mathcal{T}_{i+1,i}. \\ \mathcal{T}_{i,j} &= 0 \; for \; |i-j| \; > 1 \; . \end{aligned} \tag{A.3}$$

The matrix elements are generated automatically during the recursion process (Eq. A.2).

For our purposes, we identify

$$|p_0\rangle = \mathcal{T}^\dagger|\Psi_i\rangle, \tag{A.4}$$

and use the basis set expansion of Eq. (2.46) to represent the Krylov subspace as the sequence of column vectors $\mathbf{p}_0$, $\mathbf{p}_1$,$\mathbf{p}_2$,... Similarly, the coefficients $a_m^{(\nu)}$ are combined into a column vector $a^{(\nu)}$. Using Eq. (A.3) we have

$$\mathbf{P}_m^\dagger \mathcal{H} \mathbf{P}_m = \mathbf{T}^m, \tag{A.5}$$

where $\mathbf{T}^m$ represents the $m \times m$ tridiagonal matrix with elements resulting from performing m Lanczos iterations, Eqs. (A.1) and (A.2). Let $\mathbf{x}^m$ be the eigenvector of $\mathbf{T}^m$ with eigenvalue E_ν^m. Then $\mathbf{P}_m \mathbf{x}_\nu^m$ denotes the corresponding eigenstates of the original Hamiltonian and its spectral intensity turns out as [39]

$$\begin{aligned} \mathbf{I}_\nu^m &= |\mathbf{p}_0^\dagger \mathbf{P}_m \mathbf{x}_\nu^m|^2 \\ &= |\mathbf{p}_0^\dagger \left(\mathbf{p}_0, \mathbf{p}_1, ...\mathbf{p}_m\right) \mathbf{x}_\nu^m|^2 \\ &= |\left(1, 0, 0, ...0\right) \mathbf{x}_\nu^m|^2 \\ &= |\mathbf{x}_\nu^m(1)|^2. \end{aligned} \tag{A.6}$$

Because of the orthogonality of $\mathbf{p}_i$, and by the virtue of the choice of $|p_0\rangle$, it is only the first component $\mathbf{x}_\nu^m(1)$ of the eigenvectors of the tridiagonal matrix that determines the spectral intensity [134].

Appendix B

Finite Difference Scheme

The *intrastate* coupling parameters can be obtained from the symmetric finite difference equation as follows

$$\kappa_i = \left.\frac{\partial V}{\partial Q_i}\right|_{Q_i=Q_i^0} = \frac{V(Q_i+\Delta Q_i) - V(Q_i-\Delta Q_i)}{2\Delta Q_i}. \tag{B.1}$$

The JT coupling parameters can be defined as

$$\begin{pmatrix} E_1^0 & \lambda_i Q_i \\ \lambda_i Q_i & E_2^0 \end{pmatrix} \tag{B.2}$$

$$V_{1,2} = \frac{E_1^0 + E_2^0}{2} \pm \sqrt{\left(\frac{E_1^0 - E_2^0}{2}\right)^2 + \lambda_i^2 Q_i^2} \tag{B.3}$$

$$V_1 - V_2 = 2\sqrt{\Delta^2 + \lambda_i^2 \Delta Q_i^2} \tag{B.4}$$

where, $\Delta = \frac{E_1^0 - E_2^0}{2} = 0$ at equilibrium geometry and therefore

$$\lambda_i = \left.\frac{1}{2}\left(\frac{\partial \Delta V_E}{\partial Q_i}\right)\right|_{Q_i=Q_i^0} = \frac{V_1 - V_2}{2\Delta Q_i} \tag{B.5}$$

where, ΔV_E is the (signed) difference of the JT split PESs.

The second-order coupling parameters which represent the diabatic frequency shifts can be obtained from

$$\gamma_i = \left.\frac{\partial^2 V}{\partial Q_i^2}\right|_{Q_i=Q_i^0} = \frac{V(Q_i+\Delta Q_i) - 2V(Q_i^0) + V(Q_i-\Delta Q_i)}{(\Delta Q_i)^2}. \quad \text{(B.6)}$$

Using small normal coordinate displacements one can obtain the various intermode bilinear coupling parameters by the following set of finite difference equations

$$\gamma_{ij} = \frac{1}{h^2}\Big[V(Q_i^0+h, Q_j^0+h) - V(Q_i^0+h, Q_j^0) - V(Q_i^0, Q_j^0+h) + V(Q_i^0, Q_j^0)\Big] \quad \text{(B.7)}$$

$$\begin{aligned}\gamma_{ij} = \frac{1}{2h^2}\Big[&V(Q_i^0+h, Q_j^0+h) + V(Q_i^0-h, Q_j^0-h) - V(Q_i^0+h, Q_j^0) - V(Q_i^0-h, Q_j^0) \\ &-V(Q_i^0, Q_j^0+h) - V(Q_i^0, Q_j^0-h) + 2V(Q_i^0, Q_j^0)\Big]\end{aligned} \quad \text{(B.8)}$$

$$\begin{aligned}\gamma_{ij} = \frac{1}{4h^2}\Big[&V(Q_i^0+h, Q_j^0+h) + V(Q_i^0-h, Q_j^0-h) \\ &-V(Q_i^0+h, Q_j^0-h) - V(Q_i^0-h, Q_j^0+h)\Big]\end{aligned} \quad \text{(B.9)}$$

where, h represents the amount of displacement.

Appendix C

Group theoretical analysis of the Hamiltonian of CP^+

In this appendix we demonstrate the correctness of the Hamiltonian matrix, Eqs. (5.4-5.7j), that is, show that the various coupling terms transform totally symmetric under the symmetry operations of the pertinent point group, D_{3h}. The general reasoning is similar to the one developed for the benzene radical cation in the appendix of Ref. [26]. Only linear coupling terms will be considered here, quadratic coupling terms can be treated in an analogous way.

To simplify the analysis, we note that the proper transformation behavior under the reflection operation σ_h is already ensured by the superscripts (primes) embodied in the symmetry selection rules, Eqs. (5.2, 5.3), and the Hamiltonian matrix elements of Eqs. (5.4-5.7j). We can confine the analysis, therefore, to a suitable subgroup of D_{3h}, which we choose to be C_{3v} and thus have identical representation matrices for the E' and E'' electronic states (as well as for e' and e'' vibrational modes). These are given in the Table C.1, which focuses on only one convenient choice for the C_3 and σ_v symmetry operations.

With the underlying phase conventions, one arrives at the following transformation properties of the electronic projection operators in the E' as well as E''

Table C.1: Characters and transformation matrices of basis functions of the D_{3h} irreducible representations for some symmetry operations of the C_{3v} subgroup.

	A_1'	A_2'	E'	A_1''	A_2''	E''
E	1	1	$\begin{pmatrix} 1 & 0 \\ 0 & 1 \end{pmatrix}$	1	1	$\begin{pmatrix} 1 & 0 \\ 0 & 1 \end{pmatrix}$
C_3	1	1	$\begin{pmatrix} -\frac{1}{2} & -\frac{\sqrt{3}}{2} \\ \frac{\sqrt{3}}{2} & -\frac{1}{2} \end{pmatrix}$	1	1	$\begin{pmatrix} -\frac{1}{2} & -\frac{\sqrt{3}}{2} \\ \frac{\sqrt{3}}{2} & -\frac{1}{2} \end{pmatrix}$
σ_v	1	-1	$\begin{pmatrix} -1 & 0 \\ 0 & 1 \end{pmatrix}$	-1	1	$\begin{pmatrix} -1 & 0 \\ 0 & 1 \end{pmatrix}$

electronic function spaces (since the superscripts are not needed, the kets $|x\rangle$ and $|y\rangle$, as well as the corresponding bras, refer collectively to the first and second rows/columns of the E' as well as E'' representation matrices of the Table C.1).

$$|x\rangle\langle y| - |y\rangle\langle x| \quad \xrightarrow{C_3} \quad |x\rangle\langle y| - |y\rangle\langle x| \tag{C.1}$$

$$|x\rangle\langle y| - |y\rangle\langle x| \quad \xrightarrow{\sigma_v} \quad -\left(|x\rangle\langle y| - |y\rangle\langle x|\right) \tag{C.2}$$

$$\begin{pmatrix} |x\rangle\langle x| - |y\rangle\langle y| \\ |x\rangle\langle y| + |y\rangle\langle x| \end{pmatrix} \quad \xrightarrow{C_3} \quad \begin{pmatrix} -1/2 & \sqrt{3}/2 \\ -\sqrt{3}/2 & -1/2 \end{pmatrix} \begin{pmatrix} |x\rangle\langle x| - |y\rangle\langle y| \\ |x\rangle\langle y| + |y\rangle\langle x| \end{pmatrix} \tag{C.3}$$

$$\begin{pmatrix} |x\rangle\langle x| - |y\rangle\langle y| \\ |x\rangle\langle y| + |y\rangle\langle x| \end{pmatrix} \quad \xrightarrow{\sigma_v} \quad \begin{pmatrix} 1 & 0 \\ 0 & -1 \end{pmatrix} \begin{pmatrix} |x\rangle\langle x| - |y\rangle\langle y| \\ |x\rangle\langle y| + |y\rangle\langle x| \end{pmatrix} \tag{C.4}$$

Note that the latter two relations hold only for the specific transformation matrices given in Table C.1.

Let us denote by Q_x and Q_y the nuclear displacement coordinates transforming

as the $|y\rangle$ and $|x\rangle$ electronic basis states, respectively. Then, similar transformation laws as Eqs. (C.3 – C.4) hold for them also, and one can subsequently verify that the operator

$$\mathbf{W}_e = (Q_x, Q_y) \begin{pmatrix} |x\rangle\langle x| - |y\rangle\langle y| \\ |x\rangle\langle y| + |y\rangle\langle x| \end{pmatrix} \tag{C.5}$$

remains invariant under the C_3 and σ_v symmetry operations, i.e. transforms totally symmetric in the C_{3v} molecular point group. Since the additional symmetry operations of D_{3h} need no further consideration (see second paragraph of the Appendix), this establishes the correctness of all coupling terms linear in the coordinates of the e' and e'' modes in Eqs. (5.7a-5.7j). One notes that they have all (including the PJT coupling terms) the usual form familiar from JT theory.

We next investigate the coupling terms involving nondegenerate vibrational modes. The labeling of their vibrational coordinates follows the same indexing convention as the irreducible representations according to which they transform. Then, within an electronic state, there are only the following two totally symmetric electron-vibrational operators (cf. the Table C.1 and Eqs. (C.1, C.2)):

$$\mathbf{W}_{a_1'} = Q_1' \left(|x\rangle\langle x| + |y\rangle\langle y|\right) \tag{C.6}$$

$$\mathbf{W}_{a_2'} = Q_2' \left(|x\rangle\langle y| - |y\rangle\langle x|\right) \tag{C.7}$$

Eqs. (C.6, C.7) hold again for the E' as well as for the E'' state. Eq. (C.6) reproduces (for completeness) the well-known results about the linear coupling to totally symmetric modes, while the second term, Eq. (C.7), does not satisfy the requirement of hermiticity and the corresponding coupling element has to be dropped in the Hamiltonian (for a corresponding momentum coupling operator, however, see Ref. [135]).

Concerning the PJT coupling terms, the E' and E'' electronic basis states now have to be distinguished by corresponding superscripts. Then, Eqs. (C.1, C.2) and the Table C.1 allow to see rather easily that the following two (and

only two) electron-vibrational operators transform totally symmetric (that is, are form-invariant under the C_3 and σ_v symmetry operations):

$$\mathbf{W}_{a_1''} = Q_1'' \left(|x'\rangle\langle y''| - |y'\rangle\langle x''| \right) \tag{C.8}$$

$$\mathbf{W}_{a_2''} = Q_2'' \left(|x'\rangle\langle x''| + |y'\rangle\langle y''| \right) \tag{C.9}$$

Note that the vibrational subscripts 1 and 2 are interchanged as compared to Eqs. (C.6, C.7). This is a direct consequence of the different transformation properties of e.g. Q_1' and Q_1'' according to Table C.1. Also, the PJT coupling term (C.8) does *not* violate hermiticity because it appears in the off-diagonal 2×2 blocks of the 4×4 coupling matrix, Eq. (5.4). Taken together, in matrix form the relations (C.6 – C.9) establish the linear coupling terms also for the nondegenerate vibrational modes in Eqs. (5.7a-5.7j). Here the element $\mathbf{W}_{a_2''}$ from Eq. (C.9) is suppressed because these modes turn out to be unimportant for CP^+.

We point out that the form of $\mathbf{W}_{a_1''}$ of Eq. (C.8) may be changed by a suitable redefinition of either the E' or the E'' electronic basis states. This, however, would lead to different $E \otimes e$-JT coupling matrices in these states and underlines, that care is needed to work with a consistent choice of electronic wave functions to arrive at correct Hamiltonians for simultaneous JT and PJT interactions.

It remains to clarify the determination of the relative signs of the JT coupling constants λ' and λ'' for the various modes. These prove to be important (at least for the a_1'' coupling mode) for reasons similar to those discussed earlier for the benzene radical cation [27]. They can be determined, e.g., by using symmetry-adapted displacements of the JT active modes. In the higher-symmetry subgroup of D_{3h} (here C_{2v}) the two JT-split potential energy surfaces are then distinguished by symmetry and can be identified with either of the diagonal elements of the coupling matrix of Eqs. (5.4-5.7j). (Thus λ' and λ'' are signed quantities.)

Lacking symmetry-adapted JT displacements we may perform electronic structure calculations for simultaneous JT and PJT displacements and deduce the

relative signs of λ' and λ'' (for a given mode) from the repulsion pattern of the potential energy surfaces. This is seen by transforming the Hamiltonian (Eqs. 5.4-5.7j) to an electronic basis which is adiabatic *within* each of the E' and E'' electronic states only (resulting in an interaction matrix $\mathbf{W}^{tr}$). For a single JT-mode displacement this is achieved by the same 2×2 orthogonal matrix (in either degenerate state) which leaves the Q_1'' coupling term invariant according to the following result:

$$\mathbf{W}^{tr} = \begin{pmatrix} \lambda'\rho & 0 & 0 & \lambda Q_1'' \\ 0 & -\lambda'\rho & -\lambda Q_1'' & 0 \\ 0 & -\lambda Q_1'' & \lambda''\rho & 0 \\ \lambda Q_1'' & 0 & 0 & -\lambda''\rho \end{pmatrix} \tag{C.10}$$

Here ρ is the polar radius for the JT active mode in question, and the λ' and λ'' are signed quantities. Eq. (C.10) demonstrates that for the same sign of λ' and λ'' the PJT mode Q_1'' couples the upper with the lower sheet of the E' and E'' electronic manifolds, while for opposite signs it couples the upper sheets with each other (and also the lower ones, of course). This allows to determine the relative signs, provided the displacements are chosen suitably to reveal the difference between the two cases.

Bibliography

[1] H. A. Jahn and E. Teller, Proc. R. Soc. London, Ser. A **161**, 220 (1937).

[2] R. Englman, *The Jahn-Teller Effect in Molecules and Crystals* (Wiley, New York, 1972).

[3] I. B. Bersuker *The Jahn-Teller Effect and Vibronic Interactions in Modern Chemistry* (Plenum Press, New York, 1984).

[4] G. Fischer, *Vibronic Coupling* (Academic Press, London, 1984).

[5] *The Dynamical Jahn-Teller Effect in Localized Systems*, edited by Y. E. Perlin and M. Wagner (North-Holland, Amsterdam, 1984).

[6] I. B. Bersuker and V. Z. Polinger, *Vibronic Interactions in Molecules and Crystals* (Springer-Verlag, Berlin, 1989).

[7] I. B. Bersuker, Chem. Rev. **101**, 1067 (2001) and the references therein.

[8] I. B. Bersuker, *The Jahn-Teller Effect* (Cambridge University Press, 2006).

[9] H. C. Longuet-Higgins, U. Öpik, M. H. L. Pryce, and R. A. Sack, Proc. R. Soc. London, Ser. A **244**, 1 (1958).

[10] U. Öpik and M. H. L. Pryce, Proc. R. Soc. London, Ser. A **238**, 425 (1957).

[11] H. C. Longuet-Higgins, in *Advances in Spectroscopy*, H. W. Thompson (Ed.), Interscience, New York, 1961, Vol. II, p.429.

[12] J. E. Huheey, E. A. Keiter, and R. L. Keiter, *Inorganic Chemistry: Principles of structure and reactivity, 4th ed.* (Haper Collins, New York, 1993).

[13] M. D. Sturge, Solid State Phys. **20**, 91 (1967).

[14] M. D. Kaplan and B. G. Vekhter, *Cooperative phenomena in Jahn-Teller Crystals* (Plenum Press, New York, 1995).

[15] L. R. Falvello, J. Chem. Soc., Dalton Trans. **23**, 4463 (1997).

[16] *In Molecular Ions: Spectroscopy, Structure, and Chemistry*, edited by T. A. Miller and V. E. Bondybey (North-Holland, Amsterdam, 1983).

[17] H. Köppel, W. Domcke, and L. S. Cederbaum, Adv. Chem. Phys. **57**, 59 (1984).

[18] H. Köppel, Z. für Physikal. Chemie. **200**, 3 (1997).

[19] T. A. Barckholtz and T. A. Miller, Int. Rev. Phys. Chem. **17**, 435 (1998).

[20] T. A. Barckholtz and T. A. Miller, J. Phys. Chem. A **103**, 2321 (1999).

[21] C. C. Chancey and M. C. M. O'Brien, *The Jahn-Teller Effect in C_{60} and Other Icasahedral Complexes* (Princeton University Press, Princeton, New Jersey, 1997).

[22] A. Held and E. W. Schlag, Acc. Chem. Res. **31**, 467 (1998).

[23] Faraday Discuss. **115**, 1-442 (2000).

[24] S. Mahapatra, L. S. Cederbaum, and H. Köppel, J. Chem. Phys. **111**, 10452 (1999).

[25] S. Mahapatra, G. A. Worth, H. -D. Meyer, L. S. Cederbaum, and H. Köppel, J. Phys. Chem. A **105**, 5567 (2001).

[26] M. Döscher, H. Köppel, and P. G. Szalay, J. Chem. Phys. **117**, 2645 (2002).

[27] H. Köppel, M. Döscher, I. Bâldea, H. -D. Meyer, and P. G. Szalay, J. Chem. Phys. **117**, 2657 (2002).

[28] C. Woywod, S. Scharfe, R. Krawczyk, W. Domcke, and H. Köppel, J. Chem. Phys. **118**, 5880 (2003).

[29] E. Teller, J. Phys. Chem. **41**, 109 (1937).

[30] G. Herzberg and H. C. Longuet-Higgins, Discuss. Farad. Soc. **35**, 77 (1963).

[31] T. Carrington, Discuss. Farad. Soc. **53**, 27 (1972); Acc. Chem. Res. **7**, 20 (1974).

[32] D. R. Yarkony, J. Phys. Chem. **100**, 18612 (1996); Acc. Chem. Res. **31**, 511 (1998).

[33] M. A. Robb, F. Bernardi, and M. Olivucci, Pure and Appl. Chem. **67**, 783 (1995).

[34] F. Bernardi, M. Olivucci, and M. A. Robb, Chem. Soc. Rev. **25**, 321 (1996).

[35] *Conical intersections in photochemistry, spectroscopy and chemical dynamics*, Chem. Phys. **259**, 121-337 (2000).

[36] M. A. Robb, *Reviews in Computational Chemistry*, edited by K. Lipkowitz and D. Boyd, (Wiley, New York, **15**, 87 (2000)).

[37] *The Role of Degenerate States in Chemistry*, edited by M. Baer and G. D. Billing, Adv. Chem. Phys. Vol. **124** (Wiley, Hoboken, 2002).

[38] *Conical Intersections: Electronic Structure, Dynamics and Spectroscopy*, edited by W. Domcke, D. R. Yarkony, and H. Köppel (WorldScientific, Singapore, 2004).

[39] H. Köppel and W. Domcke, Encyclopedia of Computational Chemistry, Ed., P. V. R. Schleyer, Wiley: New York, 1998, P. 3166.

[40] M. Born and R. Oppenheimer, Ann. Physik (Leipzig) **84**, 457 (1927).

[41] M. Born and K. Huang, *The Dynamical Theory of Crystal Lattices* (Oxford University Press, London, UK, 1954).

[42] L. S. Cederbaum in Ref. [38], p.3-40.

[43] G. A. Worth and L. S. Cederbaum, Ann. Rev. Phys. Chem. **55**, 127 (2004).

[44] W. Lichten, Phys. Rev. **164**, 131 (1967); F. T. Smith, Phys. Rev. **179**, 111 (1969); T. F. O'Malley, Adv. At. Mol. Phys. **7**, 223 (1971); T. Pacher, L. S. Cederbaum, and H. Köppel, Adv. Chem. Phys. **84**, 293 (1993).

[45] M. H. Perrin and M. Gouterman, J. Chem. Phys. **46**, 1019 (1967); J. H. van der Waals, A. M. D. Berghuis, and M. S. de Groot, Mol. Phys. **13**, 301 (1967); J. H. van der Waals, A. M. D. Berghuis, and M. S. de Groot, Mol. Phys. **21**, 497 (1971); P. J. Stephens, J. Chem. Phys. **51**, 1995 (1969).

[46] M. Z. Zgierski and M. Pawlikowski, J. Chem. Phys. **70**, 3444 (1979).

[47] H. Köppel, L. S. Cederbaum, and W. Domcke, J. Chem. Phys. **89**, 2023 (1988).

[48] L. S. Cederbaum, W. Domcke, and H. Köppel, Chem. Phys. **33**, 319 (1978).

[49] G. Herzberg, *Molecular Spectra and Molecular Structure* (Van Nostrand, New York, 1966), Vol. **III**.

[50] S. Mahapatra and H. Köppel, J. Chem. Phys. **109**, 1721 (1998); H. Köppel, M. Döscher, and S. Mahapatra, Int. J. Quant. Chem. **80**, 942 (2000).

[51] R. Renner, Z. Phys. **92**, 172 (1934).

[52] J. G. Bednorz and K. A. Müller, Perovskite type oxides: The new approach to high-Tc superconductivity, in: Nobel Lectures, Physics 1981-1990, (World Scientific, Singapore, 1993).

[53] G. A. Worth, M. H. Beck, A. Jäckle, and H. -D. Meyer, The MCTDH Package, Version 8.2, (2000), University of Heidelberg, Germany. H. -D. Meyer, Version 8.3, (2002). See http://www.pci.uni-heidelberg.de/tc/usr/mctdh/

[54] H. -D. Meyer, U. Manthe, and L. S. Cederbaum, Chem. Phys. Lett. **165**, 73 (1990).

[55] U. Manthe, H. -D. Meyer, and L. S. Cederbaum, J. Chem. Phys. **97**, 3199 (1992).

[56] J. Cullum and R. Willoughby, *Lanczos Algorithms for Large Symmetric Eigenvalue Problems* (Birkhäuser, Boston, 1985), Vols. I and II.

[57] J. V. Neumann and E. P. Wigner, Physik. Z. **30**, 467 (1929).

[58] C. A. Mead and D. G. Truhlar, J. Chem. Phs. **70**, 2284 (1979).

[59] M. Desouter-Lecomte, C. Galloy, J. C. Lorquet, and M. Vaz Pires, J. Chem. Phys. **71**, 3661 (1979).

[60] W. Domcke and G. Stock, Adv. Chem. Phys. **100**, 1 (1997).

[61] C. A. Mead, Rev. Mod. Phys. **64**, 51 (1992).

[62] B. K. Kendrick, J. Phys. Chem. A, **107**, 6739 (2003).

[63] B. K. Kendrick in Ref. [38], p.521.

[64] H. Müller and H. Köppel, Chem. Phys. **183**, 107 (1994).

[65] R. Schneider, W. Domcke, and H. Köppel, J. Chem. Phys. **92**, 1045 (1990).

[66] J. Michl and V. Bonacic-Koutecky, *Electronic Aspects of Organic Photochemistry* (Wiley, New York, 1990).

[67] H. -J. Zhai, L. -S. Wang, A. N. Alexandrova, A. I. Boldyrev, and V. G. Zakrzewski, J. Phys. Chem. A **107**, 9319 (2003).

[68] T. S. Venkatesan, K. Deepika, and S. Mahapatra, J. Comput. Chem. **27**, 1093 (2006).

[69] D. W. Turner, C. Baker, A. D. Baker, and C. R. Brundle, *Molecular Photoelectron Spectroscopy* (Wiley,New York, 1970).

[70] J. W. Rabalais and A. Katrib, Molec. Phys. **27**, 923 (1974).

[71] R. A. Mackie, A. M. Sands, S. W. J. Scully, D. M. P. Holland, D. A. Shaw, K. F. Dunn, and C. J. Latimer, J. Phys. B: At. Mol. Opt. Phys. **35**, 1061 (2002).

[72] W. A. Lathan, L. A. Curtiss, and J. A. Pople, J. Am. Chem. Soc. **93**, 808 (1971).

[73] J. N. Murrell and W. Schmidt, J. Chem. Soc. Faraday Trans. **68**, 1709 (1972).

[74] K. Kimura, S. Katsumata, Y. Achiba, T. Yamazaki, and S. Iwata, *Handbook of HeI Photoelectron Spectra of Fundamental Organic Molecules* (Japan Scientific Societies Press, 1981).

[75] D. M. P. Holland, L. Karlsson, and K. Siegbahn, J. Electron Spectrosc. and Related Phenom. **125**, 57 (2002).

[76] F. J. Leng and G. L. Nyberg, J. Electron Spectrosc. Relat. Phenom. **11**, 293 (1977).

[77] H. Basch, M. B. Robin, N. A. Kuebler, C. Baker, and D. W. Turner, J. Chem. Phys. **51**, 52 (1969).

[78] A. Schweig and W. Thiel, Chem. Phys. Lett. **21**, 541 (1973).

[79] E. Lindholm, C. Fridh, and L. Åsbrink, Faraday Discuss. Chem. Soc. **54**, 127 (1972).

[80] A. W. Potts and D. G. Streets, J. Chem. Soc., Faraday Trans. II **70**, 875 (1974).

[81] P. R. Keller, J. W. Taylor, T. A. Carlson, T. A. Whitley, and F. A. Grimm, Chem. Phys. **99**, 317 (1985).

[82] E. Haselbach, Chem. Phys. Lett. **7**, 428 (1970).

[83] K. Müller-Dethlefs and J. B. Peel, J. Chem. Phys. **111**, 10550 (1999).

[84] P. Gleiter, Top. Curr. Chem. **86**, 197 (1979).

[85] J. R. Collins and G. R. Gallup, J. Am. Chem. Soc. **104**, 1530 (1982).

[86] W. J. Bouma, D. Poppinger, and L. Radom, Israel J. Chem. **23**, 21 (1983).

[87] T. Koopmans, Physica (Amsterdam), **1**, 104 (1934).

[88] W. von Niessen, L. S. Cederbaum, and W. P. Kraemer, Theor. Chim. Acta, **44**, 85 (1977).

[89] T. S. Venkatesan and S. Mahapatra, J. Chem. Phys. **123**, 114308 (2005).

[90] T. S. Venkatesan, S. Mahapatra, L. S. Cederbaum, and H. Köppel, J. Phys. Chem. A **108**, 2256 (2004).

[91] T. S. Venkatesan, S. Mahapatra, H. -D. Meyer, H. Köppel, and L. S. Cederbaum, J. Phys. Chem. A **111**, 1746 (2007).

[92] T. S. Venkatesan, S. Mahapatra, H. Köppel, and L. S. Cederbaum, J. Mol. Str. 2007 (in press).

[93] M. Born, Nachirichten Akad. Wiss. Göttingen, Math.-Physik Kl. II, Berlin, (1951).

[94] L. S. Cederbaum and W. Domcke, Adv. Chem. Phys. **36**, 205 (1977).

[95] B. H. Lengsfield and D. R. Yarkony, Adv. Chem. Phys. **82**, 1 (1992).

[96] H. C. Longuet-Higgins, Proc. Roy. Soc. London, Ser. A, **344**, 147 (1975).

[97] R. K. Preston and J. C. Tully, J. Chem. Phys. **54**, 4297 (1971).

[98] M. Baer, Chem. Phys. Lett. **35**, 112 (1975).

[99] M. Baer, Mol. Phys. **40**, 1011 (1980).

[100] G. Hirsch, P. J. Bruna, R. J. Buenker, and S. D. Peyerimhoff, Chem. Phys. **45**, 335 (1980)

[101] H. J. Werner and W. Meyer, J. Chem. Phys. **74**, 5802 (1981).

[102] C. A. Mead and D. G. Truhlar, J. Chem. Phys. **77**, 6090 (1982).

[103] T. Pacher, L. S. Cederbaum, and H. Köppel, Adv. Chem. Phys. **84**, 293 (1993).

[104] A. Thiel and H. Köppel, J. Chem. Phys. **110**, 9371 (1999).

[105] H. Köppel, J. Gronki, and S. Mahapatra, J. Chem. Phys. **115**, 23771 (2001).

[106] H. Köppel in Ref. [38], p.429

[107] E. B. Wilson Jr., J. C. Decius, and P. C. Cross, *Molecular vibrations* (McGraw-Hill, New York, 1955).

[108] H. A. Jahn, Proc. R. Soc. London, Ser. A **164**, 117 (1938).

[109] W. Domcke, H. Köppel, and L. S. Cederbaum, Mol. Phys. **43**, 851 (1981).

[110] M. H. Beck, A. Jäckle, G. A. Worth, and H. -D. Meyer, Phys. Rep. **324**, 1 (2000).

[111] P. A. M. Dirac, Proc. Cambridge Philos. Soc. **26**, 376 (1930).

[112] J. Frenkel, *Wave Mechanics* (Clarendon, Oxford, 1934).

[113] A. E. Kuznetsov and A. I. Boldyrev, Struct. Chem. **13**, 2 (2002).

[114] S. Mahapatra, Int. Rev. Phys. Chem, **23**, 483 (2004).

[115] T. H. Dunning, Jr., J. Chem. Phys. **90**, 1007 (1989).

[116] M. J. Frisch, *et al.* Gaussian 03, Revision B. 05, Gaussian, Inc., Pittsburgh PA, 2003.

[117] L. S. Cederbaum, J. Phys. B, **8**, 290 (1975).

[118] W. von Niessen, J. Schirmer, and L. S. Cederbaum, Comp. Phys. Rep. **1**, 57 (1984).

[119] S. Mahapatra and H. Köppel, Phys. Rev. Lett. **81**, 3116 (1998).

[120] R. R. Kumar, T. S. Venkatesan, and S. Mahapatra, Chem. Phys. **329**, 76 (2006).

[121] S. Mahapatra, V. Vallet, C. Woywod, H. Köppel, and W. Domcke, Chem. Phys. **304**, 17 (2004).

[122] G. J. H. van Nes and A. Vos, Acta Crystallogr. **34**, 1947 (1978).

[123] L. S. Cederbaum and W. Domcke, Adv. Chem. Phys. **36**, 205 1977.

[124] A. Markmann, G. A. Worth, S. Mahapatra, H. -D. Meyer, H. Köppel, and L. S. Cederbaum, J. Chem. Phys. **123**, 204310 (2005).

[125] D. Nijveldt and A. Vos, Acta Cryst. **B44**, 281 (1988).

[126] H. Hs. Günthard, R. C. Lord, T. K. McCubbin, Jr., J. Chem. Phys. **25**, 768 (1956).

[127] J. C. Slonczewski, Phys. Rev. **131**, 1596 (1963); J. C. Slonczewski and V. L. Moruzzi, Physics, **3**, 237 (1967).

[128] P. Habitz and W. H. E. Schwarz, Theor. Chim. Acta **28**, 267 (1973); H. Köppel, E. Haller, L. S. Cederbaum, and W. Domcke, Mol. Phys. **41**, 669 (1980).

[129] V. Engel, Chem. Phys. Lett. **189**, 76 (1992).

[130] J. Schmidt-Klügmann, H. Köppel, S. Schmatz, and P. Botschwina, Chem. Phys. Lett. **369**, 21 (2003).

[131] S. Mahapatra, V. Vallet, C. Woywod, H. Köppel, and W. Domcke, J. Chem. Phys. **123**, 231103 (2005).

[132] G. A. Worth and M. A. Robb, Adv. Chem. Phys. **124**, 355 (2002).

[133] C. Lanczos, J. Res. Natl. Bur. Stand. **45**, 255 (1950).

[134] E. Haller and H. Köppel, *Large Scale Eigenvalue Problems*, edited by J. Cullum and R. A. Willoughby (Elsevier, Amsterdam, 1986), pp.163-180.

[135] J. R. Fletcher, J. Phys. C: Solid State Phys. **14**, L491 (1981).

List of Publications

1. **T. S. Venkatesan**, S. Mahapatra, L. S. Cederbaum, and H. Köppel, *"Theoretical investigation of the Jahn-Teller dynamics in the $\widetilde{X}^2E'$ electronic manifold of cyclopropane radical cation"*, J. Phys. Chem. A **108**, 2256 (2004).

2. **T. S. Venkatesan** and S. Mahapatra, *"Exploring the Jahn-Teller and pseudo-Jahn-Teller conical intersections in the ethane radical cation"*, J. Chem. Phys. **123**, 114308 (2005).

3. **T. S. Venkatesan**, K. Deepika, and S. Mahapatra, *"The Jahn-Teller and pseduo-Jahn-Teller effects in the anion photoelectron spectroscopy of B_3 cluster"*, J. Comput. Chem. **27**, 1093 (2006).

4. R. R. Kumar, **T. S. Venkatesan**, and S. Mahapatra, *"A Theoretical investigation of the Jahn-Teller and pseudo-Jahn-Teller effects in the photoionization spectrum of ethane"*, Chem. Phys. **329**, 76 (2006).

5. **T. S. Venkatesan**, S. Mahapatra, H. -D. Meyer, H. Köppel, and L. S. Cederbaum, *"Multimode Jahn-Teller and pseudo-Jahn-Teller interactions in the cyclopropane radical cation: complex vibronic spectra and nonradiative decay dynamics"*, J. Phys. Chem. A **111**, 1746 (2007).

6. V. Sivaranjana Reddy, **T. S. Venkatesan**, and S. Mahapatra, *"Vibronic interactions in the photodetachment spectroscopy of phenide anion"*, J. Chem. Phys. **126**, 074306 (2007).

7. **T. S. Venkatesan**, S. Mahapatra, H. Köppel, and L. S. Cederbaum, *"On the Jahn-Teller and pseudo-Jahn-Teller effects in the photoelectron spectrum of cyclopropane"*, J. Mol. Struc. 2007 (in press).

Posters/Paper/Oral Presentations in Symposia

1. Poster presented in "Trends in Theoretical Chemistry (TTC 2002)", IACS, Kolkata, January 17-19, 2003.

2. Poster presented in "6th National Symposium on Chemistry (VI NSC)", IIT Kanpur, Kanpur, February 6-8, 2004.

3. Poster presented in "Symposium in Theoretical Chemistry (TSC 2004)", BARC, Mumbai, December 9-12, 2004.

4. Poster presented in "Discussion Meeting for Advances in Spectroscopy (DMAS 2004)", Indian Institute of Science, Bangalore, February 21-24, 2005.

5. Poster presented in "Current Developments in Atomic, Molecular and Optical Physics with Applications (CDAMOP 2006)", Delhi University, New Delhi, March 21-23, 2006.

6. Poster presented in "The international symposium on the Jahn-Teller effects: novel aspects of orbital physics and molecular dynamics ", ICTP, Trieste, Italy, August 28-31, 2006.

7. Poster presented in "Theoretical Chemistry Symposium (TCS 2006)", Bharathidasan University, Thiruchirappalli, December 11-13, 2006.

8. Poster presented in "Asian Spectroscopy Conference (ASC 2007)", Indian Institute of Science, Bangalore, January 29-2 February, 2007.

9. Posters presented in "Chemfest 2004, 2005, 2006, and 2007", School of Chemistry, University of Hyderabad, Hyderabad.

10. Paper presented in the Proceedings of the 2^{nd} International Conference on Current Developments in Atomic, Molecular and Optical Physics with Applications, *"Vibronic dynamics of organic hydrocarbons and radicals"*, **T. S. Venkatesan**, R. R. Kumar, V. S. Reddy, and S. Mahapatra, Edited by Man Mohan (2006) - in press.

11. Oral presentation in "Chemfest 2007", School of Chemistry, University of Hyderabad, Hyderabad, March 9-10, 2007.